Influence de la différence entre les distributions de protons et de neutrons dans le noyau sur les processus de fusion et de fission

Artur Dobrowolski

Institut Pluridisciplinaire Hubert CURIEN
STRASBOURG

UMR7178

IPHC 06-007

N° ordre 5082

Thèse

Thèse

Influence de la différence entre les distributions de protons et de neutrons dans le noyau sur les processus de fusion et de fission

Présentée par
Artur DOBROWOLSKI

Institut Pluridisciplinaire
Hubert Curien
23 rue du Loess
BP 28
F-67037 Strasbourg cedex 2
Tél. : (33) 03 88 10 62 14
Fax : (33) 03 88 10 62 92
http://wwwires.in2p3.fr/

CENTRE NATIONAL DE LA RECHERCHE SCIENTIFIQUE

IN2P3 Institut National de Physique Nucléaire et de Physique des Particules

ULP Université Louis Pasteur Strasbourg

IPHC 06-007
N° d'ordre 5082

THESE

présentée

pour obtenir le grade de

DOCTEUR DE L'UNIVERSITE LOUIS PASTEUR DE STRASBOURG

Spécialité: Physique Nucléaire Théorique

par

Artur DOBROWOLSKI

Titre:

Influence de la différence entre les distributions de protons et de neutrons dans le noyau sur les processus de fusion et de fission

Influence of differences in the proton and neutron distributions on nuclear fusion and fission

Soutenue à Lublin (Pologne) le vendredi 21 Avril 2006 devant la commission d'examen :

Philippe QUENTIN	Président et Rapporteur externe
Jacek DOBACZEWSKI	Rapporteur externe
Jerzy DUDEK	Rapporteur interne
Johann BARTEL	Directeur de thèse
Krzysztof POMORSKI	Co-Directeur de thèse
Andrzej GOZDZ	Examinateur
Wieslaw KAMINSKI	Examinateur
Wieslaw GRUSZECKI	Membre invité
Ryszard TARANKO	Membre invité
Marek ROGATKO	Membre invité

I would like to express my great thanks to Professor **Krzysztof Pomorski** *for being the director of both my master and doctoral thesises. Particularly, I am very grateful to him for his scientific advising, patience, and always brilliant ideas which have been extremely helpful for my researches. I appreciate very much frequent and precious discussions during the last six years of our collaboration. Without his optimism and motivating me to the harder work, my fellowship of the French Government could never come true.*

I address my great thanks to Professor **Johann Bartel** *who agreed to be the second director of my thesis for the huge, scientific and organizational help as well as for the hospitality which I obtained from him and his wife* **Micky** *during my numerous stays in Strasbourg. I remember well those many hours spent with him at the round table on long and fruitful discussions. His comments and often critical remarks strongly contributed to the actual contents and form of this work.*

I must not forget about the significant help from Professor **Jerzy Dudek** *who gave me a lot of useful, theoretical and practical indications during my works on the numerical codes.*

I can not find appropriate words which are able to express my special gratitude to **my parents** *for special kind of care, support and indulgence during all 23 years of my education.*

Artur Dobrowolski

Contents

Chapter 1

Introduction and motivations

In low–energy nuclear physics there exist presently two major research projects which are very intensively developed by a wide international collaboration: on one side these are the investigations on the synthesis of heavy and super–heavy elements and, on the other, the study of the lighter so–called *exotic* nuclei, far from the $\beta-$stability line and rich in protons or neutrons.

My thesis work is related to both of these topics, in particular through the study of fusion and fission reactions. This study which is based on the approach known as the *macroscopic-microscopic model* is particularly concerned with the influence of different proton and neutron density distributions on the synthesis and the stability of heavy and super–heavy nuclei. We first examine the behaviour of the liquid–drop energy with respect to different proton–neutron deformations within the semiclassical Extended Thomas–Fermi (ETF) framework and then, using the Yukawa–folding prescription. We use effective nucleon–nucleon interactions of the Skyrme type together with the previously mentioned semiclassical ETF approach to evaluate the energy–density functional of the *di–nuclear* target–projectile system and thereby calculate fusion barriers.

By selectively applying a slight variation to the ETF density radius and diffuseness parameters relative to their variational values, we investigate the importance of different proton–neutron densities on the heights of the fusion barriers.

After obtaining a simple analytical approximation of the nucleus–nucleus potential through the Skyrme ETF approach for reactions leading to super–heavy elements with atomic numbers in the range Z=108–114, the fusion cross sections are determined using the statistical Langevin formalism. The frictional force which is an essential ingredient of this approach was initially proposed by Kramer and later used by many authors. This fusion cross section which is a measure of the probability of forming a compact compound nucleus and which is depending on the height and width of the fusion barrier can be nicely reproduced using the above mentioned analytical expression for the ion–ion potential. This quantity is of crucial importance in the perspective of

the choice of the best possible target–projectile combination to be used in the experiments aiming at the synthesis of the new super–heavy or exotic elements.

Starting the investigations with the macroscopic–microscopic method we have to determine from the beginning what kind of nuclear shapes are relevant and chose the most appropriate deformation space. If one is interested in the ground–state deformations one can use an expression of the nuclear radius in terms of spherical harmonics. If, however, one deals with phenomena leading to much larger deformations, as e.g. encountered in the nuclear fission process, the previously mentioned shape description is no more adequate (because of its very slow convergence). Then one has to allow the nucleus to have more sophisticated shapes as a function of its elongation. In this work we have described nuclear surfaces in cylindrical coordinates with the help of the so–called Funny–Hills parametrization (or a slightly modified version thereof) defined by three deformation parameters: c, h, α correspond respectively to the elongation of the nucleus along the symmetry axis, the neck parameter and the reflection asymmetry parameter.

In order to apply efficiently the macroscopic–microscopic method we should be able to generate the single–particle levels for proton and neutrons which are solution of the single–particle Schrödinger equation with the effective single–particle potential in which each nucleon moves independently. We have chosen the folded–Yukawa potential obtained through the folding the uniform, deformed nuclear density distribution with a Yukawa–type function. It was shown that using this potential one is able to reproduce the masses of atomic nuclei throughout the periodic table with a mean–square error of less then 0.7 MeV. This folding procedure is particularly well suited to generate nuclear potentials for nuclei far from equilibrium where shapes with a characteristic *neck* begin to play an essential role.

During the last decades one could observe in parallel the development of selfconsistent nuclear models based mainly on the Hartree–Fock and Hartree–Fock–Bogoliubov approaches which contributed substantially to our understanding of nuclear structure. The traditional, less complicated and conceptionally more transparent macroscopic–microscopic approach continues nevertheless to provide a very powerful tool to estimate with a good accuracy, a large variety of nuclear properties such as e.g. nuclear masses and energies, fusion and fission barriers in multidimensional spaces, half–lives, cross sections, etc. For these reasons the improvement of this method can be still quite valuable bringing up the information about the nucleus in its equilibrium as well as in excited states. In our research on the average fission barriers as the smooth part of the total energy we use the Lublin–Strasbourg Drop formula (LSD) the parameters of which were fitted to the (at that moment) 2766 experimentally known binding energies. At the present time, this treatment seems to be the most performant approach of the average trends in atomic nuclei. The shell effects are described by means of the Struti-

nsky smoothing procedure while the short–range pairing correlations are determined within the BCS approximation with the so–called *uniform gap method*.

We do not only apply the macroscopic–microscopic model to analyse the fission barriers themselves, but we also wish to discuss in detail the influence on these barriers of different proton–neutron density distributions, an effect which has not been investigated so far. This study is motivated by the results of the selfconsistent Hartree–Fock–Bogoliubov calculations with an effective nucleon–nucleon interaction of the Gogny type which showed that the deformations of protons and neutrons can differ from each other by about 10% along the nuclear fission path of the four examined actinide nuclei: ^{232}Th, ^{236}U, ^{238}U, ^{240}Pu. It turns out that such an effect can by no means be neglected for the estimation of half–lives for spontaneous fission of actinide nuclei as well as for the formation of super–heavy elements.

The last section of this work is devoted to the full four–dimensional fission barriers determined with the help of the macroscopic–microscopic approach. The previously used three dimensional deformation space $\{c, h, \alpha\}$ has been extended by introducing a parameter η describing the non–axiality of the nuclear drop. We concentrate our attention here on the influence of broken reflection and axial symmetries on the barrier shapes of actinide nuclei from $^{232}_{90}$Th to $^{250}_{98}$Cf as well as of some super–heavy elements from $^{266}_{104}$Rf to $^{278}_{116}X$.

This work is organized in the following way: After this introduction we present in section 2 some short historical review of the evolution of the Liquid Drop model up to its latest version given by the Lublin–Strasbourg Drop model. As an alternative for the above, we introduce the Skyrme Extended Thomas–Fermi approach which is used in section 3 to generalize the standard liquid–drop type formulas by adding a new term corresponding to different proton–neutron deformations. The same ETF formalism is also applied in section 4 to determine fusion potentials.

We also give a simple analytical approximation of the ETF fusion potential in terms of the masses and charges of the colliding ions. Based on these calculations we discuss the influence of different proton–neutron density radii on the fusion barrier heights. In section 5 the fusion cross sections are considered using the above mentioned simple approximation of the ETF collision potential.

In order to describe adequately the large variety of shapes relevant for fission barriers we introduce in section 6 two different new versions of the *Funny–Hills* nuclear shape parametrization which turn out to be more suitable than its original version, particularly around the ground state as well as for very elongated shapes of some actinide nuclei. We then give a detailed description of the procedure which is followed here to construct a new numerical code for the diagonalization of the eigenstates of an arbitrary triaxial single–particle potential in the basis of harmonic–oscillator wave functions. Having established the basis to the microscopic calculations we give a short

presentation of the selfconsistent mean–field approach in section 7 before explaining in more detail how the microscopic shell and pairing corrections are included in the macroscopic–microscopic approach through the Strutinsky shell–correction method and the BCS pairing treatment. Section 8 is devoted to the application of the macroscopic–microscopic model to the investigation of the influence of different proton–neutron deformations on the static fission barriers of eight actinide and super–heavy elements. In section 9 we deal with the macroscopic–microscopic four–dimensional fission barriers, taking into account the mass asymmetry and non–axiality of the nuclear surface. The importance of these two additional degrees of freedom is particularly emphasised. Finally, in section 10, we draw the main conclusions of the present work and discuss its possible improvements and extensions.

Chapter 2

Macroscopic approaches of liquid drop type

2.1 History of the Liquid Drop model

Historically, the first macroscopic approach describing the average behaviour of the nuclear energy as a function of the mass of the nucleus was the liquid drop model postulated by Bethe and Weizsäcker already in 1935 [1] [2]. This simple approach is based on two fundamental principles of nuclear physics, namely: the density of the nuclear matter is approximately constant and does not depend on the number of nucleons constituting a nucleus and the fact that average nuclear binding energy per nucleon is almost the same for not to light nuclei. The consequence of the first feature is that the nuclear radius is, in the first approximation, proportional to the number of the nucleons. Both are a direct consequence of the saturation effect of nuclear interactions keeping nucleons together as a strongly bound system. The atomic nucleus, therefore resembles a charged liquid drop composed of nucleons bound by forces which have the following properties:

- strong– the binding energy is given in megaelectronvolts ($10^6\, eV$),
- attractive– inter–nucleon distance larger than the size of a nucleon ($r \geq 1\, fm$),
- strongly repulsive– when nucleons start to overlap substantially,
- short range– vanishing for $r \geq 2\, fm$,
- charge independent–apart from the Coulomb force the interaction is considered to be the same for p–p, n–n, n–p,
- depending mainly on the relative distance of two nucleons ($V_{12} = V(|\vec{r}_{12}|)$).

The first quantitative semi–empirical expression by Bethe and Weizsäcker contained three terms contributing to the binding energy

$$B = a_{vol}\, A - a_{surf}\, A^{2/3} + E_{Coul}, \tag{2.1}$$

which describes respectively the dominant effect of constant nuclear energy per nucleon ($\approx 8\, MeV$), the effect of lowering of the total energy, coming from the fact that at the surface nucleons are less bound then in the nuclear interior (effect comparable to the surface tension in a liquid drop) and the Coulomb repulsion between protons. All these terms can be also considered as the contributions of the, so called, *leptodermous expansion* of the total energy in a power series in $A^{1/3}$. Term proportional to A simulates the average bulk properties of the energy whereas the effect of diminishing the energy due to the nuclear surface tension is proportional to the surface area of the drop, namely to $A^{2/3}$. A further modification of this simple approach was proposed by Green and Bethe in 1953 by considering the effect of the isospin symmetry which has its origin in the *Fermi gas model* [3] which assumes that, due to the Pauli principle and the energy–momentum conservation, fermions can be treated as moving independently from each other. An additional symmetry–energy term in eq. (2.1) would be proportional to $I = \frac{N-Z}{N+Z}$, a quantity which is usually called the *nuclear reduced isospin*. This correction introduces the dependence of the energy on an unequal number of protons and neutrons in a nucleus. In 1967 Myers and Świątecki enriched the discussed model by such a dependence in the volume and the surface energy terms as well as by the inclusion the surface diffuseness of the charge distribution which weakens slightly the Coulomb interaction [4]. Their most important achievement is the fact that they first incorporated the deformation dependence of the binding energy to this model. This was done in such a way that each term in eq. (2.1) except for the volume contribution was multiplied by a function B_{surf} and B_{Coul} depending on the nuclear deformation. Finally, the expression for the binding energy is of the form

$$\begin{aligned} \mathcal{B}(A, Z, def) &= a_{vol}(1 - \kappa_{vol}\, I^2)\, A - a_{surf}(1 - \kappa_{surf}\, I^2)\, A^{2/3}\, B_{surf} \\ &+ \frac{3}{5}\frac{e^2 Z^2}{r_0^{ch} A^{1/3}}\, B_{Coul} - \frac{C_4 Z^2}{A}, \end{aligned} \tag{2.2}$$

where $B_{surf} = \frac{S(def)}{4/3\pi R_0^3}$ is the surface area of the deformed drop relative to the surface of the spherical one of the same volume, while $B_{Coul} = \frac{E_{Coul}(def)}{E_{Coul}(sph)}$ is the ratio of deformed to spherical Coulomb energy. The parameters a_{vol}, κ_{vol}, a_{surf}, κ_{surf}, r_0, C_4 were adjusted to the about 1200 nuclear masses experimentally known at that time. We can thus see that deformation–dependent classical energy expressions can be considered as functions of two groups of variables that describe, respectively, the nucleus itself (Z, N) and its shape, represented by an ensemble of the deformation parameters, here denoted by $\{B_{surf}, B_{Coul}\}$.

2.2 Droplet model

The Droplet Model (DM) gives a more sophisticated and accurate description of the average nuclear binding energy then pure liquid drop approach introduced in the previous section. First of all, this model makes the attempt to include a surface curvature term which, as shown in the subsequent section, improves substantialy the deformation behaviour of the macroscopic energy which has a direct influence on the shapes of nuclear fission barriers. This model takes also into account the fact that the nuclear density inside the nucleus is lowered when the deformation is increased because a certain part of nucleons in the nuclear interior migrate to the enlarging surface region. In that context, the surface asymmetry term proportional to $I^2A^{2/3}$ postulated in the liquid drop model of eq. (2.2) obtains now a clearer interpretation, namely the increase of the nuclear energy is also due to the neutron excess which appears in the nuclear surface. This process is, however, weakened by the nuclear surface tension. As we can conclude from the above, the Droplet Model rejects the assumption of uniform densities and, moreover, distinguishes between proton and neutron distributions. It was therefore necessary to introduce the following new quantities:

- t– thickness of the neutron skin,
- δ– relative excess of the neutron density,
- ε– relative deviation of the density from its nuclear matter value ρ_0,
- Σ– the effective nuclear surface situated between proton and neutron distributions.

The neutron skin is produced as a natural tendency of the nuclear matter to remain symmetric with respect to proton and neutron numbers. It means that for realistic nuclei for which $N > Z$ there exists a force which pushes the excess of neutrons out from the bulk region into the surface. The Coulomb force associated with proton distribution reduces this tendency by trying to increase the radius of the proton distribution. This force faces with the resistance on the surface which also tends to the symmetric conditions i.e. when the neutron skin does not exist. In this context the neutron skin is understood as the distance t between the locations of the proton and neutron diffused surface profiles or in other words, as the shift which is necessary to put one profile on top of the other. This leads to some enrichment of the surface layer in neutrons but not to a pure neutron layer. The above considerations yield that the force which is responsible for producing the surface neutron skin is given by

$$t = \frac{3}{2} r_0 JI/Q, \tag{2.3}$$

where r_0 is the constant radius of nuclear matter, J the nuclear symmetry energy coefficient, and Q the effective surface stiffness coefficient The inclusion of the electrostatic energy for protons (equal to about $c_1 Z^2/A^{1/3}$ with $c_1 = 3e^2/5r_0 \approx 0.7322\,MeV$) reduces this force JI and leads to

$$t = \frac{3}{2} r_0 \frac{JI - \frac{1}{12} c_1 Z A^{-1/3}}{Q}. \tag{2.4}$$

Further considerations lead to the modification of the denominator of this expression

$$t = \frac{3}{2} r_0 \frac{JI - \frac{1}{12} c_1 Z A^{-1/3}}{Q + \frac{9}{4} J A^{-1/3}}. \tag{2.5}$$

This equation correctly predicts that when for an uncharged nucleus Q tends to zero all the excess neutrons are pushed then into the surface ($t \longrightarrow t_{max} = 2/3 R_0 I$). For a nucleus of arbitrary shape the equation for t is of the form

$$t = \tilde{t} + \bar{t}, \tag{2.6}$$

where

$$\bar{t} = \frac{3}{2} r_0 \frac{JI - \frac{1}{12} c_1 Z A^{-1/3} (B_{vol}/B_{surf})}{Q + \frac{9}{4} J A^{-1/3} B_{surf}}, \tag{2.7}$$

$$\tilde{t} = \frac{3}{8} r_0 \frac{e}{Q} (\tilde{v}_s - \bar{\tilde{v}}), \tag{2.8}$$

where in the above $\tilde{v}$ is the deviation from the electrostatic potential v produced by a uniformly distributed charge Ze while $\tilde{v}_s$ is the value of $\tilde{v}$ on the surface and $\bar{\tilde{v}}$ is the surface average of $\tilde{v}_s$. The macroscopic binding energy in the Droplet Model is then expressed in the following form [5]:

$$\begin{aligned} B(A,Z,def) &= \Big(-a_1 + J\,\bar{\delta}^2 - \frac{1}{2}\,K\,\bar{\varepsilon}^2 + \frac{1}{2}\,M\,\bar{\delta}^4 \Big)\,A \\ &+ \Big(a_2 + \frac{9}{4}\,\frac{J^2}{Q}\,\bar{\delta}^2 \Big)\,A^{2/3} B_{surf} + a_3\,A^{1/3}\,B_{curv} \\ &+ c_1\,Z^2\,A^{-1/3}\,B_{Coul} - c_2\,Z^2\,A^{1/3}\,B_r(def) - c_5\,Z^2\,B_w(def) \\ &- \frac{c_3\,Z^2}{A} - \frac{c_4\,Z}{\sqrt[3]{2}} + E_{\mathrm{Wig}}, \end{aligned} \tag{2.9}$$

where B_{Coul}, B_{surf} and B_{curv} express respectively the deformation dependences of the Coulomb energy and the surface curvature energy. The functions $B_r(def)$ and $B_w(def)$ are responsible respectively for the non–homogeneous charge distribution inside and at the surface the nucleus. The Wigner term E_{Wig} is of the form [6]

$$E_{\mathrm{Wig}}(A,Z) = -10\mathrm{MeV} \cdot \exp(-42|I|/10). \tag{2.10}$$

The variables $\bar{\delta}$ and $\bar{\varepsilon}$ are the average quantities δ, ε over the effective surface Σ and are equal to:

$$\bar{\delta} = \frac{I + \frac{3}{16}\frac{c_1}{Q} Z A^{2/3} f(def)}{1 + \frac{9}{4}\frac{J}{Q} A^{-1/3} B_{surf}}, \tag{2.11}$$

$$\bar{\varepsilon} = \frac{1}{K}\Big[-2a_2 A^{-1/3} f(def) + L\bar{\delta}^2 + \ C_1 Z^2 A^{-4/3} g(def)\Big], \tag{2.12}$$

The coefficients c_i can be expressed as follows:

$$\begin{aligned} c_1 &= \frac{3}{5}\frac{e^2}{r_0}, \\ c_2 &= \frac{c_1^2}{336}\left(\frac{1}{J} + \frac{18}{K}\right), \\ c_3 &= \frac{5}{2} c_1 \left(\frac{b}{r_0}\right), \\ c_4 &= \frac{5}{4} c_1 \left(\frac{3}{2\pi}\right)^{2/3}, \\ c_5 &= \frac{1}{64} c_1 \left(\frac{c_1^2}{Q}\right). \end{aligned} \tag{2.13}$$

and the coefficients entering the eqs. (2.3) – (2.13) have the following values [5]:

$$\begin{aligned} a_2 &= 20.69\, MeV \\ K &= 240.0\, MeV \\ L &= 100.0\, MeV \\ r_0 &= 1.18\, fm \\ J &= 36.8\, MeV \\ Q &= 17.0\, MeV \\ e^2 &= 1.440\, MeV \cdot fm \\ b &= 1.0\, fm \end{aligned}$$

The Droplet model contains nine free parameters which were adjusted to experimentally known in that time masses and fission barriers. The combination of the Liquid Drop Model (see section 2) and the Droplet Model described above which preserves only the most relevant features of both these two approaches is presented in the next subsection.

2.3 Lublin–Strasbourg Drop (LSD) model

Since the idea of Bethe and Weizsäcker, the inclusion of various new terms in the average–energy expression has been proposed but the basic concept of a charged liquid

drop remains valid. It is worth reminding at this point that already in 1953 Hill and Wheeler concluded on the basis of the Fermi gas model, [3] that a curvature dependent term proportional to $A^{1/3}$ should exist in the liquid–drop energy functional. The curvature term was later studied in [7], where its magnitude was adjusted to the experimental fission–barrier heights known at that time.

Since the traditional liquid drop model without the explicit use of a curvature–energy term performed already quite well, one may expect that the inclusion of such a surface–curvature term play rather a role of correction. It turns out that such a modification is obvious and yields to a significant improvement of the liquid–drop model formula. In particular, the new r.m.s. deviation $\langle \delta M \rangle = 0.698$ MeV as compared to $\langle \delta M \rangle = 0.732$ MeV within the traditional approach, and the new fission–barrier r.m.s. deviation for nuclei with $Z > 70$, $\langle \delta V_B \rangle = 0.88$ MeV, compared to $\langle \delta V_B \rangle = 5.58$ MeV [8].

A starting point for the analysis which leads to the inclusion of curvature terms is the well known traditional liquid–drop nuclear mass expression of Myers and Świątecki (MS-LD) [4]. This expression was quite successful in reproducing the nuclear masses, but it is known that in light nuclei it overestimates the fission-barrier heights by up to about 10 MeV . The MS-LD barriers are also higher than those evaluated by Sierk [9] within the Yukawa–folding macroscopic model. The Lublin Strasbourg Drop (LSD) formula for the binding energy [8] has therefore the following form:

$$\begin{aligned} B(Z,N,def) &= a_{vol}\,(1-\kappa_{vol}I^2)\,A \\ &+ a_{surf}\,(1-\kappa_{surf}I^2)\,A^{2/3}\,B_{surf}(def) \\ &+ a_{cur}\,(1-\kappa_{cur}I^2)\,A^{1/3}\,B_{cur}(def) \\ &+ \frac{3}{5}\frac{e^2Z^2}{r_0^{ch}\,A^{1/3}}\,B_{Coul}(def) - C_4\,\frac{Z^2}{A} - E_{congr}, \end{aligned} \tag{2.14}$$

where $B_{surf}(def)$, $B_{cur}(def)$, $B_{Coul}(def)$ are explicitly calculated for the case of the modified Funny–Hills parameters in Appendix. The LSD parameters listed below are adjusted to all presently known 2766 experimental binding energies taken from the tables [10] using the microscopic corrections from [11] and the congruence energy E_{congr} estimated in [12].

a_{vol} = -15.4920 MeV	κ_{vol} = 1.8601
a_{sur} = 16.9707 MeV	κ_{sur} = 2.2938
a_{cur} = 3.8602 MeV	κ_{cur} = -2.3764
r_0^{ch} = 1.21725 fm	C_4 = 0.9181 MeV

Tab. 2.1 Parameters of the LSD model

2.4 The Skyrme ETF approach to nuclear structure

Mean–field calculations have been extremely successfull over the last 3 decades to describe the structure of stable as well as radioactive nuclei and this over a very wide range of nuclear masses. Especially effective nucleon-nucleon interactions of the type of Skyrme [13, 14] and Gogny forces [15] have been particularly efficient in this context. Such phenomenological effective interactions can be understood as mathematically simple parametrisations of a density-dependent effective G-matrix (see [16] and [17] for a review on such effective forces).

Together with the exact treatment of the mean–field problem in the Hartree–Fock (HF) approach, semiclassical approximations thereof have proven very appropriate. Especially the approach known as the Extended Thomas–Fermi (ETF) method has been shown [18] to describe very accurately average nuclear properties in the sense of the Bethe–Weizsäcker mass formula [2, 1]. In their selfconsistent version the ETF calculations determine the semi–classical (liquid–drop type) structure of a given nucleus by minimizing the total energy with respect to a variation of the neutron and proton densities, as will be explained below. Such calculations require, however, only **integrated** quantities as e.g. the total nuclear energy.

2.4.1 Skyrme interactions

For effective nucleon–nucleon interactions of the Skyrme type the total energy of a nucleus is a functional

$$E = \int \mathcal{E}\Big[\rho_q(\vec{r}), \tau_q(\vec{r}), \vec{J}_q(\vec{r})\Big]\, d^3r \ , \tag{2.15}$$

of the local densities $\rho_q(\vec{r})$, the kinetic energy densities $\tau_q(\vec{r})$ and the so called spin-orbit densities $\vec{J}_q(\vec{r})$ [14]

$$\begin{aligned}
\rho_q(\vec{r}) &= \sum_{\nu,s} |\varphi_\nu(\vec{r}, s, q)|^2 \, n_\nu^q \\
\tau_q(\vec{r}) &= \sum_{\nu,s} |\vec{\nabla}\varphi_\nu(\vec{r}, s, q)|^2 \, n_\nu^q \\
\vec{J}_q(\vec{r}) &= (-i) \sum_{\nu,s,s'} \varphi_\nu^*(\vec{r}, s', q)\vec{\nabla}\varphi_\nu(\vec{r}, s, q) \times \langle s'|\vec{\sigma}|s\rangle \, n_\nu^q,
\end{aligned} \tag{2.16}$$

where the subscript q=$\{n, p\}$ denotes the nucleon charge state, $\varphi_\nu(\vec{r}, s, q)$ are the single-particle wave functions with orbital and spin quantum numbers ν and s respectively, and n_ν^q being the corresponding occupation numbers (equal to 1 or 0 in the pure Hartree–Fock case, or v_ν^2 if pairing correlations are included).

In the case of broken time–reversal symmetry, particularly encountered in the case of rotating nuclei the energy density depends, in addition, on other local quantities [19, 20], such as the current density $\vec{j}(\vec{r})$ and the spin–vector density $\vec{\rho}(\vec{r})$. In the

following we will restrict ourselves to time–reversal symmetric systems leaving the case of broken time–reversal symmetry. The total energy determined in this way is exact within the HF formalism.

A semiclassical approximation is obtained when instead of using the exact quantum–mechanical densities of eq. (2.16) a semiclassical approximation for these quantities is used.

In the so called *Extended Thomas–Fermi model* [18] semiclassical densities $\tau_q(\vec{r})$ and $\vec{J}_q(\vec{r})$ are obtained as functions of the local density $\rho(\vec{r})$ and of its derivatives. Thomas–Fermi approximation for the functional of the kinetic energy density which is the direct result of the Fermi gas model is of the form:

$$\tau_q^{(TF)}[\rho_q] = \frac{3}{5}\,(3\pi^2)^{2/3}\,\rho_q^{5/3} \quad , \quad q{=}\{n,p\}\ . \tag{2.17}$$

Once these functional expressions are given, the total energy of the nuclear system is then uniquely determined by the knowledge of the local densities of protons and neutrons. That such a functional dependence of the total energy on the local densities $\rho_q(\vec{r})$ should exist is guaranteed by the famous theorem by Hohenberg and Kohn [21]. In the most general quantum mechanical case this functional is, however, perfectly unknown. The great advantage of the semiclassical approach used here, consists in the fact that, in connection with effective interactions of the Skyrme type such an energy functional $\mathcal{E}$ can be derived explicitly. In addition, it is to be noted that the semiclassical functionals obtained in the ETF formalism such as $\tau[\rho]$ are completely general and valid for any local interaction and any nucleus, and can therefore be determined once and forever.

Once the functional of the total energy is known, one is able, due to the Hohenberg–Kohn theorem, to perform density variational calculations, where the local densities $\rho_q(\vec{r})$ are the variational quantities. One should, however, keep in mind that, as the ETF functionals are of semiclassical nature, the density functions $\rho_q(\vec{r})$ obtained as a result of the variational procedure can only be semiclassical in nature, i.e. of the liquid-drop type. Taking into account that in such a process the particle numbers N and Z should be conserved, one can formulate the variational principle in the form

$$\frac{\delta}{\delta\rho_q}\int\left\{\mathcal{E}[\rho_n(\vec{r}),\rho_p(\vec{r})] - \lambda_n\rho_n(\vec{r}) - \lambda_p\rho_p(\vec{r})\right\}d^3r = 0 \tag{2.18}$$

with the Lagrange multipliers λ_n and λ_p to ensure the conservation of neutron and proton number.

This density variational problem has been solved in two different ways in the past: either by resolving the Euler–Lagrange equation [22, 23] resulting from eq. (2.18) or by carrying out the variational calculation in an restricted subspace of functions adapted to the problem, i.e. being of semiclassical nature, free of shell oscillations in the nuclear

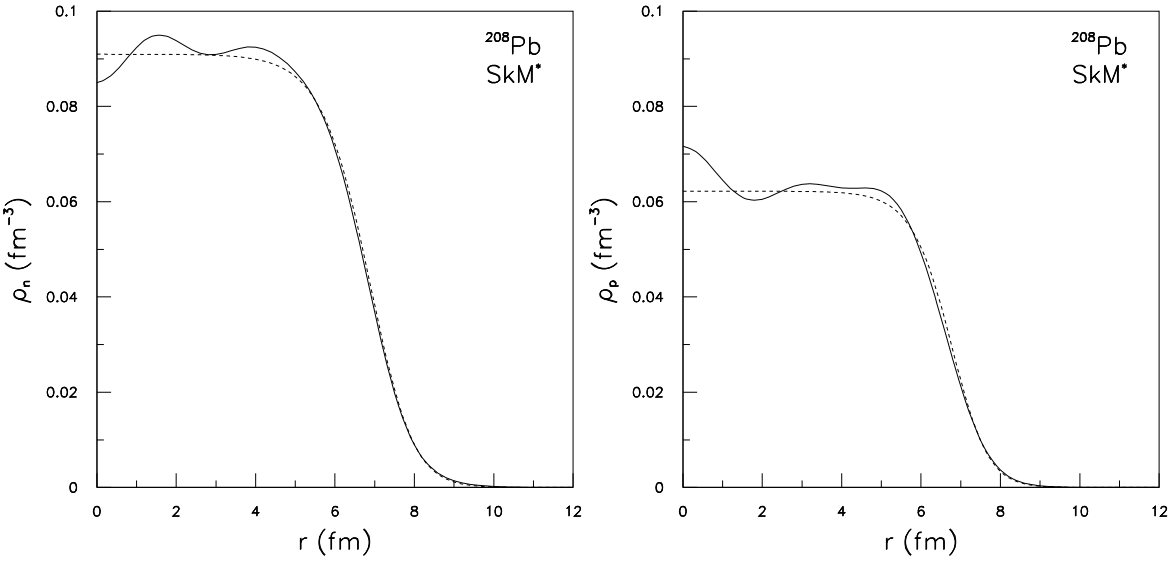

Figure 2.1: Comparison of selfconsistent neutron and proton HF (solid line) and ETF densities (dashed line) for ^{208}Pb calculated with the SkM* Skyrme force

interior and falling off exponentially in the nuclear surface. It has been shown [18, 22] that modified Fermi functions which for spherical symmetry take the form [18]

$$\rho_q(\vec{r}) = \rho_{0_q}\left[1+\exp\left(\frac{r-R_{0_q}}{a_q}\right)\right]^{-\gamma_q} \quad , \quad q{=}\{n,p\} \tag{2.19}$$

are particularly well suited in this context and that the semiclassical energies obtained are, indeed, very close to those resulting from the exact variation [22, 23].

As an example of the quality of the semiclassical density obtained by such a restricted variation in the subspace of modified Fermi functions, eq. (2.19), we show in Fig. 2.1 a comparison of the neutron and proton densities obtained in this way within the ETF approach with the corresponding Hartree–Fock densities for the nucleus ^{208}Pb calculated with the Skyrme interaction SkM* [24]. It should be emphasised here that a similarly good agreement as the one shown in Fig. 2.1 is obtained for other nuclei (see Fig. 2.2), or using other effective interactions such as the Skyrme forces SIII [25] and SLy4 [26].

The energy density $\mathcal{E}$ appearing in eqs. (2.15) and (2.18) can be written for a Skyrme interaction as defined in ref. [27] in the compact form [28]

$$\begin{aligned}\mathcal{E}(\vec{r}) &= \frac{\hbar^2}{2m}\tau + B_1\rho^2 + B_2(\rho_n^2+\rho_p^2) + B_3\rho\,\tau + B_4(\rho_n\,\tau_n+\rho_p\,\tau_p)\\ &-B_5(\vec{\nabla}\rho)^2 - B_6\left[(\vec{\nabla}\rho_n)^2+(\vec{\nabla}\rho_p)^2\right] + \rho^\alpha[B_7\rho^2+B_8(\rho_n^2+\rho_p^2)]\\ &-B_9\left[\vec{J}\cdot\vec{\nabla}\rho+\vec{J}_n\cdot\vec{\nabla}\rho_n+\vec{J}_p\cdot\vec{\nabla}\rho_p\right]+\mathcal{E}_{Coul}(\vec{r})\ ,\end{aligned} \tag{2.20}$$

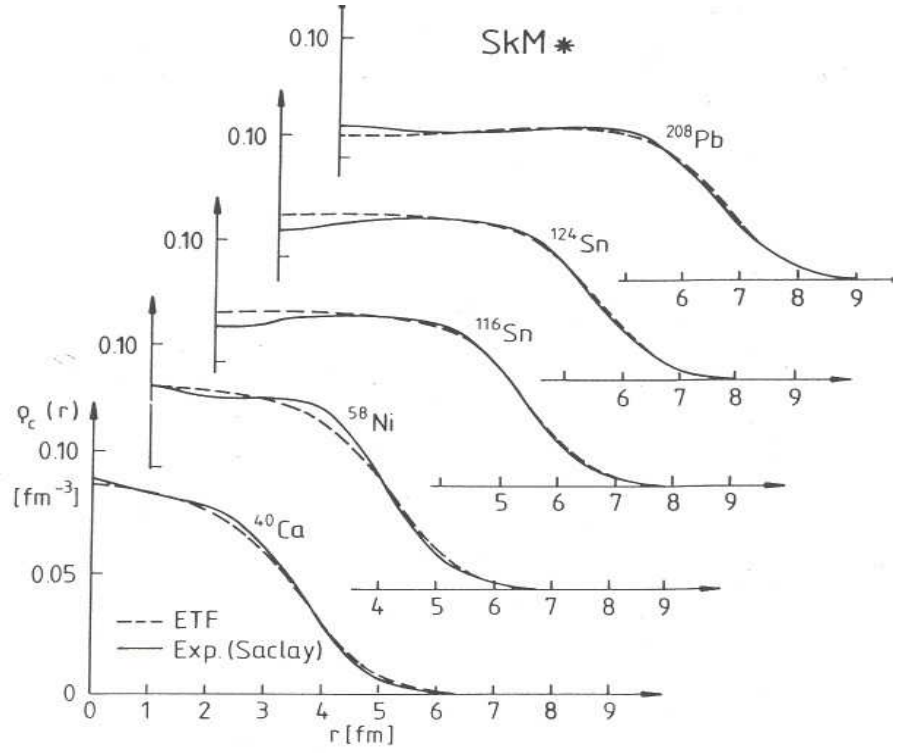

Figure 2.2: Charge densities through $4^{th}-$order ETF + SkM* approach vs the experimental ones for 5 nuclei from different mass regions

given in terms of the coefficients $B_1 - B_9$ (see Tab. 2.2) instead of the usual Skyrme force parameters $t_0, t_1, t_2, t_3, x_0, x_1, x_2, x_3, W_0$:

B_1	$\frac{1}{2}t_0(1+\frac{x_0}{2})$	B_6	$\frac{1}{16}\left[3t_1(x_1+\frac{1}{2})+t_2(x_2+\frac{1}{2})\right]$
B_2	$-\frac{t_0}{2}(\frac{1}{2}+x_0)$	B_7	$\frac{1}{12}t_3(1+\frac{x_3}{2})$
B_3	$\frac{1}{4}\left[t_1(1+\frac{x_1}{2})+t_2(1+\frac{x_2}{2})\right]$	B_8	$-\frac{1}{12}t_3(\frac{1}{2}+x_3)$
B_4	$-\frac{1}{4}\left[t_1(x_1+\frac{1}{2})-t_2(x_2+\frac{1}{2})\right]$	B_9	$-\frac{1}{2}W_0$
B_5	$-\frac{1}{16}\left[3t_1(1+\frac{x_1}{2})-t_2(1+\frac{x_2}{2})\right]$		

Tab. 2.2 Correspondence between the coefficients B_i used in the text and the usual Skyrme force parameters.

In eq. (2.20) non–indexed quantities like ρ correspond to the sum of neutron and proton densities as $\rho = \rho_n + \rho_p$ and $\mathcal{E}_{Coul}$ is the Coulomb energy density which can be written as the sum of the direct and an exchange contribution, the latter being taken into account

in the Slater approximation [29]

$$\mathcal{E}_{Coul}(\vec{r}) = \frac{e^2}{2}\rho_p(\vec{r}) \int d^3r' \, \frac{\rho_p(\vec{r'})}{|\,\vec{r} - \vec{r'}\,|} - \frac{3}{4}e^2\Big(\frac{3}{\pi}\Big)^{1/3} \rho_p^{4/3}(\vec{r}) \; . \tag{2.21}$$

The HF equation is obtained through the variational principle which states that the total energy of eq. (2.15) should be stationary with respect to any variation of the single-particle wave functions $\varphi_j^{(q)}$:

$$\hat{\mathcal{H}}_q \, \varphi_j^{(q)} = \left(-\vec{\nabla}\frac{\hbar^2}{2m_q^*(\vec{r})}\vec{\nabla} + V_q(\vec{r}) - i\vec{W}_q(\vec{r}) \cdot (\vec{\nabla} \times \vec{\sigma}) \right) \varphi_j^{(q)} = \varepsilon_j^{(q)} \, \varphi_j^{(q)} \; . \tag{2.22}$$

Here appear different form factors such as the central one-body potential $V_q(\vec{r})$, the effective mass $m_q^*(\vec{r})$ and the spin–orbit potential $\vec{W}_q(\vec{r})$ which are all defined as functional derivatives of the total energy density. One obtains from eq. (2.20) :

$$\begin{aligned} V_q(\vec{r}) &= \frac{\delta\mathcal{E}(\vec{r})}{\delta\rho_q(\vec{r})} = \\ &= 2(B_1\rho + B_2\rho_q) + B_3\tau + B_4\tau_q + 2(B_5\Delta\rho + B_6\Delta\rho_q) + (2+\alpha)B_7\rho^{\alpha+1} \\ &\quad + B_8\left[\alpha\rho^{\alpha-1}\sum_q \rho_q^2 + 2\rho^\alpha\rho_q\right] + B_9(\mathrm{div}\vec{J} + \mathrm{div}\vec{J}_q) + V_{Coul}(\vec{r})\,\delta_{pq} \; , \end{aligned} \tag{2.23}$$

$$f_q(\vec{r}) = \frac{m}{m_q^*(\vec{r})} = \frac{2m}{\hbar^2}\,\frac{\delta\mathcal{E}(\vec{r})}{\delta\tau_q(\vec{r})} = 1 + \frac{2m}{\hbar^2}\,[B_3\rho(\vec{r}) + B_4\rho_q(\vec{r})] \tag{2.24}$$

and

$$\vec{W}_q(\vec{r}) = \frac{\delta\mathcal{E}(\vec{r})}{\delta\vec{J}_q(\vec{r})} = -B_9\,\vec{\nabla}(\rho + \rho_q) \; . \tag{2.25}$$

The Coulomb potential in eq. (2.23) is easily obtained from eq. (2.21) as

$$V_{Coul}(\vec{r}) = e\int \frac{\rho_p(\vec{r'})}{|\,\vec{r} - \vec{r'}\,|}\, d^3r' - \Big(\frac{e}{\pi}\Big)^{1/3} \rho_p^{1/3}(\vec{r}) \; . \tag{2.26}$$

It is noteworthy in this connection that for such an effective mass (2.24) and the spin–orbit potential (2.25) the energy density (2.20) takes the simple form

$$\begin{aligned} \mathcal{E}(\vec{r}) = \frac{\hbar^2}{2m}\sum_q f_q\,\tau_q + B_1\rho^2 + B_2(\rho_n^2 + \rho_p^2) - B_5(\vec{\nabla}\rho)^2 - B_6\left[(\vec{\nabla}\rho_n)^2 + (\vec{\nabla}\rho_p)^2\right] \\ + \rho^\alpha[B_7\rho^2 + B_8(\rho_n^2 + \rho_p^2)] + \sum_q \vec{J}_q \cdot \vec{W}_q + \mathcal{E}_{Coul}(\vec{r}) \end{aligned} \tag{2.27}$$

which simplifies somewhat the calculation.

All the expressions derived so far (eqs. (2.21) – (2.27)) are exact and when used with densities constructed from the single-particle wave functions $\varphi_j^{(q)}(\vec{r})$, solutions of

the HF equation (2.22) these quantities contain all the quantum effects of the system. If one is interested in the semiclassical approximation of these form factors one can immediately conclude, from the analytical form of eqs. (2.24) and (2.25) and the smooth behaviour of the semiclassical densities, as demonstrated e.g. in Fig. 2.2, on the smooth behaviour of the semiclassical effective mass and spin-orbit form factors. As the nuclear quantal density is well reproduced on the average by the ETF densities it appears evident that the same is going to be the case for the effective mass and the spin-orbit potential, when semiclassical, i.e. liquid-drop type densities are used in eqs. (2.24) and (2.25).

Things are, however, less evident for the central nuclear potentials. Not only is the functional expression, eq. (2.23), much more complicated than those for the effective mass and spin-orbit potential, but the central potential is also the only of the three functional derivatives that depends not only on the local densities $\rho_q(\vec{r})$ and their derivatives but also on the kinetic energy density $\tau_q(\vec{r})$ and the spin-orbit density $\vec{J}_q(\vec{r})$ which are the quantities for which the Extended Thomas–Fermi approach has written down functional expressions. We therefore choose to study the convergence of the semiclassical series corresponding to these functional expressions of $\tau_q[\rho_q]$ and $\vec{J}_q[\rho_q]$ before investigating the quality of the agreement between the HF central potential and the one obtained when using these semiclassical ETF functionals.

2.4.2 Convergence of ETF functionals

The semiclassical expansions of kinetic energy density τ_q and spin-orbit density $\vec{J}_q$ as functions of the local density ρ_q are functional expressions with $\hbar$ as order parameter. These expressions can be obtained for instance through the semiclassical $\hbar$ expansions developed by Wigner [30] and Kirkwood [31] or through the semiclassical method of Baraff and Borowitz [32]. In either of the two approaches one obtains functional expressions like

$$\tau_q^{(ETF)}[\rho_q] = \tau_q^{(TF)}[\rho_q] + \tau_q^{(2)}[\rho_q] + \tau_q^{(4)}[\rho_q] \tag{2.28}$$

written here for the kinetic energy density $\tau_q(\vec{r})$ where $\tau_q^{(TF)}[\rho_q]$ is the well known Thomas–Fermi expression already given in eq. (2.17), $\tau_q^{(2)}[\rho_q]$ the semiclassical correction of second order and $\tau_q^{(4)}[\rho_q]$ is of fourth order in $\hbar$. The ETF expressions up to order $\hbar^4$ such as $\tau_q^{(ETF)}[\rho_q]$, eq. (2.28), are to be understood as the converging part of an asymptotic series.

The second order term $\tau_q^{(2)}[\rho_q]$ has already been derived for a Hamiltonian, eq. (2.22), with an effective mass $m_q^* = m/f_q$ and a spin-orbit potential $\vec{W}_q$

$$\tau_q^{(2)}[\rho_q] = \frac{1}{36}\frac{(\vec{\nabla}\rho_q)^2}{\rho_q} + \frac{1}{3}\Delta\rho_q + \frac{1}{6}\frac{\vec{\nabla}\rho_q \cdot \vec{\nabla} f_q}{f_q} + \frac{1}{6}\rho_q\frac{\Delta f_q}{f_q} - \frac{1}{12}\rho_q\left(\frac{\vec{\nabla} f_q}{f_q}\right)^2$$

$$+\frac{1}{2}\left(\frac{2m}{\hbar^2}\right)^2 \rho_q \left(\frac{\vec{W}_q}{f_q}\right)^2 \tag{2.29}$$

the first term of which is known as the Weizsäcker correction [1] while the last one contributes to the spin–orbit kinetic energy. The Weizsäcker correction was sometimes used in the past with an adjustable parameter (instead of $\frac{1}{36}$) in order to mock up the absence of the other second order and all of the fourth order terms. It has, however, been shown (see e.g. Ref. [18]) that such a procedure is unable to correctly describe both the slope of the surface of the nuclear mass or charge density and, at the same time, the height of nuclear fission barriers in the actinide region. From this analysis we conclude that the inclusion of $4^{th}-$ order terms (expressed in eqs. A.34, A.36 in Appendix) in the semiclassical functionals is, in fact, without credible alternatives.

Let us now investigate the spin–orbit density $\vec{J}$. It is given in Ref. [33] in the form of second rank tensor which is related to the components of the vector $\vec{J}$ by the relation

$$J_\lambda = \sum_{\mu\nu} \epsilon_{\lambda\mu\nu}\, J_{\mu\nu}, \tag{2.30}$$

where $\epsilon_{\lambda\mu\nu}$ is the Levi–Civita symbol. The spin being a purely quantal property with no classical analogon, there is no contribution to the semiclassical functional of $\vec{J}$ in lowest order, i.e. at the level of the Thomas–Fermi approach, whereas one obtains for the 2^{nd} and $4^{th}-$order contributions to the semiclassical expansion of the spin-orbit density

$$\vec{J}_q^{(2)} = -\frac{2m}{\hbar^2}\,\frac{\rho_q}{f_q}\,\vec{W}_q \tag{2.31}$$

and

$$\begin{aligned}\vec{J}_q^{(4)} = (3\pi^2)^{-2/3}\,\frac{2m}{\hbar^2}\,\frac{\rho_q^{1/3}}{8f_q}\Bigg\{&-\Big[\Delta\vec{W}_q + \vec{\nabla}(\mathrm{div}\vec{W}_q)\Big] + \frac{1}{f_q}\Big[\vec{W}_q\,\Delta f_q + (\vec{W}_q\cdot\vec{\nabla})\vec{\nabla}f_q \\ &+(\vec{\nabla}f_q\times\mathrm{rot}\vec{W}_q) + 2(\vec{\nabla}f_q\cdot\vec{\nabla})\vec{W}_q\Big] - \frac{1}{f_q^2}\left[(\vec{\nabla}f_q)^2\vec{W}_q + (\vec{\nabla}f_q\cdot\vec{W}_q)\vec{\nabla}f_q - 2\,(\frac{2m}{\hbar^2})^2\,\vec{W}_q^3\right] \\ &-\frac{1}{3\rho_q}\left[(\vec{\nabla}\rho_q\cdot\vec{\nabla})\vec{W}_q + \mathrm{div}\vec{W}_q\,\vec{\nabla}\rho_q - \frac{1}{f_q}\Big((\vec{\nabla}f_q\cdot\vec{\nabla}\rho_q)\vec{W}_q + (\vec{\nabla}f_q\cdot\vec{W}_q)\vec{\nabla}\rho_q\Big)\right]\Bigg\}.\end{aligned} \tag{2.32}$$

The total spin–orbit density functional entering eqs. (2.20 – 2.27) is then, similarly to eq. (2.28) given as

$$J_q = J_q^{(2)} + J_q^{(4)} \tag{2.33}$$

until now we have not taken into account the spin–orbit contribution to the kinetic energy. Its influence on the semiclassical ETF functionals is treated in Ref. [33] and its contribution $\tau_q^{(4)_{\mathrm{so}}}$ given by eq. (A.36) in Appendix, constitutes simply an additive term to the spin–orbit independent part of the kinetic energy density.

Finally, let us demonstrate the importance of the $4^{th}-$order ETF corrections in the series (2.28) and (2.33) by giving the contributions to the total energy obtained for the different terms at the different orders of the ETF functionals (TF, 2^{th}, 4^{th} order) for the nucleus ^{208}Pb calculated with the SkM* force (see table below)

	E^{τ}_{kin} (MeV)	$E^{s.o.}_{kin}$ (MeV)	$E_{s.o.}$ (MeV)	E_{tot} (MeV)
TF	3822.97	-	-	3822.97
$2^{nd}-$order ETF	63.37	48.74	- 97.48	14.63
$4^{th}-$order ETF	18.11	- 8.74	16.85	26.22

Tab. 2.3 Second and fourth order energy contributions to the total energy of ^{208}Pb obtained with the SkM* force.

The convergence of the kinetic energy density functional is also demonstrated in Fig. 2.3, where the spatial behaviour of kinetic–energy density is investigated for different orders of the semiclassical expansion.

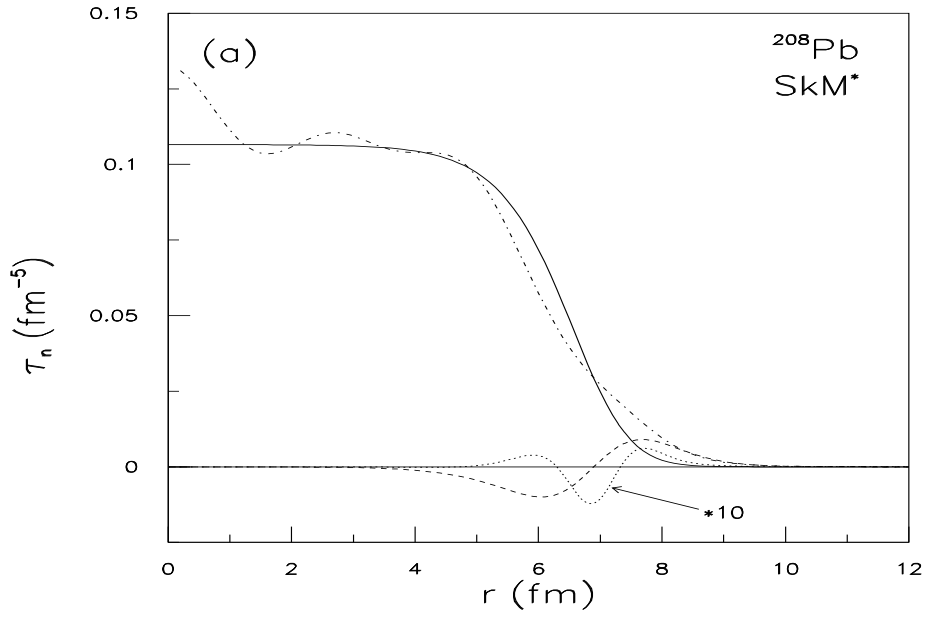

Figure 2.3: Contributions from the different orders in the semiclassical expansion to the kinetic energy density $\tau[\rho]$ for the selfconsistent density distribution shown in Fig. 2.1 for ^{208}Pb (TF (solid line), 2^{nd} order (dashed line), $4^{th}-$order multiplied (dotted line)) are compared with corresponding HF density (dashed–dotted line)

2.4.3 Asymptotic behaviour of the ETF nuclear density

Using the ETF approximation up to $4^{th}-$order we obtain asymptotic fall-off of the nuclear density [18] as

$$\rho(r) \to \frac{c}{r^6} \quad \text{where} \quad r \to \infty$$
$$c = \Big[-\frac{\hbar^2}{2m}(3\pi^2)^{-2/3}\frac{13}{45\lambda}\Big]^{3/2}. \tag{2.34}$$

This result at first seems rather disappointing since it does not give the exponential behaviour we would like to expect from the density. However, we do not know at which distance from the nuclear surface this r^{-6} behaviour is really assumed. In order to investigate this, let us take a typical value of $\lambda = -7\,\text{MeV}$. We then find that $c = 0.03\,fm^3$. If the asymptotic form of eq. (2.34) is assumed at a distance of $r = 10\,fm$ in ^{208}Pb then the density at this point is $3 \times 10^{-8}\,fm^3$.

The asymptotic behaviour obtained in Ref. [23] for the nucleus ^{208}Pb with the Skyrme SkM* force and shown in Fig. 2.4 demonstrates that in order to reproduce this asymptotic behaviour of the density correctly, the full $4^{th}-$order ETF terms have to be included in the selfconsistent semiclassical calculations. The asymptotic behaviour obtained in 2^{nd} order ETF shows a too rapid fall–off, whereas the analytically *wrong* asymptotic behaviour, eq. (2.34), of the 4^{th} order ETF approach turns out to produce an excellent reproduction of the exact quantal behaviour in the physical relevant region.

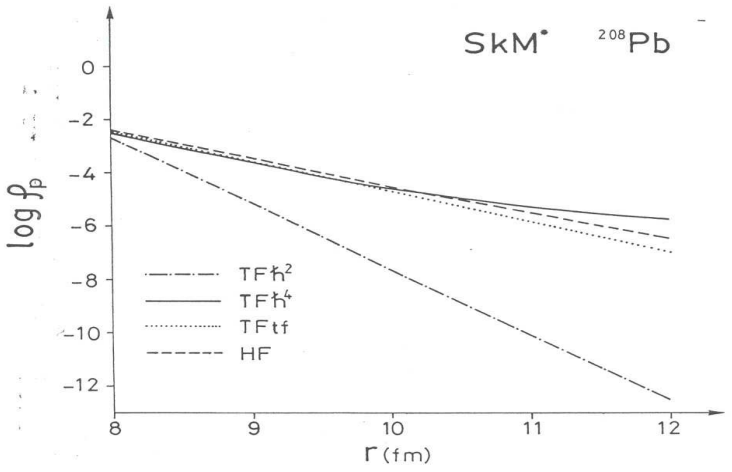

Figure 2.4: Asymptotic behaviour of the nuclear proton density obtained for the nucleus ^{208}Pb with the Skyrme SkM* force at different orders of the ETF approach. The results of the 2^{nd} (dash–dotted line) and full 4^{th} order (solid line) ETF expansions are compared with the corresponding Skyrme HF calculations (dashed line)

Figure 2.4 taken from Ref. [23] demonstrates that the ETF approach gives, indeed, an excellent reproduction of the asymptotic fall–off of the nuclear density when the full $4^{th}-$order contributions are included–and that, in spite of inappropriate fall–off of eq. (2.34), whereas the asymptotic behaviour in $2^{th}-$order ETF turns out wrong.

Chapter 3

ETF model for different density deformations

As it was mentioned in the introduction, in most nuclei, neutrons and protons have slightly different mean–square radii This is mainly due to the Coulomb repulsion between protons and unequal numbers of neutrons and protons.

In deformed nuclei, neutron and proton density distributions are expected to have not only different radii, but also exhibit different shapes, i.e. different quadrupole and higher multipole deformations. An analysis of theoretical densities based on a surface multipole moment expansion shows that significant differences between neutron and proton deformations often occur both in the ground state [34] as well as along the whole path to fission [35]. The Hartree–Fock–Bogolubov (HFB) calculation performed in Ref. [35] with the Gogny effective force for ^{232}Th, ^{236}U, ^{238}U and ^{240}Pu have shown that the multipole deformations of the proton and neutron density distributions of fissioning nuclei are far from being equal. The relative difference between them exceeds often 10 % and undergoes large variations which means that the thickness of the neutron skin does not remain constant as the fissioning nucleus elongates. The effect on the nuclear binding energy of these deformation differences was found to reach approximately 1.5 MeV, with fluctuations of the order of 1 MeV. These variations are clearly not negligible as compared to typical fission barrier heights.

The aim of the present investigation is to develop a new term in the liquid drop type mass formula which will approximate the average variation of the binding energy when protons and neutrons deform in a different way. It seems to us that the most suitable approach to this goal is the Extended Thomas–Fermi (ETF) approximation introduced in section 2.4 above in connection with the Skyrme energy functional. We present results of our calculations for a large sample of nuclei and derive a simple approximate expression which nicely reproduces the effect of the proton and neutron deformation difference in a macroscopic model [36].

3.1 Description of the applied model

In order to determine the nuclear binding energies we use effective nucleon–nucleon interactions of the Skyrme type which describes quite accurately nuclear ground–state properties as well as the low–lying collective excitations [17]. For such an interaction the total energy density $\mathcal{E}(\vec{r})$ is an algebraic function of the neutron and proton densities ρ_n and ρ_p, of the kinetic energy densities τ_n and τ_p and the spin-orbit densities $\vec{J}_n$ and $\vec{J}_p$ (see section2.4 above).

In a first approximation the nuclear energy (without Coulomb term) could be calculated by using the Skyrme functional (2.20) and the Thomas–Fermi (TF) approximation to the kinetic–energy density, eq. (2.17).

3.1.1 The model with sharp–surface distribution

If only ellipsoidal deformations are considered, we can describe the surfaces of nuclei by a very simple parametrization, using a single deformation parameter σ. In this approach the lengths of the axis of the axially symmetric ellipsoids are then given by [37] :

$$\begin{aligned} a = b &= {R_0}^{(q)} \exp\left[-\tfrac{1}{2}\sigma_q\right] \ , \\ c &= {R_0}^{(q)} \exp\left[\sigma_q\right] \ , \end{aligned} \qquad q = \{n, p\} \tag{3.1}$$

where $R_0^{(n)}$ and $R_0^{(p)}$ are the radii of the neutron and proton distributions respectively. Obviously $\sigma > 0$ correspond to prolate and $\sigma < 0$ to oblate deformations. Introducing the isospin parameter $I = \frac{N-Z}{A}$ the following dependence on A and I was obtained in the Relativistic Mean Field calculation of Ref. [38]

$$R_0^{(p)} = 1.237 \left(1 - 0.157\, I - \frac{0.646}{A}\right) A^{1/3} \text{ fm} \ , \tag{3.2}$$

$$R_0^{(n)} = 1.176 \left(1 + 0.250\, I + \frac{2.806}{A}\right) A^{1/3} \text{ fm} \ . \tag{3.3}$$

For ellipsoidal deformations it can be easily shown that the nuclear surface is given by

$$R_q(\theta) = \frac{ac}{\sqrt{a^2\cos^2(\theta) + c^2\sin^2(\theta)}} \ . \tag{3.4}$$

It is obvious that in the case of different deformations and sharp distributions of protons and neutrons there will appear regions in which there exist only protons or neutrons and other regions where both types of particles coexist. In order to evaluate the nuclear energy in such a case, the Skyrme functional depending on the nucleon densities in the form given in Ref. [14] (neglecting the spin–orbit contribution), can be separated in three terms depending only on the proton density, only on the neutron density and an interaction term depending on the densities of both type of particles, namely :

$$V_q = \frac{1}{4}t_0(1 - x_0)\rho_q^2 + \frac{1}{8}(t_1 + 3t_2)\rho_q\,\tau_q + \frac{3}{32}(t_2 - t_1)\rho_q\,\nabla^2\rho_q \ , \tag{3.5}$$

where $q = \{n, p\}$, and

$$\begin{aligned} V_{p\,n} &= t_0(1+\frac{x_0}{2})\rho_p\rho_n + \frac{1}{4}(t_1+t_2)(\rho_p\tau_n + \rho_n\tau_p) \\ &- \frac{1}{16}(3t_1 - t_2)(\rho_p\nabla^2\rho_n + \rho_n\nabla^2\rho_p) + \frac{1}{4}t_3(\rho_n^2\rho_p + \rho_p^2\rho_n) \quad . \end{aligned} \tag{3.6}$$

Finally, $\mathcal{E}$ can be written as

$$\mathcal{E} = \frac{\hbar^2}{2m}(\tau_n + \tau_p) + V_p + V_n + V_{p\,n} \quad . \tag{3.7}$$

The total nuclear energy $E_{nuc}(N, Z)$ is then given as the volume integral of $\mathcal{E}(\vec{r})$.

$$E_{nuc}(N, Z) = \int \mathcal{E}(\vec{r})\, d^3r \quad . \tag{3.8}$$

In the case of a sharp surface distribution the changes of the nuclear part of the energy ΔE_{nuc} as a function of deformation can be just expressed as the product of the volume $\Omega_{p\,n}$ where protons and neutrons coexist and the term of the energy density connected with the interaction of these two types of particles :

$$\Delta E_{nuc}(\Delta\sigma) = V_{p\,n}\,\Omega_{p\,n} \quad , \tag{3.9}$$

where (see Ref. [36])

$$\begin{aligned} \Omega_{p\,n} &= \frac{4}{3}\pi(R_0^{(p)})^3 \left\{ \left[1 - \frac{\left(\frac{R_0^{(p)}}{R_0^{(n)}}\right)^2 \exp(\Delta\sigma) - 1}{\exp(3\Delta\sigma) - 1} \right]^{3/2} - 1 \right\} \\ &- \frac{4}{3}\pi(R_0^{(n)})^3 \left\{ \left[1 - \frac{\left(\frac{R_0^{(n)}}{R_0^{(p)}}\right)^2 \exp(-\Delta\sigma) - 1}{1 - \exp(-3\Delta\sigma)} \right]^{3/2} - 1 \right\} \end{aligned} \tag{3.10}$$

with $\Delta\sigma = \sigma_n - \sigma_p$ and where the term in curly brackets ensures the volume conservation in the case of ellipsoidal deformations which are considered here (see Ref. [36]).

One should notice that for this type of nucleon densities, the terms of $\mathcal{E}(\vec{r})$ in $\nabla^2\rho$ vanish, so that the nuclear energy does not change during the deformation process as long as the proton and neutron distribution do not cross each other, since the volumes between the sharp surfaces is kept constant. After the surfaces intersect the energy rapidly decrease because there the region in which protons and neutrons coexist $\Omega_{p\,n}$ changes its volume as a function of the deformation. This fact leads to the changes of the term $V_{p\,n}$, while terms V_p and V_n are constant. A typical behaviour of the binding energy with growing proton–neutron deformation difference is presented in Fig. 3.1. The model with the uniform density distribution is, of course, too rough to make realistic estimates but nevertheless it should give some idea about the main effect.

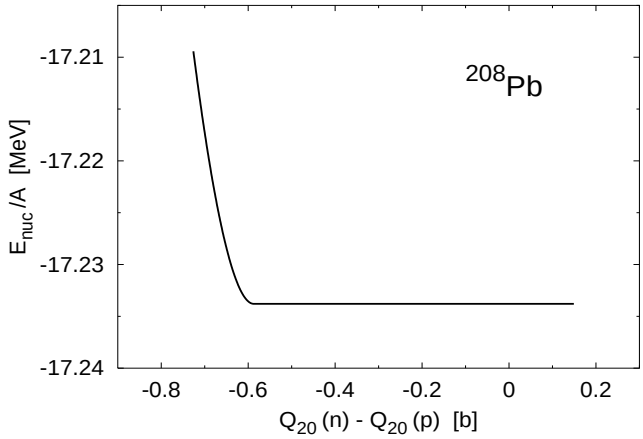

Figure 3.1: Typical behaviour of the binding energy with growing neutron–proton deformation difference for the nucleus ^{208}Pb and the sharp proton and neutron density distributions

3.1.2 The model with the Fermi–type density distribution

More accurate estimates of the change of the binding energy when the protons and neutrons deform differently can be made with diffuse density profiles. In the following we have chosen for our analysis the density distributions in the form of Fermi functions

$$\rho_q(r,\theta) = \frac{\rho_{0_q}}{1+\exp(\frac{r-R_q(\theta)}{a_q(\theta)})} \quad , \tag{3.11}$$

where ρ_{0_q} are the saturation density parameters obtained from the normalization conditions :

$$\int \rho_p(r) d^3r = Z \quad , \qquad \int \rho_n(r) d^3r = N \tag{3.12}$$

and where $R_q(\theta)$ is given by eq. (3.4). The surface width parameters a_q, are $\theta-$dependent and equal to

$$a_q(\theta) = \sqrt{\sin^4(\theta) + \cos^4(\theta) + \sin^2(\theta)\cos^2(\theta)[\exp(3\sigma_q) + \exp(-3\sigma_q)]}\ \ a_{0_q}. \tag{3.13}$$

This definition guarantees that the surface diffuseness is constant along the direction perpendicular to the surfaces of the ellipsoids. The parameters $\{R_{0_n}, a_{0_n}, R_{0_p}, a_{0_p}\}$ characterizing the spherical Fermi density distribution of neutrons and protons are obtained by the variational calculations of the energy functional (2.18) within the second order ETF approximation (2.29) and (2.31) using the Skyrme SIII force [25].

3.2 A simple analytical deformation dependence

The calculation were performed for 28 even–even nuclei involving several isotopic chains from Ni to Th. We suppose that the deformation of these nuclei can be characterized

by a single *global* deformation parameter α identical for protons and neutrons plus a quadrupole type deformation parameter $\Delta\tilde{\beta}$ measuring the difference in the proton versus neutron deformation. The global deformation α of the nucleon distribution can be e.g. defined as the parameter α introduced by Myers and Świątecki [37] through

$$\alpha^2 = 2\pi \int_0^\pi d\theta \left[\frac{R(\theta) - R_{00}}{R_{00}}\right]^2 \ , \tag{3.14}$$

where $R(\theta)$ is the half–density radius of the nucleon distribution of the deformed nucleus and R_{00} the radius of the corresponding spherical distribution. For an ellipsoidal deformation as characterized by eq. (3.1) α can be easily expressed in terms of the parameter σ by [39]

$$\alpha^2 = \sigma^2[1 - \frac{1}{7}\sigma + \mathcal{O}(\sigma^2)] \ . \tag{3.15}$$

In order to be able to express the total energy as a function of the difference $\Delta\tilde{\beta}$ between the proton versus neutron deformation we need to find a way to express this difference in a way which is independent of the specific choice of the deformation parameters like e.g. in eq. (3.1). We have chosen to define the parameters $\tilde{\beta}_q$ as :

$$\tilde{\beta}_q = \frac{Q_{20}^{(q)}}{\tilde{Q}_{00}^{(q)}} \ , \tag{3.16}$$

where the $Q_{00}^{(q)}$ are the monopole and $Q_{20}^{(q)}$ the quadrupole moments of the proton and neutron distribution with

$$Q_{\lambda 0}^{(q)} = \int \rho_q(\vec{r})\, r^2\, P_\lambda\, d^3r \ , \tag{3.17}$$

and where

$$\begin{aligned} Q_{00}^{tot} &= Q_{00}^{(n)} + Q_{00}^{(p)} \ , \\ \tilde{Q}_{00}^{(p)} &= Q_{00}^{tot} \cdot \frac{Z}{A} \ , \\ \tilde{Q}_{00}^{(n)} &= Q_{00}^{tot} \cdot \frac{N}{A} \ . \end{aligned} \tag{3.18}$$

are the so–called average monopole moments for protons and neutrons respectively.

We have found that contrary to the rapid change (Fig. 3.1) of the binding energy in case of the uniform density distribution the nuclear part of the energy varies almost parabolically with the proton and neutron deformation difference $\Delta\tilde{\beta}$, when the smooth density profile (3.11) is assumed for protons and neutrons.

The binding energy can then be parametrized in the following form

$$B(A, I, \alpha, \tilde{\beta}_n, \tilde{\beta}_p) = B_{avr}(A, I, \alpha) + a(A, I, \alpha) \cdot (\tilde{\beta}_n - \tilde{\beta}_p)^2 \ , \tag{3.19}$$

where B_{avr} is the part of the energy that is generated for *equal* deformations for protons and neutrons and which can be obtained e.g. from the standard liquid drop or droplet

model as described in section 2. In order to determine the stiffness parameter a of the parabolic form in $\Delta\tilde{\beta}$ we proceed in the following way:
For various nuclei with different values of the mass parameter A and isospin parameter I and for $\alpha \neq 0$ we find that this parameter $a(A, I, \alpha)$ can be expressed in the form

$$a(A, I, \alpha) = a_0(A, I)\,[1 - c_2\,\alpha(1 + c_3\,I)] \quad , \tag{3.20}$$

where the deformation independent coefficient $a_0(A, I)$ can be parametrized as

$$a_0(A, I) = c_1\left(A^{1/3}\right)^n \quad . \tag{3.21}$$

The values found by our fitting procedure for the parameters c_1, c_2, c_3 and n are the following

$$c_1 = 1.21\,\mathrm{MeV} \quad , \qquad c_2 = 3.0 \quad , \qquad c_3 = 3.0 \quad , \qquad n = 4 \quad .$$

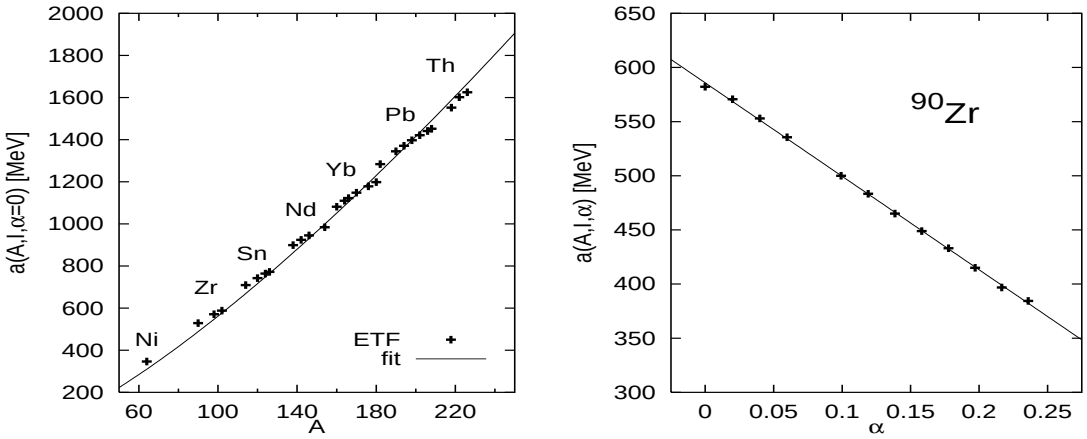

Figure 3.2: The mass number (l.h.s. figure) and the deformation (r.h.s. figure) dependence (crosses) of the stiffness parameter $a(A, I, \alpha)$ (eq. 3.19) and its approximation by the formula (3.20) (solid lines).

The stiffness parameter $a(A, I, \alpha)$ evaluated for all considered isotopic chains is compared in the Fig. 3.2 at $\alpha = 0$ deformation with the parameter $a_0(A, I)$, eq. (3.21). The α deformation dependence of the parameter $a(A, I, \alpha)$ is illustrated for the nucleus ^{90}Zr in Fig. 3.2. We have also compared the above estimate of $a(A, I, \alpha)$ with the results obtained using two other Skyrme interactions. We have found that the estimates obtained with the Skyrme SII and SVII forces are identical within 10% to those presented above for SIII. The quality of the fit of the binding energy as function of the deformation difference is demonstrated on Fig. 3.3 for three nuclei from different mass regions, namely: (^{98}Zr, ^{146}Nd and ^{208}Pb) and for three different values of the global deformation parameter α.

In order to test the predictive power of equation (3.19) we have performed an additional calculation for three dysprosium isotopes (neutron deficient, $\beta-$stable and

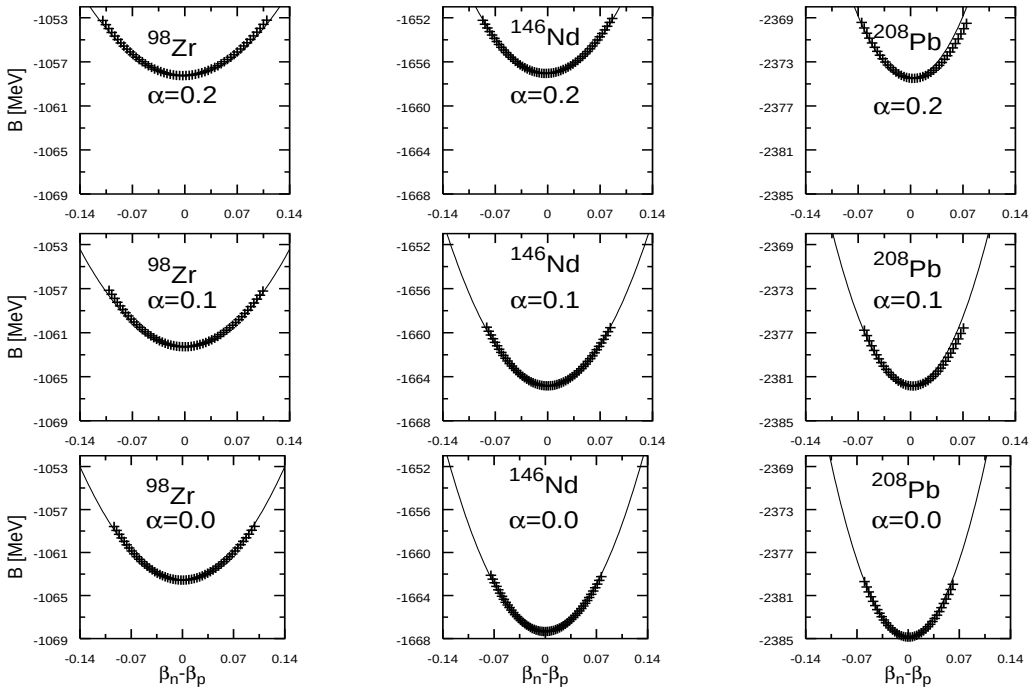

Figure 3.3: Change of binding energies due to different neutron–proton deformations obtained in the ETF approach is compared with the approximate expression of eq. (3.20).

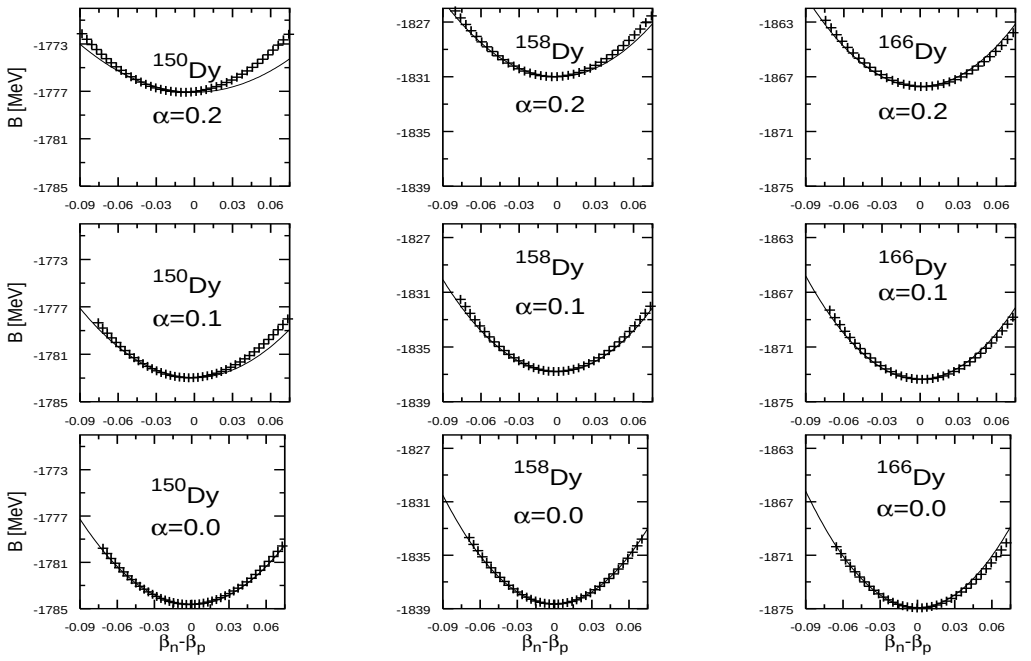

Figure 3.4: The approximation (3.19) of the binding energy (solid line) made for three Dy isotopes and at three deformations is compared with the ETF results (crosses) as function of the neutron-proton deformation difference.

neutron rich) and compare their ETF energies (see Fig. 3.4) with the approximation given by (3.19).

As can be seen in Fig. 3.4 the agreement of both results is rather satisfactory in all cases, except for the very deformed neutron deficient ^{150}Dy isotope.

When $\alpha \neq 0$ and $(\tilde{\beta}_n - \tilde{\beta}_p) = 0$, the energy B_{avr} can be reproduced by any macroscopic approximation like the liquid drop or droplet model.

The correction (3.19) in the nuclear mass formula which describes the effect of different proton–neutron deformations turns out to be, as seen from eqs. (3.20) and (3.21) proportional to the square of the deformation difference of both distributions and increases as $A^{4/3}$. It is clear that one deformation parameter $\tilde{\beta}_q$ used to parameterize the discussed effect is not sufficient when one needs to consider larger global deformations, α far beyond the equilibrium state. Then, on the nuclear way to fission, as we know, higher order multipole deformations begin to play an essential role. until now, in any type of macroscopic approach based on the leptodermous expansion, the term proportional to $A^{4/3}$ was considered as negligible small as compared to the other terms in the series (see section 2 for details). The $A^{4/3}-$dependence of the correction (3.19) corresponding to different proton–neutron deformations can therefore not be absorbed in actually existing macroscopic liquid drop approaches by a simple readjusting of their parameters and must be treated rather as the additional additive term. More advanced study of this effect is presented in section 6.4.6 within the framework of the Yukawa–folding procedure, where, apart from the where, apart from the deformation connected with the elongation of a nucleus also the possibility of forming the neck in the nuclear surface is considered.

Chapter 4

Enterance channel of heavy–ion collisions

4.1 Short historical review

The knowledge of the collective potentials between two colliding ions is absolutely crucial for the synthesis of new isotopes. This problem has been the subject of a very active research over the last decade and remains one of the most intensively studied subjects in low–energy nuclear physics in particular in the perspective of the synthesis of super-heavy elements as well as of exotic nuclei far away from the $\beta-$stability line. It has in particular been shown that models based on a macroscopic approach such as the liquid drop model or of semi–classical type like the extended Thomas-Fermi (ETF) method together with the Skyrme energy–density functional are able to reproduces quite accurately experimental data on fission and fusion barriers.

The research concerning the interaction potential between colliding ions goes back to the work of R. Bass (for a review see Ref. [40], [41]) who parameterized the total ion–ion potential $V_{12}(r,l)$ (including the centrifugal term) as function of the inter–nuclear distance r by a very simple formula:

$$V_{12}(r,l) = \frac{e^2 Z_1 Z_2}{r} - a_{surf}\, A_1^{1/3} A_2^{1/3} \frac{d}{R_{12}} \exp\Big(-\frac{r-R_{12}}{d}\Big) + \frac{\hbar^2 l^2}{2\mu r^2}, \qquad (4.1)$$

where a_{surf} is the surface parameter of the Liquid–Drop Model introduced in chapter 2, $R_{12} = R_1 + R_2 = r_0(A_1^{1/3} + A_2^{1/3})$ the center–of–mass distance between the two spherical nuclei, l the angular momentum of the system and μ its reduced mass. The variables d, r_0 are the adjustable parameters of this model.

A few years later, Krappe, Nix and Sierk proposed a folding procedure with the phenomenological Yukawa–plus–exponential interaction [42] to determine the interaction potential through the optical potential obtained within the Feshbach's theory [43]

$$U_{opt} = \Big\langle \Phi_0\Psi_0 \Big| V + VQ\frac{1}{E - QHQ + i\epsilon}QV \Big| \Phi_0\Psi_0 \Big\rangle, \qquad (4.2)$$

where V and H are the potential and Hamiltonian of the entire system ϵ is the averaging energy interval in the optical model and $Q = 1 - P$, with P being the projection operator on the elastic channel. The ground–state wave–functions Φ_0 and Ψ_0 of the target and projectile respectively are assumed to depend only on their internal coordinates. Since only the real part of the optical potential $\langle\Phi_0\Psi_0|V|\Phi_0\Psi_0\rangle$ can be identified with the Yukawa–plus–exponential double–folding potential, the following expression is used:

$$V = -V_0 + B\frac{r}{R_{12}} + C\Big(\frac{r}{R_{12}}\Big)^2 \tag{4.3}$$

with $R_{12} = R_1 + R_2$, B and C are determined by requiring that the value of the potential and its first derivative must be continuous at the touching configuration of target and projectile. That yields

$$B = 2V_0 - D\Big[\Big(\frac{R_{12}}{a} + 3\Big)F - \frac{R_{12}}{a}\Big], \tag{4.4}$$

$$C = -V_0 + D\Big[\Big(\frac{R_{12}}{a} + 2\Big)F - \frac{R_{12}}{a}\Big], \tag{4.5}$$

where D, F and V_0 are defined within the Yukawa–plus–exponential model.
Since the appearance of the idea of a proximity potential of W. J. Świątecki and coworkers in the late 1970's [44], many improvements have been proposed to make this phenomenological approach more realistic and general, in particular by taking into account the local curvature of the surfaces of target and projectile [45, 46]. One of the main challenges was, as already mentioned, to give a reliable guideline for the formation and stability of super–heavy elements.

The parameters of the proximity function are usually fitted to experimentally known fusion barriers heights. The basic idea of all proximity models is to determine the potential between the two colliding nuclei as function of the minimal distance s of their surfaces and their so–called reduced radius defined in the case of spherical nuclei as $\bar{R} = R_1\,R_2/(R_1+R_2)$, where the indices 1 and 2 refer to the target and projectile nucleus respectively.

Experimental data confirm the existence of a local minimum (pocket) in the shape of the nuclear part of the potential near the touching configuration of target and projectile which forms as the result of the competition of the short range nuclear interaction of colliding nuclei and long range Coulomb repulsion between them. This feature plays an essential role for the formation probability but also for the stability of the compound nucleus in the fusion experiments and is the first decisive step for fusion. Indeed, if the potential pocket is deep and wide, several quasi-bound states might be populated and the probability of forming that specific compound nucleus is large. If, on the other hand, this minimum is shallow and narrow no such states will exist. The pocket depth decreases with increasing size of the projectile. For example, in the case of ^{208}Pb target there exists practically no pocket for the ^{96}Zr+^{208}Pb system

and for heavier projectiles. The mentioned potential pocket is also much shallower for reactions leading to super–heavy elements then for these with lighter colliding systems. It would therefore be of great importance to have at hand a simple, yet sufficiently accurate phenomenological expression for the determination of fusion barriers in order to evaluate the most favourable reaction for the formation of a given compound nucleus.

The aim of the investigations presented below is to show that the shape of the proximity potential can be, indeed, quite accurately determined through selfconsistent semiclassical calculations. We proceed in a way similar to that suggested in Ref. [47] and recently used in Ref. [48]. For the calculation of the interaction potential between the two nuclei we need an energy–density functional which has proven its capacity to correctly describe nuclear ground-state properties. As we are interested in the potential energy resulting from the interaction of the tails of the density distributions of target and projectile, a very precise description of the nuclear surface seems crucial. The Skyrme effective interaction, in particular in the parametrizations known as SkM*, SIII, SLy4 have been one of the most successful effective nucleon–nucleon interactions over the last two decades [24, 25, 49].

4.2 Entrance channel dynamics

The fusion process is considered to be a part of the quantum–mechanical scattering process between two nuclei. In such a formulation one has to consider all kinds of possible scattering channels which are coupled to the entrance channel of the colliding nuclei. Thus we face the problem of the description of the coupling of large number of such *partial* channels which include the inelastic excitations and nucleon–transfers, quasi–fission, compound–nucleus formation and fission. To be able to deal with the complexity of this problem we have to formulate the static scattering problem in an appropriate way. It is obvious, however, that the energy dependence of the entrance–channel wave–function strongly affects the cross sections for all mentioned processes including those which lead to the compact–shape configurations. We will evaluate below the interaction potential in the entrance channel in a semiclassical approach keeping the densities of the colliding nuclei fixed.

Since the elastic channel of the ion–ion collision is uniquely defined outside the range of nucleus-nucleus interactions, there is considerable freedom inside. In principle, any model, which asymptotically describes two nuclei in their ground states, is possible if all relevant inelastic channels are included in the solution of the scattering problem. However, from a physical point of view a reasonable theoretical description should account for the essential collective dynamics in the region of the overlap. A crucial quantity, which characterizes the collective dynamics in the entrance channel during the capture process, is the nuclear interaction time τ_{coll} (collision time) as compared

to the characteristic time τ_{relax} for the relaxation of the intrinsic nuclear state due to the nucleon–nucleon interactions. The collision time τ_{coll} can be estimated [50] by

$$\tau_{coll} \approx \frac{\pi}{\omega_{pocket}} = \pi\sqrt{\frac{mA_1A_2}{(A_1+A_2)V''R_{pocket}}}, \tag{4.6}$$

where ω_{pocket} denotes the *oscillator frequency* of the interaction potential pocket $V(r)$, R_{pocket} is the distance between the centers of mass of both ions corresponding to the minimum of the interaction energy, while m, A_1 andA_2 are the bare nucleon mass and the respective numbers of nucleons of the colliding nuclei.

A typical value for ω_{pocket} in reactions leading to super–heavy elements is given by $\hbar\omega_{pocket} \approx 4MeV$. Therefore, typical collision times for such cases are $\tau_{coll} \approx 5\times10^{-22}$s. This value has to be compared to typical times for the relaxation of the intrinsic nuclear structure due to the nucleon–nucleon interactions. This time is approximately equal to [50]

$$\tau_{relax} \approx \frac{\epsilon_F}{3.2\sigma v_F \rho_0 \varepsilon^*} \approx \frac{2\times10^{-22}}{\varepsilon^*/MeV}s, \tag{4.7}$$

where ϵ_F and v_F denote respectively the Fermi energy and velocity, σ the averaged nucleon–nucleon cross section, ρ_0 the saturation density of nuclear matter and ε^* the excitation energy per nucleon. For reactions leading to super–heavy nuclei the excitation energy is very small and we have at the touching configuration $\varepsilon^* \leq (5MeV)/250 \approx$ 0.02 MeV, and hence $\tau_{relax} \geq 10^{-20}$s, i.e. more than one order of magnitude larger than the collision time τ_{coll}. Thus, we conclude that the entrance channel in the region of nucleus–nucleus overlap is well defined by the fixed configuration of the colliding nuclei. This means that the interaction energy of two overlapping nuclei with *frozen* densities is a good approximation. This frozen–density approach should, however, not be applied to very large overlaps of the density distributions of a target and projectile. A suitable extension into regions of compact shapes would be the diabatic approach of the entrance–channel configuration [51, 52] which is not going to be discussed in this work. Furthermore, the mentioned adiabatic potential should be regarded as a suitable reference for more realistic diabatic potentials and barriers.

4.3 The ETF fusion potential

Since our aim is to evaluate fusion barriers, a quantity which is essentially determined by the radii and tails of the density distributions of target and projectile, we have chosen the semiclassical Extended Thomas–Fermi (ETF) method discussed in section 2.4 to determine in a selfconsistent way the structure of projectile and target nuclei.

We have carried out the 4^{th}–order ETF calculations, to determine the structure of target and projectile nucleus. The density profiles of protons and neutrons in the

form of modified Fermi functions, given by eq. (2.19), obtained in this way are then used to determine the fusion potential between the two nuclei.

For evaluating the fusion potential we will use the *frozen–density approximation*, i.e. keeping the densities of the colliding ions fixed and neglecting all possible rearrangement effects, an approach already explained in the previous section. Thus, the total density profile of the *dinuclear* system is simply the sum of the densities of target and projectile ($\rho = \rho_{tar} + \rho_{proj}$) as showed in Fig. 4.1. The limits of this simple approximation were already discussed in the previous section. Notice, that in the case of negative intersurface distances, the total density of the target–projectile system in the overlap region exceeds the average saturation density of the nuclear matter. For low–energy nuclear collisions the Pauli principle will come fully into play, which as a consequence causes that the repulsion between nucleons violently increases as a function of their mutual distance.

For a fusion reaction the beam energy per nucleon is, indeed, quite small as compared to the Fermi energy and a kind of adiabatic treatment would be appropriate. One has, however, to keep in mind that the essential characteristics of the fusion barrier, as its structure around the above mentioned pocket, are determined at distances larger and close to the touching configuration. Defining the minimal distance s between the equivalent sharp surfaces of the liquid drops identifying the two nuclei we see that the essential features of the fusion barrier or cross sections are determined at the distances ($s > 0$), where the frozen–density approximation seems to be a very reasonable approach.

We can then evaluate the nuclear part of the interaction potential V_{nuc} of two spherical colliding ions as function of the distance d between theirs centers of mass as :

$$V_{nuc}(d\,) = \int \left\{ \mathcal{E}_{nuc}[\rho^{(1)}(\vec{r}\,) + \rho^{(2)}(\vec{r} - \vec{d}\,)] - \mathcal{E}_{nuc}[\rho^{(1)}(\vec{r}\,)] - \mathcal{E}_{nuc}[\rho^{(2)}(\vec{r} - \vec{d}\,)] \right\} d^3r \,, \quad (4.8)$$

where $\mathcal{E}_{nuc}$ is the nuclear part of the energy-density, eq. (2.27), and $\rho^{(i)}(\vec{r}\,)$ denotes the density distribution of nucleus i alone ((1) labelling e.g. the target and (2) the projectile). If the distance d between the two nuclei is much larger than the sum of the half density radii ($d \gg R_1 + R_2$) then the nuclear part of the interaction should vanish because of the short range of the nuclear forces

$$\lim_{d\to\infty} \mathcal{E}_{nuc}\Big[\rho^{(1)}(\vec{r}\,) + \rho^{(2)}(\vec{r} - \vec{d}\,)\Big] = \mathcal{E}_{nuc}\left[\rho^{(1)}(\vec{r}\,)\right] + \mathcal{E}_{nuc}\left[\rho^{(2)}(\vec{r}\,)\right] \,. \quad (4.9)$$

Thus, the nuclear part of the interaction potential (4.8) between the nuclei is non negligible only when the distance s between the nuclear surfaces of both nuclei is smaller then a few fm. The Coulomb interaction between the two ions is given as usual in the form

$$V_{Coul}(d\,) = \int \frac{\rho^{(1)}_{ch}(\vec{r}_1)\, \rho^{(2)}_{ch}(\vec{r}_2)}{|\,\vec{r}_1 - \vec{r}_2\,|}\, d^3r_1\, d^3r_2, \quad (4.10)$$

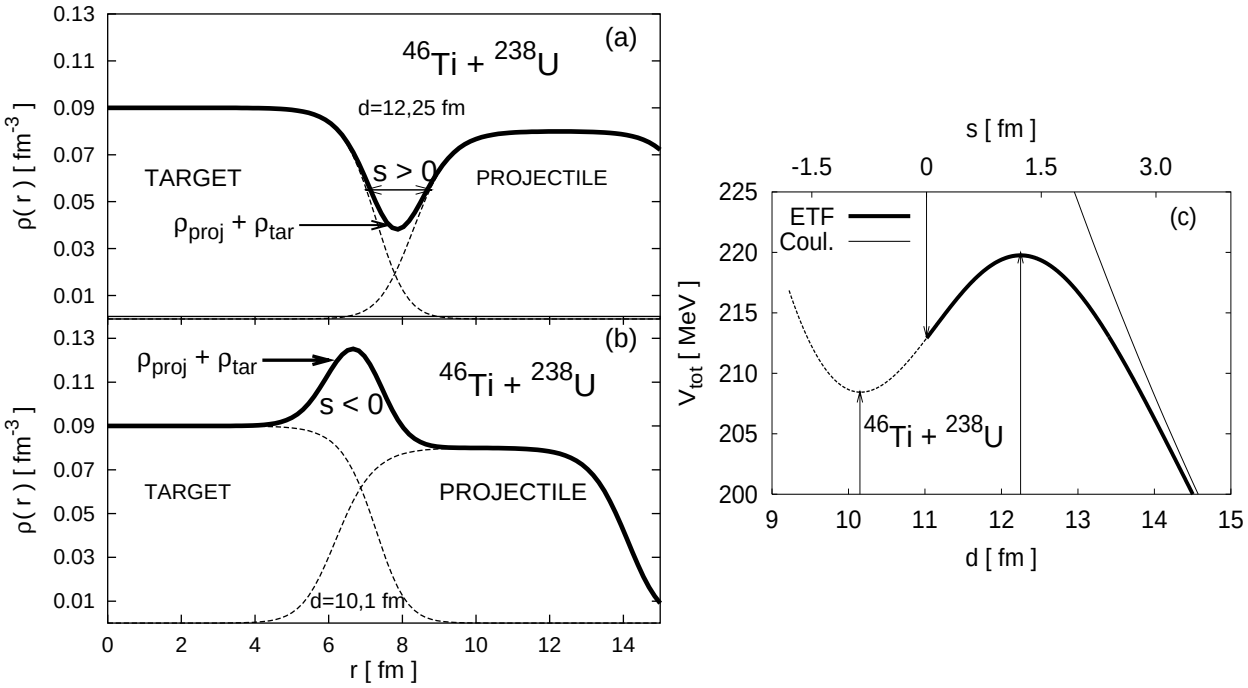

Figure 4.1: Parts (a) and (b) present the density of the *dinuclear system* $^{46}Ti + ^{238}U$ (continuous line) versus non–interacting densities of ions of ^{46}Ti and ^{238}U (thin dashed lines) for two different center-of-mass distances d. Part (c) of the figure gives the shape of fusion barrier as a function of the inter–nuclear distance s (top scale) and center-of-mass distance d (bottom scale). The thin solid line on the right represents the corresponding Coulomb barrier of the point charges

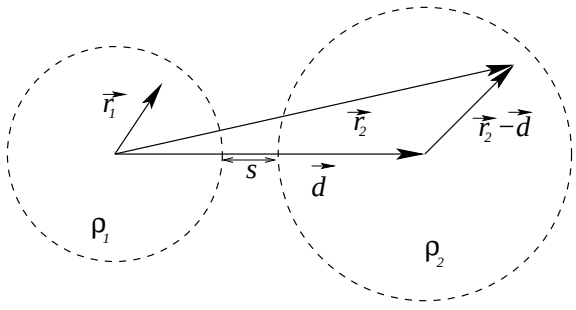

Figure 4.2: Definition of target and projectile coordinates: inter–nuclear (center–of–mass distance) d and inter–surface distance s between the equivalent sharp distributions

where we simply assume that the charge density is given in terms of the proton density by $\rho_{ch}^{(i)} \approx e\,\rho_p^{(i)}$ where in the ETF approach the latter is of the form of eq. (2.19).

4.4 Fusion barriers for super–heavy elements

The fusion barrier appears as the result of the competition between the long–range repulsive Coulomb interaction V_{Coul} and the short–range attractive nuclear forces V_{nuc} as is illustrated on Fig. 4.3, where the total fusion barrier is plotted as function of the internuclear distance d as well as of the inter–surface distance s. We notice that for distances $s \geq 3$ fm the attractive nuclear part of the fusion potential almost vanishes and the barrier is just determined by the repulsive Coulomb potential. Taking the diffuseness of the charge-density distribution into account reduces, for this distance the height of the Coulomb barrier (and as a consequence the total fusion barrier) only by about 1 MeV as compared to the barrier obtained with point charge distributions of target and projectile. It is evident that when the overlap of the densities of the

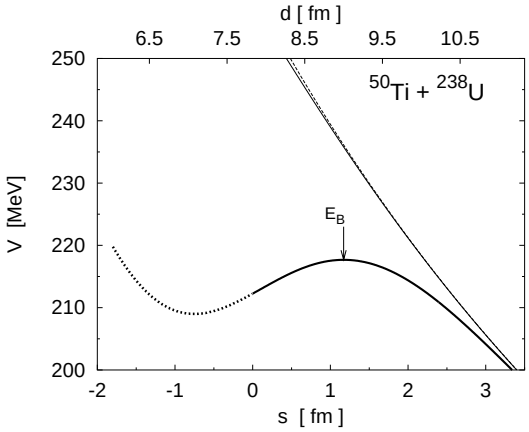

Figure 4.3: Shapes of total (nuclear + Coulomb) fusion barriers V (full line) as function of the center–of–mass distance d (top) and the distance between the equivalent sharp surfaces s (bottom) for the reaction ^{50}Ti + ^{238}U leading to the super-heavy element $^{288}_{114}X$. Also shown are the exact Coulomb barrier (thin line) and the one corresponding to two point charges (dashed line).

colliding nuclei becomes large, as e.g. when $s \leq 0$ (dotted line in Fig. 4.3) the sudden approximation used here becomes more and more questionable. Our aim, however, is not to give a precise description of the entire fusion potential, i.e. also for large negative s values, but rather to obtain some reasonable estimates of the height E_B of the fusion barrier. Fig. 4.4 shows E_B obtained in the sudden approximation and neglecting deformation effects of the colliding ions for 269 different reactions (with $\beta-$stable targets ranging from ^{168}Er to ^{238}U) leading to different isotopes of the super-heavy elements with even charge numbers between $Z=108$ and $Z=114$. The barriers

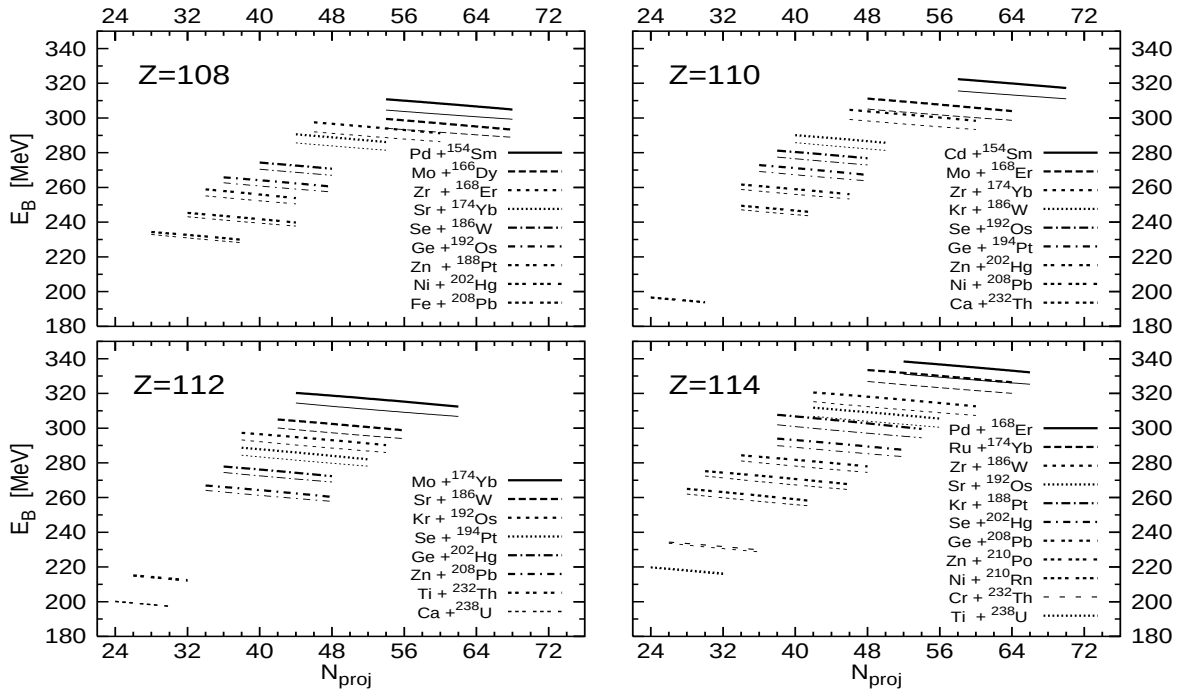

Figure 4.4: Height of fusion barriers corresponding to the different reactions leading to different isotopes of the super–heavy elements with $Z = 108, 110, 112, 114$, evaluated in our ETF approach (thick line) and in the proximity model of Ref. [53] (thin lines), as function of the projectile neutron number.

shown are the ones obtained with the Skyrme forces SkM* [24] (barriers corresponding to the Skyrme SLy4 interaction [49] are identical to within 1 MeV). The thin lines illustrate the heights of the fusion barriers obtained in the Myers–Świątecki proximity model [53]. This collision potential between **spherical** ions of the form

$$V_s = \frac{e^2 Z_1 Z_2}{d} + K\Psi(s), \tag{4.11}$$

is obtained on the basis of the droplet model [54], [55] with the newest set of parameters where the function $\Psi(s)$ is parameterized by means of the following equations:

$$\begin{cases} \Psi(s) = -0.1353 + \sum_{i=1}^{5} \frac{c_n}{n+1} (2.5 - s)^{n+1}, & \text{for} \quad 0 < s < 2.5\, fm, \\ \Psi(s) = -0.1331 \, \exp\left(\frac{2.75 - s}{0.7176}\right), & \text{for} \quad s > 2.5\, fm. \end{cases} \tag{4.12}$$

Here s denotes the inter–surface distance of both ions while the values of the coefficients c_n are given by: $c_0 = -0.1886$, $c_1 = -0.2628$, $c_2 = -0.15216$, $c_3 = -0.04562$, $c_4 = 0.069136$, $c_5 = -0.011454$. The parameter K in eq. (4.11) defined as

$$K = 4\pi\gamma \frac{R_1 R_2}{R_1 + R_2} \tag{4.13}$$

expresses the strength of the nucleon–nucleon interaction. The quantities R_1 and R_2 denote effective nuclear radii of target and projectile nuclei, the fraction $(R_1 R_2)/(R_1 + R_2)$

corresponds to the reduced curvature of the spherical surfaces of target and projectile and γ is the mean surface tension coefficient appropriate for the two nuclei given in the droplet model.

Fusion barrier heights evaluated using the prescription of Ref. [56] are very close to the former differing by not more than 2 MeV for all the reactions considered here.

4.5 A simple analytical fusion potential

The nuclear part of the potential between two colliding ions (see Fig. 4.5) can be quite accurately reproduced by the following approximate form [57]

$$V_{nuc}(d\,) \approx \tilde{V}_{nuc}(d\,) = V_0 \;\; e^{-\alpha\,(d-d_0)^2} \;\; , \tag{4.14}$$

The distance d_0, the depth V_0 and the fall–off α of the potential are a direct result of our selfconsistent, semiclassical calculation. The detailed study of the behaviour of these three quantities as functions of the masses A_1, A_2 and the reduced isospins $I_i = (A_i - 2Z_i)/A_i$ of target and projectile nuclei lead us to the following parametrization (see Fig. 4.6)

$$d_0(A_1, A_2) = r_0(A_1^{1/3} + A_2^{1/3}) + b \;\; , \tag{4.15}$$

$$V_0(A_1, A_2, I_1, I_2) = v_0 \left[1 + \kappa\,(I_1 + I_2)\right] \frac{A_1^{1/3} \cdot A_2^{1/3}}{A_1^{1/3} + A_2^{1/3}} \;\; , \tag{4.16}$$

$$\alpha = \alpha_0\,(I_1 + I_2) + \alpha_1. \tag{4.17}$$

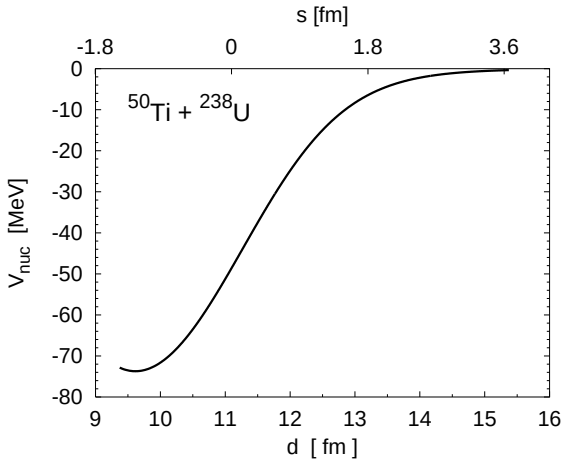

Figure 4.5: Pure nuclear part of the collision potential for ^{50}Ti+^{238}U given by eq. (4.14) as a function of internuclear distance d (lower axes) and intersurface distance (upper axes)

Carrying out the least–square fit of the ETF nuclear potential with respect to three 3 quantities d_0, V_0 and α to the ETF nuclear potential we came to the conviction

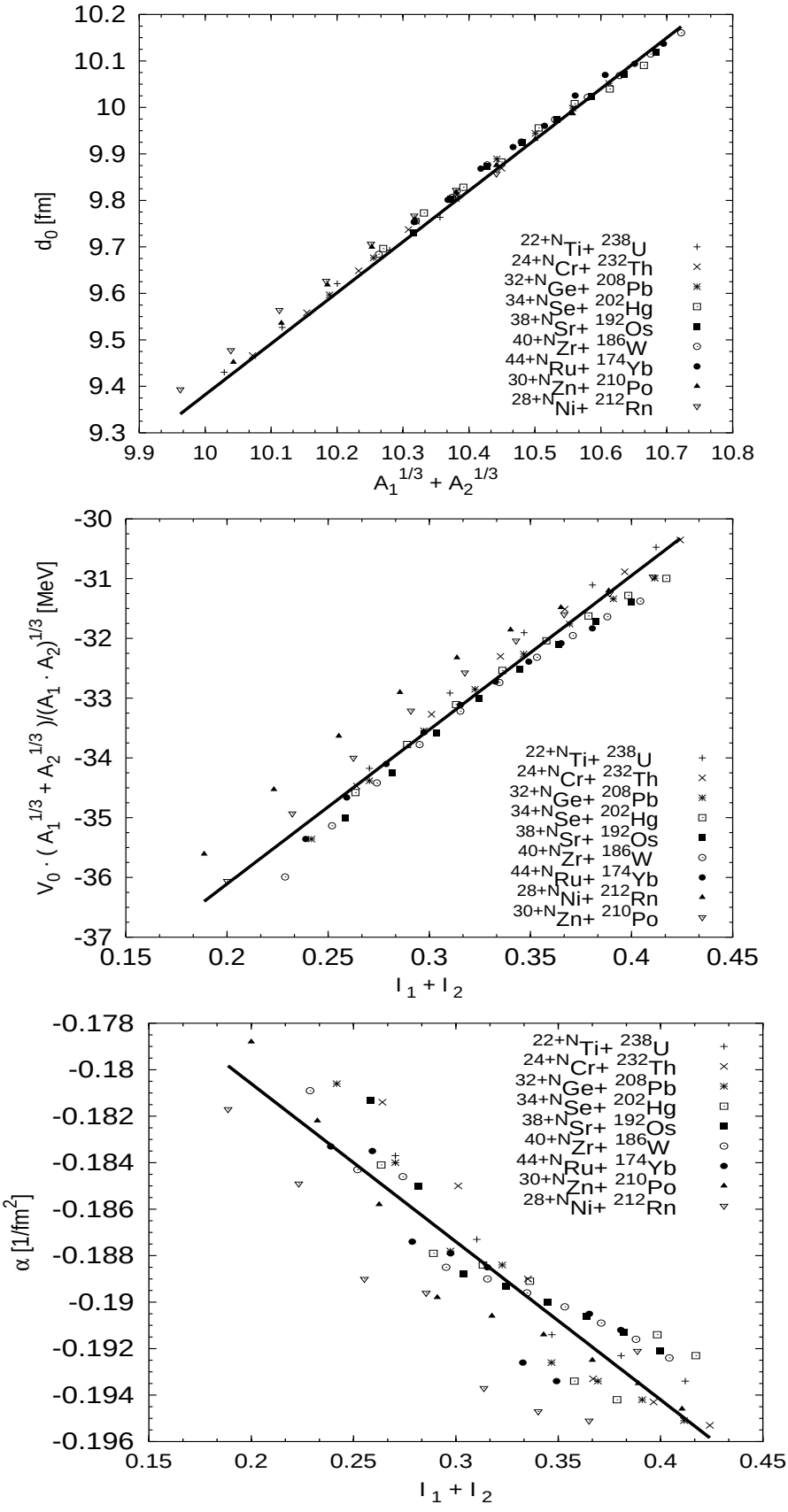

Figure 4.6: Mass and isospin dependences of the parameters entering eqs. (4.14–4.17). In the figure legend the subscript N is the projectile neutron number

that since the mean square error changes only insignificantly when giving up the isospin dependence for the fall–off parameter α we can safely admit its value to be constant which leads to the following set of parameters:

r_0 [fm]	b [fm]	v_0 [MeV]	κ	α [fm^{-2}]
1.183	-2.400	-46.07	-0.4734	0.173

Tab. 4.1 Values of parameters entering the fit of the fusion potential given by eq. (4.19)

To obtain the potential that the system of two colliding nuclei experiences we have to add the Coulomb potential, eq. (4.10), to the nuclear part. For distances large compared to the sum of the equivalent–sharp–surface radii, this Coulomb potential is very well approximated by the Coulomb potential between two point charges, but as soon as the densities of the two nuclei interpenetrate this approximation will no longer give reliable results and it turns out that the difference

$$\Delta V_{Coul}(d\,) \;=\; V_{Coul}(d\,) - \frac{Z_1\,Z_2\,e^2}{d} \tag{4.18}$$

will be, in the case of the super–heavy elements considered here, of the order of 3 MeV already in the vicinity of the contact configuration ($s = 0$).

Instead of calculating the diffuse–surface Coulomb energy explicitly for each reaction under consideration, the idea is to come up with an easy–to–use expression to approximate in a reliable way the ETF fusion potential between two nuclei developed above, including the full Coulomb potential. That is why we propose to write this potential in the form

$$\tilde{V}(d\,) \;=\; \tilde{V}_{nuc}(d\,) + \frac{Z_1\,Z_2\,e^2}{d} \quad , \tag{4.19}$$

where the term $\tilde{V}_{nuc}(d\,)$, which now contains the Coulomb–energy difference ΔV_{Coul}, eq. (4.18), in addition to the nuclear potential (4.8), is approximated by eq. (4.14) with the parameters d_0 and V_0 being given by eqs. (4.15) and (4.16). It is clear in this context that these *new* parameters can turn out to take values that could be quite different as compared to those describing the nuclear part alone.

To determine these quantities we perform a simultaneous fit of the 5 free parameters: r_0, b, v_0, κ, α to the fusion potentials of the 269 reactions obtained in the above described ETF approach (see Fig.4.4). We proceed in the following way: What we are interested in is primarily the precise description of the location d_{max} and the height V_{max} of the total fusion barrier, and we therefore attach a maximum weight in our fitting procedure to their best possible reproduction. When going to smaller distances, i.e. towards negative values of s, the Coulomb–energy difference ΔV_{Coul}, eq. (4.18), grows larger, but also the nuclear potential obtained in our sudden approximation becomes

less and less reliable. That is why we attach a decreasing importance to the reproduction of the fusion barriers for smaller and smaller distances. For increasing distances $d > d_{max}$, on the other hand, both the nuclear potential V_{nuc} as well as the Coulomb correction ΔV_{Coul} go rapidly to zero and our approximation form (4.19) becomes better and better. We therefore attach again less weight to its precise reproduction for large positive values of s. We have thus imagined a least–square–fit procedure with a normalized weight function of Gaussian form with a width of 1 fm and centered at $d = d_{max}$. The values of the parameters obtained in this way are listed in Tab. 4.1

The final criterion of the accuracy of our approach consists in its ability to reproduce the height and shape of the fusion barriers for all 269 reactions obtained within the ETF approach with the SkM* Skyrme interaction. The r.m.s. deviation of the exact ETF fusion potential and its approximation by eq. (4.19) is only of 0.27 MeV at the top of the barrier and of 0.37 MeV for the touching configuration ($s = 0$).

Such a fusion barrier is shown in Fig. 4.7 for the reaction ^{48}Ca+^{232}Th. As one can see, the ETF barrier is almost perfectly reproduced by our analytical expression, eq. (4.19) with (4.14). The barrier height is also almost the same as the one obtained in the proximity model of Ref. [53].

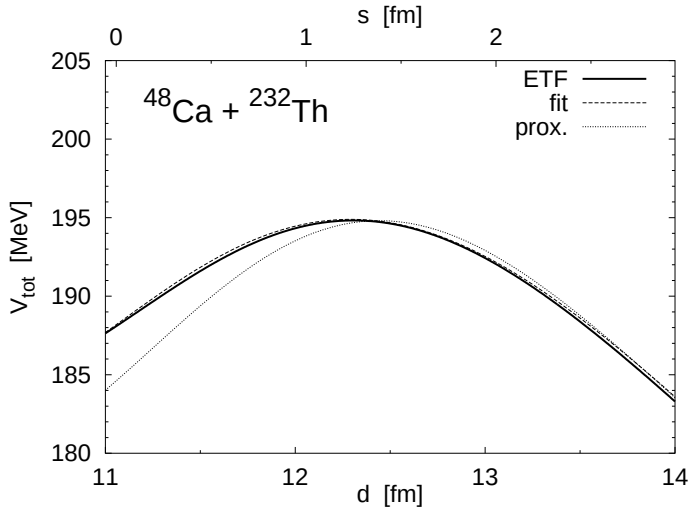

Figure 4.7: Fusion barrier for the reaction ^{48}Ca + ^{232}Th obtained within the ETF approach (full line), its approximate analytical form, eq. (4.19) (dashed line) and the proximity potential of Ref. [53] (thin line)

It is obvious from Fig. 4.4 that the agreement between our ETF approach and the proximity model is not always going to be that close. If one considers e.g. the reaction ^{110}Cd + ^{154}Sm one already concludes from Fig. 4.4 that the barrier heights of the two approaches are going to be different by some 7 MeV (or 2%). We also notice there that the minimum obtained in our ETF approach is quite shallow, whereas the

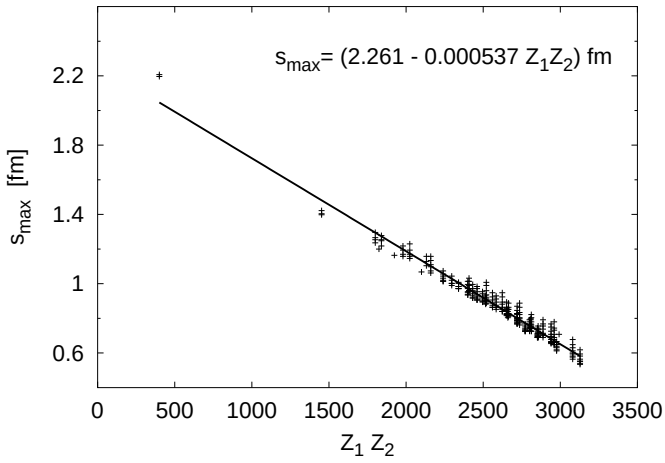

Figure 4.8: Location s_{max} of the top of the fusion barrier as function of the product $Z_1\,Z_2$ of the charge numbers of target and projectile.

proximity potential does not make any predictions about the region $s < 0$. One could now speculate about the validity of our approach close to and inside the touching configuration. The enhancement of the height of the fusion barriers related to the sudden approximation is obviously related to the concept of the *diabatic fusion barriers* advocated by W. Nörenberg and co–workers [52].

The agreement of the ETF fusion barrier heights with those obtained in the proximity approach for very asymmetric reactions ($A_1 \gg A_2$) seems to be related to the value s_{max} (corresponding to d_{max}) of the distance s of the equivalent sharp surfaces of the two colliding nuclei at the top of fusion barrier, as this is demonstrated on Fig. 4.9. Comparing Figs. 4.4 and 4.9 one can, indeed, observe that the enhancement of the ETF barrier height relative to prediction of the proximity model is larger, as the distance s_{max} gets smaller, which is the case for the nearly symmetric reactions.

Since we have only considered fusion reactions leading to super–heavy elements with even values of Z between $Z = 108 - 114$ one might doubt about the utility of the analysis presented so far for the description of fusion barriers in other regions of the atomic chart. We have therefore applied our phenomenological expression to the reactions ^{160,162,166}Dy + $^{46-50}$Ti as well as to the very light system ^{48}Ca + ^{48}Ca. To our great surprise the predictions based uniquely on our knowledge of the ETF barriers of the super–heavy system gave astonishingly good results for these lighter systems with a deviation between ETF results and those of the simple analytical expression, eq. (4.19), of less than 0.7 MeV for the former and of about $1 - 3$ MeV for the latter system.

In the above description we have presented a model allowing for a systematic investigation of fusion barriers between spherical nuclei. One might speculate immediately about the importance of deformation on the barrier heights obtained in our

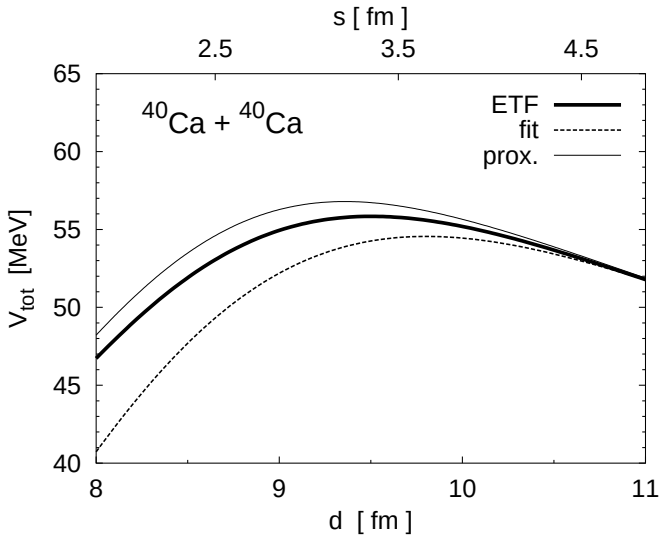

Figure 4.9: Comparison of the fusion thresholds obtained through the variational Skyrme+ETF method (thick solid line) and its approximation (4.19) (thin solid) with the results of Świątecki proximity model (eq. 4.11) (dashed line) for the very light system ^{40}Ca + ^{40}Ca

approach. It seems evident that taking into account deformation as an additional degree of freedom of the system target–projectile could often lead to a decrease of the fusion barrier [58]. One knows, indeed, that e.g. the Coulomb barrier is substantially lower for two nuclei with ellipsoidal deformation and tip–to–tip orientation as compared to a different orientation or in the absence of deformation. It is obvious that for a system like ^{110}Cd + ^{154}Sm, which we briefly discussed above, where at least, the target nucleus exhibit a substantial deformation, such an effect plays a non negligible role which implies that taking deformation into account in our ETF approach might lead to much lower fusion barriers for those systems.

Notice, however, that according to the idea of the proximity approach we can easily switch on the deformation into our consideration of the nuclear collisions within the here presented model by the inclusion in the multiplicative function K (see eq. (4.13)) which depends only on the geometry of the surface of the dinuclear system. In addition, we would like to strongly emphasise that our approach which is based on a selfconsistent, semiclassical description of the projectile and target liquid–drop structure has *no adjustable parameter* and, as one can convince oneself by looking at Fig. 4.4, predicts fusion thresholds that are quite close to the ones obtained with the phenomenological proximity approach of Ref. [53]. We have given, in addition, an analytical form allowing for a simple approximation of the ETF fusion barriers, thus providing a very simple evaluation of fusion potentials for reactions throughout the periodic table. We believe that such an approach could serve as a guideline for the experimental researches on the synthesis of super–heavy elements. As mentioned above, we also tested the ability

of the expression (4.14) to reproduce the barrier heights for the very light systems as e.g. ^{40}Ca + ^{40}Ca. What is quite astonishing is, that our simple phenomenological ansatz, eq. (4.14), adjusted to the reactions leading to super–heavy elements is able to reproduce even those fusion barriers in a quite satisfactory way with a relative error of 2 % at most.

4.6 Influence of different proton and neutron density radii on the collision potential

The analysis of the experimental data on electron and α–particle scattering, pionic atoms, and annihilation of antiprotons shows that, in most nuclei, neutrons and protons have slightly different r.m.s. radii [59]. The main reasons for this difference are the Coulomb repulsion between protons and unequal numbers of neutrons and protons.

Fully microscopic approaches of the Hartree–Fock type using the effective nucleon–nucleon interactions of the Skyrme or Gogny type [14, 15], as well as the relativistic mean field theory [60] reproduce in a rather satisfactory way the experimental proton and neutron r.m.s. radii and their isotopic shifts [34, 38, 60].

Using the ETF ion–ion potential which was successfully parameterized by the simple analytical formula, eq. (4.14), we can now describe the relative change of the fusion barrier heights as a function of nuclear proton or neutron radii for reactions where the target as well as the projectile nucleus in the equilibrium state are spherical or very close to sphericity [61].

It is commonly known that neutron, contrary to proton r.m.s. radii, are determined experimentally with relatively poor accuracy and for only a rather limited number of nuclei situated in different mass regions. On the other hand, on can easily show in a simple and straightforward calculation that the r.m.s radius given by

$$\langle r^2 \rangle = \frac{\int r^2 \, \rho(\vec{r}) \, d^3r}{\int \rho(\vec{r}) \, d^3r} \tag{4.20}$$

is the combination of all four density parameters entering eq. (2.19) when such a Fermi–function type density is used. The parameters obtained with the SkM* Skyrme force which was used in this study have proven to give an excellent estimate of nuclear radii (see e.g. Fig. 2.1). Since neither R_q nor a_q are observables we are allowed to vary to some extend these values conserving, of course, the nuclear volume. When looking at Figures 4.10 and 4.11 one can easily notice that by the change of the neutron radius in one of the colliding ion by 1 fm we are able to shift the maximum of the fusion barrier by $1 - 3$ MeV, i.e. by the order of the discrepancy between the ETF and the experimental values. When instead of the neutron we vary the proton radius we observe that this change becomes even more rapid because in such a case we affect

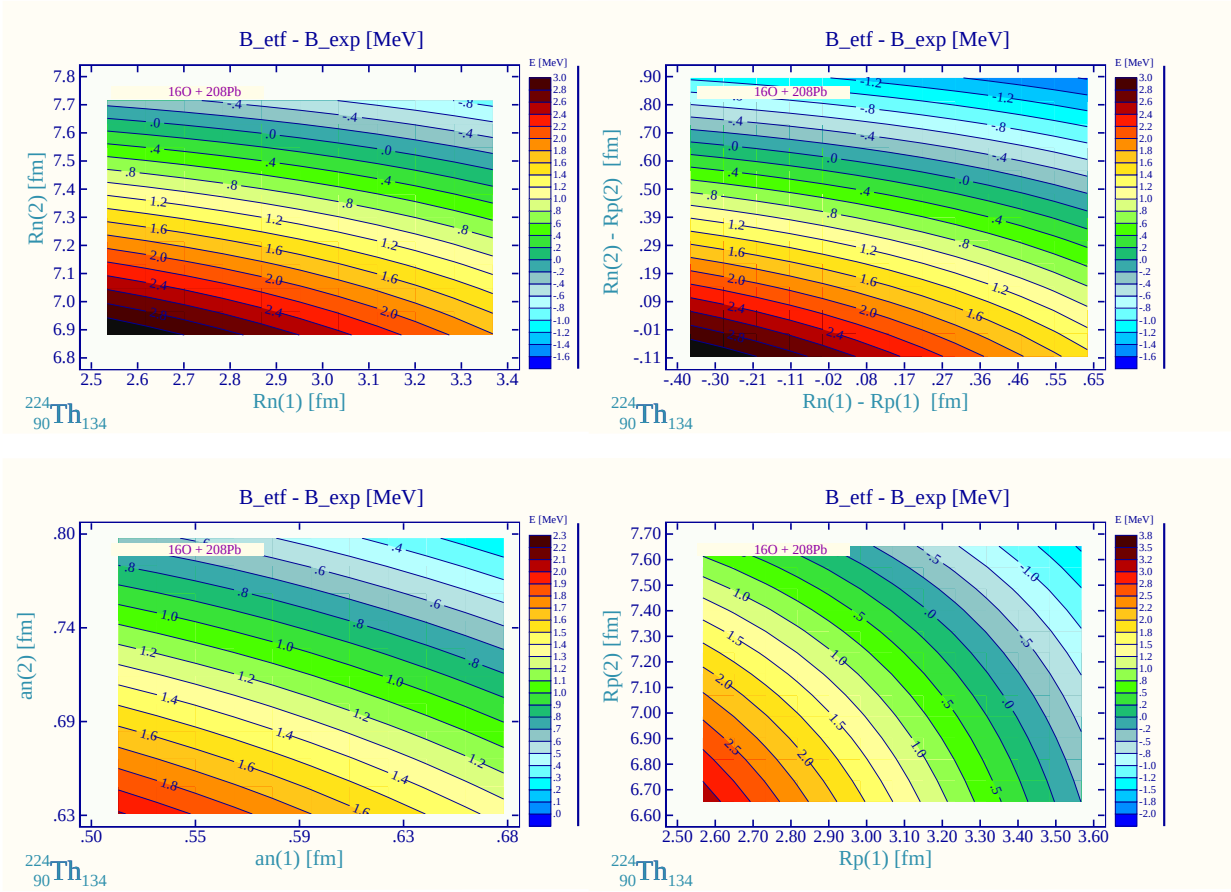

Figure 4.10: Difference between theoretical and experimental fusion barrier heights ($B_{\text{etf}} - B_{\text{exp}}$) for asymmetric reaction $^{16}O +^{208} Pb$ as function of neutron radius R_n (upper-left), the neutron skin width (defined as the difference between neutron and proton radius $R_n - R_p$) (upper-right), neutron surface diffuseness parameter a_n (lower-left) and proton radius R_p (lower-right). Labels $\{1, 2\}$ in parenthesis indicate the colliding ions. Exact variational values of the radii and surface diffuseness parameters are located at the centers of the axes. The experimental value of the barrier height is taken from Ref. [62]

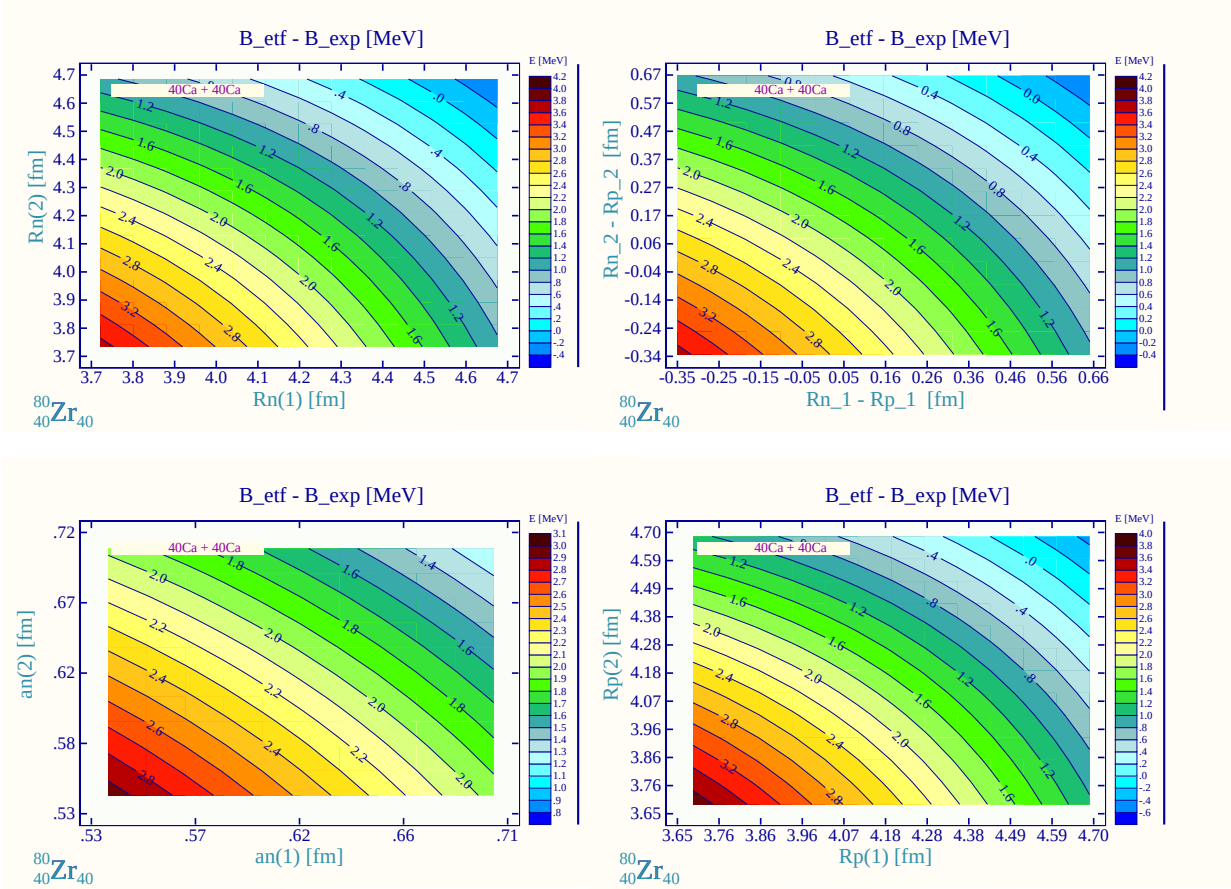

Figure 4.11: Same study as in Fig. 4.10 but for the very light system $^{40}Ca + ^{40}Ca$

simultaneously the nuclear and the Coulomb interaction which depend to some extend also on the charge density distribution of both ions, particularly when the proton distributions of both colliding nuclei come to overlap (see Fig. 4.1). The same effect, but with a somewhat smaller sensitivity, we can achieve varying the surface diffuseness parameter a_q in target and projectile.

The effect of the difference of proton versus neutron density radii gives us some orientation on how much the fusion barrier height, which, as we have already mentioned, is the quantity of capital importance for heavy–ion collisions, can depend on the macroscopic features of the nuclear densities. Finally, we would like to recall that the deformation and mutual orientation in space of both colliding ions plays even more essential role for fusion barriers as compared to the differences in proton–neutron density distributions discussed here (see Ref. [58]).

Chapter 5

Dynamics of the fusion reactions

5.1 Introduction

In this section we discuss, in a qualitative way, the physical processes which we are going to describe in later sections quantitatively by applying Langevin techniques described widely in Ref. [45]. In this review we restrict ourselves to low–energy heavy–ion collisions, with a center of mass energy per nucleon of less than 5 MeV. In a first approximation these collisions can be described in terms of classical trajectories. In such a framework each impact parameter determines a unique trajectory, and therefore the different reaction mechanisms can be classified by typical impact parameters, (as explained in Fig. 5.1)

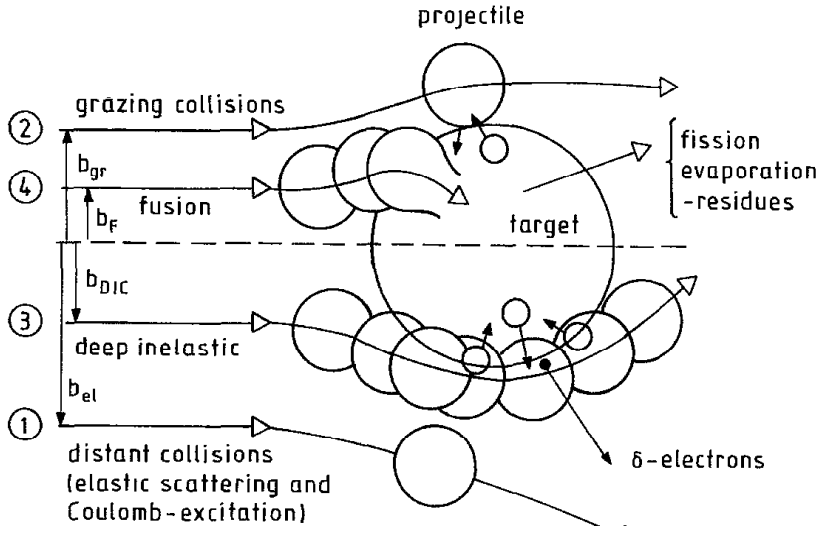

Figure 5.1: Classification of heavy–ion reactions by impact parameters [45]

Very large impact parameters b_{el} correspond to distant collisions and are associated with *elastic scattering* or, at most *Coulomb excitations*. *Grazing collisions* are characterized by smaller impact parameters b_{gr} and are classified as direct reactions, in

which only few degrees of freedom are involved. For these processes the name *quasi–elastic collisions* is also in use. At even smaller impact parameters b_{DIC} the collisions become more violent. The collision partners keep their identity up to a net exchange of a few nucleons, but, nevertheless, a large amount of energy and angular momentum is transferred from the relative motion to intrinsic excitations of the colliding ions. The corresponding reactions are therefore called *deep–inelastic collisions* (DIC). For not too heavy systems the colliding nuclei form a compound system below a still smaller impact parameter b_F, the compound nucleus, i.e. the heavy ions fuse, one speaks about a fusion reaction. This compound nucleus is hot, i.e. it is highly excited and carries a large amount of angular momentum. Therefore, it does not live for ever but decays by fission and/or evaporation of light particles. The classification of heavy–ion collisions by relating a unique impact parameter to a classical trajectory of each type of reaction is only valid if one neglects the action of a fluctuating forces. The latter, however, play an important role in a classical description of heavy–ion collisions and are connected with the frictional forces via the *fluctuation–dissipation theorem*. Due to the action of the fluctuating forces each impact parameter contributes only with a certain probability to the different types of reactions. This is schematically illustrated in Fig. 5.2.

In that figure trajectories are approaching the potential barrier between two colliding heavy ions. Let us first consider the case with no fluctuating forces [45].

A trajectory (1) is shown which just reaches the top of the static fusion barrier if no friction between the heavy ions is acting. If friction plays a role, a trajectory (2) with this initial energy would not be able to overcome the barrier because it would lose energy on the way in. Therefore, a trajectory (3) needs an extra energy, the so–called *extra push*, to reach the top of the static barrier. The energy necessary to reach the static barrier when friction is involved corresponds to the dynamical barrier B_{dyn}. Because fluctuating forces are acting besides conservative and frictional forces there exists for each impact parameter not a single trajectory but a whole bundle of trajectories, as indicated schematically in the figure. The distribution function which is created by this bundle of trajectories will be calculated in the quantitative description of the collisions by Monte–Carlo sampling of Langevin trajectories. The bundle of trajectories hits the interaction barrier. Part of the trajectories overcome the barrier, while the others are reflected. The distribution function thus bifurcates into a fusion branch and a branch for inelastic collisions. The latter is subdivided into quasi–elastic collisions (trajectories with small energy losses) and deep–inelastic collisions (trajectories with large energy losses).

The subdivision of the various reaction processes is often characterized by the corresponding differential cross section with respect to the angular momentum ℓ (or impact parameter $b = \ell/k$), the so–called spin distribution $d\sigma/d\ell$. This is shown in

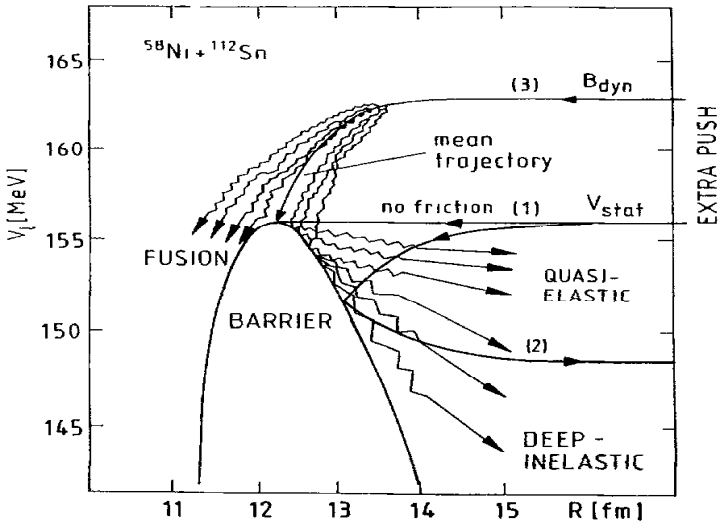

Figure 5.2: Trajectories with fluctuating forces [45]

Fig. 5.3, where also the overlap of the different reaction types with respect to contributions of the impact parameter is indicated. The areas below the different curves correspond to the total cross sections for fusion σ_F, deep–inelastic σ_{DIC} and quasi–elastic σ_{qe} collisions.

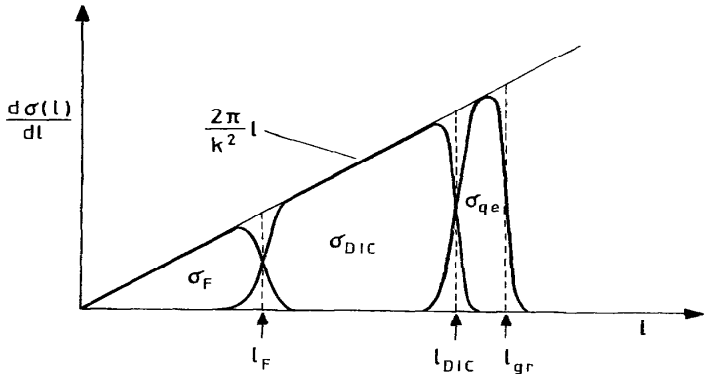

Figure 5.3: The spin distribution of a heavy-ion reaction. The regions for quasi-elastic collisions (σ_{qe}), deep-inelastic collisions (σ_{dic}), and for fusion (σ_F) are indicated [45]

Now let us discuss the further evolution of the compound nucleus, which has been formed in a heavy–ion fusion reaction. The decay of the compound nucleus is schematically illustrated in Fig. 5.4. The decay can be essentially of two types. In the first one the nucleus fissions, i.e. predominantly separates into two heavy fragments of approximately equal size. One speaks about a *fusion–fission process.* In the course of the fission process the intermediate system can evaporate light particles (n, p, α) and $\gamma-$quanta until scission when the neck is shrinking to zero. These are called *pre–scission particles.* After scission the heavy fragments can still carry substantial excitation and continue to evaporate light particles and $\gamma-$quanta. These are called

post–scission particles. It is possible (yet quite difficult) to distinguish experimentally between pre– and post–scission particles. Also, in the formation process some light particles can be emitted, which are of increasing importance with increasing bombarding energy. These particles are called *pre-compound* or *pre–equilibrium* particles.

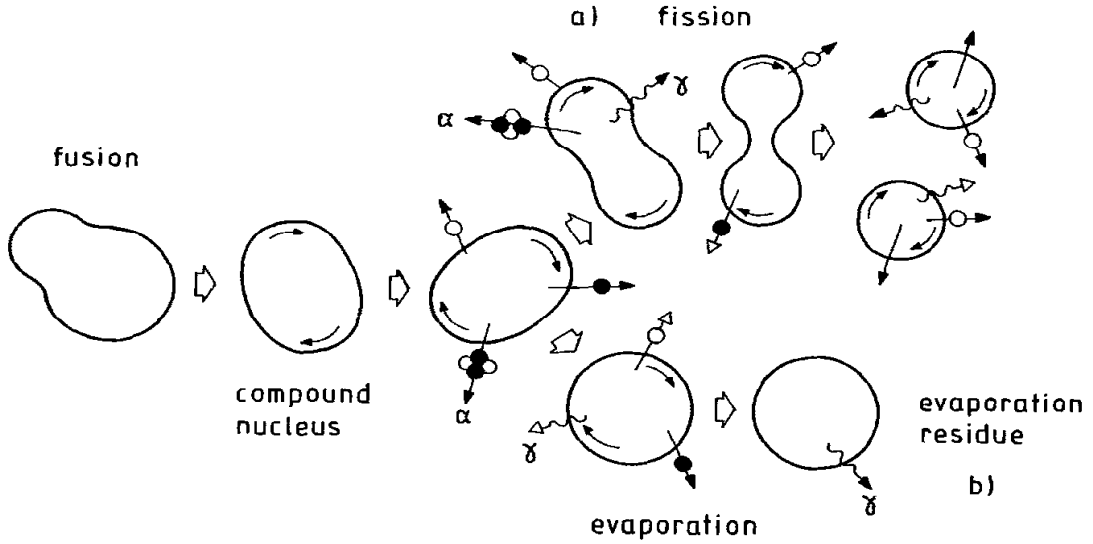

Figure 5.4: Possible decay channels of compound nucleus [45]

If the intermediate complex formed in the collision compound system is not fully equilibrated one speaks about a *fast–fission* or *quasi–fission* process. The second type of decay channel is given by a process where the excitation of the compound nucleus is not removed by fission but solely by the evaporation of light particles and $\gamma-$rays. The evaporation of light particles of a particular kind stops if a further emission is no longer possible because the excitation energy has dropped to a value below the corresponding separation energy (plus the Coulomb barrier in case of charged particles).

The deexcitation process of the compound system thus ends with, the so–called evaporation residues. For $\gamma-$quanta the emission process lasts until zero energy and the lowest possible spin values are reached. After that further $\beta-$decay is possible until one ends with a stable element of the nuclear chart. Which of the decay types dominates depends on the mass, excitation energy and angular momentum of the system under consideration. The evaporation of particles during the fission process (pre–scission particle emission) can be considered as a chain of bifurcation processes, the scenario of which is schematically illustrated in Fig. 5.5, where for simplicity only the emission of neutrons (which is the predominant process) is considered. Fission occurs with a certain probability without the emission of any particle (first–chance fission). During fission one, two, or more neutrons can be emitted (one then speaks about 2^{nd}, 3^{rd}, ...–chance fission). In actual heavy–ion–induced fission the decay

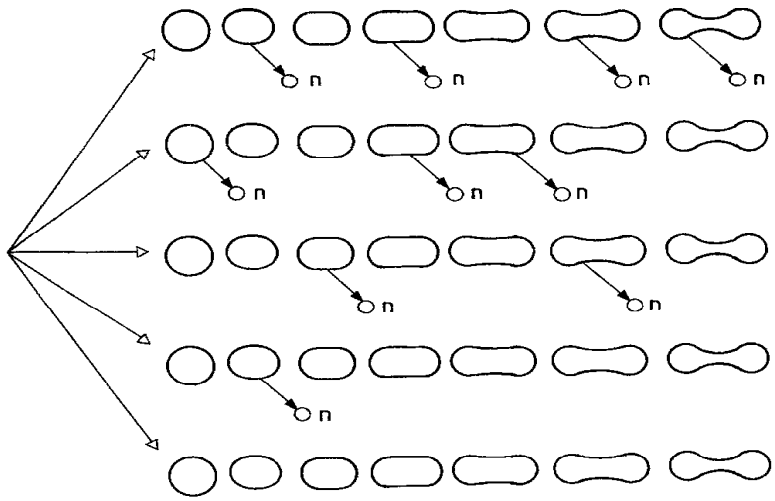

Figure 5.5: First and higher–chance fission [45]

scheme becomes even more complicated, because other kinds of light particles (p, α, d, $\gamma-$quanta) are also emitted during fission. The dynamics of deep–inelastic collisions, fusion, and heavy–ion–induced fission can be, as already mentioned above, described by Langevin equations, which are classical equations of motion governed by conservative, frictional and fluctuating forces. The description of the evaporation of light particles and $\gamma-$quanta going along with heavy–ion–induced fission and governing the formation of evaporation residues is performed in the framework of the conventional Weisskopf or the Thomas–Fermi evaporation models.

5.2 The Langevin formalism

Let us write down in the most general form the equations of motion for a single collective variable (generalized coordinate) R and its associated conjugate momentum P

$$\begin{cases} P = M\dot{R}, \\ M\ddot{R} = \tilde{F}(R) + F_{frict.}(R,\dot{R}) + F_L(R,t). \end{cases} \tag{5.1}$$

We chose a simplified version of the frictional force which in general is a rather complicated object, in this sense that its value at the time t depends on an integral over all previous times t'. We will use the frictional force in the form

$$F_{frict.}(R,\dot{R}) = -\gamma(R)\dot{R}. \tag{5.2}$$

The fluctuating (Langevin) force depends on the coordinate R and explicitly on the time t [63]

$$F_L(R,t) = \sqrt{D(R)}\,\Gamma(t), \tag{5.3}$$

where the fluctuation strength coefficient $D(R)$ is connected with the friction coefficient $\gamma(R)$ by the fluctuation–dissipation theorem [64]. Finally, we obtain from eq. (5.1) the set of **Langevin equations** in the following form:

$$\begin{cases} \dot{R} = P/M, \\ \dot{P} = \tilde{F}(R) - \gamma(R)P/M + \sqrt{D(R)}\,\Gamma(t). \end{cases} \tag{5.4}$$

The variables R and P are themselves stochastic variables, since they are solutions of the coupled eqs. (5.4) which contain the stochastic variable $\Gamma(t)$. It is convenient for later discussions to write the Langevin eqs. (5.4) in a more general multidimensional form, replacing the variables $\{R, P\}$ with the general set of dynamical variables $y = \{y_i\}$, (i=1,...,N) where

$$\dot{y_i} = h_i(y) + \sum_j g_{ij}(y)\Gamma_j(t), \tag{5.5}$$

and where $\langle\Gamma_i(t)\rangle = 0$ and $\langle\Gamma_i(t)\Gamma_j(t')\rangle = 2\delta_{ij}\delta(t-t')$. The functions $h_i(y)$ contain the conservative and frictional forces and the functions $g_{ij}(y)$ the fluctuation strength coefficients.

5.2.1 The discretized Langevin equations

For the numerical treatment we discretize the Langevin equations introduced in the previous section. We introduce the time interval τ and consider the times $t_n = n\tau$ (n integer). This interval τ is chosen larger than the correlation time ϵ of the random process $\Gamma(t)$, but smaller than, the times over which the forces and form factors in the Langevin equation vary appreciably as functions of the coordinate $R = R(t)$. We then integrate eqs. (5.4) from t_n, to $t_{n+1} = t_n + \tau$. We regard the functions $\tilde{F}(R)$, $\gamma(R)$ and $D(R)$ as constant in this interval and replace them with their values at time t_n. We denote thus $R_n = R(t_n)$ and $P_n = P(t_n)$. Discretized Langevin equations can be written then as

$$\begin{aligned} R_{n+1} &= R_n + (P_n/M)\,\tau \\ P_{n+1} &= P_n + [\tilde{F}(R_n) - \gamma(R_n)P_n/M]\,\tau + \sqrt{D(R_n)}\,W_n, \end{aligned} \tag{5.6}$$

where the stochastic variable

$$W_n = W(t_n) = \int_{t_n}^{t_{n+1}} dt'\Gamma(t') \tag{5.7}$$

is a superposition of Gaussian–distributed random numbers and is therefore again Gaussian–distributed. The quantity W_n can be written as $W_n = a_n w(t_n)$ with $w(t_n)$ being a normalized random variable which satisfies conditions $\langle w(t_n)\rangle = 0$ and $\langle w(t_n)w(t_{n'}\rangle =$

$2\delta_{nn'}$. The last equation is consistent with the assumption that τ is larger than the correlation time ϵ of the stochastic process $\Gamma(t)$, so that there is no correlation between the intervals $t_n < t_{n+1}$ and $t_{n'} < t < t_{n'-1}$. The value of the coefficient a_n is determined e.g. in Ref. [45] and is equal to $a_n = \sqrt{\tau}$. The discretized form of the Langevin equations reads then

$$\begin{aligned} R_{n+1} &= R_n + (P_n/M)\,\tau \\ P_{n+1} &= P_n + [\tilde{F}(R_n) - \gamma(R_n)P_n/M]\,\tau + \sqrt{D(R_n)}\sqrt{\tau}\,w(t_n). \end{aligned} \tag{5.8}$$

5.2.2 The Langevin equations of the Surface Friction Model (SFM)

In order to describe fusion and deep–inelastic heavy–ion collisions we now establish Langevin equations with the phenomenological input of the surface friction model [65]

$$\begin{aligned} p_{r(n+1)} &= p_{r(n)} - \left(\frac{\partial V(r)}{\partial r} + K_r\frac{p_r}{\mu}\right)\tau + \sqrt{D_{r(n)}\tau}\,w_r(t_n) \\ r_{n+1} &= r_n + \frac{p_{r(n+1)} + p_{r(n)}}{2\mu}\,\tau, \end{aligned} \tag{5.9}$$

where the relative coordinate is now denoted as r and the diagonal, radial friction form factor as $K_r = 3.5 \times 10^{-21}(\mathrm{s/MeV})\left(\frac{\partial V(r)}{\partial r}\right)^2$, μ is the reduced mass of the system. The conservative potential $V(r)$ consists of a nuclear and a Coulomb part.

The diagonal diffusion coefficient is determined within the fluctuation–dissipation theorem as

$$D_r = K_r T, \tag{5.10}$$

where the temperature T is calculated from the internal excitation energy E^* along each trajectory, $T = \sqrt{E^*/a}$, and the value $a = A/8MeV^{-1}$ is used for the level density parameter. We neglect fluctuations associated with the non–diagonal friction terms because they turn out to be small as was shown by solving the corresponding Fokker–Planck equation of the surface friction model with a moment expansion method [66]. The quantity $w_r(t_n)$ in eqs. (5.9) is the Gaussian–distributed random variable.

We have now specified the phenomenological input of the surface friction model. Let us now explain how the fusion cross sections can be calculated by Monte–Carlo sampling of trajectories.

5.3 Cross sections for fusion and deep–inelastic collisions

The total fusion cross section is usually calculated through

$$\sigma_F = \frac{\pi}{k^2}\sum_{l=0}^{\infty}(2l+1)T_l^F = \sum_l \frac{d\sigma(l)}{dl}, \tag{5.11}$$

where T_l^F is the transmission coefficient through the fusion barrier with angular momentum $L = \hbar l$. The spin distribution (partial fusion cross section with respect to the orbital angular momentum) is defined as

$$\frac{d\sigma_F(l)}{dl} = \frac{\pi}{k^2}(2l+1)T_l^F. \tag{5.12}$$

In order to describe well the fusion of heavy ions above the barrier, classical trajectory models including frictional forces but neglecting statistical fluctuations have been frequently used. One applies a sharp cut–off model for the transmission coefficient

$$T_l^F = \begin{cases} 1, & \text{for } l < l_F \\ 0, & \text{for } l > l_F \end{cases} \tag{5.13}$$

Fusion occurs for $l < l_F$. The fusion excitation function is therefore

$$\sigma_F(E) = \frac{\pi}{k^2}\sum_{l=0}^{l_F}(2l+1) = \frac{\pi\hbar^2}{2\mu E}\Big(l_F(E)+1\Big)^2. \tag{5.14}$$

The critical $l-$value for fusion l_F was determined for each center–of–mass energy E by solving eqs. (5.9) without the fluctuating forces. In this approximation, the mean trajectory determines the fusion cross section. Technically, l_F is determined by running trajectories for each energy by successively diminishing the initial $l-$value, (chosen large enough), until a trajectory with a particular $l-$value is captured behind the barrier, (i.e. loosing all its energy). This then defines the critical $l-$value for fusion, l_F. The corresponding spin distributions are of triangular form

$$\frac{d\sigma_F(l)}{dl} = \begin{cases} (\pi/k^2)(2l+1) & \text{for } l < l_F, \\ 0 & \text{for } l > l_F. \end{cases} \tag{5.15}$$

If statistical fluctuations are taken into account these formulas have to be modified in the following way: We perform a transformation of the variable l

$$l = l(x) = l_> \sqrt{x}, \tag{5.16}$$

where $l_>$ can be chosen as the grazing angular momentum, in order to write the fusion cross section in the following way

$$\sigma_F = \frac{\pi}{k^2}\sum_{l=0}^{\infty}(2l+1)T_l^F \approx \frac{\pi}{k^2}\int_0^{l_>} 2l\,dl\,T_l^F = \frac{\pi}{k^2}l_>^2\int_0^1 dx T_{l(x)}^F = \frac{\pi}{k^2}l_>^2\frac{N_F}{N}. \tag{5.17}$$

This allows to evaluate the last integral by Monte Carlo sampling of trajectories. Considering x as a uniformly distributed random variable $0 \leq x \leq 1$, one solves eqs. (5.9) including the fluctuating forces N times with initial conditions for the orbital angular momentum chosen according to eq. (5.16). The corresponding trajectories lead to fusion or they are reflected from the barrier. The transmission coefficient for fusion T_l^F is equal to one if a trajectory leads to fusion or zero if it does not. Therefore, the fusion cross section is obtained by counting the number of trajectories N_F leading to fusion normalized to the total number of trajectories N. The result does not depend on the particular choice of $l_>$, if this is chosen large enough.

Simultaneously, one obtains the total cross section for deep–inelastic collisions in the form

$$\frac{\pi}{k^2} l_>^2 \int_0^1 dx T_{l(x)}^{DIC} = \frac{\pi}{k^2} l_>^2 \frac{N_{DIC}}{N}, \tag{5.18}$$

where N_{DIC} is the number of deep–inelastic trajectories, i.e. trajectories with an energy loss larger than that for quasi–elastic events. The fusion spin distribution now is no longer of triangular shape but smeared out due to the action of the fluctuating forces. It is calculated simultaneously with the total cross section by sampling trajectories in bins j of the initial angular momentum

$$\left(\frac{d\sigma_F}{dl}\right)_j = \frac{2\pi}{k^2} l_j \frac{N_j^F}{N_j}, \tag{5.19}$$

where l_j is the initial angular momentum, N_j^F the number of fusing and N_j, the total number of trajectories in the initial angular momentum bin j. Analogously, the spin distribution for deep–inelastic collisions is obtained

$$\left(\frac{d\sigma_{DIC}}{dl}\right)_j = \frac{2\pi}{k^2} l_j \frac{N_j^{DIC}}{N_j}, \tag{5.20}$$

where N_j^{DIC} is the number of deep–inelastic collisions in the angular momentum bin j.

5.4 Fusion cross sections with the ETF ion–ion potential

Applying the Langevin formalism together with the surface friction model (SFM) described in the previous section we can now turn to the determination of the fusion cross sections as function of the center–of–mass energy of the colliding ions [67]. As a potential entering the equations (5.9) we used the one obtained with ETF approximation of section 4.5 (see eqs. (4.14) and (4.19)). However, before we start comparing three different models of the ion–ion static potential we have to realize that the proximity

barriers obtained by Myers and Świątecki in Ref. [53] were rigorously adjusted to the newest set of measurements. The deviation of 4% for a barrier of the order 200 MeV which sometimes occurred for the similar parametrization from 1981 is actually no more present.

In the Gross–Kalinowski potential [68] the nuclear part is obtained through the single–folding procedure

$$V_{12} = \int V_1(r - r')\,\rho_2(r')\,d^3r', \tag{5.21}$$

where subscripts $\{1, 2\}$ denote the colliding nucleus, V is the spherical Woods-Saxon potential $V = V_0/(1 + \exp([r - R_p]/a_p))$ with the parameters: $R_p = 1.25\,A^{1/3}\,fm$, $a_p = 0.65\,fm$, $V_0 = -50\,MeV$. The nuclear density is parameterized as$\rho = \rho_0/(1 + \exp([r - R_d]/a_d))$, $R_d = [1.12A^{1/3} - 0.86A^{-1/3}]\,fm$, $a_d = 0.54\,fm$, $\rho_0 = 0.170\,fm^{-3}$. The Coulomb potential is given as a point–charge potential. Since the expression (5.21) is not symmetric under the exchange of projectile and target, a symmetrized form thereof is used:

$$V_{nuc} = \frac{1}{2}(V_{12} + V_{21}). \tag{5.22}$$

The general behaviour of the potential (5.21) can be easily reproduced by the following simple formula:

$$V_{nuc}^{GK}(r) = -\sum_{i=1}^{5} A_n(r - R)^{n-1} \ln\Big(1 + \exp\Big[-\frac{r - R}{a}\Big]\Big), \tag{5.23}$$

where $R = 1.30\,(A_{proj}^{1/3} + A_{tar}^{1/3})\,fm$, $A_1 = 33.$, $A_2 = 2.0$, $A_3 = 3.0$, $A_4 = A_5 = 0.0$, $a = 0.61\,fm$.

The fusion cross sections estimated in the present investigations within the Langevin formalism developed recently by Fröbrich and coworkers turn out, however, to be too small, on average by one order of magnitude as compared to the experimental data available in Refs. [69, 70]. This fact is not astonishing when one compares the heights of the barriers obtained through both the ETF and Gross–Kalinowski nucleon–nucleon potentials plotted in the left hand side of figures 5.6 and 5.7. The parameters of the mentioned potential, however, were slightly refined compared to these coming from its original prescription 5.21. It was necessary to reproduce reliably, together with the simple phenomenological model of the frictional forces (see section 5.2.2), the excitation functions for large variety of target–projectile systems.

In order to improve the estimates of the cross sections one should first consider the effect of the deformation of the colliding ions which can lower the fusion barrier substantially in the case of non–spherical shapes of targets and projectiles (i.e. ^{28}Si $+^{178}$ Hf or ^{48}Ca $+^{238}$ U), mostly due to significantly lowering of the Coulomb

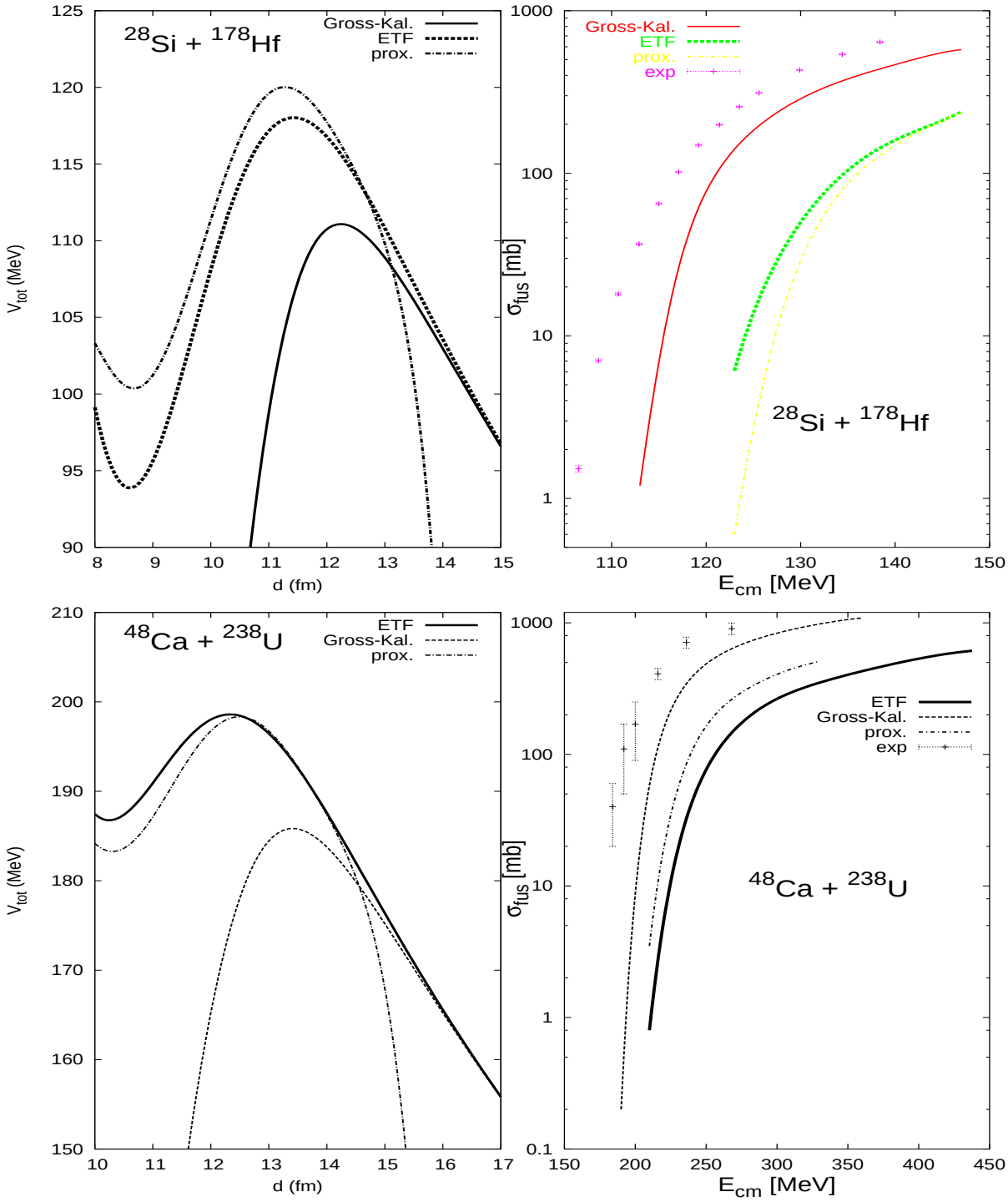

Figure 5.6: Fusion potentials and corresponding excitation functions in the ETF+SFM approaches (thick line), Myers–Świątecki proximity model with the prescription from Ref. [53] (dashed–dotted line) and the Gross–Kalinowski model Ref. [45, 68] (dashed line). Experimental data are taken from Ref. [69, 70]

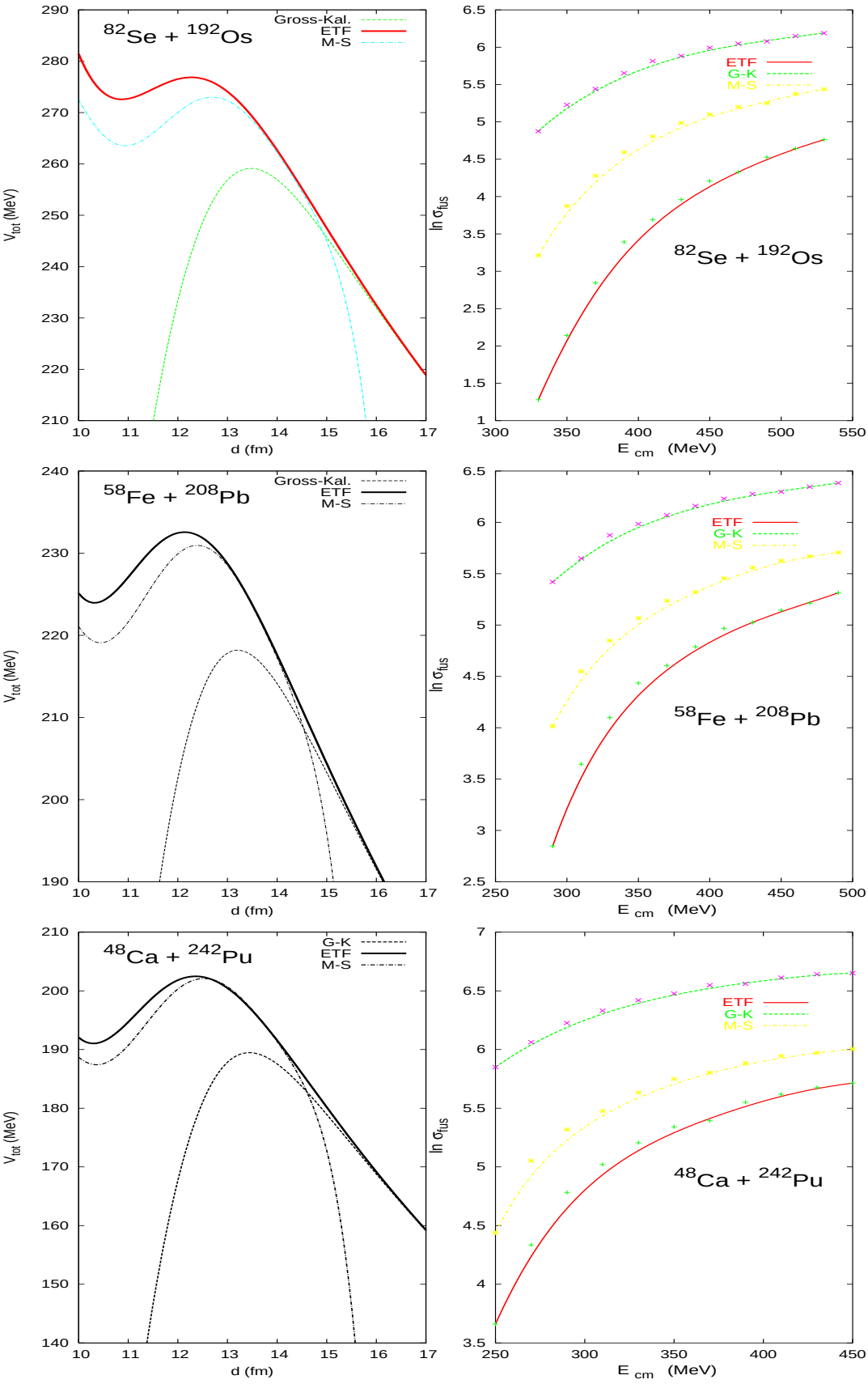

Figure 5.7: Similar study as in Fig. 5.6 performed for three reactions ^{82}Se+^{192}Os, ^{58}Fe+^{208}Pb and ^{48}Ca+^{242}Pu but without the comparison with experimental data. Continuous line corresponds to ETF+SFM model, dashed to Gross–Kalinowski approach and dashed–dotted to proximity model of Myers and Świątecki

barrier. As we can see, studying figures 5.6 and 5.7, the value of the fusion cross sections are mainly influenced, in all five cases, by the height and the width of fusion barriers which, in case of the ETF and Gross–Kalinowski potentials, differ as much as $\approx 12\,MeV$. The same investigation for both the ETF and proximity potentials gives a difference of, at most, $\approx 5\,MeV$. From the point of view of classical mechanics the influence of the barrier hight on the cross section seems to be rather clear. The trajectory with given energy value E_{traj} passes through the barrier E_{barr} when $E_{barr} \leq E_{traj}$ and will be reflected otherwise. Statistically, in the sampling method of N trajectories all of them have comparable energy value within a few percent of dispersion which is brought about by the fluctuating Langevin force. The more trajectories from this fixed bundle are reflected from the barrier of given height as compared with N, the lower the fusion cross section will be (see eq. 5.17). Now, let us try to explain what happens if the barrier width is varied. The width of the barrier has the largest influence on the frictional terms in the Langevin equations (5.9). As we can easily conclude, if the barrier hump is getting more and more narrow ($\partial V(r)/\partial r$ becomes larger), the frictional force is increasing, what in turn, implies that the energy loss for a given trajectory on its way grows. The probability of overcoming the potential barrier by this trajectory is then significantly decreased.

Since we believe that the *sudden approximation* is a reasonable treatment for inter–nuclear distances $s > 0$ fm (see Fig. 4.1a), i.e. for not too large density overlaps, the height of fusion barriers seem rather realistic there. If on the other hand, the overlap of the densities of the colliding ions becomes large for $s \approx 0$ fm then the sudden approximation used for $s < 0$ fm becomes more and more questionable because of sharply increasing density in this region (see Fig. 4.1b).

Chapter 6

Macroscopic nuclear properties

6.1 Descriptions of the nuclear surface

One of the fundamental problems in nuclear structure is the adequate description of nuclear shapes. Indeed, in the study of heavy–ion reactions, in fusion, fission, nuclear rotations and collective vibrations the nuclear deformation–energy landscape plays a predominant role. It is then obvious that the parametrization of the nuclear shape needs to be both simple (involving only a few relevant collective parameters) and flexible, i.e. allowing for a reliable description of the large variety of the above phenomena. A very successful description of the nuclear surface was proposed in Ref. [71] known as the "Funny–Hills" parametrization of the nuclear surface. This prescription has been the reference for over 30 years now. We will use in this work its slightly modified version (see [72] and section 6.2) thereof describing the nuclear shape in cylindrical coordinates.

6.1.1 The Funny–Hills (FH) deformation parameters

A very efficient parametrization of the nuclear surface, in particular for a description of the fission process, was proposed already in 1972 in Ref. [71]:

$$\rho_s^2(u) = R_0^2 c^2 \left(1 - u^2\right) \left(A + \alpha u + B u^2\right) , \tag{6.1}$$

where $\rho_s(z)$ is the distance from the symmetry axis (chosen as $z-$axis), to the surface of the nucleus. The positions of left and right ends of the nucleus are in the point $z_{min} = -z_0 + z_{sh}$ and $z_{max} = z_0 + z_{sh}$ respectively with $z_0 = cR_0$. The quantity z_{sh} is the shift of the $z-$coordinate which ensures that the nuclear center of mass stays at $z = 0$. The dimensionless coordinate u is defined as

$$u = \frac{z - z_{sh}}{z_0}. \tag{6.2}$$

The volume conservation condition

$$V = \frac{4\pi}{3}R_0^3 = \int_0^{2\pi} d\varphi \int_{z_{min}}^{z_{max}} dz \int_0^{\rho_s(z)} \rho d\rho = z_0\, c^2 R_0^2\, \pi \int_{-1}^{1} (1-u^2)(A+\alpha u + B\, u^2)\, du \tag{6.3}$$

gives the elongation parameter c:

$$c = \left(A + \frac{1}{5}B\right)^{-1/3} . \tag{6.4}$$

The parameter c measures the elongation of the nucleus in units of the radius R_0 of the corresponding spherical nucleus of the same volume. The coordinate z_{sh} is determined by requiring that the position of the center of mass of a nucleus z_{cm} is located at $z = 0$

$$z_{cm} = \frac{2\pi \int_{z_{min}}^{z_{max}} \rho_s^2(z) z\, dz}{2\pi \int_{z_{min}}^{z_{max}} \rho_s^2(z)\, dz} = \frac{R_0 c \int_{-1}^{1} (1-u^2)\,(A+\alpha u + B\, u^2) u\, du}{\int_{-1}^{1} (1-u^2)\,(A+\alpha u + B\, u^2)\, du} = 0 , \tag{6.5}$$

which yields

$$z_{sh} = -\frac{1}{5}\alpha c^3\, z_0. \tag{6.6}$$

A shape in the Funny–Hills parametrization is usually defined by the above elongation parameter c and a neck parameter h which can be expressed through the hexadecapole deformation parameter B by the relation

$$B = 2h + \frac{1}{2}(c-1)\,. \tag{6.7}$$

The case of $h = 0$ corresponds for actinide nuclei approximately to the average liquid-drop path to fission. The parameter A can easily be evaluated from the volume–conservation condition and is equal to

$$A = \frac{1}{c^3} - \frac{1}{10}(c-1) - \frac{2}{5}h\,. \tag{6.8}$$

In order to avoid unphysical *three body* shapes for certain z values for which $\rho_s^2 < 0$ for certain combinations of the $\{c, h\}$ parameters, in particular for small nuclear elongations and, in addition, to be able to better describe diamond–like shapes preferred particularly by nuclear ground states in the actinide region, an alternative analytical form was proposed in Ref. [71] for negative values of the parameter B, namely

$$\rho_s^2(u) = \begin{cases} R_0^2 c^2\ (1-u^2)\,(A+\alpha u + Bu^2) & , \quad B \geq 0 \\ R_0^2 c^2\ (1-u^2)\ (A+\alpha u)\, \exp\left(Bc^3 u^2\right) , & \quad B < 0 \end{cases} \tag{6.9}$$

The multipole moments of the uniform density distribution are given by the following integrals

$$Q_{n0} = \frac{2}{R_0^3} \int \rho_0(\vec{r})\, r^n P_n(x)\, d^3r, \tag{6.10}$$

where $\rho_0(\vec{r})$ is the nuclear density distribution, the auxiliary variable x is equal to $x = \rho_s/\sqrt{\rho_s^2 + z^2}$, $(\rho_s^2 = x^2 + y^2)$ and $P_n(x)$ is the $n^{th}-$order Legendre polynomial of x.

6.1.2 Trentalange–Koonin–Sierk (TKS) parametrization

Following the idea of Ref. [73] we might generalize the Funny-Hills parametrization by expanding the axially symmetric shape of the fissioning nucleus into a series of Legendre polynomials P_n:

$$\rho_s^2(z) = R_0^2 \sum_{n=0,2,4,\ldots}^{\infty} \alpha_n P_n\left(\frac{z - z_{sh}}{z_0}\right), \tag{6.11}$$

where R_0 and z_0 are defined in the same way as in the Funny–Hills parametrization and where the left and right tips of the nucleus are located at $z_{min} = -z_0 + z_{sh}$ and $z_{max} = z_0 + z_{sh}$ respectively and where the shift z_{sh} of the $z-$coordinate ensures that the center of mass of nucleus is located at at $z = 0$, a quantity which is zero if all odd deformation parameters α_n vanish. The condition

$$\rho_s(z_{min}) = \rho_s(z_{max}) = 0\ , \tag{6.12}$$

implies the following relations:

$$\sum_{n=0}^{\infty} a_n P_n(-1) = \sum_{n=0}^{\infty} (-1)^n \alpha_n = 0 \tag{6.13}$$

$$\sum_{n=0}^{\infty} a_n P_n(1) = \sum_{n=0}^{\infty} \alpha_n = 0 \tag{6.14}$$

The parameters α_0 and α_1 can be easily evaluated from the above equations:

$$\alpha_0 = -\sum_{n=2,4,}^{\infty} \alpha_n\ , \qquad \alpha_1 = -\sum_{n=3,5,}^{\infty} \alpha_n\ . \tag{6.15}$$

Notice, that the spherical nuclear shape corresponds to $\alpha_2 = \alpha_0 = -\frac{2}{3}$, oblate forms to $\alpha_2 < -\frac{2}{3}$ and prolate ones to $-\frac{2}{3} > \alpha_2 < 0$. When α_2 is tending to zero the nucleus becomes infinitely long.

The volume conservation condition

$$V = \frac{4\pi}{3} R_0^3 = \int_0^{2\pi} d\varphi \int_{z_{min}}^{z_{max}} dz \int_0^{\rho_s(z)} \rho d\rho =$$

$$= \pi R_0^2 \int_{z_{min}}^{z_{max}} \sum_{n=0}^{\infty} \alpha_n P_n(\frac{z - z_{sh}}{z_0}) dz =$$

$$= \pi R_0^2 z_0 \int_{-1}^{1} \sum_{n=0}^{\infty} \alpha_n P_n(u) du = 2\pi R_0^2 z_0 \alpha_0 \tag{6.16}$$

gives the following relation

$$z_0 = \frac{2}{3} \frac{R_0}{\alpha_0} , \tag{6.17}$$

where $z_0 = (z_{max} - z_{min})/2$ is the half length of the deformed nucleus. Notice, that the elongation parameter c used in Ref. [71] is equal to the half length of a nucleus in the units of spherical radius R_0

$$c = z_0/R_0 = \frac{2}{3\alpha_0} . \tag{6.18}$$

In presence of odd multipolarity deformations one has to introduce an additional condition which fixes the position of the mass center of the deformed nucleus at the origin of the coordinate system

$$z_{cm} = \int_0^{2\pi} d\varphi \int_{z_{min}}^{z_{max}} z\, dz \int_0^{\rho_s(z)} \rho\, d\rho = \pi R_0^2 \int_{z_{min}}^{z_{max}} z \sum_{n=0}^{\infty} \alpha_n P_n(\frac{z - z_{sh}}{z_0}) dz$$

$$= \pi R_0^2 z_0 \int_{-1}^{1} (z_0 u + z_{sh}) \sum_{n=0}^{\infty} \alpha_n P_n(u) du = 0 . \tag{6.19}$$

The above relation allows to evaluate the value of the coordinate z_{sh} as

$$z_{sh} = -\frac{1}{3} \frac{\alpha_1}{\alpha_0} z_0 = -\frac{2}{9} \frac{\alpha_1}{\alpha_0^2} R_0 . \tag{6.20}$$

6.2 Modified Funny–Hills parametrizations

6.2.1 Axially symmetric shapes with a Gaussian neck

The main goal of the shape definition in cylindrical coordinates is its simplicity and the relatively small number of physically relevant deformation degrees of freedom which need to be included. In order to describe in a reasonable way the nuclear fission process, i.e. reproduce very extensive fission barriers occurring e.g. for some actinide nuclei we have to incorporate quite a substantial number of octupole, hexadecapole and higher–multipolarity deformation parameters, at least, up to β_{14}. This, however, is theoretically possible but in practice not too convenient with respect to the computation time even for high–performance computational clusters. Please note, that for each deformation degree of freedom one has to construct the grid of points of, at least, 20 points. For a four–dimensional deformation space the total number of points is

$N_g = 20^4 = 1.6 \times 10^5$ grid points. For a five–dimensional space $N_g = 3.2 \times 10^6$ points etc. In each such a point the set of single–particle states for a given nucleus should be determined. After that we can come to the evaluation of the total macroscopic–microscopic energy. This problem will be discussed in further sections.

An efficient description of the nuclear surface arised from the careful study of the original FH and TKS parametrizations given by eqs. (6.9) and (6.11). Our aim is, however, not to propose a totally new shape description but rather to improve the existing ones by avoiding the problem of spurious roots of $\rho_s(z)^2$ between its end points and, if possible, by lowering the average liquid–drop energy along the fission path. Finally, we concluded [72] that the parametrization

$$\rho_s^2(z) = \frac{R_0^2}{c\, f(a,B)} (1-u^2)(1+\alpha u - B\, e^{-a^2u^2}) \tag{6.21}$$

turns out to be the most appropriate for the problems which are going to be discussed in this work. The quantities z_0 and u are defined as in the two previous shape parametrizations and the function

$$f(a,B) = 1 - \frac{3\,B}{4\,a^2}\left[e^{-a^2} + \sqrt{\pi}(a - \frac{1}{2a})\,\mathrm{Erf}(a)\right] \tag{6.22}$$

ensures the volume conservation of the deformed nucleus.

The physical meaning of the deformation parameters entering the eq. (6.21) is similar to the one given in the previous subsection, namely: c describes the elongation of the nucleus, B is responsible for the neck formation and α represents the left–right mass asymmetry. The neck width parameter a resulting from the minimization of the liquid drop energy along the fission paths yields a value $a = 1$. Very close energy values for constant elongations c (but different values of B) one obtains for $0.8 \leq a \leq 2$. A similar study for the influence of this parameter on the total nuclear energy, when taking into account microscopic (shell and pairing) corrections will be presented in section 8.2.

Similarly as in Ref. [71] it is more convenient to introduce the following linear combination of c and B

$$h = \frac{1}{2}[B - (c-1)] \tag{6.23}$$

as the neck parameter. The line $h = 0$ in the limited deformation space $\{c, h\}$ corresponds then roughly to the average liquid drop path to fission for actinide nuclei. Of course, the parameters B and h do not correspond directly to those of Ref. [71] but they have a very similar physical meaning.

The shift coordinate z_{sh} is obtained from an equation similar to (6.5) and is equal to

$$z_{sh} = -\frac{4}{15}\,\alpha\, z_0 / f(a,B)\ , \tag{6.24}$$

where the normalization factor $f(a, B)$ is given be eq. (6.22).

The parametrization (6.21) describes better the *diamond–like* shapes then the original Funny–Hills one. Let us remind that this kind of shapes are exhibited by some nuclei in the equilibrium. The desirable advantage of the parametrization presented here is, without any doubt, that we obtain no more three–body unphysical shapes, i.e. where $\rho_s^2(z) < 0$ which could show up in the Funny–Hills definitions (6.1) and (6.9). The scission point defined by $z_{sc} = 0$ is reached here at $B = 1$ for left–right symmetric shapes ($\alpha = 0$) and

$$B \approx 1 - \frac{\alpha^2}{4\,a^2} \quad \text{at} \quad u_{sc} \approx \frac{-\alpha}{2\,B_{sc}} \tag{6.25}$$

when asymmetry ($\alpha \neq 0$) is considered.

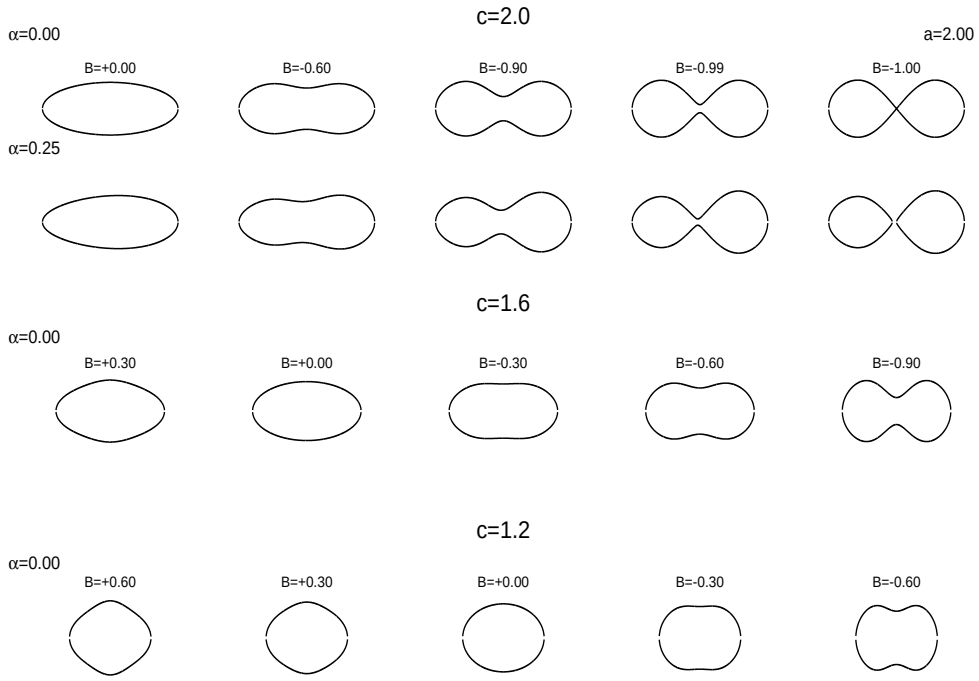

Figure 6.1: Family of shapes obtained through the modified FH parametrization with gaussian–like neck characterized by parameter B for $\{c = 2.0, \alpha = 0.0\}$ (first row), for $\{c = 2.0, \alpha = 0.25\}$ (second row), for $\{c = 1.6, \alpha = 0.0\}$ (third row) and for $\{c = 1.2, \alpha = 0.0\}$ (lower row)

6.2.2 Axial shapes with Lorentzian neck

The shape of a fissioning nucleus can be also described by the following variation of the original FH shape definition:

$$\rho_s^2\,(z) = R_0^2\,c^2\,(1 - u^2)\,(A + \alpha u + f(u))\ , \tag{6.26}$$

where z_0 and u are defined as before and

$$f(u) = \mathrm{sign}(B)\left(1 - \frac{1}{1+|B|u^2}\right) \ . \tag{6.27}$$

The parameter c as in section 6.2 describes the elongation of the drop, B is responsible for the neck formation and α gives the left–right asymmetry. As it was shown in Ref. [71] it is more convenient to introduce the following linear combination of c and B

$$h = \frac{1}{2}B - \frac{1}{4}(c-1) \tag{6.28}$$

as the neck parameter. Then the line $h = 0$ corresponds roughly to the average liquid drop path to fission for actinide nuclei. The volume conservation condition

$$\frac{4}{3}\pi R_0^3 \ = \ 2\pi \int\limits_{z_{min}}^{z_{max}} \rho_s^2(z)dz = \ 2\pi R_0^3 c^3 \int\limits_{-1}^{1} (1-u^2)\left[A + \alpha u + f(u)\right] du \ , \tag{6.29}$$

with $z_{min} = -z_0 + z_{sh}$ and $z_{max} = z_0 + z_{sh}$ allows to evaluate the adjustable parameter A

$$A = \frac{1}{c^3} - \frac{3}{4}I \ , \tag{6.30}$$

where

$$\begin{aligned} I \ &= \ \mathrm{sign}(B) \int\limits_{-1}^{1} \left(1 - \frac{1}{1+|B|u^2}\right)(1-u^2)\, du = \qquad (6.31) \\ &= \ \mathrm{sign}(B)\left\{\frac{4}{3} - \frac{2}{\sqrt{|B|}}\arctan(\sqrt{|B|}) + 2\frac{\sqrt{|B|} - \arctan(\sqrt{|B|})}{\sqrt{|B|}^3}\right\} \ . \end{aligned}$$

The shift coordinate z_{sh} is obtained from the condition (6.5):

$$z_{cm} = \frac{2\pi \int\limits_{z_{min}}^{z_{max}} \rho_s^2(z) z\, dz}{2\pi \int\limits_{z_{min}}^{z_{max}} \rho_s^2(z)\, dz} = \frac{R_0 c \int\limits_{-1}^{1} (1-u^2)\,(A + \alpha u + f(u)) u\, du}{\int\limits_{-1}^{1} (1-u^2)\,(A + \alpha u + f(u))\, du} = 0 \ , \tag{6.32}$$

and it is equal to

$$z_{sh} = -\frac{1}{5}\,\alpha\, c^3\, z_0 \ . \tag{6.33}$$

6.2.3 Nonaxial case

The Funny Hills–like parametrizations (6.1), (6.11), (6.21), (6.26) presented in previous sections are not able to describe three–axial shapes which are strongly realised by some actinide nuclei along their paths to fission. It should be realised that all these shape parametrizations contain until now only three physically relevant deformation parameters (responsible respectively for elongation, neck formation and left–right mass

asymmetry). In order to consider also nonaxial shapes, let us assume that the cross–section perpendicular to the symmetry $z-$axis is of the form of an ellipse

$$\frac{x^2}{a^2} + \frac{y^2}{b^2} = 1 \ , \tag{6.34}$$

with its half axes a and b and that this ellipse is the same for all z. In the polar coordinates the above equation reads

$$\rho^2 = \frac{a^2 b^2}{b^2 \cos^2(\varphi) + a^2 \sin^2(\varphi)}. \tag{6.35}$$

One can introduce now the deformation parameter η defined as

$$\eta = \frac{b^2 - a^2}{a^2 + b^2} \ , \tag{6.36}$$

which is related to the non–axiality of the drop. In order to keep the same volume conservation condition of the drop as for the axial case (6.16) we assume that the surface of the ellipse (6.34) is independent on η, i.e.

$$\pi \rho_s^2 = \pi a b \ , \tag{6.37}$$

where ρ_s^2 is given e.g. by eq. (6.21). The half axes of the drop cross section at given z are therefore of the form

$$\begin{aligned} a &= \rho_s(z) \left(\frac{1-\eta}{1+\eta} \right)^{1/4} \ , \\ b &= \rho_s(z) \left(\frac{1+\eta}{1-\eta} \right)^{1/4} \ . \end{aligned} \tag{6.38}$$

Finally, after exploiting the constant–volume condition (6.16), the square of the distance from an arbitrary surface point (z, φ) to the $z-$axis is given by

$$\widetilde{\rho}_s^2(z, \varphi) = \rho_s^2(z) \frac{\sqrt{1-\eta^2}}{1 + \eta \cos(2\varphi)} \ . \tag{6.39}$$

This parameter η can, in general, depend on z but in the following we assume that it is $z-$independent.

6.2.4 Ellipsoidal case

For a vanishing neck parameter, $B = 0$ eqs. (6.21, 6.39) describe a pure ellipsoid with the following main half axes:

$$\begin{aligned} \mathcal{A} &= R_0 / \sqrt{c} \left(\frac{1-\eta}{1+\eta} \right)^{1/4} \ , \\ \mathcal{B} &= R_0 / \sqrt{c} \left(\frac{1+\eta}{1-\eta} \right)^{1/4} \ , \\ \mathcal{C} &= R_0 \, c \ . \end{aligned} \tag{6.40}$$

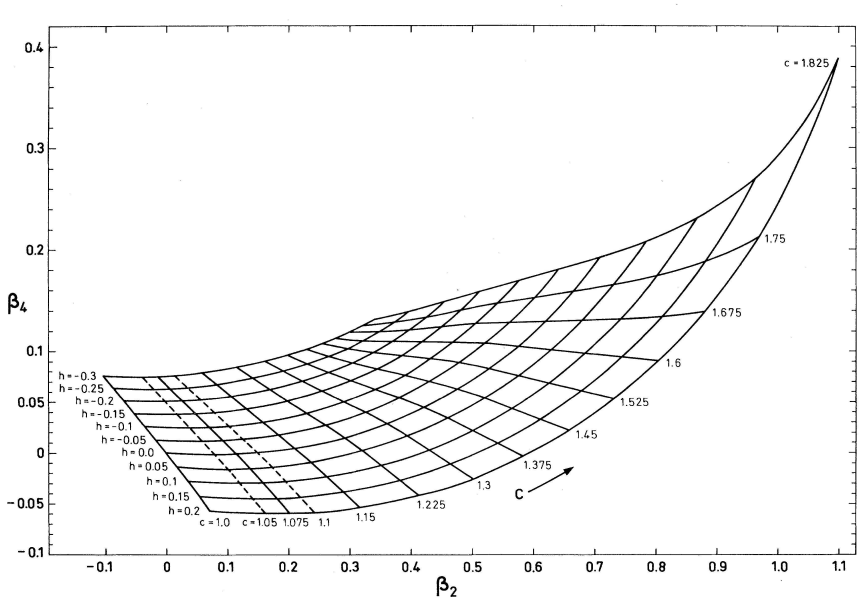

Figure 6.2: Transformation from the (c, h) to (β_2, β_4) coordinates obtained for the FH parametrization of eq. 6.1 and 6.9. Figure is taken from Ref. [71]

In the traditional (β, γ) parametrization these axes are expressed as

$$\begin{aligned} \mathcal{A} &= R(\beta,\gamma)\,[1 - k\cos(\gamma - \pi/3)]\ , \\ \mathcal{B} &= R(\beta,\gamma)\,[1 - k\cos(\gamma + \pi/3)]\ , \\ \mathcal{C} &= R(\beta,\gamma)\,[1 + k\cos(\gamma)]\ , \end{aligned} \tag{6.41}$$

where $k = \sqrt{\frac{5}{4\pi}}\beta$ and

$$R(\beta,\gamma) = R_0/\{[1 - k\cos(\gamma - \pi/3)]\,[1 - k\cos(\gamma + \pi/3)]\,[1 + k\cos(\gamma)]\}^{1/3} \tag{6.42}$$

The transformations between the coordinates $\{c, \eta\}$ and $\{\beta, \gamma\}$ are shown (both ways) in Figs. 6.3 and 6.4 respectively. The closed ovals in Fig. 6.4 correspond to the shapes with constant deformation β_2 which can occur for prolate ($\gamma \in (0 + \frac{2}{3}n\pi\,,\ \frac{\pi}{3} + \frac{2}{3}n\pi)$) as well as for oblate shapes ($\gamma \in (\frac{\pi}{3} + \frac{2}{3}n\pi\,,\ \frac{2\pi}{3} + \frac{2}{3}n\pi)$, where $(n = 1, 2, 3...)$.

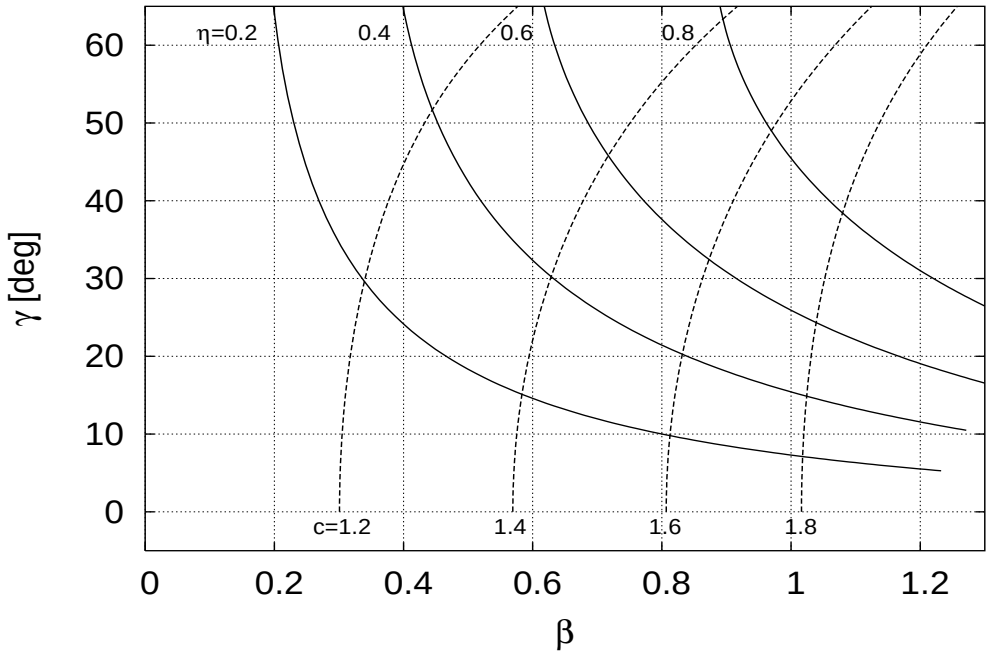

Figure 6.3: Transformation from the (β, γ) to (c, η) coordinates in the pure ellipsoidal case

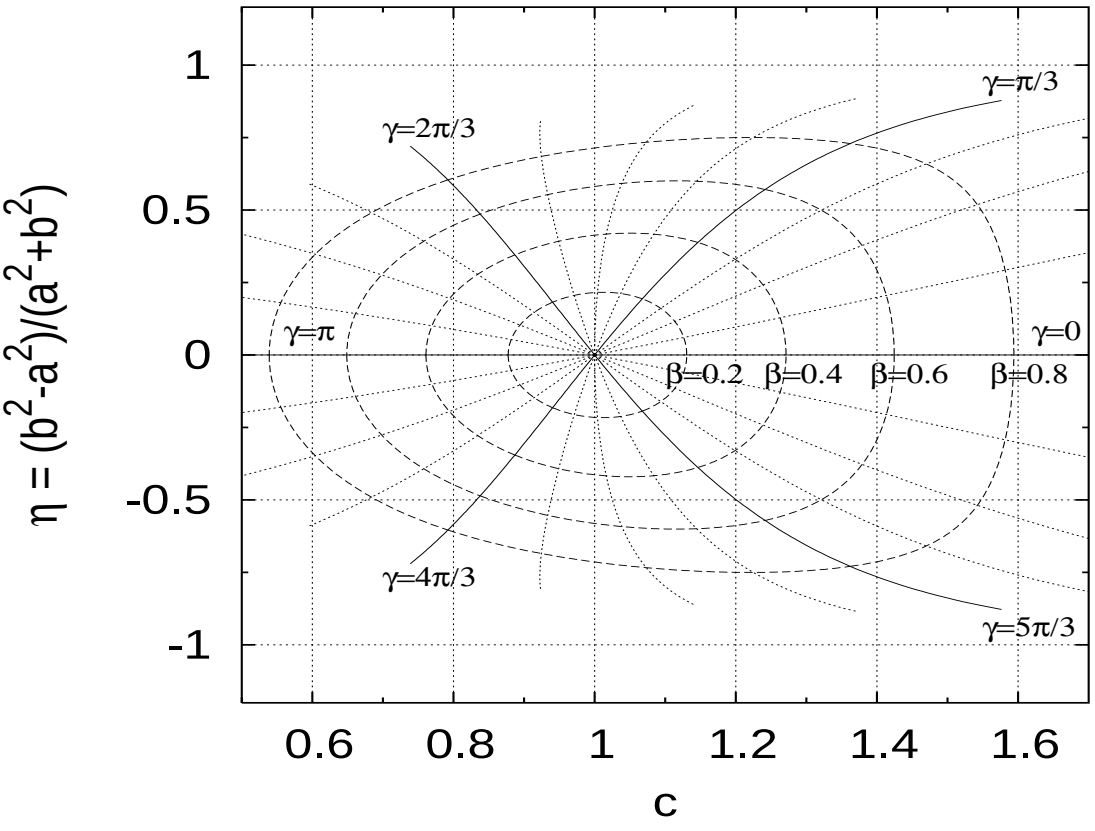

Figure 6.4: Transformation from the (c, η) to (β, γ) coordinates in the pure ellipsoidal case

6.3 Liquid drop fission barriers

The discovery of the fission process was inspired by the research work which lead to the attribution of the Nobel Prize to Enrico Fermi in 1938 for the experiment of bombarding uranium nuclei by neutrons. As it turned out later, what was observed were the fission fragments of the bombarded uranium nucleus and not some transuranium elements with atomic number larger then 92, as was initially expected. About nine years later, O. Hahn and F. Strassmann concluded that as a consequence of of the bombardment of uranium, lighter isotopes of barium are formed. The first qualitative description of the nuclear fission process was given by L. Meitner, and her collaborator O. Frisch (Nature, vol. 143, p. 239). By analogy with a charged liquid drop they explained this process as the result of the competition of the long range Coulomb repulsion between protons tending to tear the nucleons apart and the surface tension force trying to keep the nucleons together like the surface of a liquid drop. This simple idea was developed later by N. Bohr and J. A. Wheeler in their famous paper *The mechanism of nuclear fission* in Physical Review (vol. 56, p. 426). This paper has been the reference point for the next generations of nuclear physicists working on nuclear fission.

Since that breakthrough explanation of the nuclear fission phenomenon by Meitner and Frisch we have no doubt that this process is determined mainly by the strong short range attractions between the neighbouring nucleons and long range Coulomb repulsion of protons in an atomic nucleus. As we know even from the first descriptions of the liquid drop idea in nuclear physics that the volume term which is the dominant constituent of the average, liquid drop energy for the nucleus of given mass A does not change with a deformation. On the other hand the surface–energy contribution depends strongly on the nuclear surface area which is a function of the nuclear shape. The competition of the positive Coulomb and the negative surface–energy contributions gives as a consequence an energetical barrier which can be tunnelled by the nucleus on its way to fission. Summarizing, if the surface LD energy increases faster then the Coulomb energy decreases, i.e. if

$$2E_{surf} \geq E_{Coul}, \tag{6.43}$$

then such a barrier exists. Inserting the explicit expressions for E_{surf} and E_{Coul} as in the standard Liquid–Drop model discussed in section 2 and the approximations of the deformation functions B_{surf}, B_{Coul} we rewrite the condition (6.43) as

$$a_{surf}A^{2/3} \cdot \frac{2}{5}\alpha^2 \geq a_{Coul}\frac{Z^2}{A^{1/3}} \cdot \frac{\alpha^2}{5}, \tag{6.44}$$

where α is the global deformation parameter defined already by eq. (3.14). The above expression can be transformed into the more convenient form

$$\frac{2B_{surf}A}{B_{Coul}Z^2} \geq 1. \tag{6.45}$$

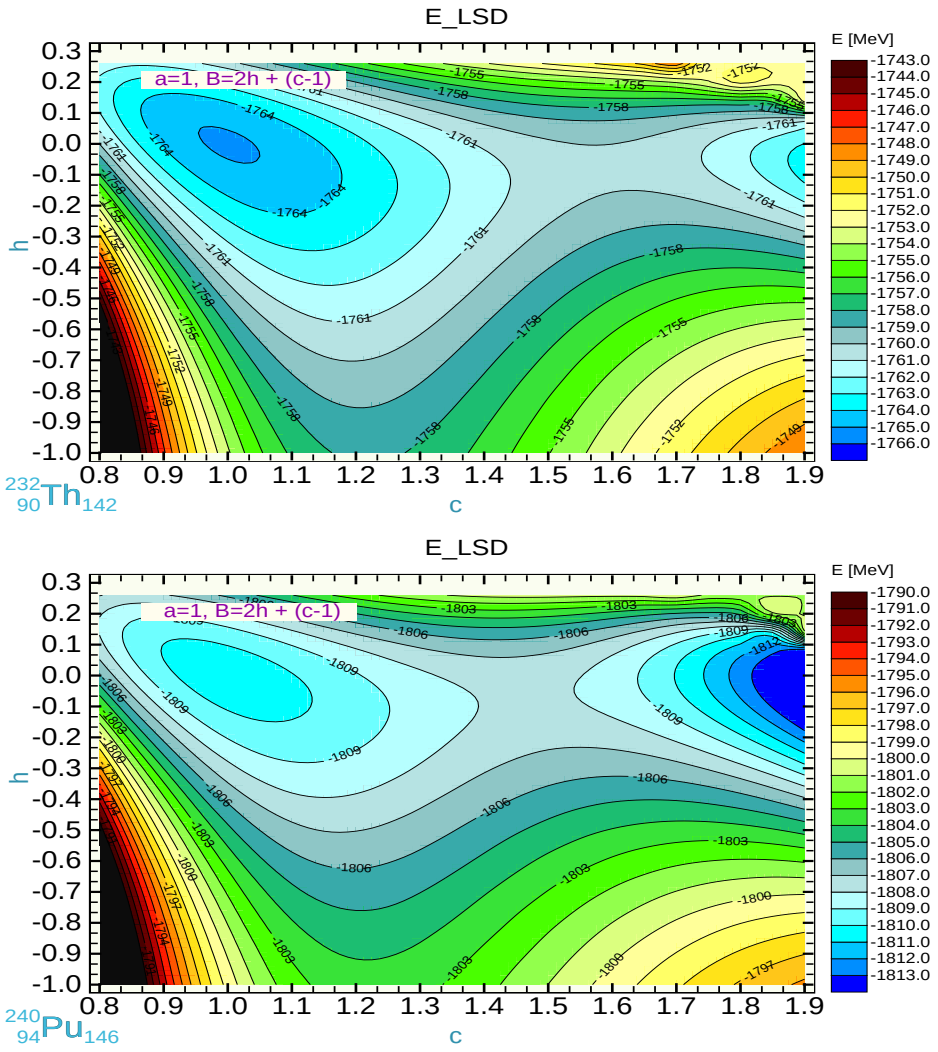

Figure 6.5: Liquid drop energy landscape as function of the elongation (c) and neck parameter (h) for ^{232}Th and ^{240}Pu

Let us define the fissility parameter x as

$$x \equiv \frac{b_{\text{Coul}} Z^2}{2 b_{\text{surf}} A} \approx \frac{Z^2}{49A}. \tag{6.46}$$

Using this parameter we can classify the atomic nuclei with respect to their ability to spontaneous fission, namely for nuclei with high fission barrier, i.e. for which the probability of fission is extremely low $x \ll 1$ and, conversely, $x > 1$ for a vanishing fission barrier

For the actinide nuclei ^{232}Th and ^{240}Pu the two dimensional LD energy landscapes are shown in Fig. 6.5, where the average fission barrier is visible as the valley which runs along the line $h = 0$ starting from the spherical minimum through the saddle visible e.g. in the case of ^{232}Th around $\{c \approx 1.6,\ h = 0\}$ to the scission point where we have to do already with two fragments. In turn, for proton–rich heavy and super–heavy nuclei we can observe that the liquid drop barrier is usually significantly reduced or even is not

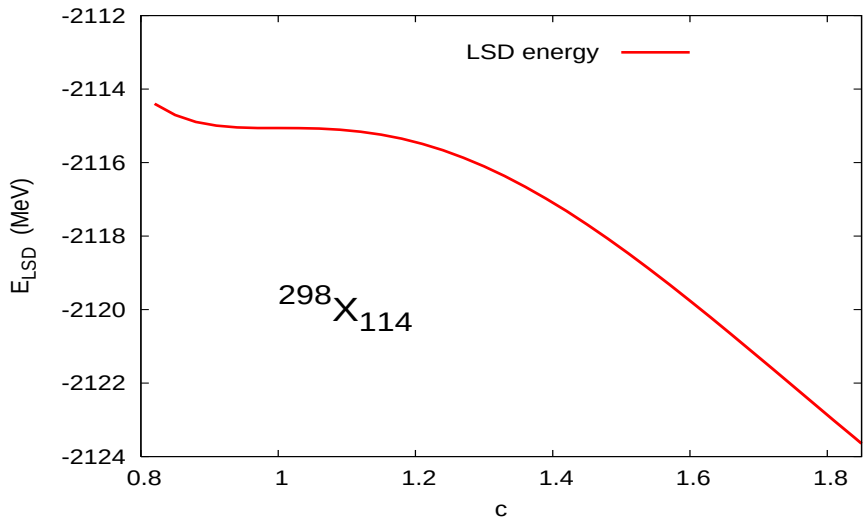

Figure 6.6: Liquid drop fission barrier within LSD model for super–heavy nucleus $^{298}X_{114}$

present at all. This can happen, in principle, due to the stronger Coulomb repulsion as compared to the nuclear attraction between the nucleons for such the nuclei. However, the experiments concerning the heavy and super–heavy elements seem to confirm that even nuclei in which the liquid drop barriers are practically inexisting can be stable against the spontaneous fission. Such an effect exists e.g. in the super–heavy elements with $Z = 114$ (see e.g. Fig. (6.6)).

Keeping in mind that the total nuclear energy contains also the quantal corrections we can immediately conclude that the shell and pairing effects are responsible for creating the fission barrier, and therefore for the stability of that nucleus. Figure 6.7 presents a comparison of the LD fission barrier of the nucleus ^{232}Th using the Lublin–Strasbourg Drop model [8] together with three different parametrizations of the nuclear surface, presented above, namely the Funny–Hills and the modified FH parametrizations. The liquid drop fission barriers of ^{232}Th evaluated with the shape definitions given by eq. (6.21) with that obtained using the original Funny–Hills parameters (6.9) reveals that the new shape definition with gaussian neck gives the lowest average barrier, however, this reduction is of the order of 100–300 keV only (see Fig. 6.7). Mentioned results we compare also, in the same figure, with the similar, possible shape description where the neck is created by a Lorentz function (see eq. (6.26) and [74]). Unfortunately, also in that case we were not able to eliminate three–body shapes appearing along the path to fission.

It appears in Fig. 6.8 that the TKS formula (6.11) gives a very satisfactory description of the barrier heights, already with three deformation parameters α_2, α_4 and α_6. The parameter α_8 brings almost negligible contributions (order of keV's) even in the region of the exit configuration from the barrier.

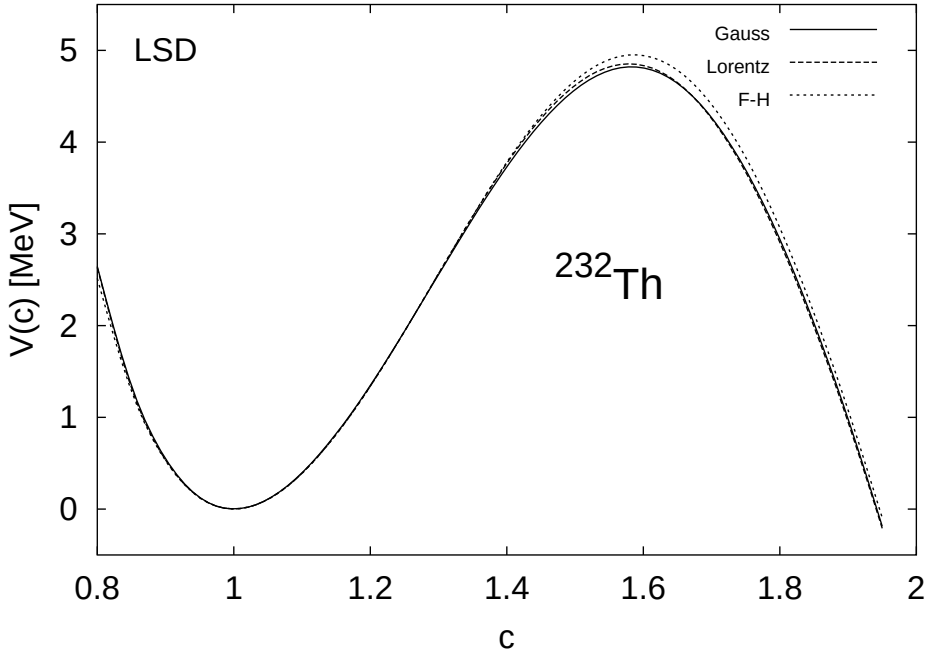

Figure 6.7: Fission barrier of ^{232}Th evaluated within the LSD (Lublin Strasbourg Drop) model for different shape descriptions: the modified Funny–Hills with the Gauss neck (6.21) and the Lorentz neck (6.26), as well as the original Funny–Hills parametrization (6.1) as a function of the elongation parameter c.

Studying Figure 6.9 we can convince ourselves about the power of the shape definitions in cylindrical coordinates. The axial liquid–drop fission barrier obtained with the use of the Funny–Hills–like parametrizations with only two parameters $\{c, h\}$ are identical, within $0.2 - 0.4\,\mathrm{MeV}$ to those, generated in spherical coordinates with the help of the multipole expansion of the form

$$R(\theta) = R_0\Big[1 + \sum_{\lambda=2}^{\lambda_{max}} (\beta_\lambda Y_{\lambda 0}(\theta) - \beta_\lambda^2/4\pi)\Big], \tag{6.47}$$

where $Y_{\lambda 0}(\theta)$ are the appropriate spherical harmonics. However, for super–heavy nuclei which shapes at the scission configuration are, in general, rather compact the definition (6.47) can be alternatively applied. In that case one does not need as many deformation parameters β_λ to reproduce such a shape, as for the actinide nuclei (e.g. ^{232}Th) which are known to exhibit more elongated shapes with substantially pronounced neck in the scission configuration. This fact is one of the main reasons for which the expansion (6.47) is still applied, (see e.g. Ref. [75]).

In order to see the convergence of the multipole expansion we have evaluated the LSD fission barrier of ^{232}Th using different number of $\beta_\lambda^{(max)}$ parameters. The results are presented in Fig. 6.10.

It can be seen from this figure that one has to use, at least, five, lowest–order

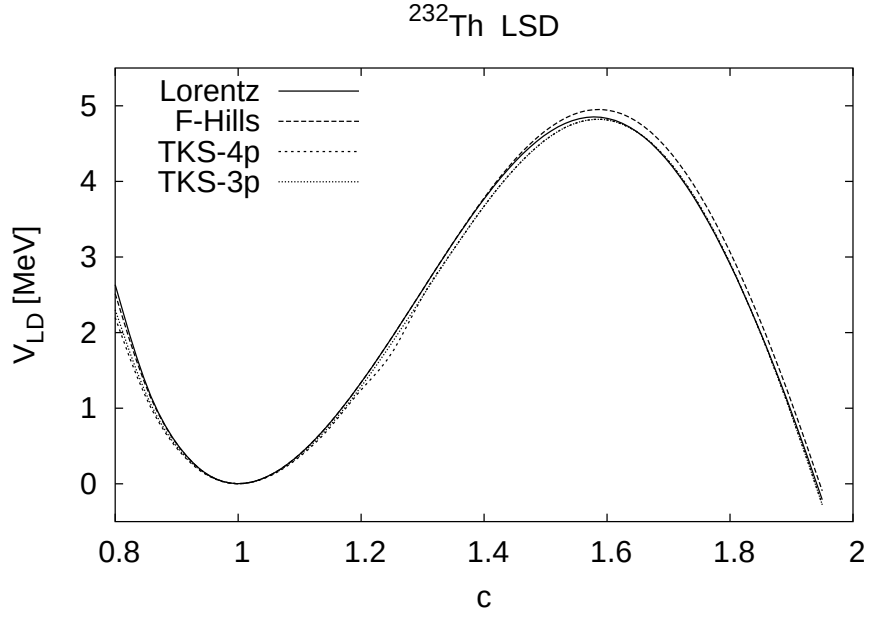

Figure 6.8: Fission barrier of ^{232}Th evaluated within the LSD model for different shape parametrizations: modified Funny–Hills (Lorentz), Funny-Hills and TKS with 3 and 4 parameters, as a function of the elongation parameter

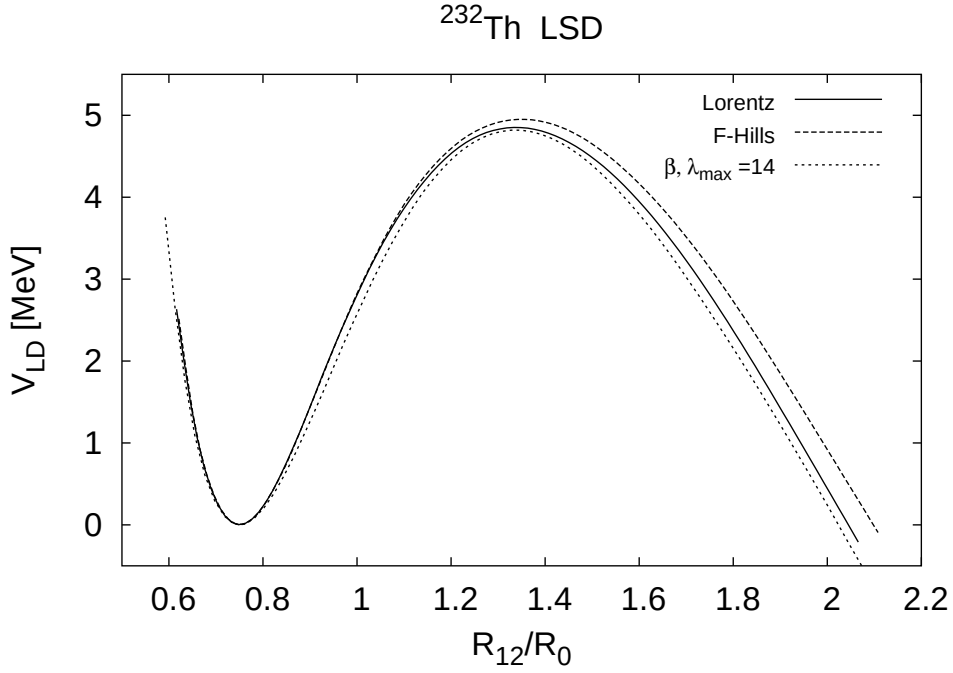

Figure 6.9: Fission barrier of ^{232}Th evaluated within the LSD model using the β_λ (with $\lambda_{max} = 14$) deformations compared with the barriers obtained with two free parameters only using the Funny-Hills prescription and its modification (Lorentz). R_{12} is the relative distance between fission fragments.

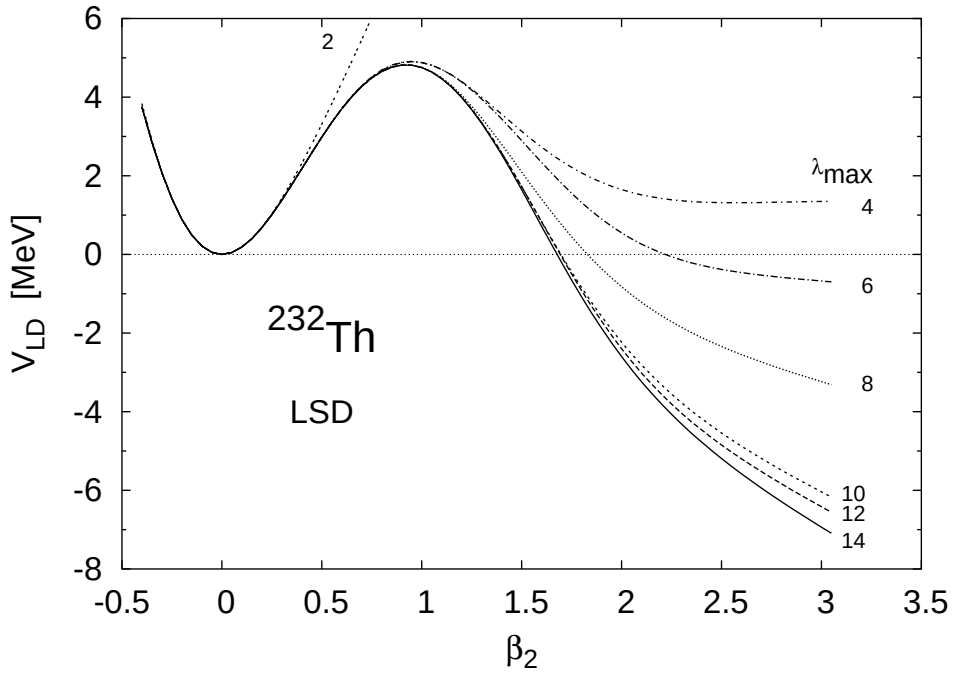

Figure 6.10: Fission barrier of ^{232}Th evaluated within the LSD model using different numbers of the $\beta_\lambda^{(max)}$ deformations.

even β_λ deformations to obtain the fission barrier comparable with that given by the original or modified Funny–Hills equation which contains in the axial and left–right symmetric case only two parameters $\{c, h\}$.

6.4 Yukawa–folding description of nuclear structure

In 1935 Hideki Yukawa presented a theory of the strong interaction where the force between two nucleons is mediated by the exchange of a meson between the two interacting particles, in the same way as the photon represents the *particle* responsible for the electromagnetic interaction. From the very short range of the strong interaction Yukawa was able to estimate the mass of this meson to be about 140 MeV/c^2, a particle which was found a couple of years later and which is known today as the $\pi-$meson. The form of the meson potential which Yukawa postulated is of the form:

$$V_{Yuk}(r) = G\,\frac{1}{r}\,e^{-\frac{m_\pi c}{\hbar}r}, \tag{6.48}$$

where G is the coupling constant and where the characteristic length of this interaction is the $\pi-$meson Compton wave length

$$\left(\frac{\lambda}{2\pi}\right)_\pi = \frac{\hbar}{m_\pi c} \tag{6.49}$$

which is of the order of 1.4 fm with a pion mass of $m_\pi \approx 139$ MeV, and therefore, indeed, of very short range.

6.4.1 Folded densities

Nuclear density in the most general way can be expressed with a help of a folding procedure of Ref. [76]:

$$\rho(\vec{r}_1) = \rho_0 \int_V d^3r_2\, g\,(\,|\vec{r}_1 - \vec{r}_2|\,), \tag{6.50}$$

where ρ_0 is the uniform density distribution of the charge or the nuclear matter

$$\rho_0(\vec{r}) = \begin{cases} \rho_0 = 3A/4\pi R_0^3, & \text{for} \quad r \leq R_0 \\ 0, & \text{for} \quad r > R_0 \end{cases}$$

which satisfies the nucleon–number conservation condition

$$\int_V \rho_0(\vec{r})\, d^3r = N(Z\,). \tag{6.51}$$

The folding function in eq. (6.50) needs to be normalized

$$\int_V g\,(\,|\vec{r}_1 - \vec{r}_2|\,)\, d^3r_2 = 1. \tag{6.52}$$

The folding function $g\,(\,|\vec{r}_1 - \vec{r}_2|\,)$ can be chosen to be of the form of the Yukawa function (6.48) with a width parameter a (of the order of the pion Compton wavelength)

$$g\,(\,|\vec{r}_1 - \vec{r}_2|\,) = \frac{1}{4\pi a^3} \frac{e^{-|\vec{r}_1 - \vec{r}_2|/a}}{|\vec{r}_1 - \vec{r}_2|/a}. \tag{6.53}$$

The function $g\,(\,|\vec{r}_1 - \vec{r}_2|\,)$ should not be misunderstood here to represent the interaction potential of two nucleons, but rather the fact that an interaction of finite (short) range between the constituents of an $N-$particle system will generate a density distribution with a diffuse surface where this surface diffuseness should be of the order of 1 fm, as this is obtained through the definition (6.50).

6.4.2 Coulomb potential

Having established the charge distribution in the nucleus in the form of eq. (6.50) the Coulomb potential can be calculated from the expression (see e.g. [76])

$$V_c(\vec{r}_1) = e \int_V d^3r_2 \frac{\rho(\vec{r}_2)}{|\vec{r}_1 - \vec{r}_2|}. \tag{6.54}$$

For two functions f and g the following equation is fulfilled:

$$\int_V d^3r_2 f(\vec{r}_1 - \vec{r}_2) g(\vec{r}_1 - \vec{r}_2) = \int_{-\infty}^{\infty} d^3k f(\vec{k}) g(\vec{k}) e^{i\vec{k}\cdot(\vec{r}_1 - \vec{r}_3)}. \tag{6.55}$$

Thus, replacing $g(\vec{r}_2 - \vec{r}_3)\frac{1}{|\vec{r}_1 - \vec{r}_2|}$ by their Fourier transforms we have

$$V_c(\vec{r}_1) = \frac{4\pi e\rho_0}{(2\pi)^{\frac{3}{2}}} \int_V d^3r_3 \int_{-\infty}^{\infty} d^3k \frac{1}{k^2} g(k) e^{i\vec{k}\cdot(\vec{r}_1 - \vec{r}_3)}, \tag{6.56}$$

where the Fourier transform of the Yukawa function of eq. (6.53) is of the form

$$g(k) = \frac{1}{2\pi} \frac{1}{(1 + a^2k^2)}. \tag{6.57}$$

Due to the fact that the function g depends only on the norm of $\vec{k}$ we can perform immediately the second integration and rewrite above expression as

$$V_c(\vec{r}_1) = 4(2\pi)^{\frac{1}{2}} e\rho_0 \int_V d^3r_3 \frac{1}{|\vec{r}_1 - \vec{r}_3|} \int_0^{\infty} dk \frac{g(k)}{k} \sin(k|\vec{r}_1 - \vec{r}_3|). \tag{6.58}$$

Inserting the Fourier transform of the Yukawa function given by the eq. (6.57) the final expression is of the form

$$\begin{aligned} V_c(\vec{r}_1) &= \frac{4(2\pi)^{\frac{1}{2}} e\rho_0}{(2\pi)^{\frac{3}{2}}} \int_V d^3r_3 \frac{1}{|\vec{r}_1 - \vec{r}_3|} \\ &\times \int_0^{\infty} dk \frac{1}{(1 + a^2k^2)} \frac{1}{k} \sin(k|\vec{r}_1 - \vec{r}_3|). \end{aligned} \tag{6.59}$$

Using the relation

$$\sin(x) = \frac{e^{ix} - e^{-ix}}{2i}, \tag{6.60}$$

we transform the last expression to the form

$$\begin{aligned} V_c(\vec{r}_1) &= \frac{2}{\pi} e\rho_0 \int_V d^3r_3 \frac{1}{|\vec{r}_1 - \vec{r}_3|} \times \int_0^{\infty} dk \frac{e^{i\vec{k}\cdot(\vec{r}_1 - \vec{r}_3)}}{2ik(k^2 + \frac{1}{a^2})} = \\ &\frac{e\rho_0}{\pi i} \int_V d^3r_3 \frac{1}{|\vec{r}_1 - \vec{r}_3|} \times \int_{-\infty}^{+\infty} dk \frac{e^{i\vec{k}\cdot(\vec{r}_1 - \vec{r}_3)}}{a^2k(k^2 + \frac{1}{a^2})}. \end{aligned} \tag{6.61}$$

Using the residues method to perform the last integral in the complex plane we come to the following relation:

$$V_c(\vec{r}_1) = V_c(\vec{r}_1; sharp) + \triangle V_c(\vec{r}_1), \tag{6.62}$$

where $V_c(\vec{r}_1; sharp)$ is the dominant term in the Coulomb potential coming from the uniform density distribution and $\triangle V_c(\vec{r}_1)$ is the correction which origins from the diffuseness of the charge distribution.
Explicitly this expressions looks like

$$V_c(\vec{r}_1; sharp) = \rho_0 e \int_V d^3r_2 \frac{1}{|\vec{r}_1 - \vec{r}_2|} \tag{6.63}$$

and

$$\Delta V_c(\vec{r}_1) = -\rho_0 e \int\limits_V d^3r_2 \frac{1}{|\vec{r}_1 - \vec{r}_2|} e^{-\frac{|\vec{r}_1 - \vec{r}_2|}{a}}. \tag{6.64}$$

Applying the Gauss–Ostrogradsky theorem allowing for the conversion of the volume integral of a given function $f(|\vec{r}_1 - \vec{r}_2|)$ over the whole space into a surface integral of the function $F(|\vec{r}_1 - \vec{r}_2|)$ over the corresponding surface in the general form

$$\int\limits_V d^3r_2\, f(|\vec{r}_1 - \vec{r}_2|) = \oint\limits_S (d\vec{S}_2 \cdot \vec{r}_{12}) F(|\vec{r}_1 - \vec{r}_2|) \tag{6.65}$$

we transform these two integrals (6.63) and (6.64) to the more convenient form (for numerical integration by e.g. Gauss–Legendre quadrature), i.e.

$$\begin{aligned} V_c(\vec{r}_1; sharp) &= -\frac{\rho_0 e}{2} \oint\limits_S [d\vec{S}_2 \cdot (\vec{r}_1 - \vec{r}_2)] \frac{1}{|\vec{r}_1 - \vec{r}_2|} \\ \Delta V_c(\vec{r}_1) &= +\frac{\rho_0 e}{a} \oint\limits_S [d\vec{S}_2 \cdot (\vec{r}_1 - \vec{r}_2)] \left(\frac{|\vec{r}_1 - \vec{r}_2|}{a} \right)^{-3} \\ \times & \left[1 - \left(1 + \frac{|\vec{r}_1 - \vec{r}_2|}{a} \right) e^{-\frac{|\vec{r}_1 - \vec{r}_2|}{a}} \right]. \end{aligned} \tag{6.66}$$

For a spherical nucleus described by the radius R_0 the integrals (6.66) can be easily evaluated analytically.

6.4.3 Coulomb energy

By analogy with the previous subsection one can derive the expressions for the Coulomb energy of deformed nucleus. This energy is defined as [76]

$$E_c = \frac{1}{2} \int\limits_V \int\limits_V d^3r_1\, d^3r_2\, \frac{1}{|\vec{r}_1 - \vec{r}_2|}\, \rho(\vec{r}_1)\, \rho(\vec{r}_2). \tag{6.67}$$

Inserting folded density (6.50) to the above we get

$$\begin{aligned} E_c = & \frac{{\rho_0}^2}{2} \int\limits_V \int\limits_V d^3r_1\, d^3r_2\, \frac{1}{|\vec{r}_1 - \vec{r}_2|} \\ & \times \int\limits_V \int\limits_V d^3r_3\, d^3r_4\, g(|\vec{r}_1 - \vec{r}_3|)\, g(|\vec{r}_2 - \vec{r}_4|)\, . \end{aligned} \tag{6.68}$$

Further calculations will be lead like in the case of the Coulomb potential generalizing eq. (6.55) for three functions f, g, h we have that

$$\begin{aligned} & \int\limits_V \int\limits_V d^3r_1\, d^3r_2\, f(|\vec{r}_1 - \vec{r}_2|)\, g(|\vec{r}_1 - \vec{r}_3|)\, h(|\vec{r}_2 - \vec{r}_4|) = \\ & \quad = (2\pi)^{\frac{3}{2}} \int\limits_\infty d^3k\, f(\vec{k})\, g(-\vec{k})\, h(\vec{k})\, e^{i\vec{k}\cdot(\vec{r}_3 - \vec{r}_4)}. \end{aligned} \tag{6.69}$$

Inserting the above identity to eq. (6.68) we obtain

$$E_c = 4\pi \, \frac{{\rho_0}^2}{2} \int\limits_V \int\limits_V d^3r_1 \, d^3r_2 \int\limits_{-\infty}^{\infty} d^3k \, \frac{1}{k^2} \, g^2(k) \, e^{i\vec{k}\cdot(\vec{r}_1-\vec{r}_2)}. \tag{6.70}$$

After performing the integral over k we come to the following formula

$$E_c = \frac{(4\pi)^2}{2} \, {\rho_0}^2 \int\limits_V \int\limits_V \frac{d^3r_1 d^3r_2}{|\vec{r}_1-\vec{r}_2|} \int\limits_0^{\infty} dk \, \frac{g^2(k)}{k} \, \sin(k|\vec{r}_1-\vec{r}_2|). \tag{6.71}$$

Applying first the Fourier transform of the function g as given in eq. (6.57) we have

$$E_c = \frac{{\rho_0}^2}{(2\pi)} \, \frac{1}{i} \int\limits_V \int\limits_V \frac{d^3r_1 d^3r_2}{|\vec{r}_1-\vec{r}_2|} \int\limits_{-\infty}^{+\infty} dk \, \frac{e^{i\vec{k}|\vec{r}_1-\vec{r}_2|}}{k(1+a^2k^2)^2}. \tag{6.72}$$

The residuum theorem brings us to the similar conclusion as before (see Appendix, section A.2.1), namely

$$E_c = E_c(sharp) + \triangle E_c, \tag{6.73}$$

where $E_c(sharp)$ is the part of the Coulomb energy generated by the uniform density distribution whereas $\triangle E_c$, like before, is the negative correction from the surface charge

$$E_c(sharp) = \frac{{\rho_0}^2}{12} \int\limits_V \int\limits_V d^3r_1 \, d^3r_2 \, \frac{1}{|\vec{r}_1-\vec{r}_2|}, \tag{6.74}$$

$$\Delta E_c = \frac{-{\rho_0}^2}{2} \int\limits_V \int\limits_V d^3r_1 \, d^3r_2 \, \frac{1}{|\vec{r}_1-\vec{r}_2|} \; e^{-|\vec{r}_1-\vec{r}_2|/a} \left(1 + \frac{1}{2} \, \frac{|\vec{r}_1-\vec{r}_2|}{a}\right). \tag{6.75}$$

Transforming double volume integral into two surface ones we are left with the expressions which are easier to compute numerically

$$E_c(sharp) = -\frac{\rho_0^2}{12} \oint\limits_S \oint\limits_S \frac{[d\vec{S}_1 \cdot (\vec{r}_1-\vec{r}_2)] \, [d\vec{S}_2 \cdot (\vec{r}_1-\vec{r}_2)]}{|\vec{r}_1-\vec{r}_2|}, \tag{6.76}$$

$$\begin{aligned} \Delta E_c = {} & \frac{\rho_0^2}{2a} \oint\limits_S \oint\limits_S \frac{[d\vec{S}_1 \cdot (\vec{r}_1-\vec{r}_2)] \, [d\vec{S}_2 \cdot (\vec{r}_1-\vec{r}_2)]}{|\vec{r}_1-\vec{r}_2|/a^4} \\ & \times \left[2\frac{|\vec{r}_1-\vec{r}_2|}{a} - 5 + \left(5 + 3\frac{|\vec{r}_1-\vec{r}_2|}{a} + \frac{1}{2}\frac{|\vec{r}_1-\vec{r}_2|^2}{a^2}\right) e^{\frac{-|\vec{r}_1-\vec{r}_2|}{a}}\right]. \end{aligned} \tag{6.77}$$

6.4.4 Yukawa–folded effective potentials

In order to obtain the potential energy landscape many authors used the well known macroscopic–microscopic model which will be the topic of more detailed studies in the section 7.2.1. Since the time when the shell effect were approximately incorporated by Myers and Świątecki [77] this model evolved continuously, to describe the total nuclear

energy as a function of deformation with better and better accuracy. At the same time, however, the alternative, more microscopic approach of the Hartree–Fock and Hartree–Fock–Bogoliubov type with effective nucleon–nucleon interactions became more and more performant. In 1966 Strutinsky proposed a new way of evaluating shell effects [78] which gave a new impetus to the macroscopic–microscopic approach, a method which played a predominant role in these kind of calculations for several decades. A drawback of the Strutinsky shell–correction method which consisted in the fact that the particle number was only conserved on the average was cured quite recently [79] by a smoothing procedure in particle number space (or rather in $N^{1/3}$ space, to be precise) which conserves the particle number precisely. Much progress was also made in the treatment of the short range pairing correlations, however, this work will only use the traditional BCS approach. The shell and pairing corrections to the average liquid drop trends are calculated for a given nucleus on the basis of the single–particle levels which change considerably as a function of the nuclear shape. One then understands that the knowledge of the nuclear mean–field potential is absolutely crucial as the basis for an appropriate treatment of processes like nuclear fission, fusion, rotations, collective excitations etc. Historically the first realistic single–particle nuclear potential was the Nillson potential [80] which was simply the harmonic oscillator well corrected by terms proportional to l^2 which deepen its bottom for the peripheral nucleons. Taking into account also the spin–orbit coupling $\sim \vec{l} \cdot \vec{s}$ one insures also the correct shell structure of the single–particle energy levels. Later, the more realistic Woods–Saxon potential [81] was proposed which after many improvements has been successfully applied until now.

Since the mean–field single–particle potential should correspond approximately to the density distribution of nucleons we can generate its shape by the convolution of the nuclear density with the Yukawa–like function which can be considered here as the spin independent two–body interaction (interaction between two infinitesimal volume elements of a nuclear drop)

$$V(r_{12}) = -\frac{V_0}{4\pi\lambda^3} \frac{e^{-|\vec{r}_1-\vec{r}_2|/\lambda}}{|\vec{r}_1-\vec{r}_2|/\lambda}, \quad r_{12} = |\vec{r}_1-\vec{r}_2|. \tag{6.78}$$

In order to obtain the central part of the single–particle potential we fold the density distribution (6.50) with the Yukawa interaction (6.78), (see e.g. Ref. [76])

$$V_{sp}(\vec{r}_1) = \int_V d^3r_2\, V(r_{12})\, \frac{\rho(\vec{r}_2)}{\rho_0}. \tag{6.79}$$

Using the Fourier transform of Yukawa function $g(k)$ as in eq. (6.57), we rewrite the above integral as follows

$$V_{sp}\left(\vec{r}_1\right) = -\frac{V_0}{(2\pi)^{3/2}} \int\limits_V d^3r_3 \int\limits_{-\infty}^{\infty} d^3k \, \frac{g(k)}{1+\lambda^2 k^2} \, e^{i\,\vec{k}\cdot(\vec{r}_1-\vec{r}_3)}. \tag{6.80}$$

Performing the second integral over the angles θ and φ in momentum–space we come to the expression for the potential:

$$V_{sp}\left(\vec{r}_1\right) = -\left(\frac{2}{\pi}\right)^{1/2} V_0 \int\limits_V \frac{d^3r_3}{|\vec{r}_1-\vec{r}_3|} \int\limits_0^{\infty} dk\, k \, \frac{g(k)}{1+\lambda^2 k^2} \, \sin(k\,|\vec{r}_1-\vec{r}_3|). \tag{6.81}$$

Inserting the explicit Fourier transform (6.57) in the place of the function $g(k)$, we obtain finally an expression which is convenient for the integration by the residues method in the complex plane

$$V_{sp}\left(\vec{r}_1\right) = -\frac{V_0}{4\pi^2 i} \int\limits_V \frac{d^3r_3}{|\vec{r}_1-\vec{r}_3|} \int\limits_{-\infty}^{\infty} dk\, k \, \frac{e^{ik|\vec{r}_1-\vec{r}_3|}}{(1+\lambda^2k^2)\,(1+a^2k^2)}. \tag{6.82}$$

In general, we assume that the range λ of the Yukawa interaction is slightly different from the range a of the folding function of the same type used to generate the density distribution in the eq. (6.50).

After analytical integration in the complex plane we observe that the single–particle potential is the sum of two terms, namely

$$V_{sp}\left(\vec{r}_1\right) = V\left(\vec{r}_1; sharp\right) + \Delta V\left(\vec{r}_1\right), \tag{6.83}$$

where the *sharp–density* potential independent on the density diffuseness a is now

$$V\left(\vec{r}_1; sharp\right) = -\frac{V_0}{4\pi\lambda^3} \int\limits_V \frac{e^{-|\vec{r}_1-\vec{r}_2|/\lambda}}{|\vec{r}_1-\vec{r}_2|/\lambda} \, d^3r_2, \tag{6.84}$$

and the correction being a function of both the diffuseness parameters λ and a reads

$$\Delta V\left(\vec{r}_1\right) = -\frac{a^2}{a^2-\lambda^2} \, V\left(\vec{r}_1; sharp\right) - \frac{V_0}{4\pi(a^2-\lambda^2)} \int\limits_V \frac{e^{-|\vec{r}_1-\vec{r}_2|/a}}{|\vec{r}_1-\vec{r}_2|} \, d^3r_2. \tag{6.85}$$

Converting the above spatial integrals into surface integrals as before we obtain

$$V\left(\vec{r}_1; sharp\right) = \frac{V_0}{4\pi\lambda^3} \oint\limits_S \left(d\vec{S}_2 \cdot \vec{r}_{12}\right) \left(\frac{|\vec{r}_1-\vec{r}_2|}{\lambda}\right)^{-3} \left[1 - \left(1+\frac{|\vec{r}_1-\vec{r}_2|}{\lambda}\right) e^{\frac{|\vec{r}_1-\vec{r}_2|}{\lambda}}\right] \tag{6.86}$$

and

$$\begin{aligned} \Delta V\left(\vec{r}_1\right) \;\; = \;\; & -\frac{a^2}{a^2-\lambda^2} \, V\left(\vec{r}_1; sharp\right) + \frac{V_0}{4\pi(a^2-\lambda^2)} \oint\limits_S \left(d\vec{S}_2 \cdot \vec{r}_{12}\right) \left(\frac{|\vec{r}_1-\vec{r}_2|}{a}\right)^{-3} \times \\ & \left[1 - \left(1+\frac{|\vec{r}_1-\vec{r}_2|}{a}\right) e^{\frac{|\vec{r}_1-\vec{r}_2|}{a}}\right]. \end{aligned} \tag{6.87}$$

For a spherical nucleus with radius R_0 the expression (6.86) can be evaluated analytically [76] and is equal to

$$V_{sph}(r_1; sharp) = \begin{cases} -V_0 \left[1 - \left(1 + \frac{R_0}{\lambda}\right) e^{-R_0/\lambda} \frac{\sinh(r_1/\lambda)}{(r_1/\lambda)}\right] & \text{for} \quad r_1 \leq R_0 \\ -V_0 \left[\frac{R_0}{\lambda}\cosh(\frac{R_0}{\lambda}) - \sinh(\frac{R_0}{\lambda})\right] \frac{e^{-r_1/\lambda}}{(r_1/\lambda)} & \text{for} \quad r_1 \geq R_0, \end{cases} \tag{6.88}$$

while (6.87)

$$\begin{aligned} \Delta V_{sph}(r_1) = & -\frac{a^2}{(a^2-\lambda^2)} V_{sph}(r_1; sharp) \\ & + \begin{cases} \frac{a^2 V_0}{(\lambda^2-a^2)} \left[1 - \left(1 + \frac{R_0}{a}\right) e^{-R_0/a} \frac{\sinh(r_1/a)}{(r_1/a)}\right] & \text{for} \quad r_1 \leq R_0 \\ \frac{a^2 V_0}{(\lambda^2-a^2)} \left[\frac{R_0}{a}\cosh(\frac{R_0}{a}) - \sinh(\frac{R_0}{a})\right] \frac{e^{-r_1/a}}{(r_1/a)} & \text{for} \quad r_1 \geq R_0, \end{cases} \end{aligned} \tag{6.89}$$

The splitting of folded quantities like Coulomb and nuclear potential as well as the corresponding folded energies into *sharp* and *diffused* component is mathematically strict, but, as was demonstrated in Ref. [76], not really necessary since the effect of the density diffuseness can be practically mocked up by a *renormalisation* of the diffuseness parameter λ of the *sharp–density* contribution. In addition, as shown in Ref. [76], the *diffuse–density* correction seems to vary very slowly with the nuclear deformation. For these reasons the corrections were no longer used in the form given by eqs. (6.64), (6.75), (6.87) in later calculations [82].

The spin–orbit component of the total single–particle mean–field interaction can be built using the central part of the potential V_{sp} in the standard way

$$V_{s.o.} = i\,\lambda^q \left(\frac{\hbar}{2Mc}\right)^2 \vec{\nabla} V_{sp} \cdot \left[\vec{\sigma} \times \vec{\nabla}\right], \qquad q = \{n, p\}, \tag{6.90}$$

where $\vec{\sigma}$ denotes the vector of 2×2 Pauli matrices $(\sigma_x, \sigma_y, \sigma_z)$.
We used the following parametrization for the depth parameter of central part of the single–particle potentials for protons and neutrons [82]:

$$\begin{aligned} V_0^p &= V_s + V_a\,\bar{\delta}, \\ V_0^n &= V_s - V_a\,\bar{\delta}, \end{aligned} \tag{6.91}$$

where

$$\begin{aligned} \bar{\delta} &= \left(I + \frac{3}{8}\frac{c_1}{Q}\frac{Z^2}{A^{5/3}}\right) \Big/ \left(1 + \frac{9}{4}\frac{J}{Q}\frac{1}{A^{1/3}}\right), \qquad I = (N-Z)/A, \\ \lambda^p &= 6.0\left(\frac{A}{240}\right) + 28.0, \\ \lambda^n &= 4.5\left(\frac{A}{240}\right) + 31.5 \end{aligned} \tag{6.92}$$

constant	value	unit
λ	0.8	$[fm]$
a	0.7	$[fm]$
V_s	52.5	$[MeV]$
V_a	48.7	$[MeV]$
J	35.0	$[MeV]$
Q	25.0	$[MeV]$
c_1	$\frac{3}{5}\frac{e^2}{r_0}$	$[MeV]$
M	938.9	$[MeV/c^2]$
r_0	1.16	$[fm]$

Tab. 6.1 Constants used in the Yukawa–folding procedure

At the end of our discussion of folded potentials let us compare in Fig. 6.11 the shape of the Yukawa–folded potential with the corresponding Woods–Saxon potential for spherical ^{240}Pu. As we can see in the above figure both, the Yukawa–folded (6.86)

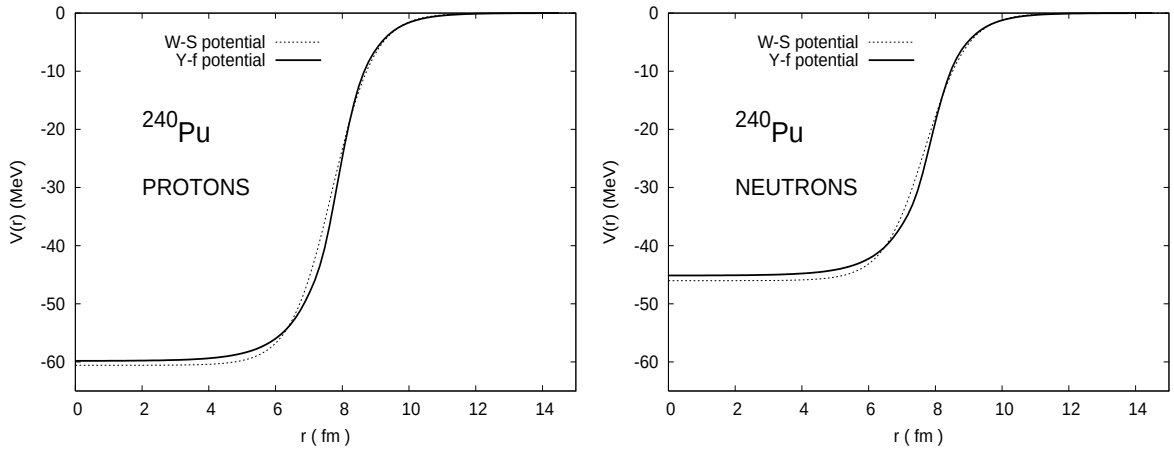

Figure 6.11: Comparison of the spherical Yukawa–folded (solid line) and Woods–Saxon (dashed line) potentials of ^{240}Pu for protons (without the Coulomb contribution) (l.h.s.) and for neutrons (r.h.s.). W-S potential parameters are taken from Ref. [83]

and Woods–Saxon with Chepurnov's parameters [83], central potentials are almost identical. A minor difference of ≈ 0.5 MeV is, however, observed in the depths of the proton and neutron wells.

6.4.5 Yukawa–folded nuclear energy

Alternatively to the liquid drop approach one can express the average nuclear energy by the double folding integral [76] as

$$E_{avr} = \frac{1}{2}\int_V\int_V d^3r_1\, d^3r_2\, V(r_{12})\, \rho(\vec{r}_1)\, \rho(\vec{r}_2)/\rho_0^2, \tag{6.93}$$

where $V(r_{12})$ is given by eq. (6.78).

The subsequent mathematical procedure is practically identical to the one presented in the earlier sections, and we will simply give here the final expressions for the nuclear folded energies $E_{avr}(sharp)$ and $\triangle E_{avr}$ [76], namely:

$$E_{avr}(sharp) = -\frac{V_0}{8\pi\lambda^3}\int_V\int_V d^3r_1\, d^3r_2\, \frac{e^{-|\vec{r}_1-\vec{r}_2|/\lambda}}{|\vec{r}_1-\vec{r}_2|/\lambda} \tag{6.94}$$

and

$$\begin{aligned}\triangle E_{avr} &= -\frac{a^2(a^2-2\lambda^2)}{(a^2-\lambda^2)^2}E_{avr}(sharp)\\ &+ \frac{V_0}{8\pi(a^2-\lambda^2)^2}\int_V\int_V d^3\vec{r}_1 d^3\vec{r}_2\left[\frac{\lambda^2}{|\vec{r}_1-\vec{r}_2|}-\frac{(a^2-\lambda^2)}{2a}\right]e^{-|\vec{r}_1-\vec{r}_2|/\lambda}.\end{aligned} \tag{6.95}$$

The two last equations, for the average nuclear energy are valid for the Yukawa folding function given e.g. by eq. (6.78). After transformation by means of the Gauss–Ostrogradsky theorem we can rewrite the above in the following form:

$$\begin{aligned}E_{avr}(sharp) &= \frac{V_0}{8\pi\lambda^3}\oint_S\oint_S \frac{[d\vec{S}_1\cdot(\vec{r}_1-\vec{r}_2)][d\vec{S}_2\cdot(\vec{r}_1-\vec{r}_2)]}{(|\vec{r}_1-\vec{r}_2|/\lambda)^4}\\ &\times \left[\frac{|\vec{r}_1-\vec{r}_2|}{\lambda}-2+\left(2+\frac{|\vec{r}_1-\vec{r}_2|}{\lambda}\right)e^{-|\vec{r}_1-\vec{r}_2|/\lambda}\right]\end{aligned} \tag{6.96}$$

and

$$\begin{aligned}&\triangle E_{avr} = -\frac{a^2(a^2-2\lambda^2)}{(a^2-\lambda^2)^2}E_{avr}(sharp)\\ &- \frac{V_0}{8\pi a(a^2-\lambda^2)^2}\oint_S\oint_S \frac{[d\vec{S}_1\cdot(\vec{r}_1-\vec{r}_2)][d\vec{S}_2\cdot(\vec{r}_1-\vec{r}_2)]}{(|\vec{r}_1-\vec{r}_2|a)^4}\left[(3a^3-5\lambda^2)+(2\lambda^2-a^2)\frac{|\vec{r}_1-\vec{r}_2|}{a}\right]\\ &+ \frac{V_0}{8\pi a(a^2-\lambda^2)^2}\oint_S\oint_S \frac{[d\vec{S}_1\cdot(\vec{r}_1-\vec{r}_2)][d\vec{S}_2\cdot(\vec{r}_1-\vec{r}_2)]}{(|\vec{r}_1-\vec{r}_2|a)^4}\\ &\times \left[(5\lambda^2-3a^2)+(3\lambda^2-2a^2)\frac{|\vec{r}_1-\vec{r}_2|}{a}-\frac{1}{2}(a^2-\lambda^2)\frac{|\vec{r}_1-\vec{r}_2|^2}{a^2}\right]e^{-|\vec{r}-1-\vec{r}_2|/a}.\end{aligned} \tag{6.97}$$

6.4.6 Folded nuclear energy with different proton–neutron density distributions

In this section we want to carry out the similar study as it was done in section 3 using the Skyrme energy functional $\mathcal{E}[\rho]$ together with the Thomas–Fermi approximation. In order to investigate the response of the nuclear energy for the relative change of neutron versus proton density deformations we recall the folding–procedure already used in the previous sections. Since the total nuclear density

$$\rho(\vec{r}) = \rho_n(\vec{r}) + \rho_p(\vec{r}) \tag{6.98}$$

is the sum of proton and neutron densities one can rewrite the expression (6.93) as follows

$$E_{nuc}(def(p), def(n)) = \frac{1}{2} \int\limits_V \int\limits_V d^3r_1 \; d^3r_2 \; V(r_{12}) \; \{\rho_p(\vec{r}_1) + \rho_n(\vec{r}_1)\} \; \{\rho_p(\vec{r}_2) + \rho_n(\vec{r}_2)\}/\rho_0^2. \tag{6.99}$$

what is equivalent to

$$\begin{aligned} E_{nuc}(def(p), def(n)) = & \; \frac{1}{2} \int\limits_{V_p} \int\limits_{V_p} d^3r_1 \; d^3r_2 \; V(r_{12}) \; \rho_p(\vec{r}_1) \; \rho_p(\vec{r}_2)/\rho_0^2 \\ + & \; \frac{1}{2} \int\limits_{V_n} \int\limits_{V_n} d^3r_1 \; d^3r_2 \; V(r_{12}) \; \rho_n(\vec{r}_1) \; \rho_n(\vec{r}_2)/\rho_0^2 \\ + & \; \frac{1}{2} \int\limits_{V_p} \int\limits_{V_n} d^3r_1 \; d^3r_2 \; V(r_{12}) \; \rho_n(\vec{r}_1) \; \rho_p(\vec{r}_2)/\rho_0^2 \\ + & \; \frac{1}{2} \int\limits_{V_p} \int\limits_{V_n} d^3r_1 \; d^3r_2 \; V(r_{12}) \; \rho_p(\vec{r}_1) \; \rho_n(\vec{r}_2)/\rho_0^2. \end{aligned} \tag{6.100}$$

Since the expressions written in the last two lines are symmetric with respect to the interchange the neutrons with protons, we can rewrite the above equation in the following form:

$$\begin{aligned} E_{nuc}(def(p), def(n)) = & \; \frac{1}{2} \int\limits_{V_p} \int\limits_{V_p} d^3r_1 \; d^3r_2 \; V(r_{12}) \; \rho_p(\vec{r}_1) \; \rho_p(\vec{r}_2)/\rho_0^2 \\ + & \; \frac{1}{2} \int\limits_{V_n} \int\limits_{V_n} d^3r_1 \; d^3r_2 \; V(r_{12}) \; \rho_n(\vec{r}_1) \; \rho_n(\vec{r}_2)/\rho_0^2 \\ + & \; \int\limits_{V_p} \int\limits_{V_n} d^3r_1 \; d^3r_2 \; V(r_{12}) \; \rho_n(\vec{r}_1) \; \rho_p(\vec{r}_2)/\rho_0^2. \end{aligned} \tag{6.101}$$

We can attribute an obvious physical interpretation to the three above terms: The first and second term describe respectively the interaction energy of protons and neutrons

(among themselves), while the third term corresponds to the interaction between protons and neutrons. Let us notice that the integration limits in eq. (6.101) are fixed for the two first terms to the proton and neutron distribution alone whereas in the last term the integration with respect to r_1 and r_2 run over the neutron (V_n) and proton (V_p) distributions respectively. The corresponding three volume integrals are identical within the integration limits to those given by eqs. (6.94) or (6.96) (q denoting protons or neutrons)

$$\begin{aligned} E_{q\,q'}(sharp) &= \frac{V_0}{8\pi\lambda^3}\frac{\rho_0^{(q)}\rho_0^{(q')}}{\rho_0^2}\oint\limits_{S_q}\oint\limits_{S_{q'}}\frac{[d\vec{S}_1\cdot(\vec{r}_1-\vec{r}_2)][d\vec{S}_2\cdot(\vec{r}_1-\vec{r}_2)]}{(|\vec{r}_1-\vec{r}_2|/\lambda)^4} \\ &\times \left[\frac{|\vec{r}_1-\vec{r}_2|}{\lambda}-2+\left(2+\frac{|\vec{r}_1-\vec{r}_2|}{\lambda}\right)e^{-|\vec{r}_1-\vec{r}_2|/\lambda}\right] \end{aligned} \tag{6.102}$$

and

$$\begin{aligned} \triangle E_{q\,q'} &= \frac{\rho_0^{(q)}\rho_0^{(q')}}{\rho_0^2}\Big\{-\frac{a^2(a^2-2\lambda^2)}{(a^2-\lambda^2)^2}E_{q\,q'}(sharp)+ \\ &- \frac{V_0}{8\pi a(a^2-\lambda^2)^2}\oint\limits_{S_q}\oint\limits_{S_{q'}}\frac{[d\vec{S}_1\cdot(\vec{r}_1-\vec{r}_2)][d\vec{S}_2\cdot(\vec{r}_1-\vec{r}_2)]}{(|\vec{r}_1-\vec{r}_2|a)^4}\left[(3a^3-5\lambda^2)+(2\lambda^2-a^2)\frac{|\vec{r}_1-\vec{r}_2|}{a}\right] \\ &+ \frac{V_0}{8\pi a(a^2-\lambda^2)^2}\oint\limits_{S_q}\oint\limits_{S_{q'}}\frac{[d\vec{S}_1\cdot(\vec{r}_1-\vec{r}_2)][d\vec{S}_2\cdot(\vec{r}_1-\vec{r}_2)]}{(|\vec{r}_1-\vec{r}_2|a)^4} \\ &\times \left[(5\lambda^2-3a^2)+(3\lambda^2-2a^2)\frac{|\vec{r}_1-\vec{r}_2|}{a}-\frac{1}{2}(a^2-\lambda^2)\frac{|\vec{r}_1-\vec{r}_2|^2}{a^2}\right]e^{-|\vec{r}-1-\vec{r}_2|/a}\Big\}, \end{aligned} \tag{6.103}$$

where $\rho_0^{(q)}=3\mathcal{N}_q/4\pi R_0^3$ is the uniform density distribution of protons or neutrons (with $\rho_0^{(p)}+\rho_0^{(n)}=\rho_0$). As V_0 we admit after Davis and Nix (see Ref. [76]) that

$$V_0=\frac{2(a^2-\lambda^2)^2a_{surf}\left[1-\kappa_{surf}((N-Z)/A)^2\right]}{(3a^5-5a^3\lambda^2+2\lambda^5)\,\pi r_0^2}, \tag{6.104}$$

where a, λ are given in Tab. 6.1 whereas a_{surf} and κ_{surf} are the LD surface–energy constants listed in Tab. 2.1 Finally, eq. (6.101) can be written in the compact form as

$$E_{nuc}(def(p),def(n))=E_{pp}+E_{nn}+2E_{pn}. \tag{6.105}$$

Please note that in order to be consistent with what is assumed for the nuclear folded proton and neutron potentials, we also use here the same radius R_0 and the surface diffuseness λ for both these distributions.

The above discussed Yukawa–folding prescription for the average energy, is unfortunately not able to give reliable predictions of LD type fission barriers. A different version of this approach known as the "Yukawa–plus–exponential" model [42] was rather developed which is much better in this respect than the version which was discussed above.

However, the aim of our investigations is to examine the sensitivity of the nuclear system for the relative change of the neutron versus proton deformations rather then the absolute energy value. The latter is well reproduced within the LSD model. What will be discussed here is rather the relative change (or stiffness) of the macroscopic energy as function of the elongation or neck–parameter difference $c_n - c_p$ or $h_n - h_p$ in the two dimensional $\{c, h\}$ deformation space.

As can be seen in Fig. 6.12 and 6.13, the average LD energy becomes less and less stiff in $c-$direction when the global elongation is increasing. This means that a more elongated nucleus is more sensible for further relative change of neutron and proton elongations. On the contrary, we do not observe a similar effect when considering the neck parameters of the proton (h_p) and neutron (h_n) density distributions. The average Yukawa–folded energy seems to be weakly dependent in $h-$direction on the global nuclear elongation. Since the magnitude of the Coulomb energy variations as a function of the relative difference of proton versus neutron deformations is substantially smaller then the corresponding change of the nuclear part (compare stiffnesses of the corresponding curves in Figs. 6.12) and 6.13) we expect that the energetical effect of proton versus neutron and neutron versus proton deformations should be, to some extent, comparable. The curves shown in Fig. 6.13 are slightly more asymmetric with respect to $c_n - c_p = 0$ then the corresponding ones in Fig. 6.12. It seems clear when we realize that proton distribution does not interact elecrostatically with the neutron one. Remember also that protons increase its Coulomb energy approaching the spherical shape and decreases it by following the larger deformations.

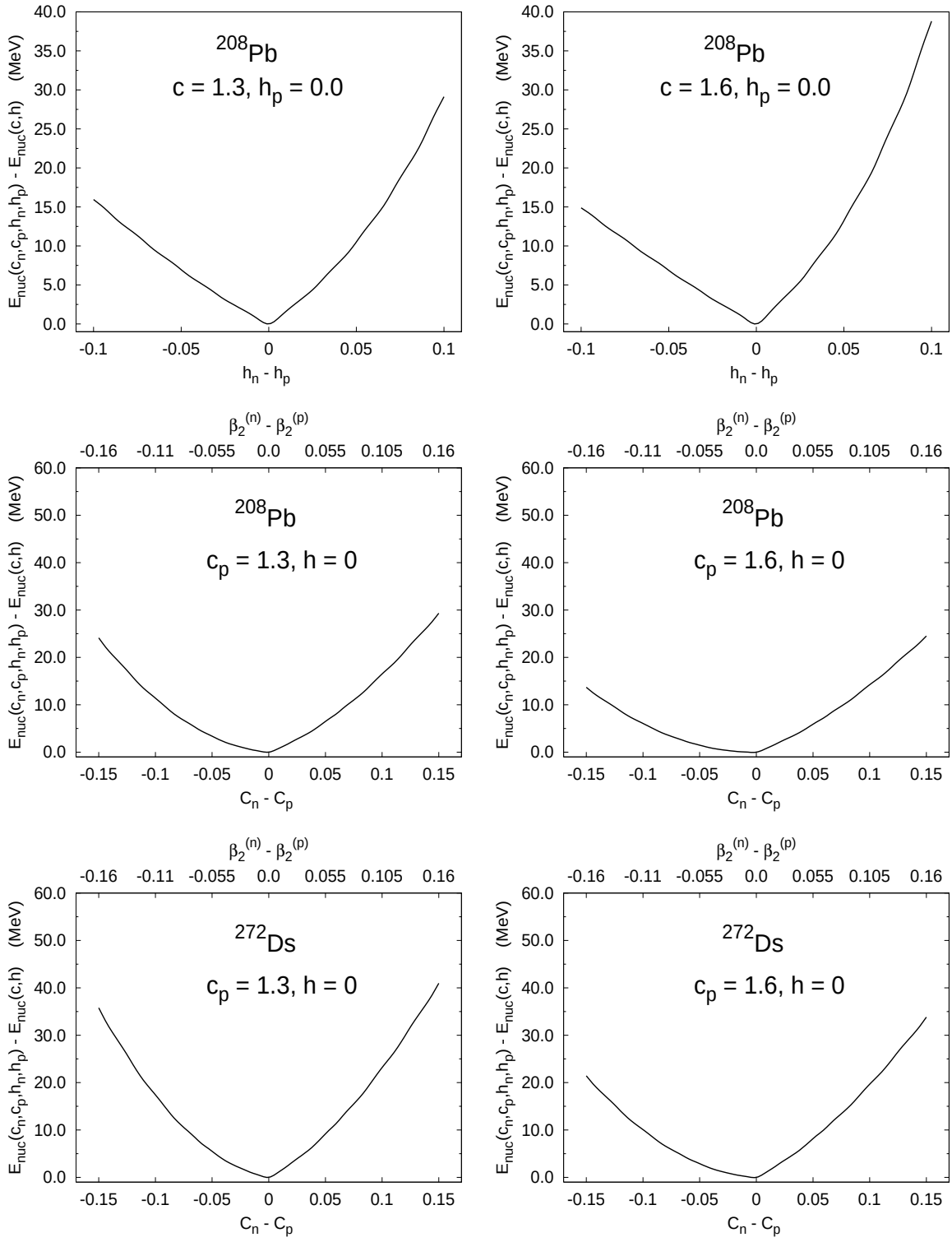

Figure 6.12: Change of macroscopic Yukawa–folded energy, as function of the **neutron versus proton deformations** expressed as the change of neutron and proton neck parameters $h_n - h_p$ (upper 2 pictures), neutron and proton elongations $c_n - c_p$ (bottom axes) and $\beta_2^{(n)} - \beta_2^{(p)}$ (top axes) for lower 4 pictures

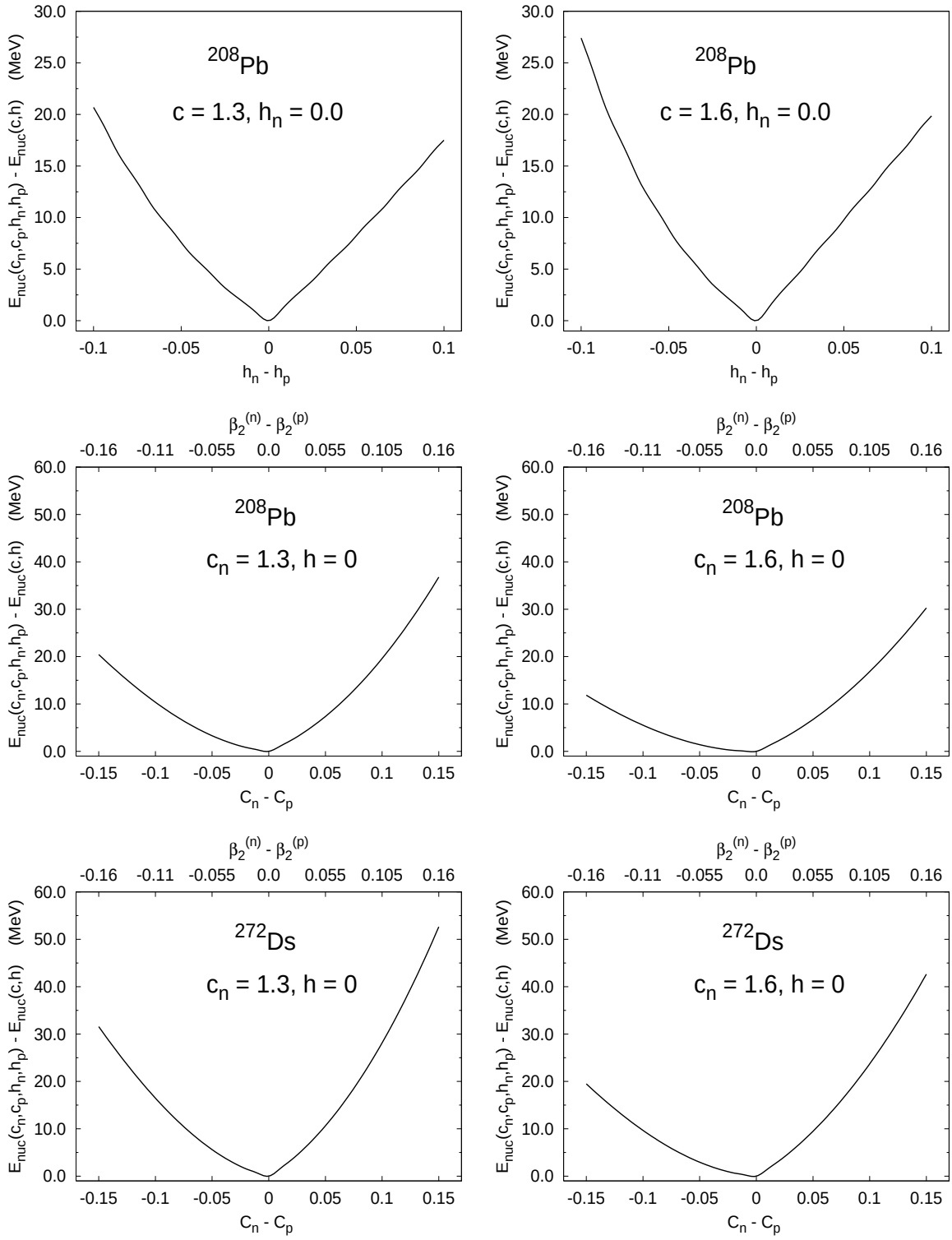

Figure 6.13: Change of macroscopic Yukawa–folded energy as function of **proton vs neutron deformations**

6.5 Diagonalization of the mean–field potentials

6.5.1 Diagonalization of the axial effective potentials

Let us consider a single–particle Hamiltonian $\hat{H}$ which has axial symmetry (e.g. containing a prolate deformed mean–field). The central potential is then independent of the angle φ in cylindrical coordinates. It is then obvious that the single–particle Hamiltonian commutes with the third component of the total angular momentum operator $\hat{J}_z = \hat{l}_z + \hat{s}_z$ and with the parity operator $\hat{P}$

$$[\hat{H}, \hat{J}_z] = 0, \qquad [\hat{H}, \hat{P}] = 0 \,, \tag{6.106}$$

where the action of the parity operator $\hat{P}$ on an arbitrary spatial function $\psi(x, y, z)$ is given by

$$\hat{P}\,\psi(x, y, z) = \psi(-x, -y, -z) \tag{6.107}$$

and its eigenvalues are equal to $\pi = \pm 1$. The eigenstates of an axially symmetric Hamiltonian are defined by a set of quantum numbers, characterizing the eigenvalues of a complete set of compatible observables. Such a set could be $\{\Omega = \Lambda + \Sigma, \pi\}$, where Ω and π are respectively the total angular momentum and parity quantum numbers. It can happen also that the reflection symmetry with respect to the $xOy-$plane is broken, e.g. when octupole deformations are taken into account. Then the parity operator no longer commutes with $\hat{H}$ and the parity π is no longer a good quantum number.

6.6 The harmonic–oscillator potential

For the case of an axially symmetric system the harmonic oscillator potential can be written as

$$V_{h.o.}(\rho, z) = \frac{1}{2} m\omega_\perp^2 \rho^2 + \frac{1}{2} m\omega_z z^2 \tag{6.108}$$

For the present case of axial symmetry one usually introduces harmonic–oscillator (h.o.) constants $\beta_\perp$ and β_z which then allow to define dimensionless coordinates ζ and η

$$\begin{aligned} \beta_z &= \frac{1}{b_z} = \sqrt{\frac{m\omega_z}{\hbar}}, \qquad \zeta = z\beta_z \\ \beta_\perp &= \frac{1}{b_\perp} = \sqrt{\frac{m\omega_\perp}{\hbar}}, \qquad \eta = \rho^2\beta_\perp^2 \end{aligned} \tag{6.109}$$

The eigenstates of an axially symmetric h.o. potential are then built with the help of the appropriate Laguere polynomial in the $\perp$ (perpendicular to the symmetry z–axis) direction and the Hermite polynomial in the $z-$direction

$$\phi_{n_\rho, n_z, \Lambda, \Sigma}(\vec{R}, \vec{\sigma}) = \psi_{n_\rho}^{\Lambda}(\rho)\, \psi_{n_z}(z)\, \frac{e^{i\Lambda\phi}}{\sqrt{2\pi}}\, \chi_\Sigma(\sigma), \tag{6.110}$$

where

$$\psi_{n_z}(z\,) = \mathcal{N}_{n_z}\,(\beta_z)^{1/2} e^{-\zeta^2/2} H_{n_z}(\zeta), \qquad \mathcal{N}_{n_z} = \sqrt{\frac{1}{\sqrt{\pi}\,2^{n_z} n_z!}}\ ,$$

$$\psi^{\Lambda}_{n_\rho}(\rho\,) = \mathcal{N}^{\Lambda}_{n_\rho}\,\beta_\perp \sqrt{2}\,\eta^{\Lambda/2} L^{\Lambda}_{n_\rho}(\eta), \qquad \mathcal{N}^{\Lambda}_{n_\rho} = \sqrt{\frac{n_\rho!}{(n_\rho+\Lambda)\,!}}\ . \tag{6.111}$$

The single–particle energies of this Hamiltonian are given as

$$E_\alpha = (\,2n_\rho + |\,\Lambda\,| + 1)\,\hbar\omega_\perp + (n_z + \frac{1}{2})\,\hbar\omega_z, \qquad \alpha = \{n_\rho\,, n_z, \Lambda, \Sigma\} \tag{6.112}$$

The corresponding eigenstates of any axially symmetric single–particle potential can be expanded in the basis of this h.o. potential

$$\Phi_i(\vec{R}, \sigma, q) = \chi_{q_i(q)} \sum_\alpha C^i_\alpha \phi_\alpha(\vec{R}, \sigma), \tag{6.113}$$

where C^i_α are in general complex coefficients. In the Schrödinger equation

$$H\Phi_i(\vec{R}, \sigma, q) \equiv [T_{kin} + V_{sp} + V_{s.o.} + V_{Coul}\,\delta_{p\,q}] = e_i \Phi_i(\vec{R}, \sigma, q), \quad q = \{p, n\} \tag{6.114}$$

for which the set of eigensolutions $\Phi_i(\vec{R}, \sigma, q)$ is expressed by the series expansion (6.113) where the coefficients C^i_α play the role of eigenvectors of the Hamiltonian matrix $H_{\alpha\beta}$ with corresponding eigenvalue e_i

$$\sum_\beta H_{\alpha\beta}\, C^i_\beta = e_i\, C^i_\alpha. \tag{6.115}$$

The matrix elements $H_{\alpha\beta}$ of the axial effective Hamiltonian

$$H_{\alpha\beta} = \Big\langle\, \alpha \,\Big|\, -\vec{\nabla}\cdot\frac{\hbar^2}{2m^*_q}\,\vec{\nabla} + V^{(q)}_{sp} + V^{(q)}_{s.o.} \,\Big|\, \beta \,\Big\rangle. \tag{6.116}$$

can be written explicitly as

$$\Big\langle\, \alpha \,\Big|\, -\vec{\nabla}\cdot\frac{\hbar^2}{2m^*_q}\,\vec{\nabla} \,\Big|\, \beta \,\Big\rangle = \sum_\sigma \int d^3R \frac{\hbar^2}{2m^*_q(\rho, z)} \vec{\nabla}\phi^*_\alpha(\vec{R}, \sigma)\cdot\vec{\nabla}\phi_\beta(\vec{R}, \sigma)$$

$$\Big\langle\, \alpha \,\Big|V^{(q)}_{sp}\Big|\, \beta \,\Big\rangle = \delta_{\Lambda,\Lambda'}\delta_{\Sigma,\Sigma'} N_{n_z} N_{n'_z} N^{\Lambda}_{n_\rho} N^{\Lambda'}_{n'_\rho} \int_0^\infty d\eta \eta^\Lambda e^{-\eta}$$

$$\times \int_{-\infty}^{\infty} e^{-\zeta^2} d\zeta H_{n_z}(\zeta)\, H_{n'_z}(\zeta) L^{\Lambda}_{n_\rho}(\eta)\, L^{\Lambda'}_{n'_\rho}(\eta)\, V^{(q)}_{sp}(\rho, z)(\eta, \zeta)\ , \tag{6.117}$$

where the left gradient operator is chosen to be acting (as the hermitian conjugate) on the left. The explicit expressions for matrix elements of the spin–orbit potential will be derived with the use of the matrix elements of the central potential in the forthcoming sections.

6.6.1 Nonaxial Hamiltonian symmetries

Let us define the following operation:

$$\hat{y} = \hat{K}\hat{\pi}_y^{-1}, \tag{6.118}$$

where $\hat{\pi}_y^{-1}$ denotes here the inverse of the reflection operation with respect to the $xOz-$plane, while $\hat{K}$ is the time–reversal operation which can be defined as

$$\hat{K} = \hat{K}_0\, e^{-i\pi\hat{s}_y} \tag{6.119}$$

with $\hat{K}_0$ being the complex conjugation operator. We can immediately note that the time–reversal operation contains the rotation operation by an angle π around the "$y-$axis" in the spin space. Let h be a single–particle Hamiltonian operator. If

$$\hat{h}|\mu\rangle = \epsilon_\mu|\mu\rangle \tag{6.120}$$

and

$$\hat{y}\hat{h}\hat{y}^{-1} = \hat{h}, \tag{6.121}$$

then it is true that

$$\hat{y}|\mu\rangle = |\mu\rangle. \tag{6.122}$$

It explicitly means that if the eigenstates of the single–particle Hamiltonian are invariant with respect to this symmetry and

$$|\mu\rangle = \sum_\alpha C_\alpha^\mu|\alpha\rangle, \tag{6.123}$$

then the coefficients of the development C_α^μ are real in the h.o. basis. For the density distribution or the total mean–field potential V this imply respectively:

$$\rho(x,y,z) = \rho(x,-y,z) \tag{6.124}$$

$$V(x,y,z) = V(x,-y,z) \tag{6.125}$$

Let us consider in more detail the case of a nonaxial potential. We can first introduce the set of three operators connected with the rotation by angle π with respect to the $i-$axis ($\{i := x,y,z\}$) acting together with the parity operator $\hat{P}$ (with parity eigenvalues equal to $\pi = \pm 1$) as

$$\hat{\pi}_i \equiv \hat{P}\hat{R}_i(\pi). \tag{6.126}$$

The action of these operators on an arbitrary spatial function $\psi(x,y,z)$ gives

$$\begin{aligned}
\hat{\pi}_x\psi(x,y,z) &= \hat{P}\hat{R}_x(\pi)\psi(x,y,z) = \hat{P}\psi(x,-y,-z) = \psi(-x,y,z),\\
\hat{\pi}_y\psi(x,y,z) &= \hat{P}\hat{R}_y(\pi)\psi(x,y,z) = \hat{P}\psi(-x,y,-z) = \psi(x,-y,z),\\
\hat{\pi}_z\psi(x,y,z) &= \hat{P}\hat{R}_z(\pi)\psi(x,y,z) = \hat{P}\psi(-x,-y,z) = \psi(x,y,-z).
\end{aligned} \tag{6.127}$$

Let us now remember that the rotation around the $i-$axis by the angle π called $i-$*signature* operation is generated by the operator

$$\hat{R}_i(\pi) = e^{-i\pi\hat{j}_i/\hbar}, \qquad \hat{j}_i = \hat{l}_i + \hat{s}_i, \tag{6.128}$$

where $\hat{l}_i$ and $\hat{s}_i$ are respectively the i–components of the orbital angular momentum and spin operators. The action of $\hat{R}_z$ on an arbitrary eigenfunction $\varphi(\vec{r};s)$ of the mean–field Hamiltonian $\hat{h}$

$$\hat{R}_z(\pi)\,\varphi(\vec{r};s) = r\,\varphi(\vec{r};s) \tag{6.129}$$

yields the eigenvalues $r = \pm i$. We recall that for the spin functions χ_{s,m_s} represented by $|+\rangle$ and $|-\rangle$ we have that

$$\begin{aligned}
\hat{s}_x|+\rangle &= \frac{1}{2}\hbar\,|-\rangle, & \hat{s}_x|-\rangle &= \frac{1}{2}\hbar\,|+\rangle,\\
\hat{s}_y|+\rangle &= \frac{1}{2}\hbar(+i)\,|-\rangle, & \hat{s}_y|-\rangle &= \frac{1}{2}\hbar(-i)\,|+\rangle,\\
\hat{s}_z|+\rangle &= \frac{1}{2}\hbar\,|+\rangle, & \hat{s}_z|-\rangle &= -\frac{1}{2}\hbar\,|-\rangle,
\end{aligned} \tag{6.130}$$

where

$$|+\rangle = \begin{pmatrix} 1 \\ 0 \end{pmatrix}, \quad |-\rangle = \begin{pmatrix} 0 \\ 1 \end{pmatrix}. \tag{6.131}$$

It is also instructive to demonstrate the action of the rotation operators $\{e^{-i\pi\hat{s}_i}\}$ on the spin functions $|+\rangle$ and $|-\rangle$, namely

$$e^{-i\pi\hat{s}_x/\hbar}\,|+\rangle = \left\{\hat{I} - i\frac{\pi}{2}\hat{\sigma}_x - \frac{1}{2}\left(\frac{\pi}{2}\right)^2\sigma_x^2 + \frac{1}{6}i\left(\frac{\pi}{2}\right)^3\hat{\sigma}_x^3 + \frac{1}{24}\left(\frac{\pi}{2}\right)^4\hat{\sigma}_x^4 + \ldots\right\}\Big|+\Big\rangle \tag{6.132}$$

Noting that $(\hat{\sigma}_i)^{2n} = \hat{I}$, $(i = 1,2,3,\ldots)$ and reordering the terms in the above as

$$\begin{aligned}
&\left[\left\{1 - \frac{1}{2}\left(\frac{\pi}{2}\right)^2 + \frac{1}{24}\left(\frac{\pi}{2}\right)^4 + \ldots\right\} - i\hat{\sigma}_x\left\{\frac{\pi}{2} - \frac{1}{6}\left(\frac{\pi}{2}\right)^3 - \frac{1}{120}\left(\frac{\pi}{2}\right)^5\right\}\right]\Big|+\Big\rangle =\\
&\left\{\cos\left(\frac{\pi}{2}\right) - i\hat{\sigma}_x\sin\left(\frac{\pi}{2}\right)\right\}\Big|+\Big\rangle = -i\hat{\sigma}_x|+\rangle = -i|-\rangle
\end{aligned} \tag{6.133}$$

we obtain explicitly that

$$\begin{aligned}
e^{-i\pi\hat{s}_x/\hbar}\,|+\rangle &= (-i)|-\rangle, & e^{-i\pi\hat{s}_x/\hbar}\,|-\rangle &= (-i)|+\rangle,\\
e^{-i\pi\hat{s}_y/\hbar}\,|+\rangle &= (+1)|-\rangle, & e^{-i\pi\hat{s}_y/\hbar}\,|-\rangle &= (-1)|+\rangle,\\
e^{-i\pi\hat{s}_z/\hbar}\,|+\rangle &= (-i)|+\rangle, & e^{-i\pi\hat{s}_z/\hbar}\,|-\rangle &= (+i)|-\rangle.
\end{aligned} \tag{6.134}$$

Collecting the properties (6.127), (6.130), (6.134) and admitting that, in general, a single–particle wave function $\varphi(\vec{r};s)$ is the product of the spatial and spin components: $\varphi(\vec{r};s) = \psi(\vec{r})\,\chi_{s,m_s}$, the parity operator $\hat{P}$ may be rewritten in terms of the operators $\hat{\pi}_i$ as

$$\hat{P} = -\hat{\pi}_x\hat{\pi}_y\hat{\pi}_z, \tag{6.135}$$

whereas, the z–signature operator $\hat{S}_z$ is given by

$$\hat{S}_z \equiv \hat{R}_z(\pi) = i\hat{\pi}_x\hat{\pi}_y. \tag{6.136}$$

The latter acting on an arbitrary wave function $\varphi(\vec{r};s)$

$$S_z\,\varphi(\vec{r};s) = q\,\varphi(\vec{r};s) \tag{6.137}$$

gives the eigenvalues $q = \pm i$. Examining the commutation properties of above introduced operators we conclude on the following properties:

$$\begin{aligned} &[\hat{P},\hat{S}_z] = 0, \\ &[\hat{\pi}_i,\hat{\pi}_j] \neq 0, \qquad \{i = x,y,z\}, \\ &\hat{\pi}_i^2 = -I. \end{aligned} \tag{6.138}$$

Let us now investigate the consequences of the combined symmetries $\hat{y}\hat{P}$ and $\hat{y}\hat{S}_z$. If the operator $\hat{y} = \hat{K}\hat{\pi}_y^{-1}$ acts following the parity operator $\hat{P}$ or the z–signature operator $\hat{S}_z$ then for the density and for the total single–particle potential we have the following properties:

- for the operation $\hat{y}\hat{P}$

$$\begin{aligned} \rho(x,y,z) &= \rho(-x,y,-z), \\ V(x,y,z) &= V(-x,y,-z), \end{aligned} \tag{6.139}$$

- and for the operation $\hat{y}\hat{S}_z$ (parity symmetry $\hat{P}$ broken),

$$\begin{aligned} \rho(x,y,z) &= \rho(-x,y,z), \\ V(x,y,z) &= V(-x,y,z). \end{aligned} \tag{6.140}$$

In the case of the symmetry (6.139) one concludes by virtue of the commutation rules (6.138) that both quantum numbers π and q can be used to identify the eigenstates of the Hamiltonian $\hat{h}$. Then the Hamiltonian matrix is composed of 4 quasi–diagonal blocks corresponding to the four possible combinations of quantum numbers $\{\pi,q\}$ as: $\{1,1\}$, $\{1,-1\}$, $\{-1,1\}$, $\{-1,-1\}$. This is not the case when the parity symmetry is broken as in expression (6.140), however, the z–signature and $\hat{y}$ symmetries are still conserved. This means that the single–particle states can then only be characterized by the quantum number q (then the Hamiltonian matrix decays only into 2 blocks corresponding to $q = \pm 1$). When, in turn, the z–signature symmetry is broken while the parity and $\hat{y}$ are conserved then the only good quantum number is the parity π (Hamiltonian matrix decaying into 2 blocks corresponding to $\pi = \pm 1$). When this is the case then both the parity and z–signature symmetries are broken, and the only symmetry to be conserved in all above cases is the $\hat{y}$ which is, in principle, the time–reversal symmetry and then no good quantum number exists.

6.6.2 Matrix elements of a triaxial arbitrary potential in the h.o. basis

As we have already mentioned in the introduction to this chapter the knowledge of the single–particle spectrum of an atomic nucleus is the starting point to any nuclear–structure investigation. For the description of the average single–particle field and in the absence of spherical or axial symmetry the cartesian coordinate system is the most suitable. In that case all three coordinates are treated on the same footing and no symmetry conditions are imposed on the basis wave–functions. Of course, in such a coordinate system the angular momentum algebra can not be applied directly to the resulting wave functions even if the symmetry of the system turns to be accidentally spherical or axial. Let us derive in the following explicitly the expressions for the matrix elements of all the components of the total single–particle Hamiltonian.

A triaxial harmonic oscillator potential can be written as

$$V_{h.o.}(x,y,z) = \frac{1}{2}m\omega_x^2 x^2 + \frac{1}{2}m\omega_y^2 y^2 + \frac{1}{2}m\omega_z^2 z^2, \tag{6.141}$$

where an energy eigenvalue is given usually as

$$E(n_x,n_y,n_z) = \hbar\omega_x\left(n_x+\frac{1}{2}\right) + \hbar\omega_y\left(n_y+\frac{1}{2}\right) + \hbar\omega_z\left(n_z+\frac{1}{2}\right) \tag{6.142}$$

and the corresponding normalized eigenstate as

$$\begin{aligned} &|n_x,n_y,n_z,\Sigma\rangle \equiv \Psi_{n_x}(x)\Psi_{n_y}(y)\Psi_{n_z}(z)\,\chi\,(\Sigma) = \\ &\sqrt{a_x a_y a_z}H_{n_x}\,H_{n_y}\,H_{n_z}\,\chi\,(\Sigma)\,e^{-\frac{1}{2}\left[(a_x x)^2+(a_y y)^2)+(a_z z)^2\right]}. \end{aligned} \tag{6.143}$$

Here H_{n_i} is the $n^{th}-$order normalized Hermite polynomial (see Appendix) and

$$a_i \equiv \sqrt{\frac{M\omega_i}{\hbar}} \tag{6.144}$$

are parameters (characteristic lengths) which allow to scale the cartesian coordinates $\{x,y,z\} \longrightarrow \{\xi,\eta,\zeta\}$, $(i=\{1,2,3\})$ in the following way:

$$\xi \equiv a_1 x, \quad \eta \equiv a_2 y, \quad \zeta \equiv a_3 z. \tag{6.145}$$

The three oscillator constants ω_i cannot be chosen arbitrarily, but are rather related by the fact that the volume does not change with the nuclear deformation. In practical calculations one usually uses the following identity:

$$\hbar\omega_0 = \hbar(\omega_x\,\omega_y\,\omega_z)^{1/3} \approx \frac{41}{A^{1/3}}\,MeV \tag{6.146}$$

which corresponds roughly to the energetical spacing between main shells in the harmonic oscillator spectrum. However, the matrix elements determined within a given

basis should essentially not depend significantly on the particular values of the involved oscillator parameters.

Let us now introduce some recursion relations of the Hermite polynomials:

$$H_{n+1}(x) = 2xH_n(x) - 2nH_{n-1}(x), \tag{6.147}$$

$$\frac{d}{dx}H_n(x) = 2nH_{n-1}, \tag{6.148}$$

where $H_0(x) = 1$, $H_1(x) = 2x$.
Multiplying both sides of ex. (6.147) by $H_{n'}(x)$ we get

$$H_{n+1}(x)\, H_{n'}(x) = 2xH_n(x)\, H_{n'}(x) - 2nH_{n-1}(x)\, H_{n'}(x). \tag{6.149}$$

In order to eliminate the undesired factor x on the right–hand side of this equation we apply again eq. (6.147) to obtain

$$H_n H_{n'} = \sqrt{\frac{n'+1}{n}} H_{n-1} H_{n'+1} + \sqrt{\frac{n'}{n}} H_{n-1} H_{n'-1} - \sqrt{\frac{n-1}{n}} H_{n-2} H_{n'}\,. \tag{6.150}$$

Matrix elements of the one–body kinetic energy operator in the base of triaxial h.o. potential can be easily derived analytically since we dispose with the relations (6.147) and (6.148):

$$\begin{aligned}
&\langle n'_x, n'_y, n'_z, \Sigma' | T_{kin} | n_x, n_y, n_z, \Sigma \rangle = \delta_{\Sigma'\Sigma} \times \\
&\Big\{ \delta_{n_x n'_x}\, \delta_{n_y n'_y} \hbar\omega_z \Big[\frac{1}{2}(n_z + \frac{1}{2}) \delta_{n_z n'_z} - \frac{1}{4}\sqrt{n_z(n_z-1)}\, \delta_{n_z-2, n'_z} \\
&- \frac{1}{4}\sqrt{n'_z(n'_z-1)}\, \delta_{n_z, n'_z-2} \Big] + cycl. \Big\}.
\end{aligned} \tag{6.151}$$

Let us calculate now the matrix elements of the mean–field effective, local potential which is admitted here as an arbitrary local potential, of arbitrary shape, invariant only with respect to the time–reversal operation

$$\langle n'_x, n'_y, n'_z, \Sigma' | V_{sp} | n_x, n_y, n_z, \Sigma \rangle = \delta_{\Sigma'\Sigma}\, \langle n'_x, n'_y, n'_z | V_{sp} | n_x, n_y, n_z \rangle, \tag{6.152}$$

where

$$\begin{aligned}
&\langle n'_x, n'_y, n'_z | V_{sp} | n_x, n_y, n_z \rangle = \\
&\qquad \int_{-\infty}^{\infty} d\xi e^{-\xi^2} H_{n'_x}(\xi) H_{n_x}(\xi) \int_{-\infty}^{\infty} d\eta e^{-\eta^2} H_{n'_y}(\eta) H_{n_y}(\eta) \\
&\qquad \times \int_{-\infty}^{\infty} d\zeta e^{-\zeta^2} H_{n'_z}(\zeta) H_{n_z}(\xi)\, V(\xi, \eta, \zeta).
\end{aligned}$$

The largest part of above matrix elements can be calculated recursively by virtue of the relation (6.150) for products of the normalized Hermite polynomials. The numerical details of this operation will be discussed at the end of this subsection. The

matrix elements of of the single–particle potential V_{sp} can be rewritten as:

$$\langle n'_x, n'_y, n'_z|V_{sp}|n_x, n_y, n_z\rangle = \sqrt{\frac{n'_z+1}{n_z}}\,\langle n'_x, n'_y, n'_z+1|V_{sp}|n_x, n_y, n_z-1\rangle$$
$$+\sqrt{\frac{n'_z}{n_z}}\,\langle n'_x, n'_y, n'_z-1|V_{sp}|n_x, n_y, n_z-1\rangle$$
$$-\sqrt{\frac{n_z-1}{n_z}}\,\langle n'_x, n'_y, n'_z|V_{sp}|n_x, n_y, n_z-2\rangle. \qquad (6.153)$$

Similar relations can be derived for recursion in the $x-$ and $y-$ direction.

In practice we can, simply by studying the parity of the integrand in eq. (6.152), find immediately the matrix elements which are, by the symmetry conditions, equal to zero. As an example, for potentials which are symmetric with respect to the $z-$axis (not necessarily strictly axially symmetric) a certain number of matrix elements vanish due to the fact that V_{sp} in eq. (6.152) is then an even function in $x-$direction ($V(x,y,z) = V(-x,y,z)$) and thus, if for the basis states, $(n'_x + n_x)$ is going to be the odd number, then the integral (6.152) over the symmetric interval $(-\infty, \infty)$ is equal to zero. A similar reasoning can be applied in the other two, (y,z) directions.

The symmetry in given direction is sometimes called the *partial parity* and is determined through to the quantum number n_i by $(-1)^{n_i}$, (i labelling the cartesian coordinates). The symmetry consideration imposed on the potential might, at fist sight, appear as a mathematical trick, but is of great importance from the physical point of view (as already discussed in the preceding section 6.6.1). The fact that one of these symmetries of the total potential is conserved implies that the basis states used in the development of the full wave function (see e.g. eq. (6.113)) can be characterized by an additional good quantum number, what is directly connected with the conservation of the corresponding quantity. Such a symmetry property is then also obeyed by the Hamiltonian matrix and makes this matrix block–diagonal what is particularly desirable for numerical diagonalization.

For axially symmetric potentials e.g., the blocks for the positive and negative $\Omega = \Lambda + \Sigma$ are identical and only one of them (e.g. for positive Ω values) needs to be calculated. A further splitting of the Hamiltonian matrix is possible when the parity symmetry π is taken into consideration in a similar way. On the other hand, as one can immediately conclude, that the discussed symmetries bring about also the corresponding simplifications of the considered nuclear shapes and, as a consequence, we are often not able to describe properly various nuclear phenomena like e.g. nuclear fission, if these symmetry properties are unduly imposed. Even for a static description of the fission process, it appears that at least four relevant deformation degrees of freedom need to be considered (see chapter 9). In the past such limitations of the symmetry were often necessary because they reduced significantly the dimensions of

the matrices to be diagonalized numerically. Being able, nowadays, to diagonalize matrices of quite appreciable dimensions and calculate numerically multidimensional integrals in an accessible time–scale, we can afford taking into account more general nuclear shapes.

The above calculated matrix elements of the central nuclear potential (6.151), (6.152) do not contain any information about the symmetries of the Hamiltonian and, at this stage, the results presented above should be understood rather as presenting the general technique of determining matrix elements of an arbitrary local potentials. In future sections we will discuss the problem of the time–reversal symmetry and its implications for the appropriate choice of the basis which the total Hamiltonian is diagonalized in. Then the required matrix elements will be certain linear combination of these, calculated above in the original h.o. basis.

Let us now come to the description of the potential which couples the spin and orbital movements in the quantum system, called spin–orbit potential. This potential, as given already in eq. (6.90) for the two nucleon charge states (q=$\{p,n\}$), can be obtained from the respective central potential V_{sp}^{q}, ($q=\{p,n\}$) through

$$V_q^{s.o.}(\vec{r}) = i\,\lambda_q \left(\frac{\hbar}{2Mc}\right)^2 \vec{\nabla} V_{sp}^{(q)} \cdot \Big[\vec{\sigma} \times \vec{\nabla}\Big], \tag{6.154}$$

where the parameters λ_q, denoting the strength of the spin–orbit coupling are given by expressions (6.93) and, as already explained before, $\vec{\sigma}$ is the vector $(\sigma_x, \sigma_y, \sigma_z)$ of (2×2) Pauli matrices. Finally, recall that this potential after obvious algebraic transformations can be written as the combination of products involving spatial and spin operators in the following form:

$$V_{s.o.} = -\frac{i\kappa}{\hbar}\left[\hat{\sigma}_x\left(\partial_y \frac{\partial V_{sp}}{\partial z} - \partial_z \frac{\partial V_{sp}}{\partial y}\right) + \hat{\sigma}_y\left(\partial_z \frac{\partial V_{sp}}{\partial x} - \partial_x \frac{\partial V_{sp}}{\partial z}\right) + \hat{\sigma}_z\left(\partial_x \frac{\partial V_{sp}}{\partial y} - \partial_y \frac{\partial V_{sp}}{\partial z}\right)\right]. \tag{6.155}$$

Since it is clear that spin–orbit interaction distinguishes protons and neutrons, we will omit the index "q" by all further expressions containing V_{sp}. As a consequence, the matrix elements of $V_{s.o.}$ are of the following form:

$$\begin{aligned}
\langle n_x', n_y', n_z'|V_{s.o.}|n_x, n_y, n_z\rangle = -\frac{i\kappa}{\hbar}\Big\{ & \\
& \langle n_x', n_y', n_z'\Big|\hat{\sigma}_x\left(\partial_y \frac{\partial V_{sp}}{\partial z} - \partial_z \frac{\partial V_{sp}}{\partial y}\right)\Big|n_x, n_y, n_z\rangle \\
+ \quad & \langle n_x', n_y', n_z'\Big|\hat{\sigma}_y\left(\partial_z \frac{\partial V_{sp}}{\partial x} - \partial_x \frac{\partial V_{sp}}{\partial z}\right)\Big|n_x, n_y, n_z\rangle \\
+ \quad & \langle n_x', n_y', n_z'\Big|\hat{\sigma}_z\left(\partial_x \frac{\partial V_{sp}}{\partial y} - \partial_y \frac{\partial V_{sp}}{\partial z}\right)\Big|n_x, n_y, n_z\rangle\Big\}
\end{aligned} \tag{6.156}$$

For further applications it is convenient to express the spin operators $\{\hat{\sigma}_x, \hat{\sigma}_y, \hat{\sigma}_z\}$ in terms of the operators $\{\hat{\sigma}_+, \hat{\sigma}_-, \hat{\sigma}_0\}$ defined as

$$\begin{aligned} \hat{\sigma}_+ &= (\hat{\sigma}_x + i\hat{\sigma}_y), \\ \hat{\sigma}_- &= (\hat{\sigma}_x - i\hat{\sigma}_y), \\ \hat{\sigma}_0 &= \hat{\sigma}_z, \end{aligned} \tag{6.157}$$

which act on the spin part of the general wave function in the following way:

$$\begin{aligned} \hat{\sigma}_+|\downarrow\rangle = |\uparrow\rangle, \quad \hat{\sigma}_+|\uparrow\rangle = 0, \\ \hat{\sigma}_-|\uparrow\rangle = |\downarrow\rangle, \quad \hat{\sigma}_-|\downarrow\rangle = 0. \end{aligned} \tag{6.158}$$

Since the partial derivation of an arbitrary local potential, as given e.g. by (6.86), is quite complicated and, in general, not possible to express analytically, it is convenient to perform explicitly the integrations by parts that appear in eq. (6.156) (noting simultaneously that Ψ_{n_i} vanishes at infinity) in order to transfer the derivative operation from the potential to the basis wave functions. These operations are easy to carry out analytically. Applying eq. (6.147) and the explicit form of the derivative of the basis wave function, given e.g. in $x-$direction as

$$\begin{aligned} \frac{d\Psi_{n_x}(a_x x)}{dx} &= \mathcal{N}_{n_x}\sqrt{a_x}\left(aH'_{n_x-1}(a_x x) - a_x^2 x H_{n_x}(a_x x)\right)e^{-\frac{1}{2}a_x^2x^2} \\ &= a_x\left[\sqrt{\frac{n_x}{2}}\Psi_{n_x-1}\Big(x\Big) - \sqrt{\frac{n_x+1}{2}}\Psi_{n_x+1}\Big(x\Big)\right] \end{aligned} \tag{6.159}$$

we obtain that

$$\langle n'_x, n'_y, n'_z, \Sigma'|V_{s.o.}|n_x, n_y, n_z, \Sigma\rangle = \frac{1}{2}\kappa\Big[\langle\Sigma'|\sigma_+|\Sigma\rangle B_- + \langle\Sigma'|\sigma_-|\Sigma\rangle B_+ + 2\langle\Sigma'|\sigma_z|\Sigma\rangle B_z\Big],$$

where

$$B_\pm \equiv B_x \mp B_y, \tag{6.160}$$

$$\begin{aligned} B_x &= \frac{1}{2}\Big(1-(-1)^{n'_y+n_y}\Big)\,a_y a_z \times \\ &\Big[-\sqrt{n'_z(n_y+1)}\langle n'_x, n'_y, n'_z-1, |V_{sp}|n_x, n_y+1, n_z\rangle \\ &-\sqrt{n_y(n'_z+1)}\langle n'_x, n'_y, n'_z+1, |V_{sp}|n_x, n_y-1, n_z\rangle \\ &+\sqrt{n'_y(n_z+1)}\langle n'_x, n'_y-1, n'_z, |V_{sp}|n_x, n_y, n_z+1\rangle \\ &+\sqrt{n_z(n'_y+1)}\langle n'_x, n'_y+1, n'_z, |V_{sp}|n_x, n_y, n_z-1\rangle\Big], \end{aligned}$$

$$
\begin{aligned}
B_y \;=\; & \frac{1}{2}\Big(1+(-1)^{n'_y+n_y}\Big)\, a_x a_z \times \\
& \Big[-\sqrt{n'_x(n_z+1)}\langle n'_x-1, n'_y, n'_z, |V_{sp}| n_x, n_y, n_z+1\rangle \\
& -\sqrt{n_z(n'_x+1)}\langle n'_x+1, n'_y, n'_z, |V_{sp}| n_x, n_y, n_z-1\rangle \\
& +\sqrt{n'_z(n_x+1)}\langle n'_x, n'_y, n'_z-1, |V_{sp}| n_x+1, n_y, n_z\rangle \\
& +\sqrt{n_x(n'_z+1)}\langle n'_x, n'_y, n'_z+1, |V_{sp}| n_x-1, n_y, n_z\rangle\Big],
\end{aligned}
\tag{6.161}
$$

$$
\begin{aligned}
B_z \;=\; & \frac{1}{2}\Big(1-(-1)^{n'_y+n_y}\Big)\, a_x a_y \times \\
& \Big[-\sqrt{n'_y(n_x+1)}\langle n'_x, n'_y-1, n'_z, |V_{sp}| n_x+1, n_y, n_z\rangle \\
& -\sqrt{n_x(n'_y+1)}\langle n'_x, n'_y+1, n'_z, |V_{sp}| n_x-1, n_y, n_z\rangle \\
& +\sqrt{n'_x(n_y+1)}\langle n'_x-1, n'_y, n'_z, |V_{sp}| n_x, n_y+1, n_z\rangle \\
& +\sqrt{n_y(n'_x+1)}\langle n'_x+1, n'_y, n'_z, |V_{sp}| n_x, n_y-1, n_z\rangle\Big].
\end{aligned}
$$

As one can see from eq. (6.160), the spin–orbit interaction, proportional to B_- and B_+, couples only the "antiparallel" spin states whereas the one containing B_z acts between states of "parallel" spin orientations. This is different from the case of the central potential which gives nonzero contributions only between states of the same spin projection. This unique feature of the spin–orbit potential leads to the energetical splitting of each single-particle level (except for s–states) into two levels of the same orbital angular momentum but opposite spin orientations.

In order to build the matrix of the central potential recursively it is enough to calculate numerically all diagonal matrix elements as well as a certain number of off–diagonal matrix elements which for certain combinations of n_x, n_y, n_z cannot be determined by recursion. The number of such elements makes only a few percent of the totality. The rest of the off–diagonal matrix elements are determined in successive, parallel lines to the main diagonal of the matrix. After the computation of the average–potential matrix elements we have to do the same for the spin–orbit potential with the help of the relation (6.160). Here also, some matrix elements must be calculated numerically. It is also possible to calculate them purely recursively under the condition that we first calculate a few necessary additional matrix elements of the central potential for which $n_x + n_y + n_z = N_{max} + 1$, (where N_{max} denotes the cut–off condition referring to the number of h.o. main shells used in the expansion of the total wave function). It is then convenient to put the basis states (6.143) (omiting the spin σ quantum number) in the following order:

$$
\begin{array}{cccc}
|0,0,0\rangle, & |0,0,1\rangle, & |0,0,\rangle, & \ldots \\
|0,1,0\rangle, & |0,1,1\rangle, & |0,1,\rangle, & \ldots \\
|1,0,0\rangle, & |1,0,1\rangle, & |1,0,\rangle, & \ldots \\
|1,1,0\rangle, & |1,1,1\rangle, & |1,1,\rangle, & \ldots \\
. & . & . & \ldots \\
. & . & . & \ldots \\
. & . & . & \ldots
\end{array}
$$

6.6.3 Time–reversal symmetry properties of the h.o. basis

In this section, on the basis of Ref. [84], we are going to investigate the harmonic oscillator basis and the corresponding transformation properties with respect to the time–reversal operation. This operation turns out to be useful when the physical operators have a well defined symmetry with respect to time–reversal, i.e. when they satisfy the condition

$$\hat{K}\hat{O}\hat{K}^{-1} = \pm\hat{O}. \tag{6.162}$$

The time–reversal operator (dependent on the sign convention) is defined as

$$\hat{K} \equiv \eta i\, \hat{\sigma}_y \hat{K}_0 \tag{6.163}$$

Above, $\eta = \pm 1$, σ_y is the second Pauli matrix and $\hat{K}_0$ is the complex conjugation operator.
The time–reversal operator $\hat{K}$ has the following properties:

- Anti–linear: $\hat{K}c = c^*\hat{K}, \quad c \in \mathbb{C}$
- Unitary: $\hat{K}\hat{K}^\dagger = \hat{K}^\dagger\hat{K} = I$,
- For two arbitrary vectors u, v, $\langle\, u|\hat{K}|v\,\rangle = \langle\, v|\hat{K}^+|u\,\rangle^*$,
- $\hat{K}^2 = +I$: if system as even number of fermions,
- $\hat{K}^2 = -I$: if system as odd number of fermions.

The two first properties define the time–reversal operator as being anti–unitary.

Kramers' theorem:

If $\hat{h}$ is a single–particle Hamiltonian of a system and $\hat{K}\,\hat{h}\,\hat{K}^{-1} = \hat{h}$, then the eigenstates of this Hamiltonian split into two groups: $\{\mu\}, \{\tilde{\mu}\}$ in such a way that

$$\hat{h}|\mu\rangle = \epsilon_\mu|\mu\rangle,$$
$$\hat{h}|\tilde{\mu}\rangle = \epsilon_\mu|\tilde{\mu}\rangle,$$

where $|\tilde{\mu}\rangle = \hat{K}|\mu\rangle$ is orthogonal to $|\mu\rangle$.

We can calculate the action of the operator $\hat{K}$ on the eigenstates of the $z-$component of the spin (the sign of η in the definition (6.163) is chosen usually as -1).

$$\hat{K}|+\rangle = +|-\rangle, \qquad |+\rangle = \begin{pmatrix} 1 \\ 0 \end{pmatrix}, \quad |-\rangle = \begin{pmatrix} 0 \\ 1 \end{pmatrix}$$
$$\hat{K}|-\rangle = -|+\rangle \tag{6.164}$$

In the most general form (with phase factor $\eta = +1$) we can write

$$\hat{K}\,|j, j_z\rangle = (-1)^{j+j_z}\,|j, -j_z\rangle \tag{6.165}$$

Let us remind the definition (6.143) of the harmonic oscillator basis with an additional phase factor $(+i)^{n_y}$

$$|b\rangle \equiv (+i)^{n_y}\,|n_x, n_y, n_z\rangle\,|s_z\rangle, \tag{6.166}$$

which has the advantage that the matrix elements of an arbitrary potential which is "partly" symmetric with respect to $z-$axis (i.e., $V(x, y, z) = V(x, -y, z)$) are real. Time–reversed h.o. state according to the definition (6.163) and the property (6.164) is of the following form:

$$|\tilde{b}\rangle \equiv (-i)^{n_y}\,|n_x, n_y, n_z\rangle\,|-s_z\rangle \tag{6.167}$$

Note, that the $\{|b\rangle\}-$basis is composed of either purely real or purely imaginary elements. To simplify the notation, we will in the following use the symbol $|n\rangle$ instead of $|n_x, n_y, n_z\rangle$.

One can also easily check the following property:

$$\hat{K}|b\rangle = +|\tilde{b}\rangle$$
$$\hat{K}|\tilde{b}\rangle = -|b\rangle$$

Now, starting from the $|b\rangle-$basis and applying the following transformation we come to the new $|t\rangle-$basis according to:

$$|t_+\rangle \equiv \frac{1}{\sqrt{2}}(i|b\rangle - |\tilde{b}\rangle)$$
$$|t_-\rangle \equiv \frac{1}{\sqrt{2}}(|b\rangle - i\,|\tilde{b}\rangle) \tag{6.168}$$

The action of the time–reversal operator on the new basis states is the following:

$$\hat{K}|t_+\rangle = +|t_-\rangle$$
$$\hat{K}|t_-\rangle = -|t_+\rangle$$

Using the results of the action of the Pauli matrices σ_i on the h.o. states (6.166) we can investigate immediately their action on the $|t\rangle-$basis:

$$\begin{aligned}
\sigma_x|t_+\rangle &= (-1)^{n_y}|t_-\rangle \\
\sigma_x|t_-\rangle &= (-1)^{n_y}|t_+\rangle \\
\\
\sigma_y|t_+\rangle &= (-1)^{n_y+1}|t_+\rangle \\
\sigma_y|t_-\rangle &= (-1)^{n_y}|t_-\rangle \\
\\
\sigma_z|t_+\rangle &= (+i)|t_-\rangle \\
\sigma_z|t_-\rangle &= (-i)|t_+\rangle
\end{aligned} \tag{6.169}$$

Let us now consider an operator $\hat{O}$ that is supposed to be purely spatial, i.e. does not act on spin coordinates. The purpose of this consideration is to give the general prescription to construct the matrix of this operator in the $t-$basis Let us order the $|b\rangle-$basis like: $\{|b\rangle\} = \{|b\rangle, |\tilde{b}\rangle\}$ This basis is orthonormal which means that

$$\begin{aligned}
\langle b'|\tilde{b}\rangle &= \langle \tilde{b}'|b\rangle = 0 \\
\langle b'|\hat{O}|\tilde{b}\rangle &= \langle \tilde{b}'|\hat{O}|b\rangle = 0
\end{aligned} \tag{6.170}$$

The latter comes from the orthonormality of the spin eigenfunctions (remind that $|b\rangle$ has spin "up" projection and $|\tilde{b}\rangle$ has spin "down" projection).

$$\begin{aligned}
\langle b'|\hat{O}|b\rangle &= i^{-n'_y+n_y}\langle n'|\hat{O}|n\rangle \\
\langle \tilde{b}'|\hat{O}|\tilde{b}\rangle &= i^{+n'_y-n_y}\langle n'|\hat{O}|n\rangle
\end{aligned} \tag{6.171}$$

By the definitions (6.166), (6.167) and (6.168) this result can be easily generalized for the $t-$basis, namely:

$$\begin{aligned}
\langle t_+|\hat{O}|t_+\rangle &= \frac{1}{2}(\langle b'|\hat{O}|b\rangle + \langle \tilde{b}'|\hat{O}|\tilde{b}\rangle) \\
&= \frac{1}{2}[i^{-n_{y'}+n_y} + i^{n_{y'}-n_y}]\langle n'|\hat{O}|n\rangle \\
&= \frac{1}{2}i^{n_{y'}-n_y}[1 + (-1)^{-(n_{y'}-n_y)}]\langle n'|\hat{O}|n\rangle
\end{aligned} \tag{6.172}$$

Introducing the function of an integer n

$$F(n) = \frac{1}{2} i^n [1 + (-1)^n], \tag{6.173}$$

the above matrix elements of the operator $\hat{O}$ can be written in the compact form

$$\begin{aligned}
\langle t'_+|\hat{O}|t_+\rangle &= F(n'_y - n_y)\langle n'|\hat{O}|n\rangle \\
\langle t'_+|\hat{O}|t_-\rangle &= F(n'_y - n_y + 1)\langle n'|\hat{O}|n\rangle \\
\langle t'_-|\hat{O}|t_+\rangle &= F(n'_y - n_y - 1)\langle n'|\hat{O}|n\rangle \\
\langle t'_-|\hat{O}|t_-\rangle &= F(n'_y - n_y)\langle n'|\hat{O}|n\rangle
\end{aligned} \tag{6.174}$$

Having calculated the matrix elements of an arbitrary spatial, local operator $\hat{O}$, let us finally determine the matrix elements of a mixed operator of the type $\hat{O}\hat{\sigma}_i$ in the t–basis, which is the product of a purely spatial and purely spin operator. This will be the direct step to the construction of the spin–orbit potential matrix elements within this basis. Starting from the previous results, we want to extend them to the case of an operator of this form: $\hat{O}\sigma_i$. What is obviously meant here is that in such a mixed operator $\hat{O}$ acts only on the spatial part of the basis and σ_i only on the spin–dependent part. Thus, the matrix elements split into two different parts. Keeping in mind relations (6.170) and (6.175) it is easy to obtain that

$$\begin{aligned}
\langle t'_+|\hat{O}\sigma_x|t_+\rangle &= F(n'_y + n_y + 1)\langle n'|\hat{O}|n\rangle \\
\langle t'_+|\hat{O}\sigma_x|t_-\rangle &= F(n'_y + n_y)\langle n'|\hat{O}|n\rangle \\
\langle t'_-|\hat{O}\sigma_x|t_+\rangle &= F(n'_y + n_y)\langle n'|\hat{O}|n\rangle \\
\langle t'_-|\hat{O}\sigma_x|t_-\rangle &= F(n'_y + n_y - 1)\langle n'|\hat{O}|n\rangle
\end{aligned}$$

$$\begin{aligned}
\langle t'_+|\hat{O}\sigma_y|t_+\rangle &= F(n'_y + n_y + 2)\langle n'|\hat{O}|n\rangle \\
\langle t'_+|\hat{O}\sigma_y|t_-\rangle &= F(n'_y + n_y + 1)\langle n'|\hat{O}|n\rangle \\
\langle t'_-|\hat{O}\sigma_y|t_+\rangle &= F(n'_y + n_y + 1)\langle n'|\hat{O}|n\rangle \\
\langle t'_-|\hat{O}\sigma_y|t_-\rangle &= F(n'_y + n_y)\langle n'|\hat{O}|n\rangle
\end{aligned} \tag{6.175}$$

$$\begin{aligned}
\langle t'_+|\hat{O}\sigma_z|t_+\rangle &= iF(n'_y - n_y + 1)\langle n'|\hat{O}|n\rangle \\
\langle t'_+|\hat{O}\sigma_z|t_-\rangle &= iF(n'_y - n_y + 2)\langle n'|\hat{O}|n\rangle \\
\langle t'_-|\hat{O}\sigma_z|t_+\rangle &= iF(n'_y - n_y)\langle n'|\hat{O}|n\rangle \\
\langle t'_-|\hat{O}\sigma_z|t_-\rangle &= iF(n'_y - n_y + 1)\langle n'|\hat{O}|n\rangle
\end{aligned}$$

The above presented transformation eq. (6.168) of the original h.o. basis given by eq. (6.143) to the $|t_\pm\rangle-$ basis is the starting point to obtain the matrix elements of

an arbitrary single–particle Hamiltonian imposing the time–reversal symmetry which is generally fulfilled, except for the *cranked*, rotating potentials which break it. The time–reversal symmetry is, of course, also broken for odd proton and/or odd neutron numbers. The matrix elements of the Hamiltonian in the new $|t_{\pm}\rangle-$basis are easily derived by summing up (with the right phase factor) the appropriate matrix elements calculated in the original h.o. basis (6.143). By virtue of the property (6.175), the full matrix of the mean–field Hamiltonian in the transformed $|t_{\pm}\rangle-$basis is shown schematically below.

$$\begin{array}{c} \begin{array}{cc} |t_+\rangle & |t_-\rangle \end{array} \\ \left(\begin{array}{c|c} \langle H\rangle_{\alpha\beta} & 0 \\ \hline 0 & \langle H\rangle^*_{\alpha\beta} \end{array}\right) \begin{array}{c} |t_+\rangle \\ \\ |t_-\rangle \end{array} \end{array}$$

6.6.4 Diagonalization of the symmetric potentials in the original h.o. basis

At the beginning of this subsection, let us recall that the formalism presented in the previous subsection is valid for an arbitrary potentials without imposing any additional symmetry with the exception of time–reversal. We now want to introduce a less general way of diagonalizing potentials which are symmetric with respect to the $z-$axis (including the case of pure axial symmetry). It can be easily concluded from eq. (6.154) that both the central and spin–orbit potentials verify the same spatial symmetries. The shape of a potential having this kind of symmetry can be described e.g. by the previously introduced modified Funny–Hills shape parametrization (6.21). Let us recall that the latter is able to describe nuclear shapes whenever the cross section perpendicular to the $z-$axis can be, at most, an ellipse. Of course, one can also imagine an infinite number of other geometrical shapes for which

$$V(x,y,z) = V(-x,-y,z). \tag{6.176}$$

is verified. Notice also that we do not impose any limitations concerning the shape in $z-$direction. For simplicity let us come back to the original h.o. basis. Repeating the argumentation given after eq. (6.153), we can come to the conclusion that for the potentials the only "good quantum number" can be (see Ref. [85])

$$q = (-1)^{n_x+n_y}\,\Sigma/|\Sigma|\,, \tag{6.177}$$

where Σ is the projection of the spin, equal to $\{1/2, -1/2\}$. As already discussed, taking into account any symmetries existing in the system makes the matrix of the Hamiltonian block–diagonal. The number of pairs of the identical blocks depends on the number of operators commuting with the Hamiltonian. Then q defined by (6.177) is the only good quantum number, our matrix will split only into two **identical** blocks with $q = 1$ and $q = -1$ respectively.

As previously explained, it is sufficient to diagonalize only the one of these blocks and, according to the Kramer's theorem, every state can then be occupied by two particles. We can see therefore that the here discussed transformations contain already the time reversal operation. Schematically the Hamiltonian matrix may be presented like:

$$
\begin{array}{c|cccc}
 & |b_{odd}\uparrow\rangle & |b_{even}\downarrow\rangle & |b_{odd}\downarrow\rangle & |b_{even}\uparrow\rangle \\
\hline
|b_{odd}\uparrow\rangle & V_{cent}+V_{s.o.;3} & V_{s.o.1}+V_{s.o.;2} & 0 & 0 \\
|b_{even}\downarrow\rangle & V_{s.o.1}-V_{s.o.;2} & V_{cent}-V_{s.o.;3} & 0 & 0 \\
|b_{odd}\downarrow\rangle & 0 & 0 & V_{cent}+V_{s.o.;3} & V_{s.o.,1}+V_{s.o.;2} \\
|b_{even}\uparrow\rangle & 0 & 0 & V_{s.o.;1}-V_{s.o.;2} & V_{cent}-V_{s.o.;3}
\end{array}
$$

The meaning of the symbols used in this scheme is the following: For example, $|b_{odd}\uparrow\rangle$, denotes the set of basis states given by (6.166) for which $n_x + n_y$ is an odd number with the spin projection $1/2$, marked symbolically by the up arrow. By the analogy, the meaning of the three other type of basis states is obvious. The quantities V_{centr} and $V_{s.o.;n}$ are the following: $V_{centr} = V_{kin} + V_{sp} + V_{Coul}\,\delta_{pq}$, $(q = \{p, n\})$ and $V_{s.o.;n}$, $(n = \{1, 2, 3\}$) corresponds to the spin–orbit term entering the eq. (6.160) proportional to B_x, B_y, B_z respectively. Keeping in mind the argumentation given after eqs. (6.153) and (6.177) we conclude that the upper–left and the lower–right blocks of the full matrix must be identical, i.e. must have the same eigensolutions.

6.6.5 Numerical accuracy of the calculations

The primary source of the error in calculating the single–particle energies and wave functions is the truncation of the h.o. basis. Integration errors involved in the cal-

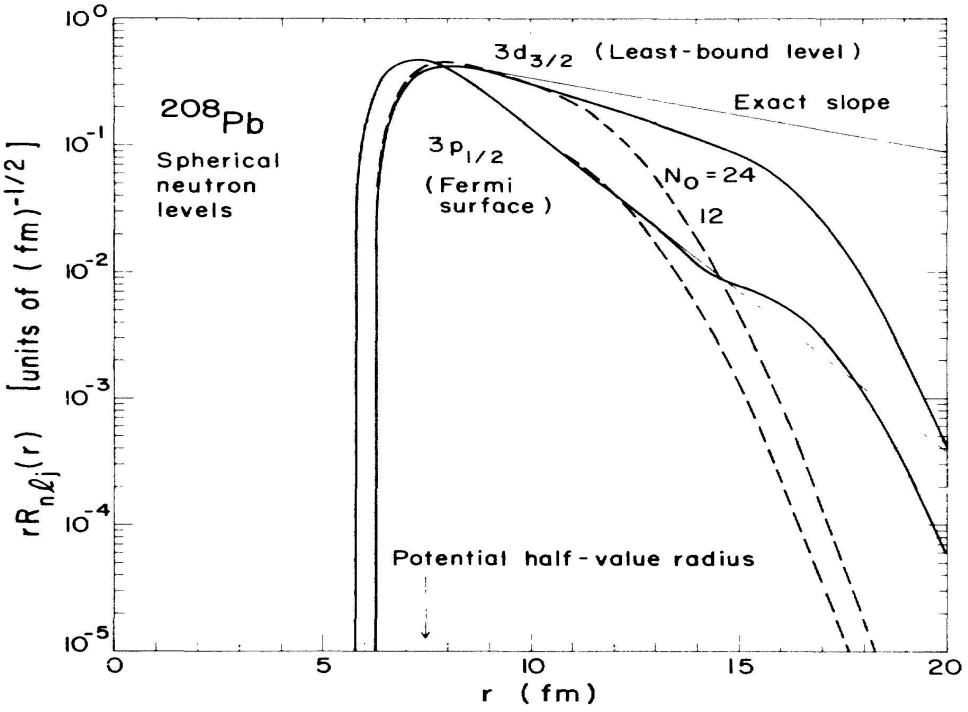

Figure 6.14: Asymptotic behaviour of neutron wave function for a spherical ^{208}Pb. The product of r times the radial wave function is plotted vs r beyond the last level for the Fermi surface and the least-bound level. The thin solid straight line shows the exact slope, the thick, solid curves gives the results for the harmonic–oscillator basis containing up to 24 main shells while the dashed curve illustrates the results for 12 h.o. shells. This picture is taken from Ref. [86].

culation of the matrix elements, folding of the potential and diagonalization of the Hamiltonian matrix can in practice be made negligibly small compared to this truncation error. Looking at Fig. 6.14 we conclude that levels below the Fermi surface converge fairly rapidly with the size of the basis, whereas bound states close to zero energy converge more slowly. We can state therefore that the unbound levels from the energy–continuum approach to zero energy as the basis becomes infinite. This statement is true since we know that **any** positive energy is a solution of the Schrödinger equation. In order to simulate the energy continuum the density of the unbound levels must approaches infinity what is possible only when the basis is going to be infinite. Thus, levels calculated with a finite basis **do not** represent any physical resonant states. Nevertheless, they are used in calculating the microscopic (shell and pairing) corrections which require the knowledge of the density of levels $g(e)$.

Chapter 7

General remarks on the mean–field models

7.1 Selfconsistent approach

The Hamiltonian of the N–body system is, to a good approximation, given by

$$\hat{\mathcal{H}} = \hat{T} + \hat{V} = \sum_{i=1}^{N} \hat{t}_i + \frac{1}{2} \sum_{\substack{i,j=1 \\ i \neq j}}^{N} \hat{v}_{ij}, \tag{7.1}$$

where $\hat{t}_i = \frac{\vec{p}_i^2}{2m} = -\frac{\hbar^2}{2m}\vec{\nabla}^2$ is the kinetic energy operator of the i^{th} particle and v_{ij} is the interaction between the i^{th} and j^{th} particle.

Formally, it is evident that the Hamiltonian $\mathcal{H}$ in the form

$$\hat{\mathcal{H}} = \sum_{i=1}^{N} (\hat{t}_i + \hat{U}_i) + \left(\frac{1}{2} \sum_{i,j=1}^{N} \hat{v}_{ij} - \sum_{i=1}^{N} \hat{U}_i \right) = \hat{\mathcal{H}}_0 + \hat{\mathcal{H}}_1 \tag{7.2}$$

is identical to the operator (7.1). Such a writing is useful under the condition that the one–body operator $\hat{\mathcal{H}}_0$ is a very good approximation of $\hat{\mathcal{H}}$ and that $\hat{\mathcal{H}}_1$ can be treated as a perturbation. Writing the total Hamiltonian in the form of eq. (7.2) we can choose as the one–body **mean–field** potential U an arbitrary potential which leaves the potential $\hat{\mathcal{H}}_1$ small as compared to $\hat{\mathcal{H}}_0$. This mean–field potential is often chosen e.g. as a Nilsson potential or, more realistically, a Woods–Saxon or Yukawa–folded potential. For such a choice of the one–body potential the solution of the Schrödinger equation for $\hat{\mathcal{H}}_0$ is

$$\hat{\mathcal{H}}_0 |\phi_j\rangle = \sum_{i=1}^{N} \left(\hat{t}_i + \tilde{U}_i \right) |\phi_j\rangle = E_j |\phi_j\rangle \tag{7.3}$$

for which we can find the solution for the N–body wave function $|\phi_j\rangle$ in the form of the tensor product

$$|\phi_j\rangle = |\varphi_1(1)\rangle \otimes |\varphi_2(2)\rangle \otimes \ldots \otimes |\varphi_N(N)\rangle, \tag{7.4}$$

where the single–particle states $|\varphi_\nu\rangle$ are the eigensolutions of the single–particle Hamiltonian $\hat{h}$

$$\hat{h}|\varphi_\nu\rangle = (\hat{t} + \tilde{U})|\varphi_\nu\rangle = \varepsilon_\nu|\varphi_\nu\rangle. \tag{7.5}$$

Since we discuss the system of N identical fermions, we have to realize that, because of the Pauli principle, the $N-$body wave function is not of the form (7.4) but is rather expressed as the linear combination which is totally antisymmetric with respect to the interchange of the coordinates of two arbitrarily chosen particles. Such a form is offered e.g. by the Slater determinant

$$|\phi_j\rangle = \frac{1}{\sqrt{(N!)}} \begin{vmatrix} \varphi_1(1) & \varphi_1(2), & \dots & ,\varphi_1(N) \\ \varphi_2(1) & \varphi_2(2), & \dots & ,\varphi_2(N) \\ \quad . & & & \\ \quad . & & & \\ \quad . & & & \\ \varphi_N(1) & \varphi_N(2), & \dots & ,\varphi_N(N) \end{vmatrix}. \tag{7.6}$$

When we manage to diagonalize the matrix which corresponds to the total Hamiltonian $\hat{\mathcal{H}}$ (which, in general, is of the infinite size) in the basis of the eigenvectors $|\phi_j\rangle$ of $\hat{\mathcal{H}}_0$, giving us the coefficients of the development of the eigenstates of $\hat{\mathcal{H}}$ in the basis of $\hat{\mathcal{H}}_0$, the problem is solved. This, of course, is not possible and we need to constraint ourselves to the diagonalization in the truncated Hilbert spaces (of finite size) which is the domain of the nuclear shell model. The **Hartree–Fock** method yields a one–body Hamiltonian $\hat{\mathcal{H}}_0$ with the corresponding single–particle mean–field $\tilde{U}$ which is generated in the variational procedure (as will be shortly demonstrated below) by the sum of all nucleon–nucleon interactions constituting the two–body operator $\hat{V}$ in eq. (7.1). The best one–body potential $\hat{U}$ and the corresponding $N-$body ground–state wave function $|\phi_0\rangle$ is obtained within the HF approach through the variational method which says that the ground–state energy has to be minimal with respect to all variations of the single–particle states which constitutes $|\phi_0\rangle$, i.e.

$$\delta \frac{\langle\, \phi_0|\hat{\mathcal{H}}|\, \phi_0\,\rangle}{\langle\, \phi_0|\phi_0\,\rangle} = 0 \qquad \Longrightarrow \qquad \langle\, \phi_0|\hat{\mathcal{H}}|\, \delta\phi_0\,\rangle = 0 \tag{7.7}$$

When we write the ground–state function $|\phi_0\rangle$ in coordinate space in the form of the Slater determinant, we come to the conclusion that the variation $|\delta\phi_0\rangle$ consists in replacing the single particle state φ_i in (7.6) by $\varphi_i + \delta\varphi_j$. If now $j < N$, i.e. if φ_j corresponds to a single–particle state which is already occupied in $|\phi_0\rangle$ then we add in the Slater determinant corresponding to the state $|\phi_0\rangle$ the multiple of the line j to the line i which shows that variations of $|\phi_0\rangle$ which correspond to the transformations inside the the Hilbert space of the already occupied states do not change the value of $|\phi_0\rangle$ and are not physically interesting. We can, therefore, limit $|\delta\phi_0\rangle$ to variations

which project on the exterior of the occupied space in the $|\phi_0\rangle$. In the formalism of second quantization we can then write the variation $|\delta\phi_0\rangle$ as

$$|\delta\phi_0\rangle = \delta c_{sj} a_s^+ a_j |\phi_0\rangle, \qquad j \leq \alpha_N, \quad s > \alpha_N, \quad \delta c_{sj} \in \mathbb{C}. \tag{7.8}$$

The variational principle (7.7) then leads to

$$\langle\, \phi_0 | \hat{\mathcal{H}} a_s^+ a_j | \phi_0 \rangle = 0 \tag{7.9}$$

and writing the operator $\hat{\mathcal{H}}$ in the second quantization we finally have

$$\sum_{\alpha\beta} \langle\, \alpha|\hat{t}|\beta\rangle \, \langle \phi_0 | a_\alpha^+ a_\beta \, a_s^+ a_j | \phi_0 \rangle \; + \frac{1}{2} \sum_{\alpha\beta\gamma\delta} \langle \alpha\beta|\hat{v}|\gamma\delta\rangle \, \langle\, \phi_0 | a_\alpha^+ a_\beta^+ a_\delta a_\gamma a_s^+ a_j | \phi_0 \,\rangle = 0. \tag{7.10}$$

Evaluating the two–body term one finds

$$\frac{1}{2} \sum_{\alpha\beta\gamma\delta} \langle\, \alpha\beta|\hat{v}|\gamma\delta\rangle \, \langle \phi_0 | a_\alpha^+ a_\beta^+ a_\delta \, a_\gamma \, a_s^+ a_j | \phi_0 \rangle = \sum_{k=1}^{N} [\langle\, jk|\hat{v}|sk\rangle - \langle\, jk|\hat{v}|ks\rangle] \tag{7.11}$$

and the variation (7.7) can be written in the form

$$\langle\, j|\hat{t}|s\rangle + \sum_{k=1}^{N} [\langle\, jk|\hat{v}|sk\rangle - \langle\, jk|\hat{v}|ks\rangle] = 0. \tag{7.12}$$

If we define a one–body Hamiltonian $\hat{\mathcal{H}}_0$ as

$$\hat{\mathcal{H}}_0 = \sum_{\mu\nu} \left[\langle\, \mu|\hat{t}|\nu\rangle + \sum_{k=1}^{N} \left(\langle\, \mu k|\hat{v}|\nu k\rangle - \langle\, \mu k|\hat{v}|k\nu\rangle \right) \right] a_\mu^+ a_\nu, \tag{7.13}$$

we conclude that the matrix element of $\hat{\mathcal{H}}_0$ between the ground state ϕ_0 and the state ϕ_1 which corresponds to an one particle–one hole excitation is equal to zero

$$\langle \phi_0 | \hat{\mathcal{H}}_0 | \phi_1 \rangle = 0. \tag{7.14}$$

Defining the one–body potential U by

$$\langle\, \mu|\hat{U}|\nu\rangle = \sum_{k=1}^{N} \left(\langle\, \mu k|\hat{v}|\nu k\rangle - \langle\, \mu k|\hat{v}|k\nu\rangle \right) \tag{7.15}$$

we can rewrite $\hat{\mathcal{H}}_0$ in the following form:

$$\hat{\mathcal{H}}_0 = \sum_{\mu\nu} \langle \mu| \, \hat{t} + \hat{U} |\nu\rangle a_\mu^+ a_\nu \; . \tag{7.16}$$

The interpretation of the one–body operator $\hat{U}$ is evident: $\hat{U}$ is the mean–field felt by a particle when it is interacting with all the other particles of the system. Since $\hat{\mathcal{H}}_0 = \sum_{i=1}^{N} \hat{h}_0^{(i)}$ depends on the states φ_k being the eigenfunctions of $\hat{h}_0$ we have the following selfconsistent problem:

Starting from the potential U_0, we solve the Schrödinger equation $(\hat{t}+\hat{U}_0)\,\varphi_j = \varepsilon_j\varphi_j$. Having the N single–particle states φ_j of $(\hat{t}+\hat{U}_0)$ with their eigensolutions ε_j we construct through eq. (7.15) the new mean–field $\hat{U}_1$ with which we repeat the procedure until the convergence is obtained. The Hartree–Fock problem is therefore solved in an iterative way. The fact that the occupied and the unoccupied states are completely uncoupled implies that the Hamiltonian $\hat{\mathcal{H}}_0$ can be diagonalized in these two subspaces separately. This is obtained if the HF selfconsistent states are generated by $\hat{\mathcal{H}}_0$

$$\hat{h}_0|j\rangle = (\hat{t}+\hat{U})|j\rangle = \varepsilon_j|j\rangle \tag{7.17}$$

which implies that

$$\langle\, k\,|\hat{\mathcal{H}}_0|\,j\,\rangle = \varepsilon_j\delta_{kj}, \qquad j,k \le \alpha_N. \tag{7.18}$$

We rewrite the HF equation (7.17) in the coordinate space using (7.15) as

$$\langle\,\vec{r}_1|\hat{t}+\hat{U}|m\rangle = \langle\,\vec{r}_1|\hat{t}|\,m\rangle + \langle\,\vec{r}_1|\,\hat{U}|m\rangle = \varepsilon_m\langle\,\vec{r}_1|m\rangle \tag{7.19}$$

$$\int d^3r_2\,\langle\vec{r}_1|\hat{t}|\vec{r}_2\rangle\,\langle\,\vec{r}_2|m\rangle + \sum_k\langle\,\vec{r}_1|k\rangle\,\langle\,k|U|m\rangle = \varepsilon_m\langle\,\vec{r}_1|m\rangle \tag{7.20}$$

$$-\frac{\hbar^2}{2m}\vec{\nabla}^2_{r_1}\varphi_m(\vec{r}_1) + \sum_k\sum_{l=1}^{N}\varphi_k(\vec{r}_1)[\langle\,kl|\hat{v}|ml\rangle\,\langle\,kl|\hat{v}|lm\rangle] = \varepsilon_m\varphi_m(\vec{r}_1) \tag{7.21}$$

$$\begin{aligned}-\frac{\hbar^2}{2m}\vec{\nabla}^2_{r_1}\varphi_m(\vec{r}_1) \;+\; &\sum_{i=1}^{N}\int d^3r_2\int d^3r_3\Big[\sum_k\varphi_k(\vec{r}_1)\varphi^*_k(\vec{r}_3)\varphi^*_l(\vec{r}_2)v(|\vec{r}_3-\vec{r}_2|)\varphi_m(\vec{r}_3)\varphi_l(\vec{r}_2)\\ -\;&\sum_k\varphi_k(\vec{r}_1)\varphi^*_k(\vec{r}_3)\varphi^*_l(\vec{r}_2)v(|\vec{r}_3-\vec{r}_2|)\varphi_l(\vec{r}_3)\varphi_m(\vec{r}_2)\Big] = \varepsilon_m\varphi_m(\vec{r}_1)\end{aligned} \tag{7.22}$$

$$\begin{aligned}-\frac{\hbar^2}{2m}\vec{\nabla}^2_{r_1}\varphi_m(\vec{r}_1) \;+\; &\Big[\sum_{l=1}^{N}\int d^3r_2\varphi^*_l(\vec{r}_2)v(|\vec{r}_1-\vec{r}_2|)\varphi_l(\vec{r}_2)\Big]\varphi_m(\vec{r}_1) -\\ &\sum_{l=1}^{N}\int d^3r_2\varphi^*_l(\vec{r}_2)v(|\vec{r}_1-\vec{r}_2|)\varphi_l(\vec{r}_1)\varphi_m(\vec{r}_2)\Big] = \varepsilon_m\varphi_m(\vec{r}_1)\end{aligned} \tag{7.23}$$

Let us define

$$U_H(\vec{r}_1) = \sum_{l=1}^{N}\int d^3r_2\,\varphi^*_l(\vec{r}_2)v(|\vec{r}_1-\vec{r}_2|)\varphi_l(\vec{r}_2) \tag{7.24}$$

and

$$U_F(\vec{r}_1,\vec{r}_2) = \sum_{l=1}^{N}\varphi^*_l(\vec{r}_2)v(|\vec{r}_1-\vec{r}_2|)\varphi_l(\vec{r}_1) \tag{7.25}$$

which allows us to rewrite the HF equation (7.23) in the coordinate space in the following form:

$$-\frac{\hbar^2}{2m}\vec{\nabla}^2_{r_1}\varphi_m(\vec{r}_1) + U_H(\vec{r}_1)\varphi_m(\vec{r}_1) - \int U_F(\vec{r}_1,\vec{r}_2)\varphi_m(\vec{r}_2)\,d^3r_2 = \varepsilon_m\varphi_m(\vec{r}_1), \tag{7.26}$$

where the local part $U_H(\vec{r}_1)$ is called the Hartree potential and the non–local part $U_F(\vec{r}_1, \vec{r}_2)$ the Fock potential. The latter has its origin in the antisymmetrization of the N–body wave function. The Hartree–Fock potential is then non–local but, in fact, the same for all the occupied states. We can define thus the potential

$$U(\vec{r}_1, \vec{r}_1\,') = \sum_{l=1}^{N} \int \varphi_l^*(\vec{r}_2) v(|\vec{r}_1 - \vec{r}_2|) \varphi_l(\vec{r}_2)\, d^3r_2 \delta(\vec{r}_1, \vec{r}_1\,') - \sum_{l=1}^{N}\sum_{k=1}^{N} \varphi_l^*(\vec{r}_2) v(|\vec{r}_1 - \vec{r}_2|) \varphi_k(\vec{r}_2)\, d^3r_2 \cdot \varphi_k^*(\vec{r}_1\,') \varphi_l(\vec{r}_1). \tag{7.27}$$

Keeping in mind that

$$\int \varphi_k^*(\vec{r}_1\,') \varphi_m(\vec{r}_1\,')\, d^3r_1\,' = \delta_{km} \tag{7.28}$$

we rewrite (7.23) as

$$-\frac{\hbar^2}{2m}\vec{\nabla}_{r_1}^2 \varphi_m(\vec{r}_1) + \int U(\vec{r}_1, \vec{r}_1\,')\, \varphi_m(\vec{r}_1\,')\, d^3r_1\,' = \varepsilon_m \varphi_m(\vec{r}_1). \tag{7.29}$$

The potential $U(\vec{r}_1, \vec{r}_1\,')$ which appears in eq. (7.29) is independent on the single–particle state on which it acts since in eq. (7.27) the sum runs over all occupied states. This potential is therefore the same for all the single–particle states of the system. We can see in eq. (7.27) that the direct (Hartree) part depends on the integral of $|\varphi_l(\vec{r}_2)|^2 v(\vec{r}_1, \vec{r}_2\,)$ whereas the exchange (Fock) part contains the integral of the term $\varphi_l^*(\vec{r}_2)\varphi_k(\vec{r}_2) v(\vec{r}_1, \vec{r}_2\,)$. If the states l and k are very different to each other then the product $\varphi_l^*(\vec{r}_2)\varphi_k(\vec{r}_2)$ will change its sign frequently in the region where $v(\vec{r}_1, \vec{r}_2\,)$ is essentially non–zero which makes, as a consequence, this term substantially smaller as compared to the direct term where $|\varphi_l(\vec{r}_2)|^2$ contributes maximally. This fact implies that the exchange part of the potential is usually small compared to the direct contribution (not always !, depending on the form of the interaction).

The energy of the ground state is given as

$$\begin{aligned} E_{HF} &= \langle\, \phi_0|\hat{\mathcal{H}}|\phi_0\rangle = \sum_{j=1}^{N} \langle\, j|\hat{t}|j\rangle + \frac{1}{2}\sum_{j,k=1}^{N} (\langle\, jk|\hat{v}|jk\rangle - \langle\, jk|\hat{v}|kj\rangle) = \\ &\sum_{j=1}^{N} \varepsilon_j - \frac{1}{2}\sum_{j,k=1}^{N} (\langle\, jk|\hat{v}|jk\rangle - \langle\, jk|\hat{v}|kj\rangle) = \\ &\sum_{j=1}^{N} \langle\, j|\hat{t} + \frac{1}{2}\hat{U}|j\rangle = \sum_{j=1}^{N} \left(\varepsilon_j - \frac{1}{2}\langle\, j|\hat{U}|j\rangle\right) \end{aligned} \tag{7.30}$$

7.2 Non–selfconsistent approaches

7.2.1 Microscopic–macroscopic model

Over the years, considerable effort has been devoted to calculating the potential energy of a nucleus as a function of its geometrical shapes. The average trends of the nuclear

potential energy are described quantitatively by the Liquid–Drop Model (LDM), but there exists also regular deviations from the LDM energy. The most visible deviations are associated with shell effects: Close–shell, so–called *magic* nuclei are more tightly bound than the *average* nucleus. The second, most important deviation is associated with nuclear pairing correlations, which also lead to an increased binding in some nuclei relative to others. These shell and pairing corrections to the liquid drop energy are both examples of single–particle effects and arise because of fluctuations in the actual distribution of the single–particle levels in the nucleus relative to a smooth distribution of levels. Single–particle effects are responsible for many important phenomena which occur particularly in the deformed ground–state shapes and secondary minima.

It is rather clear, that the most fundamental approach for calculating the nuclear potential energy would be to start with an adequately chosen nucleon–nucleon interaction and solve the resulting many–body problem in some mean–field or shell–model approximation.

In the macroscopic–microscopic method which is introduced here, the total nuclear potential energy E is given by

$$E(N,Z;def) = E_{LDM}(N,Z;def) + \delta E_{shell}(N,Z;def) + \delta E_{pair}(N,Z;def) \tag{7.31}$$

that is, by the sum of a liquid–drop type energy E_{LDM}, a shell correction energy δE_{shell} and a pairing energy δE_{pair}. The liquid–drop term describes the smooth trends of the potential energy, while the shell and pairing–energy corrections, which are calculated from single–particle energies, give the fluctuations about the smooth behaviour.

The procedure of determining the single–particle levels in general consists of three steps: (1) specifying the geometrical shape of the nucleus, (2) generating the single–neutron and single–proton potential related to this shape, and (3) solving the Schrödinger equation for this single–particle potential. In order to obtain the single–particle potential that is related physically to a given shape, one can fold an adequately chosen function, e.g. of Yukawa type, with a uniform sharp–surface generating density distribution of appropriate shape. The parameters of this folding function are obtained in Ref. [82] through the global fit to nuclear masses and fission barrier heights . To solve the Schrödinger equation for the above potential we used an expansion of the single–particle wave function in the basis of triaxially deformed harmonic–oscillator wave functions. The details of this procedure are described in the previous chapter. When the single–proton and single–neutron levels are computed at a given deformation, the shell correction is determined by means of the method suggested by Strutinsky [78], while the pairing correlations are obtained within the BCS approach with a constant value of the pairing strength G_{pair} [71].

7.2.2 The shell correction

The shell correction for a system with a specified particle number N is simply given by the difference between the sum of the single–particle levels and the smooth distribution $\tilde{e}(n)$ obtained by "washing–out" of the shell structure, (see e.g. [86])

$$\delta E_{shell} = \sum_{n=1}^{N} e_i - \int_0^{\infty} \tilde{e}(n)dn. \tag{7.32}$$

The primary advantage of Strutinsky's averaging method is that it can be used for arbitrary single–particle spectra which arise from some realistic potentials.

The summation in eq. (7.32) should extend only over the occupied states with the continuum states, represented by an appropriate, continuous expression. However, since the continuum states affect the final shell correction only in determining the smooth curve $\tilde{e}(n)$ for particle numbers n below the Fermi surface, for this purpose they can be approximated by discrete states. The next step is to separate the exact level density $g(e)$ into a smoothly varying part $\tilde{g}(e)$ and a part $\delta g(e)$ that describes its local fluctuations, i.e.,

$$g(e) = \tilde{g}(e) + \delta g(e). \tag{7.33}$$

This is achieved by expanding the $\delta-$function in the series of Hermite polynomials. Since Hermite polynomials of low order exhibit less oscillations more slowly than those of high order, the first few of them in the above equation represent the smoothly changing contribution $\tilde{g}(e)$ and the remaining terms the fluctuating contribution $\delta g(e)$. This expansion includes automatically a Gaussian weighting functions and leads to

$$g(e) = \frac{1}{\gamma}\sum_{n=1}^{\infty}\delta(u_n) = \frac{1}{\gamma\sqrt{\pi}}\sum_{n=1}^{\infty} e^{-u_n^2}\sum_{m=0}^{\infty} c_m H_m(u_n), \tag{7.34}$$

where we use the abbreviation

$$u_n = (e - e_n)/\gamma \tag{7.35}$$

and where the coefficients c_m are given by

$$c_m = \begin{cases} \frac{(-1)^{m/2}}{2^m(m/2)!}, & m \text{ even}, \\ 0, & m \text{ odd}. \end{cases} \tag{7.36}$$

The scaling factor γ, which has the dimension of energy, has been introduced to make the arguments dimensionless and to control the range over which the Gaussian weighting function is effectively nonzero. The summation over m in eq. (7.34) includes even values only, since the coefficients of all odd Hermite polynomials are zero. Therefore, the smooth level density is given by an expression analogous to eq. (7.34) but with the

summation over m extending only to p which defines the order of the shell correction. The oscillations in the Hermite polynomials lead to an unpleasant feature of Strutinsky's method. In the process of decreasing to zero below bottom level, the smooth level density $\tilde{g}(e)$, in general, becomes slightly negative for certain energies. This, in turn, causes the average particle number $\tilde{n}(e)$ also slightly negative for certain energies below the bottom level. Therefore, the lower limit of the integrals over particle number n in eq. (7.32) should in principle start at $-\infty$ rather than at zero. The average particle number can now be evaluated explicitly

$$\tilde{n}(e) = \int_{-\infty}^{e} \tilde{g}(e')de' = \sum_{n=1}^{\infty} \Big\{ \frac{1}{2}[1 + \mathrm{erf}(u_n)] - \frac{1}{\sqrt{\pi}} e^{-u_n^2} \sum_{m=1}^{p} c_m H_{m-1}(u_n) \Big\}. \tag{7.37}$$

In practice, it is more convenient to transform the integration over the particle number in eq. (7.32) into an integration over energy, namely

$$\int_{0}^{N} \tilde{e}(n)dn = \int_{-\infty}^{\tilde{\lambda}} e\, \tilde{g}(e)de. \tag{7.38}$$

The upper limit $\tilde{\lambda}$ can be interpreted as the Fermi energy of the smooth distribution of levels and is directly determined by the equation

$$\tilde{n}(\tilde{\lambda}) = \int_{-\infty}^{\tilde{\lambda}} \tilde{g}(e)de = N, \tag{7.39}$$

which in practice is usually solved iteratively with $\tilde{n}(\tilde{\lambda})$ given by eq. (7.37). The integral eq. (7.38) can be evaluated explicitly

$$\begin{aligned} \int_{0}^{N} \tilde{e}(n)dn = \sum_{n=1}^{\infty} \Big\{ & \frac{1}{2}[1 + \mathrm{erf}(\tilde{u}_n)] - \frac{1}{2\sqrt{\pi}} \gamma e^{-\tilde{u}_n^2} - \\ & \frac{1}{\sqrt{\pi}} e^{-\tilde{u}_n^2} \sum_{m=1}^{p} c_m \Big[\gamma H_m(\tilde{u}_n) + e_n H_{m-1}(\tilde{u}_n) + m\gamma H_{m-2}(\tilde{u}_n) \Big] \Big\}, \end{aligned} \tag{7.40}$$

where $\tilde{u}_n = (\tilde{\lambda} - e_n)/\gamma$. This result gives finally the shell correction. As we can see, the shell correction depends explicitly on the single–particle energies e_n and the smooth $\tilde{e}(n)$ only below the Fermi surface $\tilde{\lambda}$. States above the Fermi surface enter only in determining the smooth function $\tilde{e}(n)$ for $n \leq N$, and the contributions of the higher states ($n \gg N$) rapidly approaches to zero. In particular, in eq. (7.37) and eq. (7.40) a given term n approaches zero as the energy e_n exceeds the smooth Fermi energy $\tilde{\lambda}$ by an amount that is large compared to the smoothing range γ. This means that the summations in these equations can be truncated as soon as $(e_n - \tilde{\lambda})/\gamma \gg 1$.

Since neither the smoothing parameter γ nor the order p of the shell correction represent physical quantities, the value of the shell correction should be insensitive

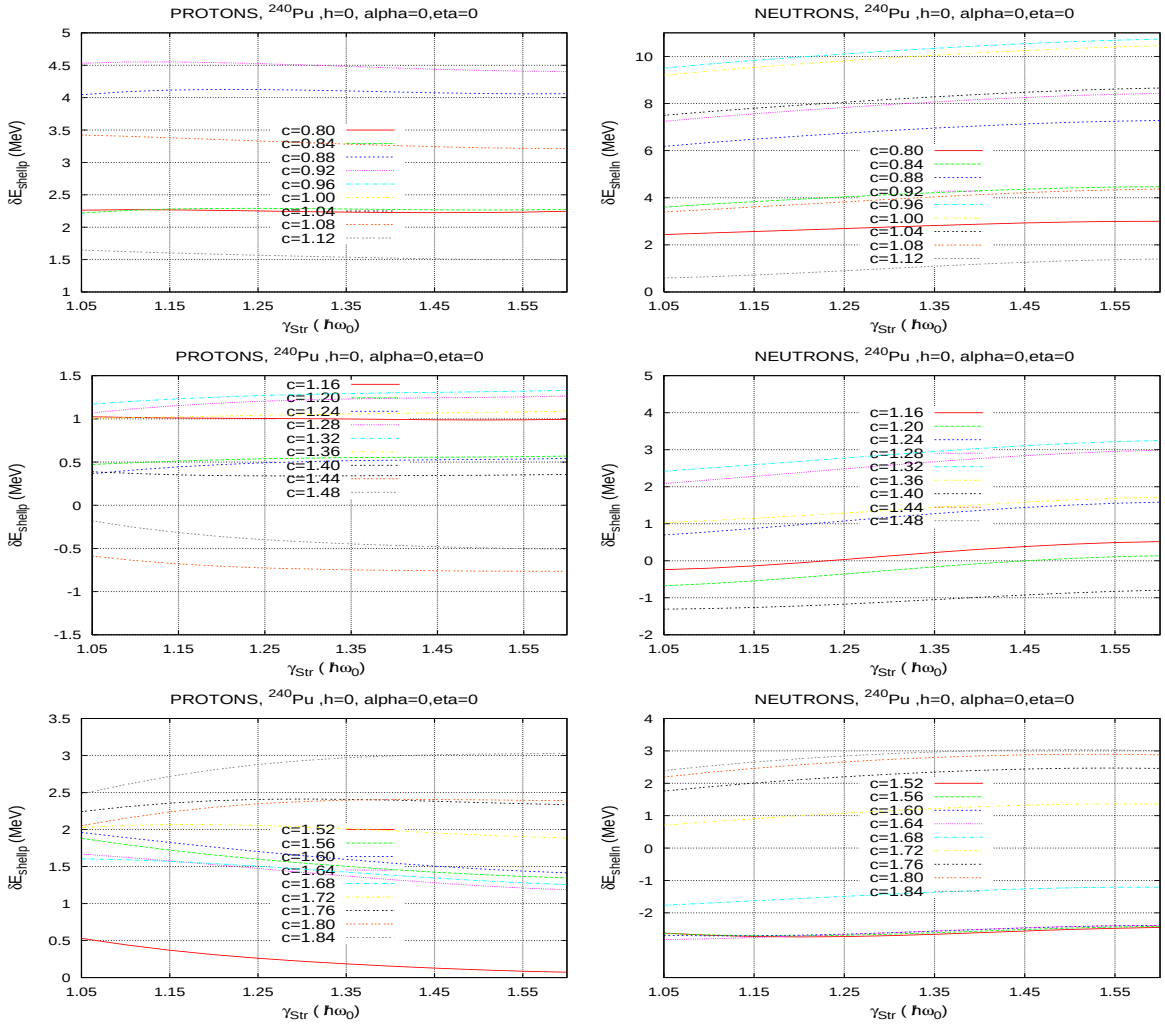

Figure 7.1: Study of the plateau condition of the Strutinsky method with Yukawa–folded set of s–p states of ^{240}Pu. Only purely ellipsoidal shapes are discussed which are described uniquely by the elongation parameter c. The left hand side pictures correspond to the proton shell corrections while the r.h.s to the neutron shell corrections. The order of the correction is $p = 6$

to the choice of these quantities (see Fig. 7.1). Since the smooth function $\tilde{e}(n)$ is determined by the single–particle levels, the $\gamma-$value should be comparable to the spacing between them, and should be large enough to average over the levels between major shells.

7.2.3 The BCS approach

The existence of the two–body *pairing* interaction in an atomic nucleus between nucleons of the antiparallely correlated total angular momenta (corresponding to time–reversed states) is confirmed by numerous experimental facts, as e.g.:

- The total angular momentum of an even–even nucleus is equal to zero whereas

for odd nuclei it is determined by the unpaired particle,

- The differences of binding energies of neighbouring even–even and even–odd nuclei indicate a lower separation energy of the odd valence particle as compared to the even nucleon,
- The large energy gap between the ground state and the first excited state of even–even nuclei,
- The moments of inertia which well reproduce the rotational spectra of atomic nuclei require the inclusion of the pairing interactions.

In spite of such very rich experimental evidence of the pairing correlations in atomic nuclei it is, in fact, not easy to extract pure pairing effects from the mixture of other collective, short and long range correlations which influence the experimental results.

The method originally introduced by Bardeen, Cooper and Schrieffer (BCS) [87] for treating pairing correlations in solid–state physics has been adapted to nuclear physics by Belyaev [88].

This interaction is of short range and the states of *paired* nucleons are characterized by the time–reversal transformation

$$|\tilde{\alpha}\rangle = \hat{K}|\alpha\rangle, \tag{7.41}$$

where $|\alpha\rangle = |j,m\rangle, \qquad |\tilde{\alpha}\rangle = |j,-m\rangle$ while j and m being respectively the total angular momentum quantum number of a nucleon and its projection on the quantization axes. The set of single–particle levels around the Fermi surface affected by this interaction is usually refered to a *pairing window.*

Let us consider the $j-$shell in a nucleus. The set of quantum numbers characterizing this shell is $|\mu\rangle$:

$$(j,m) \Longrightarrow \mu$$

$$|\mu\rangle = c^{+}_{\mu}\,|0\rangle = |j,m\rangle = c^{+}_{jm}|0\rangle \tag{7.42}$$

and the time–reversed state

$$|\bar{\mu}\rangle = (-1)^{j+m}|j,-m\rangle = (-1)^{j+m}c^{+}_{j-m}|0\rangle. \tag{7.43}$$

Suppose that the interaction in a multi–fermion system leads to the scattering of the particles. Initially, only the lowest states below the Fermi surface are occupied and the others are empty. When the interaction is switched on, each level has a certain probability of being occupied or empty. Let u_ν be the probability amplitude that the single–particle state e_ν is empty and v_ν–that this state is occupied (with $v_\nu + u_\nu = 1$). The wave function corresponding to this situation can be written as a

linear combination of the vacuum state of the fermion system $|0\rangle$ and the state occupied by the pair $|\nu,\bar{\nu}\rangle = c_\nu^+ c_{\bar{\nu}}^+ |0\rangle$

$$|\phi_\nu\rangle = u_\nu|0\rangle + v_\nu\, c_\nu^+ c_{\bar{\nu}}^+ |0\rangle, \tag{7.44}$$

where c_ν, c_ν^+ are respectively the annihilation and creation operators of a fermion in state $|\nu\rangle$ for which the anticommutator relation $\{c_\nu, c_{\nu'}^+\} = \{c_\nu^+, c_{\nu'}\} = \delta_{\nu\nu'}$ holds. As a consequence, we can expect that the total wave function of the even system of N_{wind} fermions contained in the *pairing window* can be written as

$$|\phi\rangle = \prod_{\nu\in N_{wind}} (u_\nu + v_\nu\, c_\nu^+ c_{\bar{\nu}}^+)|0\rangle, \tag{7.45}$$

where it can be shown that the amplitudes u_ν, v_ν of the probability that the state ν is either occupied or empty, fulfil the normalization condition

$$\langle\phi|\phi\rangle = 1 \qquad \text{if and only if} \qquad u_\nu^2 + v_\nu^2 = 1, \quad \nu = 1,\ldots,N_{wind}. \tag{7.46}$$

Since it is experimentally known that the ground state of even–even nuclei always have an angular momentum equal to zero, we conclude that the scattering caused by the pair interaction never breaks a pair, but rather scatters one pair $(\alpha,\bar{\alpha})$ to another pair $(\beta,\bar{\beta})$ which implies that the pairing Hamiltonian can be written in the form

$$\hat{H}_{pair} = \sum_{\alpha\beta} G_{\alpha\beta}\, c_\beta^+ c_{\bar{\beta}}^+ c_{\bar{\alpha}} c_\alpha, \tag{7.47}$$

where $G_{\alpha\beta} = \langle\beta\bar{\beta}|\hat{v}|\alpha\bar{\alpha}\rangle$ is the appropriate pairing matrix elements of the two–body interaction.

Comparing now the above expression with the general expression for the two–body Hamiltonian

$$\hat{H}(2) = \frac{1}{2}\sum_{\alpha\beta\gamma\delta} \langle\alpha\beta|\hat{v}|\gamma\delta\rangle\, c_\alpha^+ c_\beta^+ c_\delta c_\gamma \tag{7.48}$$

we get

$$\langle\alpha\beta|\hat{v}|\gamma\delta\rangle = G_{\alpha\beta}\delta_{\widetilde{\beta\alpha}}\delta_{\widetilde{\gamma\delta}}.$$

It is frequently assumed that the matrix elements $G_{\alpha\beta}$ are state independent, i.e. $G_{\alpha\beta} \equiv G_{pair}$. The Hamiltonian (7.47) then corresponds to the so–called *monopol–pairing* interactions between nucleons of the same charge state q and in time reversed states.

The values of the coefficients u_ν and v_ν are still unknown. In order to determine their values we use the variational method to minimize the energy of the system

$$\delta\left(\langle\phi|\hat{H}_{pair}|\phi\rangle_{u_\nu,v_\nu}\right) = 0, \tag{7.49}$$

where now u_ν, v_ν are the variational parameters. The unpleasant feature of the BCS wave function (7.45) is that it contains terms corresponding to different numbers of

particles. As an example, let us write explicitly this function for the simplest case, where only two nucleon single–particle states are available:

$$\begin{aligned} |\phi\rangle_2 &= (u_\alpha + v_\alpha c^+_\alpha c^+_{\bar{\alpha}})(u_\beta + v_\beta c^+_\beta c^+_{\bar{\beta}})|0\rangle = \\ & (u_\alpha u_\beta)|0\rangle + (u_\alpha v_\beta c^+_\beta c^+_{\bar{\beta}} + u_\beta v_\alpha c^+_\alpha c^+_{\bar{\alpha}})|0\rangle - v_\alpha v_\beta c^+_\alpha c^+_\beta c^+_{\bar{\alpha}} c^+_{\bar{\beta}}|0\rangle. \end{aligned} \quad (7.50)$$

From the above we can see that $|\phi\rangle_2$ contains three type of states: one zero–particle state, two two–particle states and one four–particle state. For atomic nuclei of N neutrons and Z protons we have to postulate that in the BCS method the number of particles (Z and N) must, at least, be conserved on the average, i.e. with the particle number operator

$$\hat{\mathcal{N}} = \sum_{\nu \in N_{wind}} (c^+_\nu c_\nu + c^+_{\tilde{\nu}} c_{\tilde{\nu}}) \quad (7.51)$$

we should have

$$\langle \phi | \hat{\mathcal{N}} | \phi \rangle = N_{wind}. \quad (7.52)$$

The variational principle (7.49) with the above constraint can be rewritten in the form

$$\delta \left(\langle \phi | \hat{H}_{pair} - \lambda \hat{\mathcal{N}} | \phi \rangle_{u_\nu, v_\nu} \right) = 0 \quad (7.53)$$

which leads (for a constant pairing matrix element $G_{\alpha\beta} = G_{pair}$) to the set of coupled BCS equations of the form:

$$\begin{cases} N_{wind} = \sum\limits_{\nu \in N_{wind}} 2v^2_\nu = \sum\limits_{\nu \in N_{wind}} \left\{ 1 - \frac{e_\nu - \lambda}{\sqrt{(e_\nu - \lambda)^2 + \Delta^2}} \right\}, \\ \frac{2}{G_{pair}} = \sum\limits_{\nu \in N_{wind}} \frac{1}{\sqrt{(e_\nu - \lambda)^2 + \Delta^2}}, \end{cases} \quad (7.54)$$

where

$$\Delta = G_{pair} \sum_{\nu \in N_{wind}} u_\nu \, v_\nu. \quad (7.55)$$

The occupation probabilities appearing in eq. (7.45) are given by

$$v^2_\nu = \frac{1}{2} \left\{ 1 - \frac{e_\nu - \lambda}{\sqrt{(e_\nu - \lambda)^2 + \Delta^2}} \right\}. \quad (7.56)$$

The pairing gap Δ and the Lagrange multiplier λ which has the meaning of the BCS Fermi energy are given by the solutions of the above, coupled BCS equations.

Taking into account the pairing correlations, the ground–state energy of the nucleus is given within the BCS model as

$$E^{(BCS)}_{g.s.} = \min \left[\langle \phi | \hat{H}_{pair} - \lambda \hat{N} | \phi \rangle \right]. \quad (7.57)$$

or explicitly by

$$E^{(BCS)}_{g.s.} = \sum_{\nu \in N_{wind}} 2e_\nu v^2_\nu - \frac{\Delta^2}{G_{pair}} - G_{pair} \sum_{\nu \in N_{wind}} v^4_\nu. \quad (7.58)$$

7.2.4 Pairing correction

The second type of microscopic single–particle correction, the pairing correction, arises from short–range interaction of correlated pairs of nucleons moving in time–reversed orbits described in the previous section. This is the most important and relatively easy treated residual interaction felt by nucleons. This interaction always lowers the total potential energy relative to the energy without pairing. However, one has to keep in mind that the macroscopic part of the total energy of a nucleus contains already the average effect of the pairing correlations so that the pairing correction fluctuates around zero. The lowering of the total energy is larger when more pairs of nucleons are able to interact, which occurs, when the level density near the Fermi surface is high. This is opposite to the behaviour of the shell correction, where the potential energy is lowered mostly when the level density is low. This leads to a partial cancellation of these two effects (see Fig. 7.3). The shell contribution is the larger of these two corrections and it therefore determines the main trends of the total microscopic energy. The most essential features of the pairing correlations can be described in terms of a constant pairing interaction G_{pair} acting between pairs of particles. The standard pairing calculation in the BCS approximation tells how much the energy is lowered for the actual distribution of levels. A similar calculation performed for the same number of particles distributed smoothly with a level density $\tilde{g}(e)$ determines the lowering in energy for an average nucleus. The difference between the lowering for the realistic and the uniform level densities gives finally the pairing correction. In calculations of the pairing contribution for either neutrons or protons, we consider N_{wind} pairs of particles, with $\frac{1}{2}N_{wind}$ pairs lying above the sharp Fermi surface and $\frac{1}{2}N_{wind}$ lying below (we limit the discussion to an even number of nucleons because only such will be the subject of our investigations). Then, for a specified pairing strength G_{pair}, the pairing correlation energy being the difference between the ground–state energy in the BCS model (7.58) and the sum of the single–particle energies up to the Fermi energy is given by

$$\delta E_{pair} = E_{g.s.}^{(BCS)} - \sum{}' 2e_\nu = \\ 2\Big(\sum_{\nu=1}^{N_{wind}} e_\nu v_\nu^2 - \sum{}' e_\nu\Big) - \frac{\Delta^2}{G_{pair}} - G_{pair}\Big(\sum_{\nu=1}^{N_{wind}} v_\nu^4 - \sum{}' 1\Big), \qquad (7.59)$$

where $\sum{}'$ denotes a sum over the occupied single–particle states only and the pairing gap Δ and the Fermi level λ are the solutions of the coupled BCS equations (7.54).

There exist a couple of methods of determining the pairing strength G_{pair}. One of them proposed in [71] called *uniform gap method* consist in determining the average pairing strength G_{pair} through the equation similar to (7.54) when the sum over the states lying in the *pairing window* is replaced by the appropriate integral over the

smooth level–density $\tilde{g}(e)$ as

$$\frac{2}{G_{pair}} = \int_{\tilde{\lambda}-\Omega}^{\tilde{\lambda}+\Omega} \frac{\tilde{g}(e)\,de}{[(e-\tilde{\lambda})^2+\tilde{\Delta}^2]^{1/2}} \approx 2\tilde{g}(\tilde{\lambda}) \ln \frac{2\Omega}{\tilde{\Delta}}. \tag{7.60}$$

The cut–off energy Ω (half of the energetical pairing window) is related to the number of states ($2 \times N_{wind}$) taken into account in the sum (7.54) by the relationship

$$2\Omega = N_{wind}/\tilde{g}(\tilde{\lambda}), \tag{7.61}$$

where $\tilde{g}(\tilde{\lambda})$ is the average level density at the Fermi surface. The average pairing gap $\tilde{\Delta}$ is experimentally found to be well approximated by $\tilde{\Delta} = 12MeV/\sqrt{A}$. It was shown in [89] that reasonable estimates of the pairing gaps Δ_p and Δ_n can be obtained using $N_{wind} = \sqrt{15\mathcal{N}}$, ($\mathcal{N} = \{Z, N\}$). However, if we are increasing continuously the number of pairs N_{wind} participating in the pairing interaction we would observe that the resulting quantities Δ and G_{pair} become less and less sensitive for this change.

The coupled equations (7.54) are solved iteratively until convergence is achieved. We start from the estimate of G given by eq. (7.60) and insert it together with the first guess of the diffused Fermi energy $\tilde{\lambda} = \frac{1}{2}[e(\mathcal{N}) + e(\mathcal{N}+1)\,]$ into the second equation in (7.54). Then, having the initial estimation of the pairing gap Δ we insert it into the first equation (7.54). We then calculate the new position of λ. We repeat this procedure until the values of λ and Δ between two successive iterations differ by ε, where ε is desired accuracy. This procedure must be repeated for all deformation points of the multidimensional space. The deformation dependences of the proton and neutron pairing gaps Δ_p and Δ_n are plotted in Fig. 7.2 for the nuclei ^{232}Th and ^{240}Pu.

In order to make the pairing correction as a function of the nuclear deformation oscillate about zero we have to subtract from eq. (7.59) the average pairing energy which was already taken into account in the fit of LSD model parameters. The average energy of pairing correlations is determined from an expression analogous to eq. (7.59) but with the summation over the discrete states e_ν replaced by the integral over the smooth function $\tilde{e}(n)$ (similarly as it was done in eq. (7.60)). However, the resulting integrals can now be evaluated analytically if $\tilde{e}(n)$ is replaced by a linear function (obtained by making a Taylor expansion of the nuclear number around the sharp–Fermi surface and neglecting quadratic and higher order terms). The average density of pairs is then given by

$$\tilde{\rho} = \frac{1}{2}\tilde{g}(\tilde{\lambda}). \tag{7.62}$$

For such a uniform levels distribution the discrete sums in eq. (7.59) need to be replaced by the corresponding integrals according to the following prescription

$$\sum_{\nu \in N_{wind}} f(e_\nu - \lambda) \Longrightarrow \tilde{\rho} \int_{y_1}^{y_2} f(y)dy$$

with $y_1 = \frac{-1/2\, N_{wind}}{\widetilde{\rho}}$ and $y_2 = \frac{1/2\, N_{wind}}{\tilde{\rho}}$ we get the average pairing correlation energy in the form

$$\delta\widetilde{E}_{pair} = -\frac{1}{4}\frac{N_{wind}^2}{\widetilde{\rho}}\left\{\left[1+\left(\frac{2\widetilde{\rho}\widetilde{\Delta}}{N_{wind}}\right)^2\right]^{1/2}-1\right\}+\frac{1}{2}\widetilde{\rho}\widetilde{\Delta}\widetilde{G}_{pair}\arctan\left(\frac{N_{wind}}{2\widetilde{\rho}\widetilde{\Delta}}\right) \quad (7.63)$$

with the pairing strength G_{pair} and the average pairing gap $\widetilde{\Delta}$ related by

$$\frac{1}{\widetilde{G}_{pair}} = \widetilde{\rho}\,\ln\left\{\left[\left(\frac{N_p}{2\widetilde{\rho}\widetilde{\Delta}}\right)^2+1\right]^{1/2}+\frac{N_p}{2\widetilde{\rho}\widetilde{\Delta}}\right\}. \quad (7.64)$$

The pairing correction for either neutrons or protons is then finally given by

$$\Delta E_{pair} = \delta E_{pair} - \delta\widetilde{E}_{pair}. \quad (7.65)$$

The average value of the pairing gap $\widetilde{\Delta}$ is assumed to remain constant with deformation. In Figs. 7.2 the typical oscillating behaviour of the proton and neutron pairing gaps are presented. Comparing Fig. 7.2 and Fig. 7.3 the obvious coincidence between the peaks of the $\Delta_{p(n)}-$values and the corresponding extrema of the total pairing correction can be observed. The total value of the pairing correction ($\delta E_{pair} = \delta E_{pair}^{(p)} + \delta E_{pair}^{(n)}$) for the majority of the here investigated nuclei, two of which are shown in Figs. 7.2 and 7.3 oscillates about 2 MeV.

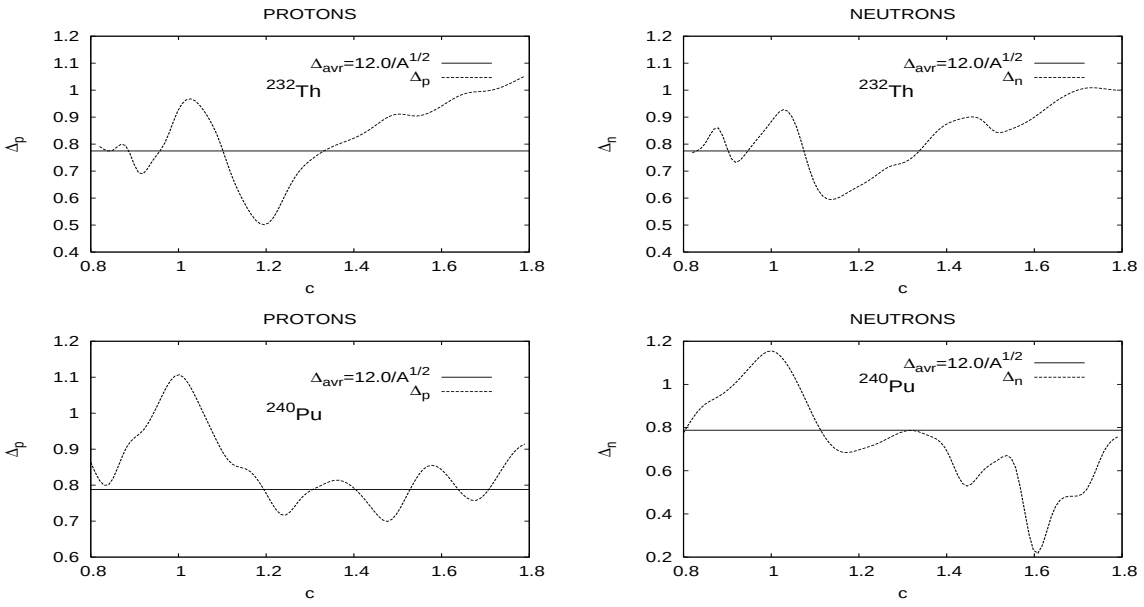

Figure 7.2: Proton and neutron pairing gaps for ^{232}Th and ^{240}Pu as a function of elongation c with $h = 0$ calculated within the uniform gap method. The straight solid line corresponds to the average pairing gap $\widetilde{\Delta}$

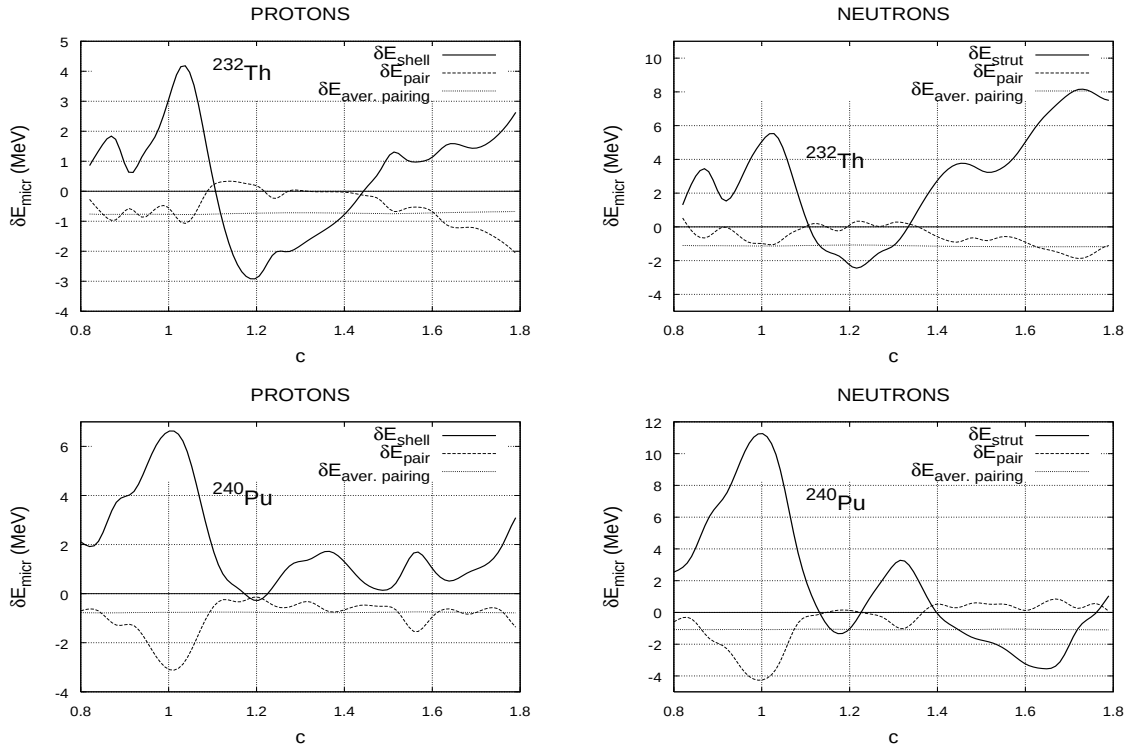

Figure 7.3: Shell and pairing corrections for the nuclei presented in Fig. 7.2 with ellipsoidal deformation. The solid continuous line denotes the Strutinsky shell correction whereas the thin correspond to the BCS and the average pairing energy (7.63) respectively

Chapter 8

Static description of the nuclear fission

8.1 Total energy landscapes for equal proton and neutron deformations

Before we investigate the influence of different proton–neutron deformations on the total fission barriers as function of the $\{c, h\}$ deformation parameters which respectively describe the elongation and the neck of a nucleus, let us first consider the surfaces of the total nuclear energy for equal deformations of both these distributions. The nuclear–energy surface is usually defined for a nucleus of given mass number A and proton (Z) or neutron (N) number as the total energy function depending on the deformation parameters.

Recalling the argumentation given in sections 6.1.1 and 6.2 we state that the two deformation parameters $\{c, h\}$ are the most relevant degrees of freedom for the description of the fission process in cylindrical coordinates, either by the original or by the modified Funny–Hills parametrization.

The total nuclear energy is understood as the sum of a liquid drop average part given e.g. by the LSD model (see section 2) and the shell plus pairing correction energy, (see Fig. 8.1) which are of quantum origin. The shell energy contribution is obtained within the traditional Strutinsky averaging method introduced in section 7.2.2. The pairing correlations, in turn, are treated here by means of the BCS method presented in section 7.2.3 where the constant value of pairing strength G_{pair} is imposed.

Figures 8.2–8.3 illustrate the total potential energy landscapes of two actinide nuclei ^{232}Th, ^{240}Pu and the super–heavy elements: ^{268}Hs, $^{266}_{112}X$, $^{298}_{114}X$, $^{266}_{116}X$ as function of the elongation parameter c and the neck parameter h. For ^{240}Pu we observe well pronounced stationary points corresponding to the ground state ($c \approx 1.20, h \approx -0.3$), the isomeric minimum ($c \approx 1.40, h \approx -0.05$) as well as two major saddle points ($c \approx 1.30, h \approx 0.0$) and ($c \approx 1.65, h \approx -0.2$). The energy landscapes of other actinides e.g. $^{236,238}U$ are very similar to those shown in Fig. 8.2 in this sense that the positions

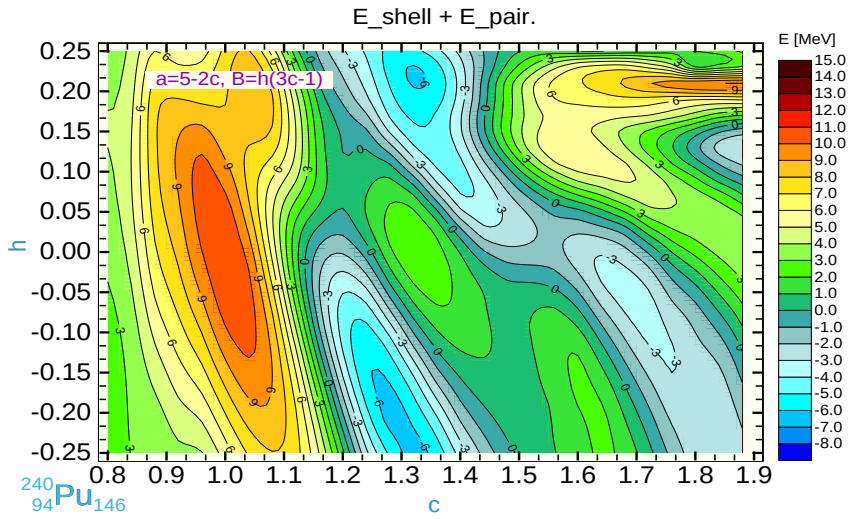

Figure 8.1: Total quantum correction in two dimensional space $\{c, h\}$ for ^{240} Pu

of the main stationary points are almost identical within $\Delta c \approx \Delta h \approx \pm 0.02$. For lighter actinides we notice, what was already remarked for LD barriers in section 6.3, that now the exit configuration from the barrier appears for very elongated shapes (c reaches 1.9) while the same is observed for super–heavy elements already for $c \approx 1.5$. We can therefore say that, in general, the width of the total fission barrier depends on the mass number A. On the contrary to the above discussed cases the second minimum is situated in the super–heavy element $^{298}_{114}X$ (see Fig. 8.3) significantly higher than the ground state by approximately 4.5 MeV and the outer barrier is reduced to a height of hardly 2MeV. For a large number of other super–heavy nuclei the second minimum and the outer barrier are not present at all (see, e.g. Fig. 8.3 for $^{266}_{112}X$). In this context, we would like to focus our attention again on the structure of the potential–energy landscapes corresponding to the two heavy isotopes $^{270}_{112}X$ and $^{276}_{112}X$. As seen in Fig. 8.4, we can clearly distinguish relatively well pronounced second minimum in $^{278}_{112}X$ which, however, is higher than the ground state minimum by about 4MeV. Also the second saddle can be visible around $c \approx 1.4, h \approx 0$. These outer stationary points do not appear in the case of the isotope $^{270}_{112}X$.

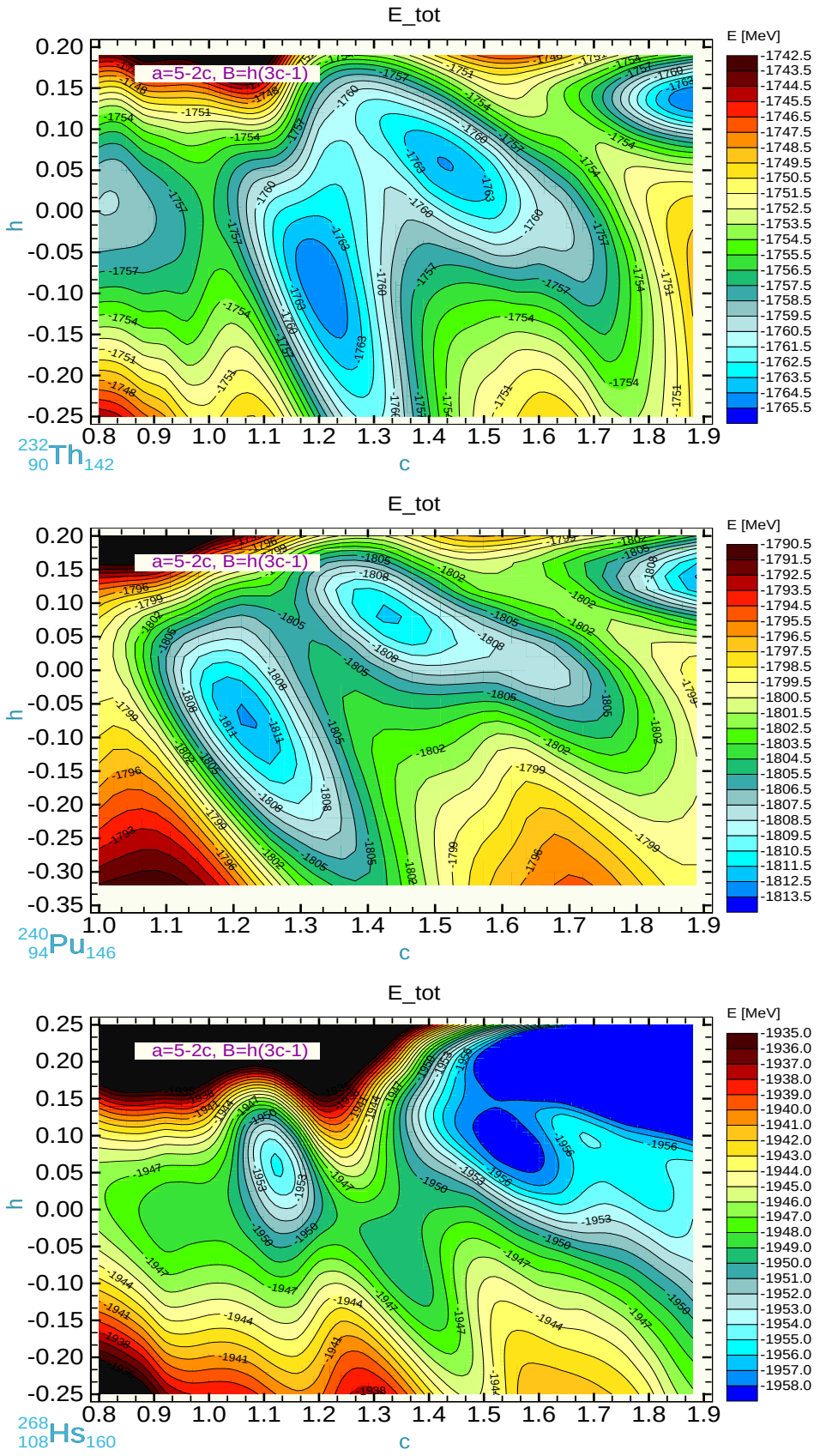

Figure 8.2: Total nuclear energy as a function of the elongation parameter c and the neck parameter h for two actinides ^{232}Th and ^{240}Pu and the heavy element ^{268}Hs

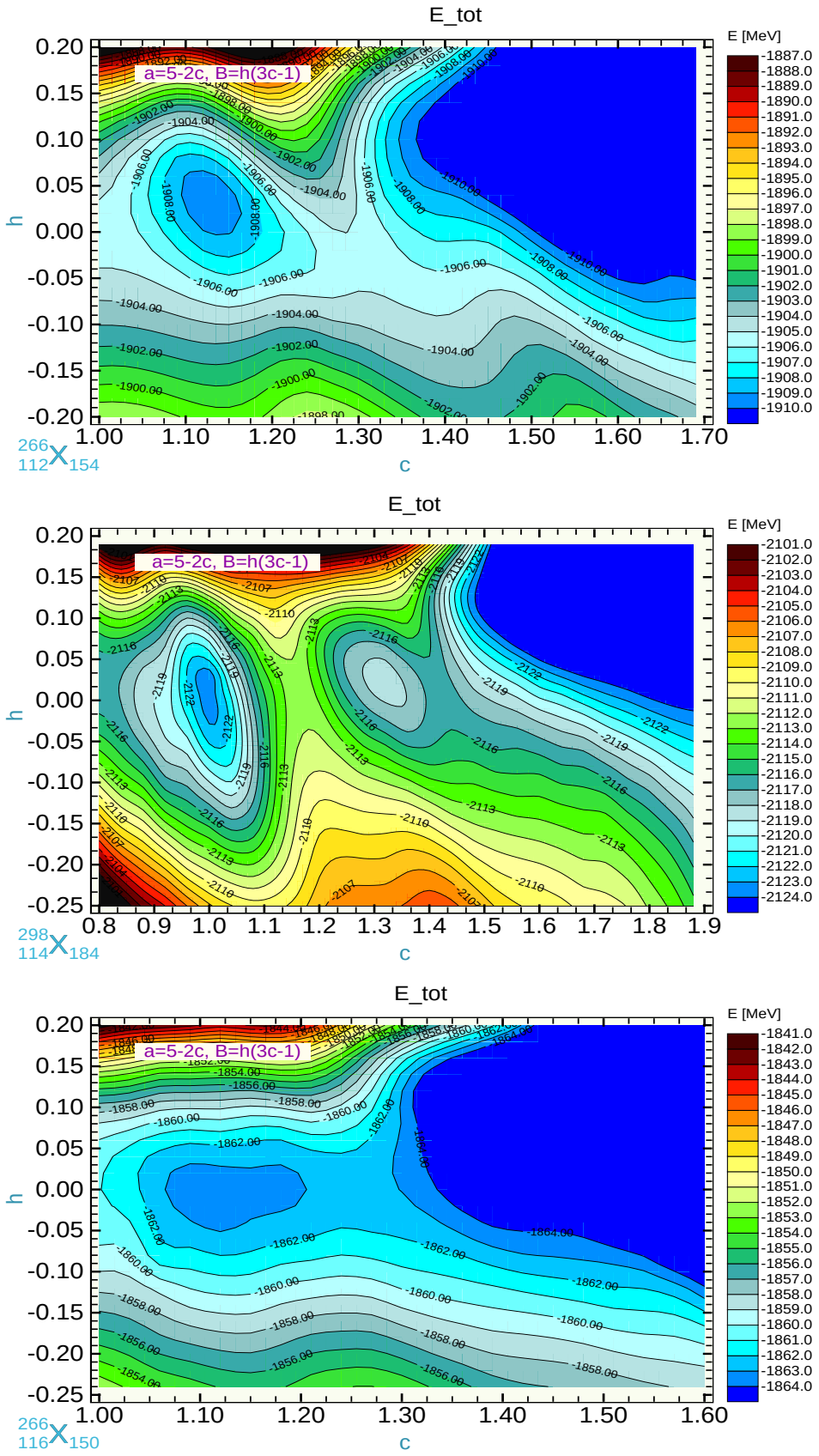

Figure 8.3: The total–energy landscape for three super–heavy elements: $^{266}_{112}X$, $^{298}_{114}X$, and $^{266}_{116}X$

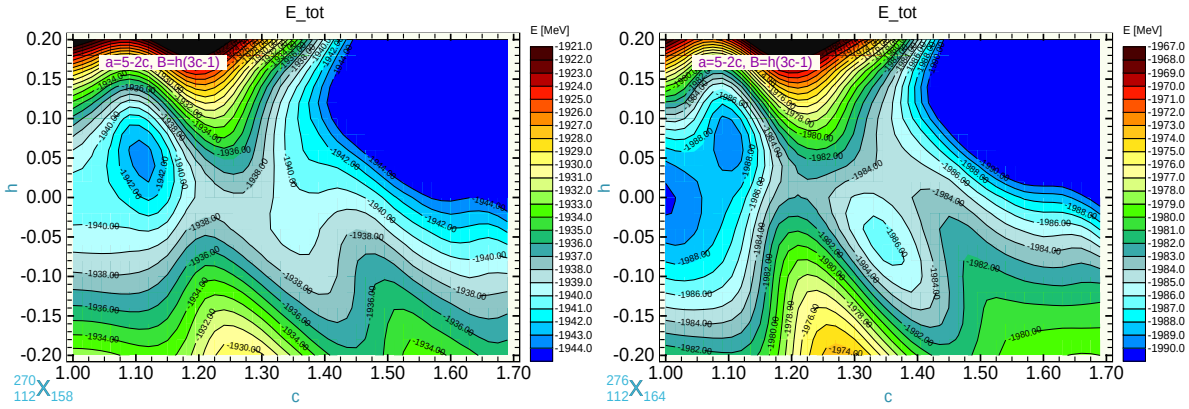

Figure 8.4: Total nuclear energy for two elements ${}^{270}_{112}X$ and ${}^{276}_{112}X$

8.2 Total nuclear energy versus neck shape

In section 6.2 we have introduced the modified version of the FH shape parametrization which for a long time was the alternative for the shape definitions by the spherical harmonics. We also discussed the LD energy as function of the neck parameter a in eq. (6.21) stating that for a large range of its value the LD energy–landscapes remain practically unchanged to within 100–300 keV. Having now the ability of describing the shell and pairing energy contributions we would like to carry out a similar investigation and examine the influence of the neck parameter a on the total nuclear energy.

a	$E_{g.s.}$(MeV)	E_I^{max}(MeV)	E_{II}^{min}(MeV)	E_{II}^{max}(MeV)
1.0	-1811.9	-1806.5	-1810.7	-1802.5
2.0	-1812.1	-1805.9	-1810.9	-1801.9
3.0	-1812.1	-1805.5	-1810.9	-1799.9
4.0	-1811.8	-1804.5	-1811.1	-1798.6
5.0	-1811.7	-1804.7	-1810.7	not existing

Tab. 8.1 Fission–barrier stationary points of ^{240}Pu as function of the neck parameter a.

Studying Tab. 8.1 we observe that for the lowest values of parameter a, i.e. $a = 1.0$ and $a = 2.0$, the second saddle point and the *exit* point from the barrier lie energetically lower than for the higher $a-$values. This reasoning shows that for very elongated nuclear shapes close to the scission configuration a reasonable choice of the neck parameter is $a \approx 1.0$. Notice also that the height of the first barrier is quite insensitive to this parameter. Likewise, the ground state and the isomeric minimum are practically unaffected by the particular choice of the $a-$value. However, for $a = 5.0$ both these minima go slightly up by approximately $0.5 - 1.2$ MeV. A similar behaviour is observed also for other investigated, actinide nuclei such as ^{236,238}U or

^{232}Th. Summarizing, we can conclude that, since the total energy landscapes are only weakly dependent on the particular choice of the $a-$value for a wide range of $\{c, h\}$ deformations, we propose to let the parameter a change linearly as a function of the elongation c

$$a = 5 - 2c. \tag{8.1}$$

Such a treatment of this deformation degree of freedom allows to minimize the total energy of the main minima and saddle points which, as we have already noticed, are the stationary points of the nuclear path to fission. Of course, the most appropriate treatment of the above problem would be to consider a as the fifth, additional deformation parameter to the four–dimensional deformation space proposed in section 6.2. This, however, is not a crucial point of this work since we are interested mostly in that part of the whole energy–landscape which is close to the average way to fission in the deformation space.

8.3 Two dimensional static path to fission

In the current section we try to find an efficient method of searching the trajectory in the deformation space which a nucleus would follow on its way to fission. Constraining ourselves only to a two dimensional deformation space is, of course, not sufficient to fully describe the physical reality of the nuclear fission which is much more complex. What we want to propose here is, in fact, a fast way of searching the energy landscape for the approximate positions of the energetical stationary points, i.e. the main minima and saddles, not taking too much care on what is the path followed by the nucleus between these points. The least–action method proposed here does not take into account the mass parameters associated with a given deformation degree of freedom and therefore delivers only a crude approximation of a more realistic, dynamical fission–path treatment, and serves solely as a "guide–line" in the energy landscape.

Let us imagine a two–dimensional static path to fission $h(c)$ which corresponds to the least–action trajectory in the $\{c, h\}-$deformation plane satisfying the condition

$$\int_{c_{g.s.}}^{c_{sc.}} \Big(V_{pot}\left(c, h\left(c\right)\right) - V_{pot}\left(g.s.\right) \Big) \sqrt{1 + \frac{dh(c)}{dc}}\, dc \;=\; \min, \tag{8.2}$$

where $c_{g.s.}$ and $c_{sc.}$ are respectively the elongations of the ground state and the scission point while $V_{pot}\left(c, h\left(c\right)\right)$ is the total potential energy.

The two dimensional path to fission can then be approximated by the following expression:

$$h(c) = \left[h_{gs} + \frac{(h_{sc} - h_{gs})(c - c_{gs})}{c_{sc} - c_{gs}} \right] + \sum_{i=1}^{N} a_i \sin\left(i\pi \frac{c - c_{gs}}{c_{sc} - c_{gs}} \right), \tag{8.3}$$

where $h_{g.s.}$ and $h_{sc.}$ correspond to the neck parameters of the equilibrium and scission shape respectively. As we can easily notice, the first term of expression eq. (8.3) in nothing but a linear interpolation between these two points which produces some average path, while the second term describes the deviation of the desired, more realistic fission path from this average trend. The minimization of expression (8.2) allows to determine the free parameters a_i of the Fourier expansion (8.3). For the sake of keeping the computational time within reasonable limits we need to truncate this series. Taking into account, at most, 25 first harmonic components yields, however, as seen in Fig. 8.3, a very reasonable convergence already using only 15 first terms in the Fourier series. Studying the behaviour of the bundle of two–dimensional fission paths in Fig. 8.3

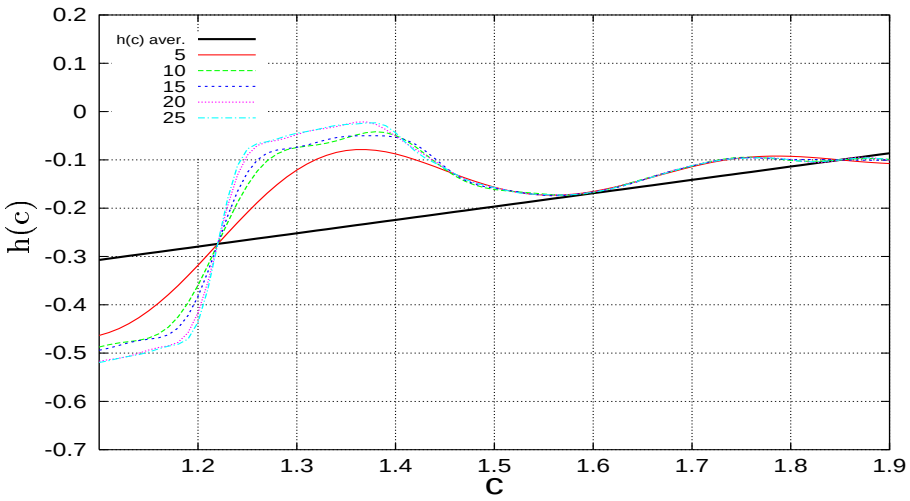

Figure 8.5: Convergence of the Fourier development of the 2 dimensional fission path $h(c)$ given by eq. (8.3) for ^{240}Pu. The position of the ground state is determined by the crossing point of all curves with the straight line

as functions of the number of basis harmonics (N) used in the series (8.3) we can conclude that this method can have the tendency to slightly underestimate the energy of the saddles and overestimate local minima of the energy landscape when too few harmonics are used. We also made the experience that such a method is difficult to handle in a deformation space of more than two dimensions. That is why we restricted its use to the investigations of unequal proton versus neutron deformations in the two–dimensional $\{c, h\}$ deformation space. An alternative method to locate extremal points in a multidimensional deformation space will be discussed in chapter 9.

8.4 Energy landscapes with unequal proton–neutron deformations

Until now a large majority of macroscopic–microscopic calculations of potential–energy surfaces of fissioning nuclei assumes equal deformations of proton and neutron distributions for both, densities and single–particle potentials (see e.g. [90, 91, 92]). In view of the results obtained in Ref. [35], one can expect that such calculations predict fission barriers that are systematically about 1 MeV too high. In the following section we would like to take advantage of our experience achieved so far and perform the macroscopic–microscopic calculations assuming that protons and neutrons can deform independently [74], [93]. Motivated by the results of Ref. [35] we want to investigate the effect of such an additional degree of freedom on the total energy of a nucleus along its way to fission.

The obtained results will then be compared to those of the selfconsistent Hartree–Fock approach where deformation energy surfaces are usually generated through calculations with a constraint on some multipole moments of the total mass distribution, which leaves protons and neutrons free to deform differently within this constraint, even though it, of course, turns out that these deformations are quite close to one another. We should note, however, that only fluctuating with the deformation part of the quantal corrections for the proton and neutron deformation difference can actually influence barrier heights calculated with the macroscopic–microscopic approach, since the average trend of this difference can be taken into account in the fitting procedure of the parameters of the macroscopic (e.g. liquid drop) model.

Studying the results presented in Ref. [35] we suggest that it might be useful to generalize the currently used macroscopic–microscopic approaches in order to allow protons and neutrons to have different deformations. We can start from the following expression for the total energy:

$$E_{tot} = E_{macr}(\{c_p, h_p, \alpha_p, \eta_p\}, \{c_n, h_n, \alpha_n, \eta_n\}) + \delta E_{micr}(\{c_p, h_p, \alpha_p, \eta_p\}, \{c_n, h_n, \alpha_n, \eta_n\}) \tag{8.4}$$

Since we know the response of the nuclear liquid drop for the relative change of proton and neutron deformations (see chapter 3 and section 6.4.6) let us include in our consideration the quantum (shell+pairing) effects introduced respectively in section 7.2.2 and 7.2.3 and which are seen here to be the terms inducing the effect of different proton–neutron deformations. We will proceed in the following way:

We start from equal proton and neutron deformations $c_n = c_p$, $h_n = h_p$ assuming for further simplification that $\alpha_p = \alpha_n = 0$ and $\eta_p = \eta_n = 0$. Let, in the beginning, $\{c_p, h_p\}$ determine the deformation of the fissioning nucleus, denoted as $\{c, h\}$. For given values of $\{c, h\}$ we find the corresponding set of neutron parameters $\{c_n, h_n\}$ for

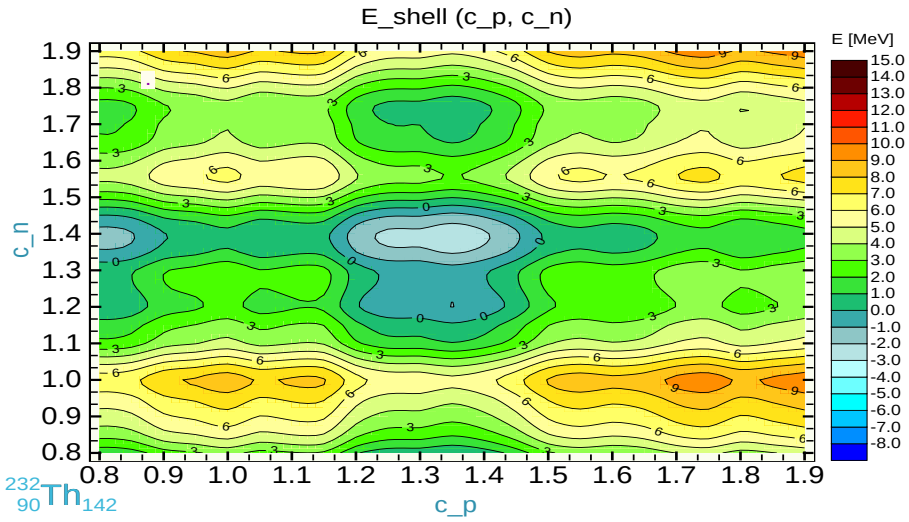

Figure 8.6: Total shell correction as a function of proton and neutron elongations c_p and c_n for ^{234}Th

which the total energy is minimal. The proton and neutron density deformations then are obviously expected to be quite close to each other. Indeed, keeping in mind the results of Ref. [35] the relative difference of both these deformations reaches, at most, 10%.

The final proton and neutron deformation is the result of the interplay of purely liquid drop and shell effects. The LD contribution tends, as we can observe in Fig. 6.12 and 6.13, to keep both distributions deformed identically, whereas the quantal (shell+pairing) correction can have its minima not always for identical proton (c_p) and neutron (c_n) deformations (see Figs. 8.6 and 8.7). What is interesting is that the minima situated for substantially different p–n deformations, which are visible particularly in Fig. 8.7, can not produce any significant p–n deformation difference because of a strong resistance of the LD part against such a variation, what has been already discussed in section 6.4.6. Summing up the macroscopic (given by eq. (6.105)) and the microscopic contributions, described in sections 7.2.2, 7.2.3 and minimizing the total energy with respect to neutron deformations we obtain that $\{c_p, h_p\}$ and $\{c_n, h_n\}$ are usually slightly different. The magnitude of these difference depends on the strength of the total shell effect for a given value of the deformation and, on the other hand, on the macroscopic resistance of the nuclear system against such a variation.

Looking at Figs. 8.8 and 8.9 we observe that the differences $c_n - c_p$ strongly depend on the deformation of the nucleus and are always negative for prolate deformations, except for ^{232}Th, ^{234}Th and ^{236}U for which they are slightly positive in the closest vicinity of the spherical shape. We also see that the difference $h_n - h_p$ weakly depends on the deformation and oscillates usually around zero–value, being mostly positive in all presented cases. It is not misleading since we realize that the stiffness of the macroscopic

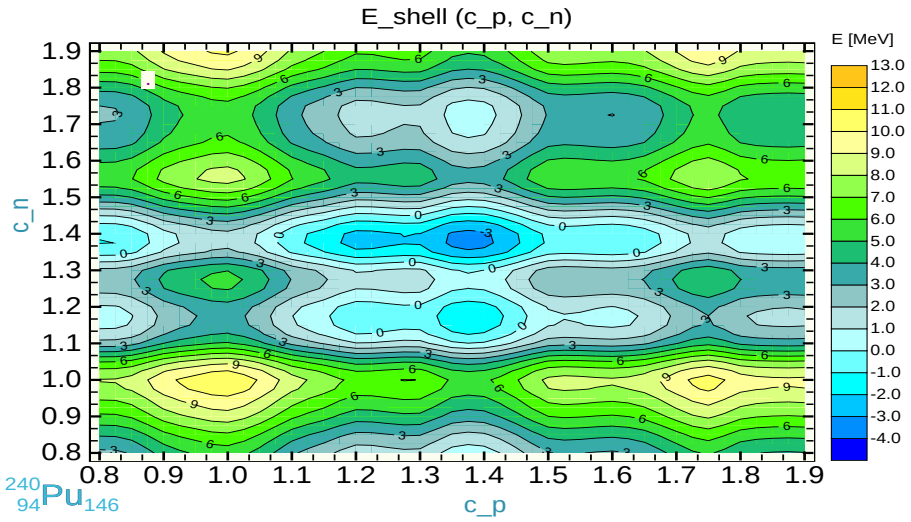

Figure 8.7: The same study as in Fig. 8.6 for ^{240}Pu

energy as function of $h_n - h_p$ almost does not depend on the deformation (see Fig. 6.12 and 6.13). The strongest variations of $h_n - h_p$ are noticed around the ground states and the second minima, however for ^{272}Ds its maximal amplitude coincides with the same for $c_n - c_p$ which manifests particularly about the saddle point (see Fig. 8.9). A similar but significantly weaker effect occurs for $^{298}_{114}X$. Large values of proton–neutron deformation–difference are obtained for all examined nuclei. This difference can be translated directly on the proportionally large energy difference of nuclei with unequal and equal proton–neutron deformations, reaching even 3 MeV with oscillations of about 1.5 MeV at the second barrier, particularly for the actinides. Heavier element, i.e. ^{272}Ds undergoes such the effect in the region between the equilibrium and the first barrier hump, being negligibly small on its top. The similar can be said looking at Fig. 8.9 for $^{298}_{114}X$, except that before the second minimum lying ≈ 4 MeV higher that the ground state, the energy gain due to different p–n deformations is almost not present.

These results can indicate that rearrangement effects of the nuclear structure along the fission path leads to an increase of the difference between neutron and proton deformations with the proton deformations becoming significantly larger than the neutron ones beyond the fission isomeric state.

For smaller nuclear deformations, i.e. before the second minimum the lowering of the total energy due to different p–n deformations is on the average practically the same for all these 8 elements and oscillates about 0.3 MeV being peaked slightly before the first barrier maximum, At the maximum itself, however, the effect seems to die out. This can be explained by the fact that the total (shell + pairing) correction itself is almost negligible at the first saddle what is well visible for ^{240}Pu in Fig. 8.1 and, clearly, cannot bring about a sizable effect. As a consequence, the peak of the first barrier is mainly due to the LD energy.

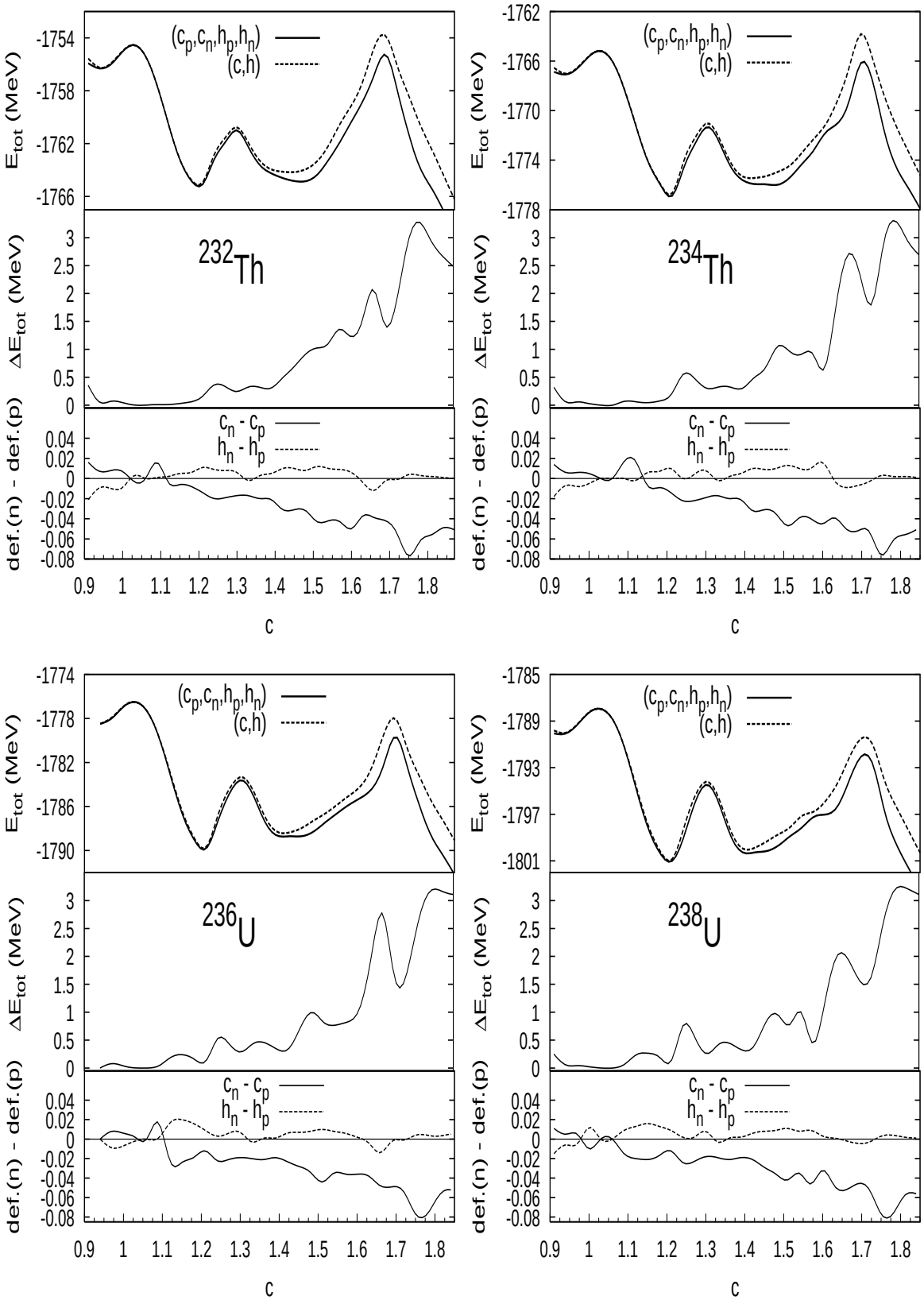

Figure 8.8: Total fission barriers with the effect of different proton–neutron deformations for the actinide nuclei: ^{232}Th, ^{234}Th, ^{236}U, ^{238}U

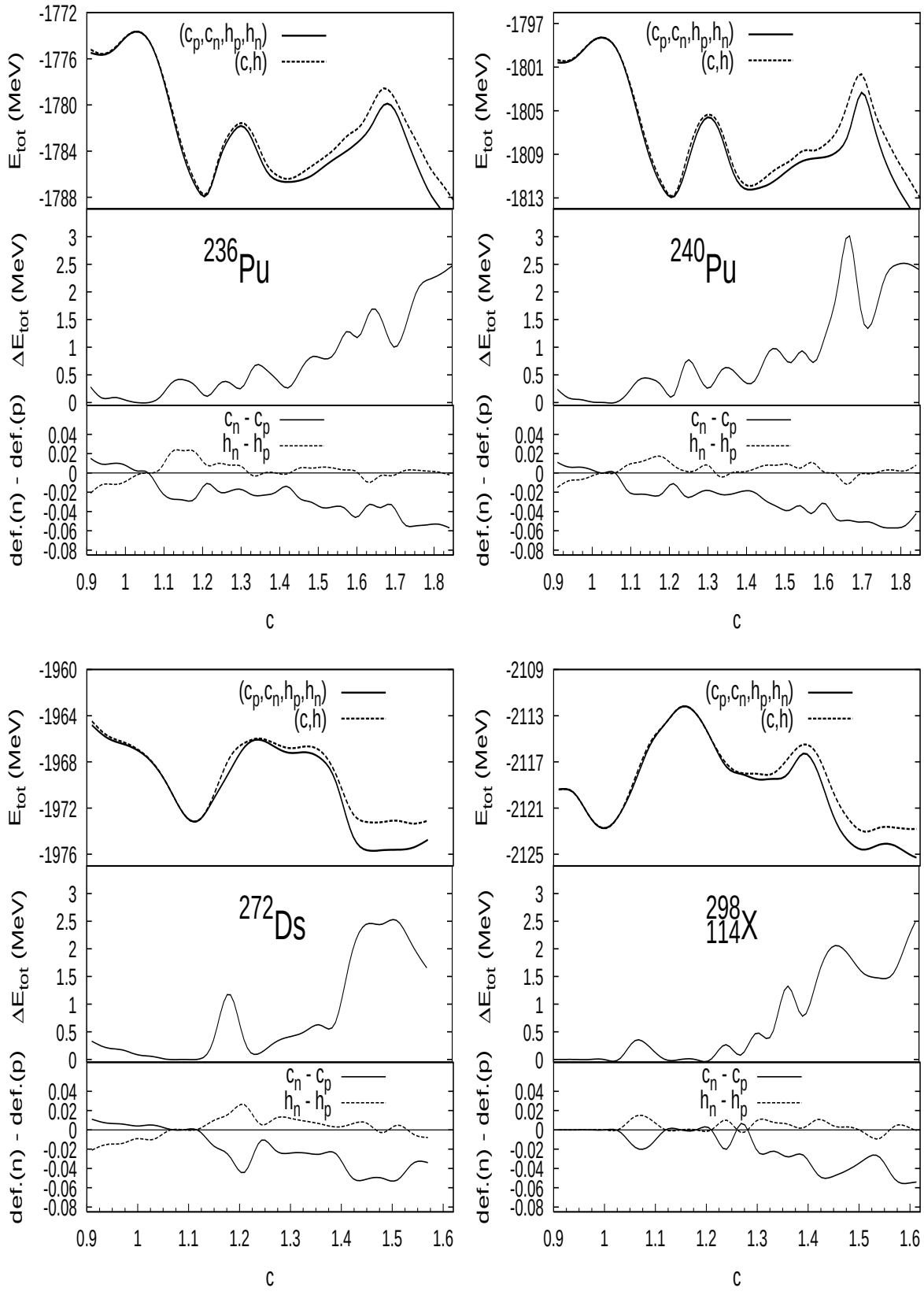

Figure 8.9: Same study as in Fig. 8.8 but for ^{236}Pu, ^{240}Pu and two super–heavy nuclei ^{272}Ds and $^{298}_{114}$X

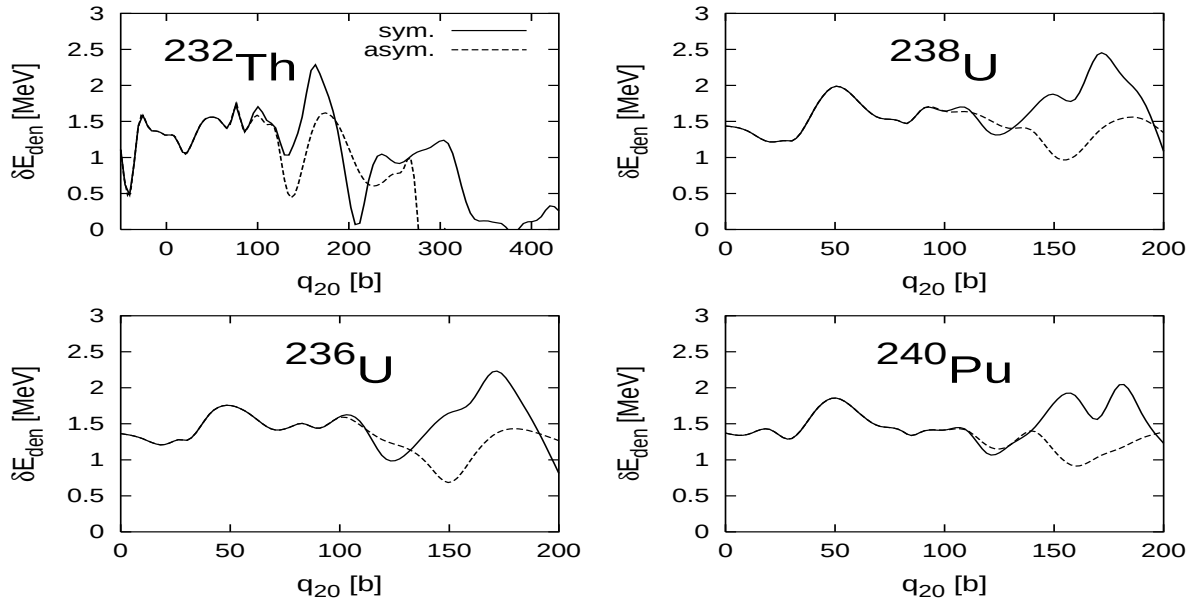

Figure 8.10: Differences between the fission barriers obtained with and without the condition of equal proton and neutron deformations in the HFB procedure with the Gogny effective interaction for ^{232}Th, ^{236}U, ^{238}U, ^{240}Pu. Dashed line describes the fission barrier with left–right mass asymmetry included whereas the solid one corresponds to the reflection–symmetric case. Figure is taken from Ref. [35]

Collecting all previous conclusions we can say clearly that the proton and neutron density distributions of fissioning nuclei are far from being equal. The relative difference between them often exceeds 10% particularly behind the second saddle. This also means that the thickness of the neutron skin does not remain constant with the elongation of the fissioning nucleus. The effect of these deformation differences on the nuclear binding energies is found to be approximately 0.5 MeV.

Nuclear masses are not strongly affected by the examined effect, but the estimates of the decay and fission lifetimes of heavy and super–heavy nuclei can certainly be substantially improved in this way.

The above presented results confirm those obtained in Ref. [35] with the use of the selfconsistent HFB method and the effective interaction of the Gogny type. The quantitive, energetical effect of different proton–neutron deformations studied within the macroscopic–microscopic framework is, however, not as spectacular as the one obtained through the HFB procedure. We suppose that the effect would be more dramatic when the octupole and nonaxial deformations ($\alpha \neq 0$, $\eta \neq 0$) are additionally included in our investigations. This, in principle, is not as conceptually complicated as numerically time–consuming. Certainly, the HF or HFB selfconsistent methods give the nuclei much more flexibility with respect to a possible rearrangement of their density structure than the commonly used macroscopic–microscopic methods. Usually, the only constraint imposed on the selfconsistent HF or HFB densities concerns the

mass quadrupole moment while the nucleus deforms along its way to fission. In the case of the traditional Strutinsky method nuclear density distribution is imposed at the beginning in the form of a phenomenological function with an in advance fixed number of degrees of freedom to be varied as e.g. the average radius, surface diffuseness, etc. (see section 2.4). In our study we used the Yukawa–folding average energy expression (6.93), where the uniform density distribution was inserted as the folding function. This kind of distribution does not allow **at all** for any flexibility in the rearrangement of the liquid drop structure with deformation but the magnitude of the central density ρ_0 in eq. (2.19). If concerned the microscopic quantal corrections, the field of possible improvements is rather constrained by the manners of determining the shell and pairing corrections themselves. As we remember, the Strutinsky as well as the BCS approach consist in some kind of smoothing out the single–particle proton and neutron spectra and that is why both these methods are not very sensitive to the details of the single–particle potential where these spectra come from. Besides, there exists also the numerical problem of the accuracy of approximating the microscopic energy values on the given deformation grid. This, however, can be efficiently controlled on the average but it is impossible to eliminate its local, sometimes quite substantial deviations. For such subtle effects like the ones discussed here, this problem is not without importance. To approximate the energy between the mesh points of the deformation grid we used a new method based on a Gauss–Hermite washing out of the discrete structure of the mesh, developed recently by K. Pomorski and presented briefly in Appendix in one–dimensional case.

Chapter 9

Nonaxial and mass–asymmetric fission barriers

The last section of this work will be devoted to the fission barriers obtained through the macroscopic–microscopic approach using the modified Funny–Hills parameters $\{c, h, \alpha, \eta\}$ to describe the shape of fissioning nucleus.

In the previous chapter (chapter 8) we gave an introduction to this problem considering the fission barriers in a two dimensional deformation space, with $\{c, h\}$ being the predominant shape coordinates for the nuclear fission problem. The other two parameters $\{\alpha, \eta\}$ respectively describe left–right asymmetric shapes and thus allowing for unequal masses of the fission fragments and giving up the restriction to axially symmetric shapes. Recall, however, that in our approach both fragments are assumed to have exactly the same non–axiality, i.e. the parameter η does not depend explicitly on the $z-$coordinate which determines the direction of nuclear elongation in a cylindrical coordinate system.

It is a well known fact that practically for almost all investigated actinide nuclei from ^{230}Th to ^{250}Cf and the heavier nuclei, ^{268}Rf–$^{278}_{116}$X their saddle points exhibit nonaxial shapes as well as octupole deformations. Of course, as we will convince ourselves later, the importance of these two additional deformation degrees of freedom is not the same for all discussed elements. This fact is not a surprise when we realize that the shell structure which is responsible for the non–spherical shapes of nuclei in the equilibrium changes remarkably from one nucleus to another. This effect is even more pronounced in super–heavy nuclei.

In order to reproduce the fission barrier one has to know, as previously mentioned, at least its stationary points, i.e. the ground state minimum and the the first saddle and, if these exist, the second isomeric minimum and the second saddle. These are the points which the fission path of each fissioning nucleus must pass through. Finding these energy minima in the multidimensional deformation space does not cause too many technical troubles but it are the saddle points which correspond to the actual

peak of the fission barrier, which require much more care.

9.1 A procedure for searching saddle points

There exist a couple of ways of searching a multidimensional deformation space for the saddle point. We would like to sketch here three often applied methods.

For the first approach, one requires to find two primary shape coordinates which would determine the average fission path. For the shape definition in the form of the multipole expansion (eq. 6.47), β_2 and β_4 are good candidates, because the first describes the nuclear elongation while the second, being *orthogonal* to β_2, modifies the nuclear surface in the *perpendicular direction* allowing for *diamond–like* or *necked* shapes. For the Funny–Hills–like parametrizations discussed in section 6.2 the equivalent two parameters would be c and h.

Having established two dominant deformation parameters, one minimizes the total energy for each such pair of points $\{\beta_2, \beta_4\}$ or $\{c, h\}$ with respect to the additional degrees of freedom as e.g. β_3, α_{22} or, in the case of Funny–Hills type parametrization, α, η, which describe the octupole and nonaxial deformations respectively. This procedure allows us to reduce the dimensionality of the problem and look for the saddle points only in the $\{\beta_2, \beta_4\}$ or $\{c, h\}$ spaces. This simplifies the treatment substantially but we do not have any guarantee that the resulting saddle corresponds, in fact, to the real maximum of the fission barrier. During our investigations we frequently faced the problem of local minima trying to minimize the total energy over α, η for a given point $\{c, h\}$ (see Fig. 9.1). As we see in this figure for certain pairs $\{c, h\}$ we could identify two, or sometimes even more energy minima corresponding to physically dissimilar shapes for which the total energy differs by less than 1 MeV. Such minor differences could be the results of the numerical uncertainty of the macroscopic–microscopic method itself, so that the systematic search for the lowest minimum could lead to a kind of *shape phase transitions*.

Keeping in mind the above disadvantages we decide to use another method to search the full four–dimensional space $\{c, h, \alpha, \eta\}$ finding all existing saddle points in the $\{c, h\}-$subspace and chose as the appropriate the lowest ones, which are located between the main minima. Technically, we solved this problem in the following way:

On the given mesh in the four–dimensional deformation space $\{c, h, \alpha, \eta\}$ we look for the points for which the length of the gradient vector

$$|\vec{\nabla} V_{pot}| = \sqrt{\left(\frac{\partial V_{pot}}{\partial c}\right)^2 + \left(\frac{\partial V_{pot}}{\partial h}\right)^2 + \left(\frac{\partial V_{pot}}{\partial \alpha}\right)^2 + \left(\frac{\partial V_{pot}}{\partial \eta}\right)^2} \tag{9.1}$$

is lower than for the $3^4 - 1$ neighbouring points. After identifying such a point we search the energy in its neighbourhood to localize the point for which the expression

(9.1) is equal to zero with the desired numerical accuracy. In the next step we use basic mathematical analysis rules to determine whether the found point, in the two–dimensional subspace $\{c, h\}$ of the dominant deformation parameters, is a minimum, a maximum or a saddle point. For the cases where the two first possibilities can be excluded, we check the properties of the point which is suspected to be a physically relevant saddle point. Recall that in the $c-$direction there has to be a local maximum which in the $h-$direction is a local minimum. This means that the determinant of the second derivatives matrix $\mathcal{H}$

$$det\,\mathcal{H} = \begin{vmatrix} \frac{\partial^2 V_{pot}}{\partial c^2}, & \frac{\partial^2 V_{pot}}{\partial c \partial h} \\ \\ \frac{\partial^2 V_{pot}}{\partial h \partial c}, & \frac{\partial^2 V_{pot}}{\partial h^2} \end{vmatrix} \tag{9.2}$$

in this point must be negative and, in addition, the conditions $\frac{\partial^2 V_{pot}}{\partial c^2} < 0$ and $\frac{\partial^2 V_{pot}}{\partial h^2} > 0$ must be simultaneously fulfilled. Such a procedure finds usually many saddle points which satisfy the above conditions. One then has to decide which of them correspond to the fission barrier.

Finally, the third method of distinguishing a saddle point which we have mentioned above is the *"test of water"* [94, 95]. After finding the energy minimum corresponding to the ground state we then progressively fill it up with "water" determining the first point in the fission valley which is getting "wet". By adjusting carefully the increase of the water level one is able unambiguously identify the location and the energy of the true saddle.

9.2 Fission barrier heights

Using the second of the above mentioned method of determining the physically relevant saddles we performed the calculations for 18 chosen actinide as well as for 47 super–heavy nuclei which have not yet been investigated experimentally with respect to their fission properties.

In Fig. 9.2 we show the heights of the fission barriers for these actinide nuclei calculated within the macroscopic–microscopic framework, as the difference between the total ground–state energy and the energy of the inner saddle point, found in the above described way. In the same figure we also plotted the difference of the experimental and theoretical barriers for these nuclei. Because of a lack of experimental barriers for nuclei heavier then ^{252}Cf, we give their theoretical estimates obtained in the same macroscopic–microscopic model separately in Fig. 9.3.

Looking at Fig. 9.2 we observe that our macroscopic–microscopic approach with the LSD macroscopic energy, the Strutinsky shell correction and the pairing treatment in terms of the BCS method is able to reproduce the fission barrier heights on the

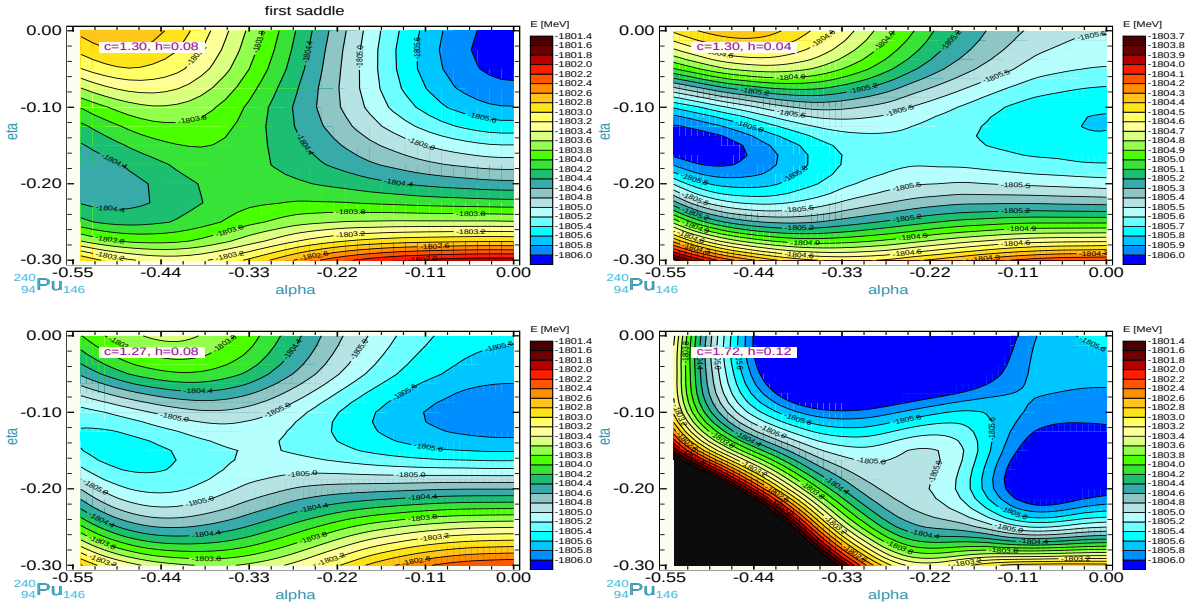

Figure 9.1: $\{\alpha, \eta\}-$energy landscapes for three different values of elongation (c) and neck (h) parameters

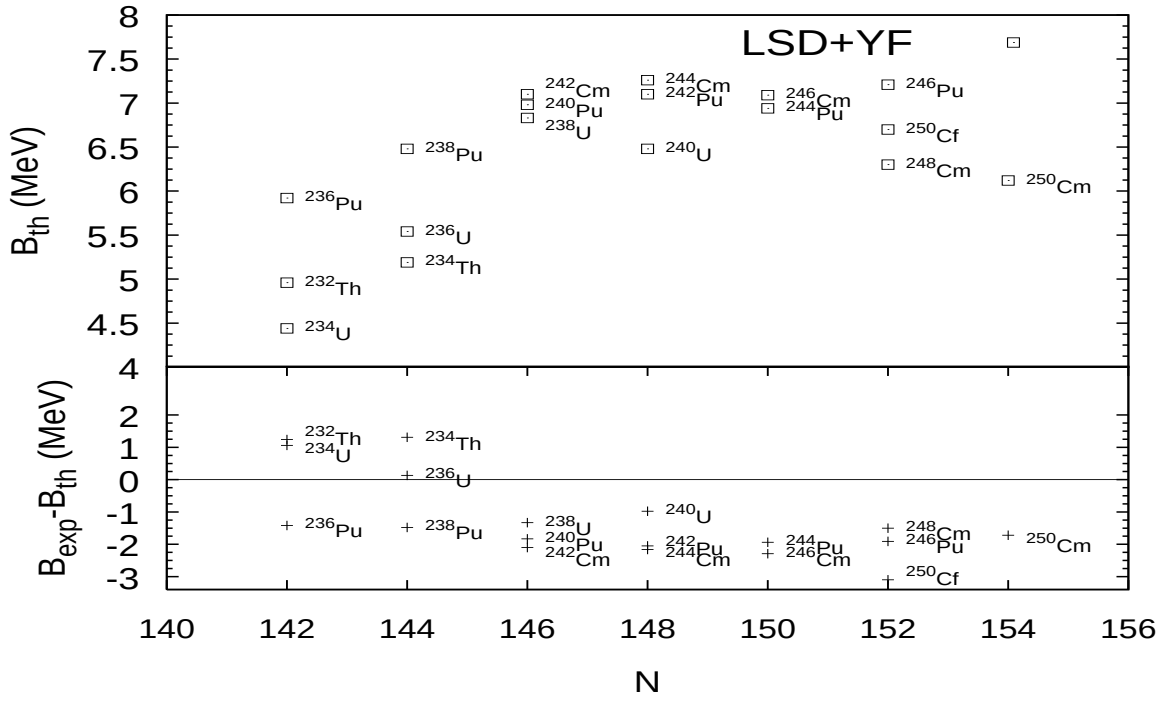

Figure 9.2: Theoretical fission–barrier heights (B_{th}) for actinide nuclei from ^{232}Th to ^{250}Cf as function of the neutron number obtained with the macroscopic–microscopic model of section 7.2.1 (upper part) and difference between experimental [96] and theoretical barrier heights (lower part), (see also Tab. 1A in Appendix)

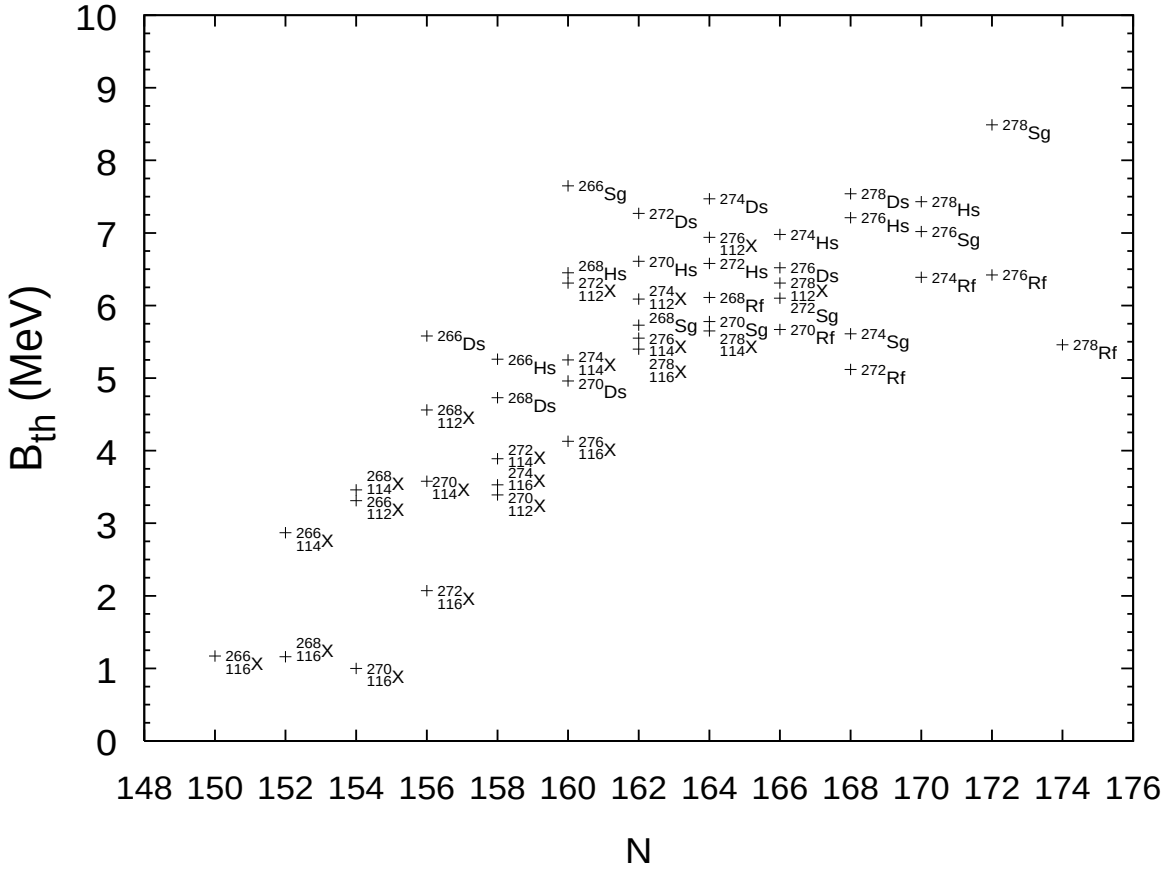

Figure 9.3: Study of fission barrier heights similar as in Fig. 9.2 for heavy and super–heavy elements ^{268}Rf–$^{278}_{116}X$, (see Tab. 4A in Appendix)

average within 2 MeV. This accuracy is almost of the same quality as the theoretical barrier–heights estimations by Möller and coworkers in Ref. [96], keeping in mind that there, the parameters of the macroscopic FRLDM 2002 formula were re–adjusted to reproduce, in the best possible way, the experimental values of these barriers. Note also that the parameters of the LSD model were adjusted only to the in 2002 experimentally known nuclear masses and evidently its very good performance for the problem of fission barriers, proves that the physics is contained in the appropriate way with the use of a minimal number of adjustable parameters. Since we use the same mean–field potential and Strutinsky shell correction method as in Ref. [96] one element which can change significantly the fission–barrier heights is the pairing treatment. It is known that in different pairing approaches, as e.g. the pure BCS or the Lipkin–Nogami methods (applied in [96]), this correction can differ around the region of the ground state by about 1 MeV [97]. This uncertainty, by the definition, changes directly the height of the fission barrier. It is clear that the BCS+*uniform gap method* used in our studies is too elementary to be efficiently applied in the detailed descriptions of the nuclear microscopic properties. The results presented here, at this stage, should

be rather treated as some preliminary estimations. A possible improvement of our results can also be also obtained by permitting a $z-$dependence of the non–axiality parameter η of eq. (6.36) in the used extended version of the Funny–Hills nuclear shape parametrization with gaussian–like *neck*.

As we have demonstrated in section 8.4, a substantial reduction of the fission barrier, exceeding often 2 MeV, can be reached by taking into consideration the effect of different proton–neutron deformations. Please recall that the corresponding energy lowering is most pronounced beyond the second energy minimum for most often discussed actinide and super–heavy nuclei.

Since the total nuclear energy is determined with the use of the Strutinsky model which requires the knowledge of the single–particle spectra in each deformation point, the density of the deformation mesh used in the calculations plays also a crucial role. We re–scaled the single–particle states for the given actinide or super–heavy nucleus from our knowledge of neighbouring nuclei, using a relation which is strictly fulfilled for the eigensolutions of the harmonic–oscillator potential:

$$e_n = e_n^{(ctr)} \left(\frac{A^{(ctr)}}{A} \right)^{1/3}, \tag{9.3}$$

where e_n and $e_n^{(ctr)}$ are respectively the n^{th} single–particle state of the given and the neighbouring (central) nucleus of mass A and $A^{(ctr)}$. Comparing the total energies of the first saddles of the chosen actinides listed in Tabs. 1A and 2A in Appendix, calculated on the basis of the re–scaled single–particle spectra of ^{240}Pu and ^{250}Cm respectively, we can see that the largest energy difference of about 1.2 MeV occurs for ^{246}Pu while for ^{242}Cm there is practically no such difference. The single–particle spectra for super–heavy nuclei considered here are obtained by the same rescaling procedure of eq. (9.3) from ^{272}Ds.

We performed the search of the ground–state energies and the inner saddle points for the selected actinide nuclei on two different meshes in the $\{c, h, \alpha, \eta\}$ space, (Δ denotes the step in a given direction of the deformation grid): $\{\Delta c = 0.03, \Delta h = 0.04, \Delta\alpha = 0.03, \Delta\eta = 0.05\}$ and the denser mesh $\{\Delta c = 0.01, \Delta h = 0.01, \Delta\alpha = 0.03, \Delta\eta = 0.05\}$ which are listed in Tabs. 1A, and 2A for the denser mesh and Tab. 3A for the wider mesh.

Comparing the values of both the first minima and first saddles in Tabs. 1A and 3A we observe that their energies may differ by up to 2.3 MeV (as e.g. ^{234}U). If, due to this difference, the ground state (or saddle) is shifted more down in energy then the saddle point (or ground state), the barrier height is then effectively increased (decreased). It is clear that a denser mesh will give us more accurate results within the framework of our approach, but we, of course, have no garentee that the agreement with the experimental barriers will necessarily improve in this way.

Let us now compare the absolute energy values of the nonaxial and mass asymmetric, ($\alpha \neq 0, \eta \neq 0$) four–dimensional, inner and outer saddle points with the two–dimensional, axial and left–right symmetric ones ($\alpha = 0, \eta = 0$) obtained through the least–action method of eq. (8.2).

	Inner saddle energy (MeV)			Outer saddle energy (MeV)		
Nucleus	$\alpha = 0,\ \eta = 0$	$\alpha \neq 0,\ \eta \neq 0$	ΔE_I	$\alpha = 0,\ \eta = 0$	$\alpha \neq 0,\ \eta \neq 0$	ΔE_{II}
^{232}Th	-1759.94	-1760.37	-0.43	-1754.21	-1760.40	-6.19
^{234}Th	-1771.01	-1771.30	-0.29	-1765.16	-1766.80	-1.64
^{234}U	-1772.32	-1772.70	-0.38	-1765.16	-1772.07	-6.91
^{236}U	-1783.56	-1783.75	-0.19	-1778.29	-1782.16	-3.87
^{238}U	-1793.99	-1793.99	0.0	-1791.05	-1796.59	-5.54
^{240}U	-1804.99	-1805.30	-0.31	-1799.60	-1806.56	-6.96
^{236}Pu	-1781.03	-1781.25	-0.22	-1778.65	-1781.89	-3.24
^{238}Pu	-1793.70	-1793.84	-0.14	-1790.77	-1793.26	-2.49
^{240}Pu	-1805.34	-1805.69	-0.35	-1802.87	-1805.09	-2.22
^{242}Pu	-1816.84	-1817.35	-0.51	-1813.25	-1818.08	-4.83
^{244}Pu	-1827.84	-1828.65	-0.81	-1824.44	-1827.00	-2.56
^{246}Pu	-1838.45	-1839.54	-1.09	-1835.10	-1839.31	-4.21
^{242}Cm	-1814.93	-1815.59	-0.66	-1813.93	-1815.46	-1.53
^{244}Cm	-1827.09	-1827.89	-0.80	-1825.95	-1830.67	-4.72
^{246}Cm	-1838.87	-1840.12	-1.25	-1837.25	-1841.98	-4.73
^{248}Cm	-1850.53	-1852.30	-1.77	-1848.58	-1851.85	-3.27
^{250}Cm	-1861.56	-1862.90	-1.34	-1859.71	-1862.64	-2.93
^{250}Cf	-1860.52	-1862.46	-1.94	-1861.39	-1862.84	-1.45

Tab. 9.1 Influence of the non–axiality and mass asymmetry on the energy of the inner and outer fission–barrier maxima for investigated actinide nuclei (see also Ref. [98]). Columns 2 and 5 correspond to the energies determined through eq. (8.2) while in columns 3 and 6 the energies of the saddles obtained in full, four–dimensional deformation space are listed (see also Tabs. 1A and 3A). Columns 4 and 7 corresponds to the difference between the saddle energies without and with the non–axiality and mass–asymmetry.

As seen in Tab. 9.1 the reduction of both the barrier heights (columns 4 and 7) due to the inclusion of two additional degrees of deformational freedom α, η depends, as we mentioned in the introduction to this chapter, on the considered nucleus (note that the main barrier minima are axially and left–right symmetric). Concerning the first barrier ($c \approx 1.3$), the weakest barrier lowering (up to 0.6 MeV) is observed for the lighter actinides ($A = 234 - 240$) whereas for the heavier ones ($A = 242 - 250$) this

effect is much more pronounced reaching up to $0.7 - 2\,\mathrm{MeV}$. A much more remarkable barrier lowering ($1.4 - 7\,\mathrm{MeV}$) is observed for the outer–barrier ($c \approx 1.6$) of the same actinide nuclei.

9.3 Numerical accuracy of the results

Studying the energy values of the Tables 1A to 3A we can immediately notice that using a denser deformation grid we obtain, in a few cases, the ground–state energy shifted up (see Tab. 1A, ^{234}Th, ^{244}Pu). This effect, however at the first sight peculiar, indicates that the grid with steps $\{\Delta c = 0.03, \Delta h = 0.04\}$ is, with no doubt, not sufficiently dense to avoid the substantial errors coming from the numerical interpolation of the energy values.

As we already mentioned, the problem of finding the physically important saddle points causes a lot of problems since we are, for numerical reasons, restricted to do this on a discrete mesh. If the deformation grid is too scarce we can often loose a precious details of the energy landscape. On the other hand, a two times denser mesh in all of the four direction implies a 16 times longer computation time. Consequently, one has always to find a compromise between the accuracy and the computation time, in order to generate the results in an accessible time–scale and still retain the essential physical details with a reasonable accuracy.

We should also not neglect the fact that the analytical approximation of the energy in a multidimensional deformation space (see Appendix A.4) can introduce some spurious energy–landscape structures like spurious minima, maxima and saddles. Using the derivative method described previously which acts, by definition, only in the closest vicinity of a given grid point, makes such artificial structures extremely difficult to identify. In order to minimize the risk of producing these kind of undesired stationary points in the energy landscape we enlarged the order of the correction polynomial and simultaneously, the value of the smearing parameter γ in the Strutinsky–like approximation method presented in Appendix A.4. We used at the same time as the approximation base 7^4, instead of, usually sufficient 5^4 neighbouring mesh points (7 instead of 5 in each direction).

Chapter 10

Summary

Some essential ingredients for the theoretical description of fusion and fission dynamics are discussed in this work. For the fusion process, the nucleon–nucleon collision potential, elaborated here on the basis of the semiclassical Extended Thomas–Fermi approach is essential, whereas, for the fission process, the total potential–energy landscape in a multidimensional deformation space plays a central role. This potential–energy landscape is obtained using an extension of the so–called "Funny–Hills" shape parametrization which, beside the deformation parameters: c, h, α, describing respectively the nuclear elongation, neck degree of freedom and left–right mass asymmetry, contains an additional parameter responsible for the non–axiality of the nuclear shape.

We have, in particular, studied the effect of the differences between the proton and neutron density distributions on both these processes. In the case of the nuclear fusion potential, this was realized by different proton and neutron density radii of target and projectile obtained by means of a HF–type variational calculation with the semiclassical Skyrme ETF energy–density functional. Our theoretical fusion barriers, which serve with the use of the Langevin formalism as an input to the dynamical calculations of the fusion cross sections are quite close to the experimental barriers but are systematically overestimating these by a few MeV, in particular in deformed systems whereas we have restricted our study to spherical shapes for target and projectile. The deformation of the colliding nuclei which could be included in future investigations, e.g. by means of the local curvature approximation would reduce the fusion–barrier heights by a couple of MeV as compared to the corresponding spherical system, mainly due to the decrease of the Coulomb barrier. One should also not forget that, in fact, the nuclear deformation, from the point of view of quantum mechanics, is a dynamical process, in the sense, that the nuclear surface vibrates around some equilibrium shape. The amplitude of these collective vibrations depends on the total–energy stiffness in the vicinity of the ground state and the appropriate inertia parameters. Due to the mentioned effect the ETF estimates of the fusion barriers are expected to be close to the experimental values.

We have also made sure, that the small variations of the proton or neutron radii of colliding spherical nuclei generated by the use of different Skyrme effective forces

(ensuring some realistic predictions of the nuclear binding energies) can influence the fusion barrier heights only within $1-2\,\mathrm{MeV}$, out of several hundred, i.e. the order of disagreement between the ETF values with the corresponding experimental data.

Using the ETF model, we have enriched the usually used macroscopic–energy expression, of e.g. the liquid drop or droplet–type, by an additional term which describes the change of the nuclear binding energy due to different proton and neutron deformations and effective radii. As a consequence of these additional degrees of freedom, we can observe a reduction of the fission–barrier heights in a two dimensional deformation space (elongation and neck degree of freedom). For all investigated actinide and super–heavy elements, this reduction of the barrier height is of the order of 0.5 MeV with quite sizable fluctuations, of more than 1 MeV in the region of the first barrier.

The next step was to investigate the influence of additional deformation parameters on the potential–energy landscapes, calculated in our macroscopic–microscopic approach, that is, we have used the full four–dimensional description of the nuclear fission barriers with broken axial and reflection symmetries. Our four–dimensional calculation of the barrier heights within the Lublin–Strasbourg Drop (LSD) and the Yukawa–folding model reproduces the experimental data on the average and is in good agreement with the latest, theoretical estimates, obtained recently by P. Möller and co–workers within the framework of a similar, but more involved multidimensional approach.

We have shown that the inclusion of the mass–asymmetry and non–axiality can reduce the energy of the inner saddle point in the actinide nuclei by $1-2\,\mathrm{MeV}$ (mainly non–axiality) whereas the second saddle can be lowered by as much as $7\,\mathrm{MeV}$ (mainly mass asymmetry). It should be noticed, that the ground state and the isomeric minima are essentially not affected by these additional degrees of freedom. Considering the effect of different proton–neutron deformations discussed above in the four dimensional deformation space $\{c_p, h_p, c_n, h_n\}$ does, of course, not totally describe the complexity of the problem. Its influence on the fission barriers, is, however, as demonstrated above in the two–dimensional case, far from being negligible. We should also take into consideration the fact that the macroscopic energy obtained in our approach by a simple folding procedure starting from sharp–edge densities obviously overestimates the *stiffness* of the binding energy as function of the relative change of the neutron versus proton deformations. The inclusion of the energy contribution coming from the nuclear surface diffuseness as well as the left-right mass asymmetry and non–axiality should be the topic of future investigations.

The results discussed in this work mostly refer to static fission barriers. It is, however, clear that they can be used as an ideal starting point for a more realistic, dynamical treatment of the nuclear fission process based on the Langevin equation. Work in this direction is currently on the way.

Appendix A

Appendix

A.0.1 Leptodermous expansion

In the case of spherical nuclei the leptodermous expansion of the energy functional around the diffused thin nuclear surface of thickness a, where $a/R \ll 1$ can be written as follows:

$$\begin{aligned} E &= b_{vol}\, A + \int\limits_{V} (\eta - b_{vol}\, \rho)\, d^3r = \\ &= b_{vol}\, A + \int\limits_{\Omega} R^2 d\Omega \int\limits_{0}^{\infty} (\eta - b_{vol}\, \rho) \frac{r^2}{R^2}\, dr \end{aligned} \tag{A.1}$$

where R usually represented as $R = r_0 A^{1/3}$ is the radius of the spherical surface, ρ is the one–body density of the nuclear matter in nucleus, and η is the energy density given as

$$\begin{aligned} \rho &= A \int\int\int ... \int \psi^\star \psi d\tau_2 ... d\tau_A, \\ \eta &= \int\int ... \int \psi^\star \hat{H} d\tau_2 ... d\tau_A, \end{aligned} \tag{A.2}$$

where $\hat{H}$ is a many–body nuclear Hamiltonian, while ψ the ground–state wave function of the nucleus. Exploiting of the identity

$$\frac{r^2}{R^2} = 1 + \frac{2}{R}(r - R) + \frac{1}{R^2}(r - R)^2 \tag{A.3}$$

one can rewrite the remaining surface–related integral and transform the energy expression as follows:

$$\begin{aligned} E &= b_{vol}\, A \\ &+ \int\limits_{S} R^2 d\Omega \int\limits_{0}^{\infty} (\eta - b_{vol}\, \rho) dr \end{aligned} \tag{A.4}$$

$$+ \int_S 2R d\Omega \int_0^\infty (\eta - b_{vol}\,\rho)(r-R)dr \tag{A.5}$$

$$+ \int_S d\Omega \int_0^\infty (\eta - b_{vol}\,\rho)(r-R)^2 dr \tag{A.6}$$

Above three expressions contain terms proportional to R^2, R^1, and R^0, respectively, thus at the same time, proportional to $A^{2/3}$, $A^{1/3}$, and A^0. In the present context, they should be interpreted as representing the surface, curvature, and Gauss–curvature contributions, respectively. The nuclear part of the total energy of a spherical nucleus can thus be written down as

$$E = b_{vol}\,A + 4\pi R^2\,I_0 + 8\pi R\,(I_1 - I_0\,R) + 4\pi\,(I_2 - 2RI_1 + R^2 I_0) \tag{A.7}$$

where all the terms except for the first one are proportional respectively to $\sim b_{surf}A^{2/3}$, $\sim b_{cur}A^{1/3}$ and $\sim b_{curG}A^0$. Quantities I_0, I_1, I_2 are given as follows

$$\begin{aligned} I_0 &= \int_0^\infty (\eta - b_{vol}\,\rho)dr \\ I_1 &= \int_0^\infty (\eta - b_{vol}\,\rho)r dr \\ I_2 &= \int_0^\infty (\eta - b_{vol}\,\rho)r^2 dr. \end{aligned} \tag{A.8}$$

A.1 Derivation of the ETF approach

A.1.1 Wigner-Kirkwood expansion

In the following paragraph we want to sketch the semiclassical $\hbar-$expansion developed by Wigner [30] and Kirkwood [31] which provides a convenient tool to derive the ETF functionals $\tau[\rho]$ and $J[\rho]$ which we are interested in. We will presently restrict ourselves to the case of N nucleons (one kind only) in a given local one–body potential $V(\vec{r})$ [18]. Let φ_ν and ε_ν be the eigenfunctions and eigenvalues of the corresponding one–body Schrödinger equation:

$$\hat{H}\varphi_\nu = [\hat{T} + V(\vec{r})]\phi_\nu = \varepsilon_\nu\,\varphi_\nu. \tag{A.9}$$

The $N-$body system in this local potential is described by the one–body density matrix

$$\rho(\vec{r},\vec{r}\,') \;=\; \sum_{j=1}^{N} \varphi_j^*(\vec{r}\,')\,\varphi_j(\vec{r}). \tag{A.10}$$

Defining the Bloch-density operator

$$\hat{C}_\beta = e^{-\beta\,\hat{\mathrm{H}}} \tag{A.11}$$

we can define, in turn, the Bloch–density matrix

$$C(\vec{r},\vec{r}';\beta) = <\vec{r}\,|\,\hat{C}_\beta\,|\,\vec{r}'> = \sum_j \varphi_j(\vec{r})\;\varphi_j^*(\vec{r}')\,e^{-\beta\,\varepsilon_j}, \tag{A.12}$$

which satisfies the following equation:

$$\left[\frac{\partial}{\partial\beta} + \hat{\mathcal{H}}\right] C(\vec{r},\vec{r}';\beta) = 0. \tag{A.13}$$

The sum in eq. (A.12) goes over the complete spectrum. From C we obtain by an inverse Laplace transform the one–body density matrix

$$\rho(\vec{r},\vec{r}') = \mathcal{L}^{-1}_{\beta\to\lambda}\;\left[\frac{1}{\beta}\,C(\vec{r},\vec{r}';\beta)\right] = \frac{1}{2\pi i}\int\limits_{c-i\infty}^{c+i\infty} e^{\beta\lambda}\,\frac{C(\vec{r},\vec{r}';\beta)}{\beta}\,d\beta \tag{A.14}$$

$$= \sum_j \varphi_j(\vec{r})\;\varphi_j^*(\vec{r}')\,\Theta(\lambda-\varepsilon_j)$$

from which, in turn, the local densities $\rho(\vec{r})$ and $\tau(\vec{r})$ can be determined

$$\rho(\vec{r}) = \sum_{\nu=1}^{N} |\phi_\nu(\vec{r})|^2 = \rho(\vec{r},\vec{r})\Big|_{r=r'}$$

$$\tau(\vec{r}) = \sum_{\nu=1}^{N} |\nabla\phi_\nu(\vec{r})|^2 = \nabla_r\cdot\nabla_{r'}\,\rho(\vec{r},\vec{r})\Big|_{r=r'}. \tag{A.15}$$

In equation (A.14) λ is the Fermi energy which has to be fixed in such a way that by the particle number conservation condition

$$\int \rho(\vec{r})\,d^3r = N. \tag{A.16}$$

is fulfilled. One can also define the partition function

$$Z(\beta) = \mathrm{Tr}\left(\hat{C}_\beta\right) = \int C(\vec{r},\vec{r};\beta)\;d^3r = \sum_j^N\; e^{-\beta\,\varepsilon_j} \tag{A.17}$$

which allows to calculate the single–particle level density

$$g(\varepsilon) = \mathcal{L}^{-1}_{\beta\to\varepsilon}\left[Z(\beta)\right] = \sum_j^N \delta(\varepsilon-\varepsilon_j), \tag{A.18}$$

the number of particles

$$N = \int\limits_0^\lambda g(\varepsilon)\,d\varepsilon = \mathcal{L}^{-1}_{\beta\to\lambda}\left[\frac{Z(\beta)}{\beta}\right], \tag{A.19}$$

and the total single–particle energy of the system

$$E_{s.p.} = \sum_{n=1}^{N}\varepsilon_n = \int\limits_0^\lambda \varepsilon\,g(\varepsilon)\,d\varepsilon = \lambda N - \int\limits_0^\lambda\int\limits_0^\varepsilon g(\varepsilon')\,d\varepsilon' = \lambda N - \mathcal{L}^{-1}_{\beta\to\lambda}\left[\frac{Z(\beta)}{\beta^2}\right]. \tag{A.20}$$

The idea of Wigner and Kirkwood was to expand the overall density matrix $C(\vec{r},\vec{r}';\beta)$ in a series expansion around its value obtained in the Thomas-Fermi approximation where $\hbar$ is the order parameter

$$C(\vec{r},\vec{r}';\beta) = C_{TF}(\vec{r},\vec{r}';\beta)(1+\hbar\chi_1+\hbar^2\chi_2+\ldots) \tag{A.21}$$

and where C_{TF} is given by

$$C_{TF}(\vec{r},\vec{r}';\beta) \;=\; \frac{1}{4\,\pi^{3/2}\,\beta^{3/2}}\left(\frac{2m}{\hbar^2}\right)^{3/2}\; e^{-m/2\hbar^2\beta\,(\vec{r}-\vec{r}\,')^2-\beta\,V(\vec{R}\,)} \tag{A.22}$$

with

$$\begin{aligned}\vec{R} &= \frac{\vec{r}+\vec{r}\,'}{2},\\ \vec{s} &= \vec{r}-\vec{r}\,'.\end{aligned} \tag{A.23}$$

The χ_n are functions of $\vec{r}$, $\vec{r}\,'$ and β and contain combinations of n gradients acting on $V(\vec{r})$. There exists the recursion relation to obtain the χ_n successively [99]. Using the inverse Laplace transform of eq. (A.22) we obtain the Thomas–Fermi density matrix

$$\rho_{TF}(\vec{r},\vec{r}\,') \;=\; \rho_{TF}(\vec{R}\,)\;\frac{3}{k_F(\vec{R}\,)\,s}\;j_1(k_F(\vec{R}\,)\,s) \tag{A.24}$$

with the local TF density

$$\rho_{_{TF}}(\vec{r}\,) = \frac{1}{3\,\pi^2}\left(\frac{2m}{\hbar^2}\right)^{3/2}\Big[\lambda-V(\vec{r}\,)\Big]^{3/2}\Theta\left[\lambda-V(\vec{r}\,)\right]. \tag{A.25}$$

A.1.2 Beyond the Thomas–Fermi approximation

In order to calculate $Z(\beta)$ given in general by eq. (A.17) one has to determine the trace of Bloch-density matrix in the basis of the single–particle wave functions

$$\mathrm{Tr}\left(\hat{C}_\beta\right) = \frac{2}{(2\pi\hbar)^3}\iint e^{-i\vec{r}\cdot\vec{p}/\hbar}\,e^{-\beta\hat{\mathcal{H}}}\,e^{i\vec{r}\cdot\vec{p}/\hbar}\,d^3r\,d^3p, \tag{A.26}$$

where $\vec{r}$ and $\vec{p}$ are the classical quantities, but $\hat{\mathcal{H}}$ is an operator with the following properties:

$$\begin{aligned}&e^{-\beta\hat{\mathcal{H}}} \neq e^{-\beta\hat{T}}\,e^{-\beta\hat{V}}\\ &e^{-\beta\hat{\mathcal{H}}}\,e^{i\vec{r}\cdot\vec{p}/\hbar} = e^{-\beta H_{cl}}\,e^{i\vec{r}\cdot\vec{p}/\hbar}\,w(\vec{r},\vec{p};\beta) = u(\vec{r},\vec{p};\beta)\end{aligned} \tag{A.27}$$

The differential equation for $w(\vec{r},\vec{p};\beta)$ can be solved by developing $w(\vec{r},\vec{p};\beta)$ into the series, where $\hbar$ is the order parameter

$$w(\vec{r},\vec{p};\beta) = 1+\hbar\,w_1(\vec{r},\vec{p};\beta)+\hbar^2\,w_2(\vec{r},\vec{p};\beta)+\cdots \tag{A.28}$$

After carrying out the above calculations we finally obtain $Z_{W-K}(\beta)$ and $C_{W-K}(\vec{r},\vec{r}\,';\beta)$ as

$$Z_{W-K}(\beta) = \frac{1}{4\,\pi^{3/2}\,\beta^{3/2}}\left(\frac{2m}{\hbar^2}\right)^{3/2}\int e^{-\beta\,V(\vec{r})}\left\{1-\frac{\beta^2}{12}\,\frac{\hbar^2}{2m}\vec{\nabla}^2 V\right.$$
$$\left.+\frac{\beta^3}{1440}\left(\frac{\hbar^2}{2m}\right)^2\left[-7\vec{\nabla}^4 V+5\beta(\vec{\nabla}^2 V)^2+\beta\vec{\nabla}^2(\vec{\nabla}V)^2\right]+\cdots\right\}d^3r \quad \text{(A.29)}$$

and

$$C_{W-K}(\vec{r},\vec{r}\,';\beta) = \frac{1}{4\pi^{3/2}\,\beta^{3/2}}\left(\frac{2m}{\hbar^2}\right)^{3/2}e^{-\beta\,V(\vec{r})}\left\{1+\frac{\beta^2}{6}\frac{\hbar^2}{2m}\left[\vec{\nabla}^2 V-\frac{\beta}{2}(\vec{\nabla}V)^2\right]\right.$$
$$+\frac{\beta^3}{12}\left(\frac{\hbar^2}{2m}\right)^2\left[\frac{\vec{\nabla}^4 V}{20}+\frac{\beta}{24}\,(\vec{\nabla}^2 V)^2+\frac{\beta}{15}\,\vec{\nabla}V\cdot\vec{\nabla}^3 V+\frac{\beta}{60}\,\vec{\nabla}^2(\vec{\nabla}V)^2\right.$$
$$\left.\left.-\frac{\beta^2}{24}\,(\vec{\nabla}V)^2\vec{\nabla}^2 V-\frac{\beta^2}{40}\,\vec{\nabla}V\cdot\vec{\nabla}(\vec{\nabla}V)^2+\frac{\beta^3}{96}(\vec{\nabla}V)^4\right]+\cdots\right\} \quad \text{(A.30)}$$

which yields the semiclassical development for the semiclassical densities

$$\rho_{\rm sc}(\vec{r}) = \frac{1}{3\,\pi^2}\left(\frac{2m}{\hbar^2}\right)^{3/2}\left\{\Big[\lambda-V(\vec{r})\Big]^{3/2}-\right.$$
$$\left.-\frac{\hbar^2}{16m}\left[\frac{\vec{\nabla}^2 V}{\Big[\lambda-V(\vec{r})\Big]^{1/2}}+\frac{1}{4}\frac{\Big(\vec{\nabla}V\Big)^2}{\Big[\lambda-V(\vec{r})\Big]^{3/2}}\right]+\cdots\right\}\Theta\left[\lambda-V(\vec{r})\right] \quad \text{(A.31)}$$

$$\tau_{\rm sc}(\vec{r}) = \frac{1}{5\,\pi^2}\left(\frac{2m}{\hbar^2}\right)^{3/2}\left\{\Big[\lambda-V(\vec{r})\Big]^{5/2}-\right.$$
$$\left.-\frac{3\hbar^2}{16m}\left[\frac{5}{3}\vec{\nabla}^2 V\Big[\lambda-V(\vec{r})\Big]^{1/2}-\frac{3}{4}\frac{\Big(\vec{\nabla}V\Big)^2}{\Big[\lambda-V(\vec{r})\Big]^{1/2}}\right]+\cdots\right\}\Theta\left[\lambda-V(\vec{r})\right]. \quad \text{(A.32)}$$

Summarizing, let us give the final expressions for $\tau[\rho]$ in all possible orders of the semiclassical expansion:

- TF: $\tau[\rho] = \frac{3}{5}\,(3\pi^2)^{2/3}\,\rho^{5/3}$
- order $\hbar^2$: $\tau[\rho] = \tau_{TF}[\rho] + \frac{1}{36}\,\frac{\left(\vec{\nabla}\rho\right)^2}{\rho} + \frac{1}{3}\,\vec{\nabla}^2\rho$
- order $\hbar^4$: $\tau[\rho] = \tau_{TF}[\rho] + \tau_2[\rho] + \tau_4[\rho]$.

As mentioned in the main text we gather here the expressions for $\tau[\rho]$ in the $4^{\rm th}-$order ETF approach.

For the $4^{\rm th}-$order spin independent part of the kinetic energy density, of eq. (2.28) reads

$$\tau_q^{(4)}[\rho_q]=(3\pi^2)^{-2/3}\frac{\rho_q^{1/3}}{4320}\left\{24\frac{\Delta^2\rho_q}{\rho_q}-60\frac{\vec{\nabla}\rho_q\cdot\vec{\nabla}(\Delta\rho_q)}{\rho_q^2}-28\left(\frac{\Delta\rho_q}{\rho_q}\right)^2-14\frac{\Delta(\vec{\nabla}\rho_q)^2}{\rho_q^2}\right.$$
$$+\frac{280}{3}\frac{(\vec{\nabla}\rho_q)^2\Delta\rho_q}{\rho_q^3}+\frac{184}{3}\frac{\vec{\nabla}\rho_q\cdot\vec{\nabla}(\vec{\nabla}\rho_q)^2}{\rho_q^3}-96\left(\frac{\vec{\nabla}\rho_q}{\rho_q}\right)^4-36\frac{\Delta^2 f_q}{f_q}+36\frac{\Delta(\vec{\nabla}f_q)^2}{f_q^2}$$
$$-18\left(\frac{\Delta f_q}{f_q}\right)^2-72\frac{\vec{\nabla}f_q\cdot\vec{\nabla}(\vec{\nabla}f_q)^2}{f_q^3}+54\left(\frac{\vec{\nabla}f_q}{f_q}\right)^4+12\frac{\Delta(\vec{\nabla}f_q\cdot\vec{\nabla}\rho_q)}{f_q\,\rho_q}$$
$$\left.+24\frac{\vec{\nabla}f_q\cdot\vec{\nabla}(\Delta\rho_q)}{f_q\,\rho_q}-36\frac{\vec{\nabla}\rho_q\cdot\vec{\nabla}(\Delta f_q)}{f_q\,\rho_q}+24\frac{\vec{\nabla}\rho_q\cdot\vec{\nabla}(\vec{\nabla}f_q)^2}{f_q^2\,\rho_q}-12\frac{(\vec{\nabla}f_q\cdot\vec{\nabla}\rho_q)\Delta f_q}{f_q^2\,\rho_q}\right\}. \tag{A.33}$$

Carrying out the straightforward analytical transformations we are finally left with the expression for $\tau_q^{(4)}[\rho_q]$ of the form (primes denoting derivatives with respect to the radial variable r) :

$$\tau_q^{(4)}[\rho]=(3\pi^2)^{-2/3}\frac{\rho_q^{1/3}}{4320}\left\{\frac{24}{\rho_q}\left[\rho_q^{(4)}+\frac{4}{r}\rho_q^{'''}\right]-\frac{8}{\rho_q^2}\left[11\rho_q^{'''}\rho_q^{'}+7(\rho_q^{''})^2+\frac{36}{r}\rho_q^{''}\rho_q^{'}-\frac{1}{r^2}(\rho_q^{'})^2\right]\right.$$
$$+\frac{8}{3\,\rho_q^3}\left[81\rho_q^{''}(\rho_q^{'})^2+\frac{70}{r}(\rho_q^{'})^3\right]-\frac{96}{\rho_q^4}(\rho_q^{'})^4-\frac{36}{f_q}\left[f_q^{(4)}+\frac{4}{r}f_q^{'''}\right]+\frac{18}{f_q^2}\left[4f_q^{'''}f_q^{'}+\right.$$
$$\left.+3(f_q^{''})^2+\frac{4}{r}f_q^{''}f_q^{'}-\frac{4}{r^2}(f_q^{'})^2\right]-\frac{144}{f_q^3}f_q^{''}(f_q^{'})^2+\frac{54}{f_q^4}(f_q^{'})^4+\frac{12}{f_q\,\rho_q}\left[3f_q^{'}\rho_q^{'''}+2f_q^{'''}\rho_q^{''}\right.$$
$$\left.-2f_q^{'''}\rho_q^{'}+\frac{6}{r}f_q^{'}\rho_q^{''}-\frac{4}{r}f_q^{''}\rho_q^{'}+\frac{2}{r^2}f_q^{'}\rho_q^{'}\right]+\frac{12}{f_q^2\,\rho_q}\left[f_q^{'}f_q^{''}\rho_q^{'}-2(f_q^{'})^2\rho_q^{''}-\frac{2}{r}(f_q^{'})^2\rho_q^{'}\right]$$
$$\left.-\frac{4}{f_q\,\rho_q^2}\left[11f_q^{''}(\rho_q^{'})^2+32f_q^{'}\rho_q^{'}\rho_q^{''}+\frac{26}{r}f_q^{'}(\rho_q^{'})^2\right]+\frac{30}{f_q^2\,\rho_q^2}(f_q^{'})^2(\rho_q^{'})^2+\frac{260}{3\,f_q\,\rho_q^3}f_q^{'}(\rho_q^{'})^3\right\} \tag{A.34}$$

When giving the spin dependent part of $\tau_q^{(4)}[\rho]$ we take advantage of the fact that the spin-orbit potential $\vec{W}_q$ has for Skyrme forces the simple form of eq. (2.25) which allows us to introduce the quantity

$$A_q=\rho+\rho_q \qquad \Longrightarrow \qquad \vec{W}_q=-B_9\vec{\nabla}A_q. \tag{A.35}$$

Using the vector identity

$$\mathrm{rot}(\mathrm{rot}\,\vec{a})=\vec{\nabla}(\mathrm{div}\,\vec{a})-\Delta\,\vec{a}$$

one shows that because of the form of the spin-orbit potential, eq. (2.25), one simply has

$$\vec{W}\cdot\Delta\vec{W}=\vec{W}\cdot\vec{\nabla}(\mathrm{div}\vec{W})$$

which then allows us to write the spin dependent part of $\tau_q^{(4)_{\mathrm{so}}}$ in the form of the local densities ρ_n and ρ_p and of their derivatives :

$$\tau_q^{(4)_{\mathrm{so}}}[\rho]=(3\pi^2)^{-2/3}(\frac{mW_0}{\hbar^2})^2\frac{\rho_q^{1/3}}{4f_q^2}\left\{\left[\frac{3}{4}\vec{\nabla}A_q\cdot\vec{\nabla}^3A_q+\frac{1}{8}\Delta(\vec{\nabla}A_q)^2+\frac{1}{4}(\Delta A_q)^2\right]\right.$$

$$-\frac{1}{2f_q}\Big[\Delta A_q(\vec{\nabla}f_q\cdot\vec{\nabla}A_q)+2\vec{\nabla}A_q\cdot(\vec{\nabla}f_q\cdot\vec{\nabla})\vec{\nabla}A_q+\vec{\nabla}f_q\cdot(\vec{\nabla}A_q\cdot\vec{\nabla})\vec{\nabla}A_q+\Delta f_q(\vec{\nabla}A_q)^2$$
$$+\vec{\nabla}A_q\cdot\vec{\nabla}(\vec{\nabla}A_q\cdot\vec{\nabla}f_q)-\frac{1}{2}\vec{\nabla}f_q\cdot\vec{\nabla}(\vec{\nabla}A_q)^2\Big]+\frac{3}{4f_q^2}\Big[(\vec{\nabla}f_q)^2(\vec{\nabla}A_q)^2+(\vec{\nabla}f_q\cdot\vec{\nabla}A_q)^2$$
$$-(\frac{mW_0}{\hbar^2})^2(\vec{\nabla}A_q)^4\Big]+\frac{1}{6\rho_q}\Big[\vec{\nabla}A_q\cdot(\vec{\nabla}\rho_q\cdot\vec{\nabla})\vec{\nabla}A_q+\Delta A_q(\vec{\nabla}\rho_q\cdot\vec{\nabla}A_q)\Big]$$
$$-\frac{1}{6f_q\rho_q}\Big[(\vec{\nabla}f_q\cdot\vec{\nabla}\rho_q)(\vec{\nabla}A_q)^2+(\vec{\nabla}f_q\cdot\vec{\nabla}A_q)(\vec{\nabla}\rho_q\cdot\vec{\nabla}A_q)\Big]\Big\} \tag{A.36}$$

which for spherical symmetry reads

$$\tau_q^{(4)_{\rm so}}[\rho]=(3\pi^2)^{-2/3}\left(\frac{mW_0}{\hbar^2}\right)^2\frac{\rho_q^{1/3}}{4f_q^2}\Big\{\frac{1}{2}\Big[2A'_qA'''_q+(A''_q)^2+\frac{6}{r}A'_qA''_q-\frac{1}{r^2}(A'_q)^2\Big]$$
$$-\frac{A'_q}{f_q}\Big[f''_qA'_q+2f'_qA''_q+\frac{2}{r}f'_qA'_q\Big]+\frac{3(A'_q)^2}{4f_q^2}\Big[2(f'_q)^2-(\frac{mW_0}{\hbar^2})^2(A'_q)^2\Big]$$
$$+\frac{\rho'_qA'_q}{3f_q\rho_q}\Big[f_q(A''_q+\frac{1}{r}A'_q)-f'_qA'_q\Big]\Big\}\quad. \tag{A.37}$$

The $4^{\rm th}$ order spin-orbit density $\vec{J}_q^{(4)}[\rho]$, eq. (2.32) written in terms of the function A_q defined above is given by

$$\vec{J}_q^{(4)}[\rho]=(3\pi^2)^{-2/3}\,\frac{mW_0}{\hbar^2}\,\frac{\rho_q^{1/3}}{8f_q}\Big\{-2\vec{\nabla}^3A_q+\frac{1}{f_q}\Big[\Delta f_q\,\vec{\nabla}A_q+(\vec{\nabla}A_q\cdot\vec{\nabla})\vec{\nabla}f_q$$
$$+2(\vec{\nabla}f_q\cdot\vec{\nabla})\vec{\nabla}A_q\Big]-\frac{1}{f_q^2}\Big[(\vec{\nabla}f_q)^2\vec{\nabla}A_q+(\vec{\nabla}f_q\cdot\vec{\nabla}A_q)\vec{\nabla}f_q$$
$$-2\,(\frac{mW_0}{\hbar^2})^2\,(\vec{\nabla}A_q)^3\Big]-\frac{1}{3\rho_q}\Big[(\vec{\nabla}\rho_q\cdot\vec{\nabla})\vec{\nabla}A_q+\Delta A_q\vec{\nabla}\rho_q\Big]$$
$$+\frac{1}{3f_q\rho_q}\Big[(\vec{\nabla}f_q\cdot\vec{\nabla}\rho_q)\vec{\nabla}A_q+(\vec{\nabla}f_q\cdot\vec{\nabla}A_q)\vec{\nabla}\rho_q\Big]\Big\} \tag{A.38}$$

which in the case of a spherically symmetric system takes the form

$$\vec{J}_q^{(4)}[\rho]=(3\pi^2)^{-2/3}\,\frac{mW_0}{\hbar^2}\,\frac{\rho_q^{1/3}}{4f_q}\Big\{-\Big[A'''_q+\frac{2}{r}A''_q-\frac{2}{r^2}A'_q\Big]+\frac{1}{f_q}\Big[f''_qA'_q+f'_qA''_q+\frac{1}{r}f'_qA'_q\Big]$$
$$-\frac{A'_q}{f_q^2}\Big[(f'_q)^2-(\frac{mW_0}{\hbar^2})^2(A'_q)^2\Big]-\frac{\rho'_q}{3f_q\rho_q}\Big[f_q(A''_q+\frac{1}{r}A'_q)-f'_qA'_q\Big]\Big\}\,\vec{u}_r \tag{A.39}$$

with the unit vector in radial direction $\vec{u}_r$.

A.2 Some numerical utilities

In this section we want to give the outline of the derivations of some useful expressions which frequently occur in the calculations presented within this work. These are purely mathematical problems, so we do not put them in the main text. However, these expressions turn out to be helpful for developing numerical codes or calculating analytically various integrals.

A.2.1 Solution of the integral $\int_{-\infty}^{\infty} \frac{e^{izd}}{z(z^2+A^2)}\,dz$

Let us calculate explicitly the integral of the form

$$I = \int_0^{\infty} \frac{e^{izd}}{z(z^2+\frac{1}{a^2})}\,dz \tag{A.40}$$

We can split this integral into three terms, namely:

$$I = \int_{-R}^{-\varepsilon} \frac{e^{ixd}}{x(x^2+\frac{1}{a^2})}\,dx + \int_{-\varepsilon}^{\varepsilon} \frac{e^{izd}}{z(z^2+\frac{1}{a^2})}\,dz \int_{-\varepsilon}^{R} \frac{e^{ixd}}{x(x^2+\frac{1}{a^2})}\,dx + \int_{\Gamma_{R(-R)}} \frac{e^{izd}}{z(z^2+\frac{1}{a^2})}\,dz, \tag{A.41}$$

The last integral approaches zero since the contour $\Gamma_{R(-R)}$ is chosen as an arbitrary curve connecting points $x = R$ and $x = -R$ above the $x-$axis and letting $R \longrightarrow \infty$. This contour should be, however, chosen in such a way that the integral (A.40) has to be convergent. Expression (A.40) has only one single pole on the interval $(0, \infty)$ in $x_1 = \frac{1}{a}$. Replacing $x \longrightarrow -x$ in the first term of (A.43) we can associate it with the third one, whereas the second term can be performed in the complex plane, by inserting

$$\begin{aligned} z &= \varepsilon e^{i\varphi} \\ z^2 &= \varepsilon^2 e^{i2\varphi} \\ dz &= i\varepsilon e^{i\varphi}\,d\varphi. \end{aligned} \tag{A.42}$$

Now, we get the integral (A.41) in the following form:

$$I = 2i \int_{\varepsilon}^{R} \frac{\sin(zd)}{z(z^2+\frac{1}{a^2})} + i \int_0^{\pi} \frac{e^{id\,\varepsilon e^{i\,\varphi}}}{(\varepsilon^2 e^{i2\varphi}+\frac{1}{a^2})}\,d\varphi + 0 \tag{A.43}$$

In the above, the first term can be developed using the residues theorem in the complex plane, (assuming that $\varepsilon \longrightarrow 0$ and $R \longrightarrow \infty$), where, by the definition, the residues are given as

$$res_i \equiv \lim_{z \to p_i} \frac{1}{(k-1)!} \frac{d^{k-1}}{d^{k-1}z} \Big[(z-p_i)^k f(z) \Big], \tag{A.44}$$

where k is the multiplicity of the given pole p_i. In our case, $x = 1/a$ is the only single pole $(k = 1)$, so

$$res_1 = \lim_{z \to \frac{1}{a}} \frac{(z-\frac{1}{a})\,e^{izd}}{z(z-\frac{1}{a})(z+\frac{1}{a})} = -\frac{a^2}{2}\,e^{-d/a}. \tag{A.45}$$

Finally,

$$2i \int_0^{\infty} \frac{\sin(zd)}{z(z^2+\frac{1}{a^2})} = 2\pi i \sum_i res_i = 2\pi a^2\,e^{-d/a}. \tag{A.46}$$

The second integral in eq. (A.43) is solved directly, putting $\varepsilon \longrightarrow 0$ and noting that its integrand diverges for $\varphi \in (\pi, 2\pi)$

$$i \int_0^{\pi} \lim_{\varepsilon \to 0} \frac{e^{id\,\varepsilon e^{i\,\varphi}}}{(\varepsilon^2 e^{i2\varphi} + \frac{1}{a^2})}\, d\varphi = i \int_0^{\pi} \frac{1}{0 + \frac{1}{a^2}}\, d\varphi = ia^2\pi \tag{A.47}$$

Collecting the results (A.46) and (A.47) we may rewrite the expression (A.40) as

$$I = ia^2\pi + 2\pi a^2\, e^{-d/a}. \tag{A.48}$$

In the similar way we can consider the integral (A.40) on the interval $(-\infty, 0)$. It is now clear that in the above the first constant component corresponds to the value denoted in section 6.4 as *sharp* whereas the second depending on $d \equiv |\vec{r} - \vec{r}\,'|$ is usually treated as a correction.

A.2.2 Expression $|\vec{r} - \vec{r}\,'|$

Generally, the vector $\vec{r} - \vec{r}$ in the cylindrical coordinates is equal to

$$\vec{r} - \vec{r}\,' = \vec{e}_\rho(\rho - \rho' \cos(\varphi - \varphi')) + \vec{e}_\varphi \rho' \sin(\varphi - \varphi') + \vec{e}_z(z - z') \tag{A.49}$$

or

$$\vec{r} - \vec{r}\,' = \vec{e}_{\rho'}(-\rho' + \rho\cos(\varphi - \varphi')) + \vec{e}_{\varphi'}\rho \sin(\varphi - \varphi') + \vec{e}_{z'}(z - z')\ . \tag{A.50}$$

in the "prime" coordinates. The length of the vector $\vec{r} - \vec{r}\,'$ is

$$|\vec{r} - \vec{r}\,'| = \sqrt{\rho^2 + \rho'^2 - 2\rho\rho' \cos(\varphi - \varphi') + (z - z')^2}. \tag{A.51}$$

A.2.3 Surface area in the cylindrical coordinates

In the cylindrical coordinates the surface element can be written as

$$dS = \sqrt{1 + \frac{1}{\rho^2}\left(\frac{\partial \rho}{\partial \varphi}\right)^2 + \left(\frac{\partial \rho}{\partial z}\right)^2}\, \rho\, dz\, d\varphi\ , \tag{A.52}$$

and its vector form is

$$d\vec{S} = \vec{n} \cdot dS, \tag{A.53}$$

where $\vec{n}$ is the normal vector to the surface

$$\vec{n} = \frac{\left[1, -\frac{1}{\rho}\frac{\partial \rho}{\partial \varphi}, -\frac{\partial \rho}{\partial z}\right]}{\sqrt{1 + \frac{1}{\rho^2}\left(\frac{\partial \rho}{\partial \varphi}\right)^2 + \left(\frac{\partial \rho}{\partial z}\right)^2}}\ . \tag{A.54}$$

The last two equations lead to the following form for the vectorized surface element

$$d\vec{S} = \left[\rho, -\frac{\partial \rho}{\partial \varphi}, -\rho\frac{\partial \rho}{\partial z}\right] dz\, d\varphi\ . \tag{A.55}$$

We have used in the above the vector decomposition in the cylinder coordinates $[\vec{e}_\rho, \vec{e}_\varphi, \vec{e}_z]$.

A.3 Deformation functions of the LSD model

By virtue of the relations derived in the previous section the relative surface area $B_{sur} = S(def)/S(0)$ of deformed nucleus is given by

$$B_{sur} = \frac{1}{4\pi R_0^2} \int_{-z_0}^{z_0} dz \int_0^{2\pi} \sqrt{\rho^2 + \left(\frac{\partial \rho}{\partial \varphi}\right)^2 + \left(\rho \frac{\partial \rho}{\partial z}\right)^2}\, d\varphi \ . \tag{A.56}$$

The parameter B_{cur} entering also the LSD formula describes the relative change of the first order curvature of the deformed drop reads

$$B_{cur} = \frac{1}{8\pi R_0} \iint_{\Sigma} \left(\frac{1}{R_1} + \frac{1}{R_2}\right) dS, \tag{A.57}$$

$$\tag{A.58}$$

where $R_1(z,\varphi)$ and $R_2(z,\varphi)$ are the local main radii of the surface. In the cylinder coordinates this parameter is equal to

$$\begin{aligned} B_{cur} &= \frac{1}{8\pi R_0} \int_{z_{min}}^{z_{max}} dz \int_0^{2\pi} \left\{ \rho^2 + \rho^2 \left(\frac{\partial \rho}{\partial z}\right)^2 + \left(\frac{\partial \rho}{\partial \varphi}\right)^2 \right\}^{-1} \cdot \\ &\cdot \left\{ \rho^2 \left(\frac{\partial \rho}{\partial z}\right)^2 - \rho \left(\frac{\partial \rho}{\partial z}\right)^2 \frac{\partial^2 \rho}{\partial \varphi^2} + \rho^2 - \rho \frac{\partial^2 \rho}{\partial \varphi^2} + 2 \left(\frac{\partial \rho}{\partial \varphi}\right)^2 \right. \\ &+ \left. 2 \frac{\partial \rho}{\partial z} \frac{\partial \rho}{\partial \varphi} \rho \frac{\partial^2 \rho}{\partial z \partial \varphi} - \rho^3 \frac{\partial^2 \rho}{\partial z^2} - \rho \frac{\partial^2 \rho}{\partial z^2} \left(\frac{\partial \rho}{\partial \varphi}\right)^2 \right\} d\varphi \ . \end{aligned} \tag{A.59}$$

A.4 Gauss–Hermite approximation formula

Discussing the problem of multidimensional potential–energy surfaces we face with the problem of approximation the energy values between points in the multidimensional deformation space. Of course, problem is rather simple for two dimensions, a little more complicated for three, but yet four dimensional deformation grid requires a lot of efforts. In 2004 Pomorski invented very efficient method of approximating multidimensional functions using well–known Strutinsky's idea of the gauss–folding procedure applied in the Strutinsky shell correction. Let us focus here only on the main points of this idea.

We consider an ensemble of N points x_i which have to cover the whole one–dimensional interval $[a,b]$ and ordered, i.e. $x_{i+1} > x_i$). Let x_i be a one–dimensional discrete argument of a given function $y(x)$, while $y_i = y(x_i)$ its value in this point.

Let $j_n(x,x')$ be a symmetric function of its arguments, (i.e. $j_n(x,x') = j_n(x',x)$) having the following properties:

$$\int_{-\infty}^{+\infty} j_n(x,x')\, dx = 1. \tag{A.60}$$

Let us assume now after Strutinsky that

$$P_k(x) = \int_{-\infty}^{+\infty} P_k(x')\, j_n(x, x')\, dx' \ , \tag{A.61}$$

where $k \leq n$ are even natural numbers and P_k is an arbitrary polynomial of the order k. In the following, the function $j_n(x, x')$ will be called the folding function of the $n^{\text{th}}-$order. Let each discrete point (x_i, y_i) be represented by the function $\widetilde{y}_i(x)$ defined as

$$\widetilde{y}_i(x) = \int_{-\infty}^{+\infty} y_i\, \delta(x' - x_i)\, j_n(x, x')\, dx' \ , \tag{A.62}$$

where $\delta(x)$ is the Dirac $\delta-$function, so that

$$\widetilde{y}_i(x) = y_i\, j_n(x, x_i) \ . \tag{A.63}$$

We can immediately note that the above operation transforms the well–defined point in the coordinate system into an object similar to a "diffused wave packet".

Using eq. (A.60) which says that each folding function should be normalized to the unity we have that

$$\int_{-\infty}^{+\infty} \widetilde{y}_i(x)\, dx = y_i \ . \tag{A.64}$$

Now, we construct the function $\widetilde{y}(x)$ by summing up all functions $\widetilde{y}_i(x)$ corresponding to each point x_i

$$\widetilde{y}(x) = \sum_{i=1}^{N} \omega_i\, \widetilde{y}_i(x) \ . \tag{A.65}$$

The function $\widetilde{y}(x)$ is now an approximation of $y(x)$ if the weights ω_i are determined from the assumption that the integrals of the original and folded functions are (approximately) equal:

$$\int_a^b y(x)\, dx \approx \int_{-\infty}^{+\infty} \widetilde{y}(x)\, dx = \sum_{i=1}^{N} \omega_i\, y_i \ . \tag{A.66}$$

The Riemann summation formula for the integral of the function $y(x)$ between limits a and b gives

$$\int_a^b y(x)\, dx = \lim_{N\to\infty} \sum_{i=1}^{N} y(x_i)\, \Delta x_i \ , \tag{A.67}$$

where Δx_i is chosen in the middle of the distance of neighbouring argument points

$$\Delta x_i = \frac{1}{2}\,(x_{i+1} - x_{i-1}) \tag{A.68}$$

with $x_0 = a$ and $x_{N+1} = b$. Comparing eqs. (A.66) and (A.67) one can see that a reasonable choice of the weight would be

$$\omega_i = \Delta x_i \ . \tag{A.69}$$

If the number N of sample pairs (x_i, y_i) is large enough then the condition (A.66) is fulfilled fairly strictly.

Finally, the folded function $\widetilde{y}(x)$ which approximates the true function $y(x)$ is given by

$$\widetilde{y}(x) = \sum_{i=1}^{N} y_i \, \Delta x_i \, j_n(x, x_i) \ . \tag{A.70}$$

Let the folding function $j_n(x, x')$ be a modified Gauss function

$$j_n(x, x') = \frac{1}{\gamma\sqrt{\pi}} \exp\left\{ -\left(\frac{x - x'}{\gamma} \right)^2 \right\} f_n\left(\frac{x - x'}{\gamma} \right) \ , \tag{A.71}$$

where γ is the parameter and $f_n(\frac{x-x'}{\gamma})$ is the so–called correction polynomial of the order n determined by the Strutinsky condition (A.61). Heving performed the calculations similar to these made in the Strutinsky's description of the shell correction we obtain explicit expressions for the correction polynomials f_n, (where $u = \frac{x-x'}{\gamma}$):

$$\begin{aligned} f_0(u) &= 1 \ , \\ f_2(u) &= \tfrac{3}{2} - u^2 \ , \\ f_4(u) &= \tfrac{15}{8} - \tfrac{5}{2}u^2 + \tfrac{1}{2}u^4 \ , \\ f_6(u) &= \tfrac{35}{16} - \tfrac{35}{8}u^2 + \tfrac{7}{4}u^4 - \tfrac{1}{6}u^6 \ , \end{aligned} \tag{A.72}$$

Finally the function $\widetilde{y}(x)$ approximated by the Gauss–Hermite folding function reads:

$$\widetilde{y}(x) = \frac{1}{\gamma\sqrt{\pi}} \sum_{i=1}^{N} y_i \, \Delta x_i \exp\left\{ -\left(\frac{x - x_i}{\gamma} \right)^2 \right\} f_n\left(\frac{x - x_i}{\gamma} \right) \ . \tag{A.73}$$

Since our aim is to approximate the function stored in a mesh $\{x_i, y_i\}$, the smearing parameter γ should be related to the distance Δx_i between subsequent points. The equation (A.73) can be directly generalized for the multidimensional case (see Ref. [100]).

A.5 Legendre polynomials

The lowest order Legendre polynomials are:

$$\begin{aligned} P_0(x) &= 1 \\ P_1(x) &= x \\ P_2(x) &= \frac{1}{2}(3x^2 - 1) \\ P_3(x) &= \frac{1}{2}(5x^3 - 3x) \\ P_4(x) &= \frac{1}{8}(35x^4 - 30x^2 + 3) \\ P_5(x) &= \frac{1}{8}(63x^5 - 70x^3 + 15x) \\ P_6(x) &= \frac{1}{16}(231x^6 - 315x^4 + 105x^2 - 5) \\ P_7(x) &= \frac{1}{16}(429x^7 - 693x^5 + 315x^3 - 35x) \end{aligned} \tag{A.74}$$

A.6 Fission–barrier–stationary points

Z A	Energy (MeV)	c	h	α	η	Q_2 (b)	Q_3 $(b^{3/2})$	Q_4 (b^2)	Q_{22} (b)	I Barr. (MeV)
90	I M=-1765.33	1.18	-0.11	0.00	0.08	21.1	0.0	7.2	-6.6	4.96
232										(6.20)
	I S=-1760.37	1.28	0.10	-0.06	-0.10	60.8	2.7	8.6	6.6	(5.45)
90	I M=-1776.48	1.21	-0.12	0.00	0.00	26.5	0.0	8.8	0.0	5.19
234										(6.50)
	I S=-1771.29	1.28	0.10	-0.03	-0.10	61.7	1.3	8.8	6.7	(5.36)
92	I M=-1777.14	1.22	-0.06	0.00	-0.08	32.8	0.0	8.3	6.0	4.44
234										(5.50)
	I S=-1772.70	1.28	0.03	-0.12	0.00	52.7	3.9	10.7	0.0	(4.89)
92	I M=-1789.28	1.20	-0.10	0.00	0.00	28.3	0.0	8.6	0.0	5.54
236										(5.67)
	I S=-1783.74	1.28	0.08	-0.06	0.00	60.0	2.5	9.674	0.0	(4.98)
92	I M=-1800.82	1.21	-0.10	0.00	0.00	28.9	0.0	8.7	0.0	6.83
238										(5.50)
	I S=-1793.99	1.33	0.00	0.00	-0.05	60.6	0.0	16.6	3.5	(5.48)
92	I M=-1811.78	1.21	-0.10	0.00	0.00	29.1	0.0	8.9	0.0	6.48
240										(5.50)
	I S=-1805.30	1.30	0.07	-0.06	-0.10	64.5	2.5	12.3	6.9	(6.27)
94	I M=-1787.17	1.21	-0.10	0.00	0.00	28.4	0.0	8.5	0.0	5.92
236										(4.50)
	I S=-1781.25	1.30	0.07	-0.15	-0.05	62.2	6.2	12.0	3.4	(4.35)
94	I M=-1800.32	1.21	-0.10	0.00	0.00	28.9	0.0	8.7	0.0	6.48
238										(5.00)
	I S=-1793.83	1.29	0.07	-0.09	0.00	61.5	3.7	11.1	0.0	(4.39)
94	I M=-1812.67	1.21	-0.09	0.00	0.00	29.4	0.0	8.8	0.0	6.98
240										(5.15)
	I S=-1805.69	1.30	0.07	-0.06	-0.10	64.4	2.5	12.3	7.0	(4.83)

Tab. 1A First saddles and minima of chosen actinides on the mesh $\{\Delta c = 0.01, \Delta h = 0.01, \Delta\alpha = 0.03, \Delta\eta = 0.05\}$. Abbreviations "I M", "I S" denote respectively the first minimum and first saddle point respectively. Underlined energy values in column 11, (I Barr.), give the heights of the fission barriers calculated within the model presented in this work whereas values in parenthesis give experimental and theoretical [96] estimates respectively. Single–particle spectra to calculate the microscopic–energy corrections are re–scaled, using the relation (9.3), from ^{240}Pu.

Z A	Energy (MeV)	c	h	α	η	Q_2 (b)	Q_3 ($b^{3/2}$)	Q_4 (b^2)	Q_{22} (b)	I Barr (MeV)
94	I M=-1824.45	1.21	-0.06	0.00	0.00	32.5	0.0	8.2	0.0	7.10
242										(5.05)
	I S=-1817.35	1.31	0.06	-0.09	-0.10	65.9	3.8	13.9	7.0	(5.55)
94	I M=-1835.60	1.21	-0.05	0.00	0.00	33.9	0.00	8.2	0.0	6.94
244										(5.00)
	I S=-1828.66	1.31	0.05	-0.09	-0.10	65.4	3.68	14.4	7.2	(6.29)
94	I M=-1846.75	1.18	-0.02	0.00	0.00	32.7	0.0	5.9	0.0	7.21
246										(5.30)
	I S=-1839.54	1.32	0.06	-0.03	-0.15	69.9	1.34	15.5	10.8	(7.01)
96	I M=-1822.70	1.21	-0.10	0.00	0.00	29.7	0.0	9.0	0.0	7.1
242										(5.00)
	I S=-1815.59	1.34	0.01	-0.09	-0.20	64.5	3.1	17.8	14.2	(4.28)
96	I M=-1835.28	1.21	-0.06	0.00	0.00	33.0	0.0	8.4	0.0	7.26
244										(5.10)
	I S=-1828.02	1.33	0.04	0.00	-0.15	68.2	0.0	16.7	10.6	(5.02)
96	I M=-1847.26	1.21	-0.05	0.00	0.00	34.6	0.0	8.2	0.0	7.09
246										(4.80)
	I S=-1840.12	1.33	0.05	-0.06	-0.15	69.1	0.0	17.0	10.8	(5.81)
96	I M=-1858.60	1.21	-0.04	0.00	0.00	35.6	0.00	8.2	0.0	6.30
248										(4.80)
	I S=-1852.30	1.25	0.03	-0.39	-0.20	46.6	12.9	9.6	16.1	(6.40)
96	I M=-1869.02	1.21	-0.04	0.00	0.00	36.7	0.0	8.2	0.0	6.12
250										(4.40)
	I S=-1862.90	1.33	0.03	-0.12	-0.10	69.4	4.8	18.0	7.4	(5.98)
98	I M=-1869.16	1.21	-0.04	0.00	0.00	36.6	0.0	8.2	0.0	6.70
250										(3.60)
	I S=-1862.46	1.33	0.03	-0.09	-0.15	69.2	3.6	17.9	11.2	(5.88)

Tab. 1A continuation

Z A	Energy (MeV)	c	h	α	η	Q_2 (b)	Q_3 $(b^{3/2})$	Q_4 (b^2)	Q_{22} (b)	I Barr (MeV)
94 244	I M=-1835.38	1.21	-0.05	0.00	0.00	34.0	0.0	8.1	0.0	<u>6.49</u>
	I S=-1828.89	1.30	0.05	0.00	-0.10	63.5	0.0	13.2	7.2	
94 246	I M=-1845.96	1.21	-0.04	0.00	0.00	35.3	0.0	8.0	0.0	<u>6.38</u>
	I S=-1839.58	1.32	0.06	0.00	-0.15	69.9	0.0	15.4	10.8	
96 242	I M=-1822.50	1.21	-0.06	0.00	0.00	32.5	0.0	8.2	0.0	<u>7.1</u>
	I S=-1815.80	1.33	-0.02	0.00	-0.25	58.3	0.0	17.0	18.2	
96 244	I M=-1835.05	1.21	-0.06	0.00	0.00	32.9	0.0	8.4	0.0	<u>7.02</u>
	I S=-1828.03	1.31	0.05	-0.06	-0.10	65.5	2.4	14.3	7.2	
96 246	I M=-1847.05	1.21	-0.05	0.00	0.00	34.5	0.0	8.2	0.0	<u>6.88</u>
	I S=-1840.17	1.30	0.05	0.00	-0.10	64.4	0.0	13.5	7.3	
96 248	I M=-1858.42	1.21	-0.04	0.00	0.00	35.6	0.0	8.2	0.0	<u>6.57</u>
	I S=-1851.85	1.33	0.04	-0.06	-0.15	69.9	2.5	17.4	10.9	
96 250	I M=-1868.81	1.21	-0.04	0.00	0.00	36.7	0.0	8.2	0.0	<u>5.74</u>
	I S=-1863.07	1.32	0.03	0.00	-0.10	67.7	0.0	16.8	7.5	
98 250	I M=-1868.97	1.21	-0.04	0.00	0.00	36.5	0.0	8.2	0.0	<u>6.80</u>
	I S=-1862.17	1.31	0.03	0.00	-0.10	65.5	0.0	15.6	7.5	
98 252	I M=-1880.16	1.21	-0.03	0.00	0.00	37.4	0.0	8.2	0.0	<u>5.86</u>
	I S=-1874.30	1.32	0.02	0.00	-0.10	67.1	0.0	17.3	7.6	

Tab. 2A Same as in Tab. 1A but with the single–particle spectra rescaled from ^{250}Cm

Z A	Energy (MeV)	c	h	α	η	Q_2 (b)	Q_3 $(b^{3/2})$	Q_4 (b^2)	Q_{22} (b)	I Barr (MeV)
90	I M=-1765.44	1.20	-0.08	0.00	0.00	27.9	0.0	7.9	0.0	5.04
232	II M=-1764.66	1.42	0.06	0.00	0.00	85.7	0.0	27.2	0.0	(6.20)
	I S=-1760.40	1.30	0.08	-0.15	-0.05	61.8	6.2	11.3	3.2	(5.45)
	II S=-1760.40	1.57	0.08	-0.39	-0.05	114.4	25.4	54.8	2.7	
90	I M=-1776.92	1.20	-0.08	0.00	0.00	29.3	0.0	8.0	0.0	5.92
234	II M=-1776.10	1.42	0.06	0.00	0.00	85.9	0.0	27.0	0.0	(6.50)
	I S=-1771.00	1.30	0.08	-0.15	-0.05	62.7	6.3	11.5	3.3	(5.36)
	II S=-1766.80	1.51	0.08	-0.30	-0.20	104.9	18.4	42.6	11.6	
92	I M=-1777.22	1.21	-0.09	0.00	0.00	28.8	0.0	8.3	0.0	6.92
234	II M=-1776.24	1.42	0.07	0.00	0.00	87.1	0.0	26.9	0.0	(5.50)
	I S=-1770.30	1.36	0.04	-0.33	-0.05	66.6	12.2	18.8	3.2	(4.89)
	II S=-1772.07	1.60	0.00	0.00	-0.05	112.3	0.0	57.7	2.8	
92	I M=-1789.51	1.21	-0.08	0.00	0.00	29.7	0.0	8.3	0.0	6.78
236	II M=-1788.47	1.41	0.07	0.00	0.00	87.1	0.0	26.2	0.0	(5.67)
	I S=-1782.73	1.30	-0.04	-0.03	-0.30	47.6	0.7	13.5	21.0	(4.98)
	II S=-1782.16	1.51	0.08	-0.27	-0.15	107.5	16.9	43.7	8.8	
92	I M=-1800.82	1.21	-0.07	0.00	0.00	31.0	0.0	8.1	0.0	6.55
238	II M=-1800.08	1.40	0.08	0.00	0.00	87.4	0.0	25.2	0.0	(5.50)
	I S=-1794.27	1.30	0.04	-0.12	0.00	59.4	4.3	12.8	0.0	(5.48)
	II S=-1796.59	1.54	0.04	-0.21	-0.05	108.9	11.0	49.2	2.9	
92	I M=-1811.81	1.20	-0.05	0.00	0.00	31.8	0.0	7.4	0.0	6.83
240	II M=-1810.97	1.40	0.08	0.00	0.00	89.2	0.0	25.3	0.0	(5.50)
	I S=-1804.98	1.30	0.08	-0.12	-0.10	65.5	5.3	12.1	6.9	(6.27)
	II S=-1806.56	1.54	0.04	-0.39	0.00	106.0	19.8	49.2	0.0	

Tab. 3A Inner and outer stationary points of chosen actinide nuclei found on the deformation grid $\{\Delta c = 0.03, \Delta h = 0.04, \Delta\alpha = 0.03, \Delta\eta = 0.05\}$. Abbreviations "II M" and "II S", by analogy to Tab. 1A, denote respectively the second minimum and second saddle.

Z A	Energy (MeV)	c	h	α	η	Q_2 (b)	Q_3 $(b^{3/2})$	Q_4 (b^2)	Q_{22} (b)	I Barr (MeV)
94	I M=-1787.46	1.21	-0.09	0.00	0.00	29.6	0.0	8.6	0.0	6.64
236	II M=-1786.41	1.42	0.07	0.00	0.00	89.0	0.0	27.0	0.0	(4.50)
	I S=-1780.82	1.30	0.08	-0.12	-0.10	63.6	5.1	11.6	6.7	(4.35)
	II S=-1781.89	1.57	0.04	-0.18	-0.10	114.1	9.8	54.5	5.6	
94	I M=-1800.59	1.21	-0.08	0.00	0.00	30.4	0.0	8.6	0.0	6.92
238	II M=-1799.46	1.41	0.08	0.00	0.00	88.9	0.0	26.2	0.0	(5.00)
	I S=-1793.67	1.30	0.04	-0.12	0.00	59.4	4.3	12.8	0.0	(4.39)
	II S=-1793.26	1.63	0.04	-0.27	-0.15	127.2	16.2	69.2	8.4	
94	I M=-1812.73	1.21	-0.073	0.00	0.00	31.5	0.0	8.4	0.0	7.32
240	II M=-1811.91	1.40	0.083	0.00	0.00	89.4	0.0	25.5	0.0	(5.15)
	I S=-1805.41	1.30	0.080	-0.12	-0.10	65.4	5.3	12.1	6.9	(4.83)
	II S=-1805.09	1.57	0.080	-0.24	-0.15	125.6	17.5	59.4	8.6	
94	I M=-1824.51	1.20	-0.05	0.00	0.00	32.1	0.0	7.5	0.0	7.38
242	II M=-1823.68	1.40	0.09	0.00	0.00	91.1	0.0	25.5	0.0	(5.05)
	I S=-1817.13	1.36	0.00	0.00	-0.25	66.9	0.0	20.1	17.6	(5.55)
	II S=-1818.08	1.60	0.04	-0.21	-0.10	125.4	12.5	64.9	5.8	
94	I M=-1835.87	1.19	-0.04	0.00	0.00	32.1	0.0	6.7	0.0	7.64
244	II M=-1834.68	1.39	0.10	0.00	0.00	92.3	0.0	24.8	0.0	(5.00)
	I S=-1828.23	1.33	0.04	-0.18	-0.10	67.5	7.1	16.9	7.1	(6.29)
	II S=-1827.00	1.48	0.08	-0.30	-0.15	105.6	18.9	40.8	9.5	
94	I M=-1846.75	1.18	-0.02	0.00	0.00	32.7	0.0	5.9	0.0	7.58
246	II M=-1844.73	1.39	0.09	0.00	0.00	93.8	0.0	25.5	0.0	(5.30)
	I S=-1839.17	1.33	0.04	-0.18	-0.10	68.4	7.2	17.2	7.2	(7.01)
	II S=-1839.31	1.54	0.08	-0.24	-0.10	123.6	17.4	55.5	6.1	

Tab. 3A continuation

Z A	Energy (MeV)	c	h	α	η	Q_2 (b)	Q_3 $(b^{3/2})$	Q_4 (b^2)	Q_{22} (b)	I Barr (MeV)
96	I M=-1822.35	1.19	-0.05	0.00	0.00	31.6	0.0	7.5	0.0	7.03
242	II M=-1821.89	1.40	0.08	0.00	0.00	91.7	0.0	26.3	0.0	(5.00)
	I S=-1815.32	1.30	0.04	0.00	-0.05	61.4	0.0	13.2	3.5	(4.28)
	II S=-1815.46	1.54	0.08	-0.18	-0.15	121.2	12.8	53.1	8.9	
96	I M=-1835.06	1.19	-0.04	0.00	0.00	32.1	0.0	7.02	0.0	7.02
244	II M=-1834.50	1.39	0.09	0.00	0.00	93.3	0.0	26.01	0.0	(5.10)
	I S=-1828.02	1.33	0.04	0.00	-0.15	68.2	0.0	16.72	10.6	(5.02)
	II S=-1830.67	1.60	0.04	-0.24	0.00	126.7	14.5	66.2	0.0	
96	I M=-1847.31	1.18	-0.03	0.00	0.00	32.3	0.0	6.5	0.0	7.14
246	II M=-1846.35	1.39	0.10	0.00	0.00	94.5	0.0	25.5	0.0	(4.80)
	I S=-1840.17	1.33	0.04	0.00	-0.15	69.1	0.0	17.0	10.8	(5.81)
	II S=-1841.98	1.57	0.04	-0.30	0.00	119.9	17.3	59.6	0.0	
96	I M=-1859.03	1.18	-0.02	0.00	0.00	32.9	0.0	5.8	0.0	7.16
248	II M=-1857.28	1.39	0.10	0.00	0.00	96.3	0.0	25.7	0.0	(4.80)
	I S=-1851.87	1.33	0.04	0.00	-0.15	70.0	0.0	17.3	10.9	(6.40)
	II S=-1851.85	1.51	0.08	-0.24	-0.10	117.7	16.7	49.3	6.3	
96	I M=-1869.70	1.17	-0.01	0.00	0.00	33.1	0.0	5.2	0.0	7.28
250	II M=-1867.85	1.39	0.10	0.00	0.00	99.3	0.0	26.8	0.0	(4.40)
	I S=-1862.42	1.36	0.04	-0.27	-0.10	75.5	11.6	21.8	7.3	(5.98)
	II S=-1862.64	1.51	0.08	-0.24	-0.10	119.3	17.0	50.2	6.4	
98	I M=-1869.75	1.17	-0.01	0.00	0.00	33.5	0.0	5.6	0.0	7.18
250	II M=-1868.22	1.40	0.11	0.00	0.00	100.9	0.0	27.6	0.0	(3.60)
	I S=-1862.57	1.33	0.04	0.00	-0.15	71.0	0.0	17.6	11.1	(5.88)
	II S=-1862.84	1.51	0.08	-0.24	-0.10	119.2	16.9	50.1	6.4	

Tab. 3A continuation

Z A	Energy (MeV)	c	h	α	η	Q_2 (b)	Q_3 $(b^{3/2})$	Q_4 (b^2)	Q_{22} (b)	I Barr (MeV)
104	I M=-1967.20	1.11	0.06	0.00	0.00	31.0	0.0	-0.19	0.0	
268	II M=-1962.79	1.34	-0.07	0.00	0.00	65.4	0.0	24.1	0.0	6.11
	I S=-1961.09	1.24	0.04	-0.18	-0.20	56.0	7.5	9.7	18.0	
	II S=-1958.76	1.45	0.08	-0.36	-0.25	111.8	25.2	42.5	19.3	
104	I M=-1977.84	1.10	0.05	0.00	0.00	28.7	0.0	-0.22	0.0	
270	II M=-1973.48	1.33	-0.06	0.00	0.00	66.8	0.0	23.4	0.0	5.67
	I S=-1972.17	1.24	0.00	-0.18	-0.05	52.6	6.2	11.5	4.6	
	II S=-1973.16	1.39	0.04	0.00	-0.10	96.2	0.0	31.3	8.0	
104	I M=-1988.42	1.09	0.03	0.00	0.00	23.8	0.0	0.13	0.0	
272	II M=-1985.18	1.34	0.02	0.00	-0.15	81.0	0.0	23.5	13.5	5.12
	I S=-1983.30	1.21	0.04	0.00	-0.15	51.7	0.0	7.1	14.0	
	II S=-1980.78	1.42	0.08	-0.33	-0.25	107.4	23.3	37.3	20.1	
104	I M=-1999.02	1.08	0.01	0.00	0.00	20.5	0.0	0.68	0.0	
274	II M=-1994.46	1.28	-0.02	0.00	0.00	61.9	0.0	17.7	0.0	6.39
	I S=-1992.63	1.21	0.04	-0.30	-0.10	49.7	12.1	7.9	9.6	
	II S=-1994.39	1.36	0.04	-0.33	-0.15	86.0	16.7	26.8	12.8	
104	I M=-2009.18	1.07	0.00	0.00	0.00	18.1	0.0	0.83	0.0	
276	II M=-2004.70	1.27	-0.02	0.00	0.00	61.4	0.0	16.5	0.0	6.42
	I S=-2002.76	1.21	0.04	-0.24	-0.10	51.4	9.9	7.8	9.6	
	II S=-2004.53	1.36	0.04	-0.30	-0.15	87.8	15.6	27.3	12.9	
104	I M=-2018.72	1.06	0.03	0.00	-0.02	16.7	0.0	-0.80	2.8	
278	II M=-2014.63	1.25	0.00	0.00	0.00	59.9	0.0	13.9	0.0	5.46
	I S=-2013.26	1.18	0.04	-0.27	0.00	44.4	10.7	5.5	0.0	
	II S=-2014.00	1.36	0.04	-0.33	-0.15	88.1	17.3	27.7	13.1	
106	I M=-1950.10	1.12	0.04	0.00	0.00	30.8	0.0	0.56	0.0	
266	II M=-1944.77	1.33	-0.08	0.00	0.00	62.8	0.0	22.9	0.0	7.65
	I S=-1942.45	1.15	0.04	-0.15	-0.25	33.9	5.4	2.5	24.12	
	II S=-1945.05	1.39	0.04	-0.15	-0.10	92.9	7.8	30.1	7.86	
106	I M=-1963.15	1.11	0.06	0.00	0.00	31.5	0.0	-0.13	0.0	
268	II M=-1958.41	1.33	-0.07	0.00	0.00	64.7	0.0	23.8	0.0	5.73
	I S=-1957.42	1.24	0.04	0.00	-0.20	57.1	0.0	9.5	17.9	
	II S=-1955.23	1.39	0.04	-0.36	0.00	89.9	18.1	30.6	0.0	

Tab. 4A Same study as in Tab. 3A but for chosen heavy and super–heavy elements on the deformation mesh $\{\Delta c = 0.03, \Delta h = 0.04, \Delta\alpha = 0.03, \Delta\eta = 0.05\}$. Abbreviation "n.e." means "not exists". Meanings of the abbreviations "I M", "II M", "I S", "II S" same as in Tabs. 1A–3A

Z A	Energy (MeV)	c	h	α	η	Q_2 (b)	Q_3 $(b^{3/2})$	Q_4 (b^2)	Q_{22} (b)	I Barr (MeV)
106	I M=-1975.62	1.11	0.06	0.00	0.00	31.4	0.0	-0.68	0.0	
270	II M=-1971.16	1.34	-0.07	0.00	0.00	66.7	0.0	24.8	0.0	5.78
	I S=-1969.84	1.24	0.04	0.00	-0.20	57.8	0.0	9.6	18.1	
	II S=-1967.19	1.45	0.08	-0.36	-0.25	113.1	25.8	43.2	19.5	
106	I M=-1987.03	1.10	0.06	0.00	0.00	28.5	0.0	-1.26	0.0	
272	II M=-1982.56	1.33	-0.06	0.00	0.00	68.4	0.0	24.6	0.0	6.10
	I S=-1980.93	1.27	0.04	-0.30	-0.20	62.7	13.1	13.6	18.1	
	II S=-1982.07	1.42	0.04	0.00	-0.15	104.9	0.0	37.5	11.9	
106	I M=-1998.25	1.09	0.03	0.00	0.00	23.7	0.0	-0.21	0.0	
274	II M=-1993.84	1.32	-0.05	0.00	0.00	68.2	0.0	23.3	0.0	5.61
	I S=-1992.64	1.27	0.00	-0.33	0.00	58.6	11.9	15.2	0.0	
	II S=-1991.77	1.45	0.08	-0.39	-0.20	115.3	28.4	45.2	16.0	
106	I M=-2009.64	1.08	0.01	0.00	0.00	19.6	0.0	0.51	0.0	
276	II M=-2004.87	1.31	-0.03	0.00	0.00	67.6	0.0	21.6	0.0	7.02
	I S=-2002.62	1.21	0.04	-0.30	-0.10	50.2	12.2	8.0	9.7	
	II S=-2002.89	1.39	0.04	-0.24	-0.05	97.6	13.2	33.4	4.1	
106	I M=-2020.61	1.07	0.01	0.00	0.00	17.2	0.0	0.57	0.0	
278	II M=-2015.70	1.30	-0.02	0.00	0.00	66.8	0.0	20.1	0.0	8.49
	I S=-2012.12	1.21	0.04	-0.18	-0.30	50.3	7.7	7.2	29.8	
	II S=-2013.80	1.48	0.04	-0.36	-0.20	118.7	22.6	52.4	16.2	
108	I M=-1940.52	1.12	0.04	0.00	0.00	31.1	0.0	0.62	0.0	
266	II M= n.e.									5.26
	I S=-1935.26	1.27	0.04	-0.21	-0.20	61.9	8.9	12.7	17.3	
	II S=-1935.54	1.42	0.08	-0.24	-0.15	106.8	16.2	35.9	11.4	
108	I M=-1955.00	1.11	0.05	0.00	0.00	31.3	0.0	-0.07	0.0	
268	II M=-1949.70	1.34	-0.07	0.00	0.00	66.5	0.0	24.4	0.0	6.45
	I S=-1948.55	1.21	0.04	0.00	-0.15	50.4	0.0	6.8	13.7	
	II S=-1948.40	1.45	0.08	-0.39	-0.20	111.0	27.1	42.9	15.4	
108	I M=-1968.92	1.11	0.06	0.00	0.00	32.1	0.0	-0.67	0.0	
270	II M=-1964.13	1.34	-0.07	0.00	0.00	67.6	0.0	25.0	0.0	6.61
	I S=-1962.31	1.24	0.04	-0.15	-0.15	57.5	6.3	9.9	13.5	
	II S=-1961.95	1.45	0.08	-0.42	-0.20	111.1	29.3	43.6	15.6	

Tab. 4A continuation

Z A	Energy (MeV)	c	h	α	η	Q_2 (b)	Q_3 $(b^{3/2})$	Q_4 (b^2)	Q_{22} (b)	I Barr (MeV)
108	I M=-1982.23	1.11	0.07	0.00	0.00	31.9	0.0	-1.14	0.0	
272	II M=-1977.69	1.35	-0.07	0.00	0.00	69.5	0.0	26.3	0.0	6.58
	I S=-1975.65	1.24	0.04	-0.12	-0.15	58.5	5.1	10.0	13.7	
	II S=-1975.18	1.45	0.08	-0.42	-0.20	112.5	29.8	44.4	15.8	
108	I M=-1994.43	1.09	0.07	0.00	0.00	28.7	0.0	-1.79	0.0	
274	II M=-1989.93	1.34	-0.05	0.00	0.00	71.0	0.0	25.1	0.0	6.98
	I S=-1987.45	1.18	0.04	-0.15	-0.25	42.9	5.9	4.7	24.6	
108	I M=-2006.34	1.08	0.03	0.00	0.00	22.1	0.0	-0.31	0.0	
276	II M=-2001.96	1.32	-0.04	0.00	0.00	70.6	0.0	23.8	0.0	7.21
	I S=-1999.13	1.21	0.04	-0.36	-0.10	48.8	14.4	8.2	9.7	
	II S=-2000.26	1.45	0.08	-0.39	-0.20	116.7	28.8	46.0	16.1	
108	I M=-2018.75	1.07	0.00	0.00	0.00	17.1	0.0	0.56	0.0	
278	II M=-2013.70	1.32	-0.03	0.00	0.00	70.8	0.0	23.1	0.0	7.43
	I S=-2011.32	1.21	0.04	-0.21	-0.25	50.7	8.9	7.5	24.7	
	II S=-2012.11	1.45	0.08	-0.39	-0.20	118.1	29.2	46.7	16.3	
110	I M=-1927.21	1.12	0.04	0.00	0.00	31.2	0.0	0.66	0.0	
266	II M=-1922.99	1.38	0.00	0.00	0.00	84.4	0.0	28.7	0.0	5.58
	I S=-1921.63	1.27	0.00	-0.39	-0.05	54.2	13.0	14.1	4.4	
	II S=-1922.90	1.42	0.08	-0.30	-0.15	105.2	19.9	35.9	11.4	
110	I M=-1943.06	1.11	0.05	0.00	0.00	31.2	0.0	0.02	0.0	
268	II M=-1938.27	1.38	0.00	0.00	0.00	85.5	0.0	29.2	0.0	4.73
	I S=-1938.33	1.27	0.04	0.00	-0.25	63.6	0.0	12.4	21.9	
	II S=-1938.17	1.42	0.08	-0.33	-0.15	105.6	22.1	36.6	11.6	
110	I M=-1958.39	1.11	0.06	0.00	0.00	31.6	0.0	-0.56	0.0	
270	II M=-1954.86	1.35	0.00	0.00	0.13	79.3	0.0	25.3	-11.3	4.96
	I S=-1953.43	1.27	0.04	-0.06	-0.20	64.9	2.6	12.9	17.7	
	II S=-1952.86	1.42	0.08	-0.36	-0.15	105.8	24.2	37.3	11.8	
110	I M=-1973.16	1.11	0.07	0.00	0.00	32.5	0.0	-1.06	0.0	
272	II M=-1968.43	1.34	-0.05	0.00	0.00	69.2	0.0	24.7	0.0	7.27
	I S=-1965.89	1.24	0.00	-0.15	-0.05	53.5	5.3	11.6	4.6	
	II S=-1966.86	1.42	0.04	0.00	-0.20	104.3	0.0	37.1	15.9	

Tab. 4A continuation

Z A	Energy (MeV)	c	h	α	η	Q_2 (b)	Q_3 $(b^{3/2})$	Q_4 (b^2)	Q_{22} (b)	I Barr (MeV)
110	I M=-1987.26	1.11	0.07	0.00	0.00	32.3	0.0	-1.43	0.0	
274	II M=-1982.74	1.34	-0.06	0.00	0.00	71.1	0.0	26.4	0.0	7.47
	I S=-1979.79	1.24	0.00	-0.12	-0.05	54.5	4.3	11.8	4.6	
	II S=-1980.81	1.36	0.04	-0.15	-0.05	89.9	7.8	27.0	4.2	
110	I M=-2000.18	1.09	0.07	0.00	0.00	29.3	0.0	-2.03	0.0	
276	II M=-1995.87	1.33	-0.04	0.00	0.00	72.7	0.0	25.3	0.0	6.52
	I S=-1993.66	1.15	0.04	0.00	-0.25	36.7	0.0	2.5	25.5	
	II S=-1994.10	1.36	0.04	-0.12	-0.05	91.3	6.4	27.4	4.2	
110	I M=-2013.13	1.06	0.00	0.00	0.00	14.9	0.0	0.47	0.0	
278	II M=-2008.63	1.33	-0.03	0.00	0.00	72.4	0.0	24.4	0.0	7.54
	I S=-2005.59	1.21	0.04	-0.21	-0.25	50.7	8.9	7.5	24.7	
	II S=-2007.70	1.39	0.08	-0.33	-0.10	104.1	22.4	33.6	8.4	
112	I M=-1909.87	1.12	0.03	0.00	0.00	30.6	0.0	1.41	0.0	3.31
266	II M=-1905.10	1.30	0.00	0.00	0.00	65.9	0.0	17.5	0.0	
	I S=-1906.56	1.45	0.08	-0.33	-0.20	111.8	23.1	42.1	15.0	
	II S=-1906.57	1.45	0.08	-0.33	-0.20	111.9	23.1	42.1	15.1	
112	I M=-1926.91	1.12	0.04	0.00	0.00	29.6	0.0	0.84	0.0	4.56
268	II M=-1922.03	1.30	0.00	0.00	0.00	66.7	0.0	17.8	0.0	
	I S=-1922.35	1.18	0.04	-0.39	0.00	39.1	13.9	5.5	0.0	
	II S=-1923.62	1.42	0.08	-0.33	-0.10	105.9	22.0	36.8	7.7	
112	I M=-1943.50	1.11	0.04	0.00	0.00	29.4	0.0	0.38	0.0	3.39
270	II M=-1938.58	1.30	0.00	0.00	0.00	67.5	0.0	18.1	0.0	
	I S=-1940.11	1.39	0.08	-0.21	-0.15	101.9	13.8	30.9	11.9	
	II S=n.e.									
112	I M=-1959.52	1.10	0.06	0.00	0.00	29.1	0.0	-0.77	0.0	
272	II M=-1956.81	1.35	0.00	0.00	0.13	81.1	0.0	25.9	-11.0	6.31
	I S=-1953.21	1.21	0.04	-0.39	-0.05	47.1	15.0	8.1	4.7	
	II S=-1955.59	1.39	0.08	-0.24	-0.15	102.5	16.0	31.5	12.0	
112	I M=-1974.94	1.10	0.07	0.00	0.00	29.5	0.0	-1.49	0.0	
274	II M=-1971.41	1.33	-0.04	0.00	0.00	71.0	0.0	24.5	0.0	6.09
	I S=-1968.85	1.12	0.00	-0.06	-0.35	22.8	1.9	3.2	37.3	
	II S=-1970.54	1.39	0.08	-0.30	-0.10	102.5	19.9	32.4	8.1	

Tab. 4A continuation

Z A	Energy (MeV)	c	h	α	η	Q_2 (b)	Q_3 $(b^{3/2})$	Q_4 (b^2)	Q_{22} (b)	I Barr (MeV)
112	I M=-1989.89	1.09	0.07	0.00	0.00	29.4	0.0	-1.93	0.0	
276	II M=-1986.44	1.33	-0.04	0.00	0.00	72.1	0.0	25.2	0.0	6.94
	I S=-1982.95	1.21	0.04	-0.36	-0.05	49.0	14.4	8.2	4.8	
	II S=-1984.99	1.39	0.08	-0.33	-0.10	102.8	22.1	33.0	8.3	
112	I M=-2003.92	1.09	0.07	0.00	0.00	27.6	0.0	-2.00	0.0	
278	II M=-2000.38	1.34	-0.04	0.00	0.00	74.5	0.0	25.9	0.0	6.31
	I S=-1997.61	1.21	0.04	-0.30	0.00	51.1	12.3	8.1	0.0	
	II S=-1998.69	1.36	0.04	0.00	-0.05	93.0	0.0	27.9	4.2	
114	I M=-1888.50	1.12	0.01	0.00	0.00	28.6	0.0	2.42	0.0	
266	II M=-1885.62	1.28	0.00	0.00	0.00	61.3	0.0	15.1	0.0	2.87
	I S=-1885.62	1.30	0.00	-0.24	-0.05	64.0	8.7	17.4	4.2	
	II S=-1887.24	1.42	0.08	-0.42	-0.10	101.3	26.8	36.2	7.7	
114	I M=-1906.78	1.12	0.02	0.00	0.00	28.2	0.0	1.82	0.0	
268	II M=-1903.60	1.28	0.00	0.00	0.00	62.1	0.0	15.4	0.0	3.46
	I S=-1903.32	1.30	0.04	-0.42	0.00	66.2	17.8	17.1	0.0	
	II S=-1905.63	1.45	0.12	-0.36	-0.20	121.6	32.2	44.5	15.1	
114	I M=-1924.64	1.10	0.03	0.00	0.00	26.6	0.0	0.65	0.0	
270	II M=-1922.13	1.32	0.00	0.00	0.00	72.2	0.0	20.7	0.0	3.58
	I S=-1921.06	1.24	0.00	-0.09	-0.05	53.3	3.1	11.4	4.5	
	II S=-1923.42	1.39	0.08	-0.24	-0.10	101.5	15.7	31.1	7.9	
114	I M=-1942.06	1.10	0.04	0.00	0.00	25.9	0.0	0.07	0.0	
272	II M=-1938.82	1.30	0.00	0.00	0.00	68.3	0.00	18.4	0.0	3.89
	I S=-1938.17	1.24	0.04	-0.03	-0.30	56.8	1.3	9.4	27.8	
	II S=-1940.26	1.39	0.08	-0.24	-0.10	102.8	15.9	31.7	8.0	
114	I M=-1958.82	1.09	0.04	0.00	0.00	26.0	0.0	-0.25	0.0	
274	II M=-1957.32	1.35	0.00	0.00	-0.11	83.0	0.0	26.6	9.8	5.25
	I S=-1953.57	1.27	0.04	-0.15	-0.35	63.2	6.9	12.6	32.4	
	II S=-1956.07	1.39	0.08	-0.33	-0.05	101.7	21.7	32.6	4.1	
114	I M=-1974.83	1.09	0.04	0.00	0.00	25.9	0.0	-0.50	0.0	
276	II M=-1972.99	1.33	-0.04	0.00	0.00	73.0	0.0	25.0	0.0	5.55
	I S=-1969.28	1.24	0.04	-0.15	-0.30	57.4	6.7	9.8	28.6	
	II S=-1971.86	1.42	0.08	-0.39	-0.10	108.9	27.1	39.5	8.2	

Tab. 4A continuation

Z A	Energy (MeV)	c	h	α	η	Q_2 (b)	Q_3 $(b^{3/2})$	Q_4 (b^2)	Q_{22} (b)	I Barr (MeV)
114	I M=-1990.44	1.08	0.04	0.00	0.00	24.5	0.0	-0.51	0.0	
278	II M=-1988.75	1.34	-0.04	0.00	0.00	73.8	0.0	25.7	0.0	5.65
	I S=-1984.79	1.18	0.04	-0.09	-0.25	44.4	3.7	4.7	25.1	
	II S=-1987.21	1.42	0.08	-0.39	-0.10	110.2	27.5	40.1	8.3	
116	I M=-1920.93	1.08	0.00	0.00	0.00	20.1	0.0	1.07	0.0	2.07
272	I S=-1918.86	1.27	0.00	-0.24	0.00	59.4	8.7	14.8	0.0	
116	I M=-1939.17	1.06	0.00	0.00	0.00	15.4	0.0	0.91	0.0	
274	II M=-1938.80	1.35	0.00	0.00	0.00	83.7	0.0	26.7	0.0	3.53
	I S=-1935.64	1.27	0.04	-0.18	-0.35	62.9	8.3	12.7	32.5	
	II S=-1938.64	1.39	0.08	-0.27	-0.10	103.3	18.1	32.3	8.1	
116	I M=-1957.19	1.05	0.00	0.00	0.00	12.3	0.0	0.94	0.0	
276	II M=-1956.35	1.35	0.00	0.00	-0.10	83.9	0.0	26.6	9.0	4.13
	I S=-1953.06	1.27	0.04	-0.06	-0.35	64.7	2.8	12.7	32.7	
	II S=-1955.45	1.39	0.04	0.00	-0.10	99.6	0.0	32.8	8.2	
116	I M=-1974.96	1.05	-0.06	0.00	0.00	8.2	0.0	3.84	0.0	
278	II M=-1973.17	1.34	-0.03	0.00	0.00	75.2	0.0	25.8	0.0	5.40
	I S=-1969.56	1.24	0.04	0.00	-0.30	58.9	0.0	9.8	28.8	
	II S=-1974.09	1.48	0.12	-0.36	-0.20	138.7	37.0	57.2	15.7	

Tab. 4A continuation

Bibliography

[1] C.F. v. Weizsäcker, Z. Phys. **96** (1935) 431,

[2] H.A. Bethe, F. Bacher, Rev. Mod. Phys. **8** (1936) 426,

[3] D.L. Hill and J.A. Wheeler, Phys. Rev. **89** (1953) 1102,

[4] W.D. Myers, W. Świątecki, Ark. Phys. **36** (1967) 343,

[5] W.D. Myers, W.J. Świątecki, Ann. Phys. **55** (1970) 395,

[6] W.D. Myers, W.J. Świątecki, Nucl. Phys. **A81** (1966) 1,

[7] H.v. Groote and E. Hilf, Nucl. Phys. **A129** (1969) 513,

[8] K. Pomorski, J. Dudek, Phys. Rev. **C67** 044316 (2003),

[9] A. J. Sierk, Phys. Rev. **C33** (1986) 2039,

[10] M. S. Antony, Nuclide Chart 2002, Strasbourg 2002, Impressions

[11] P. Möller, W.D. Myers, W.J. Świątecki, J. Treiner,
At. Data Nucl. Data Tables **39** (1988) 225,

[12] W.D. Myers, W.J. Świątecki, Nucl. Phys. **A601** (1996) 141,

[13] T.H.R. Skyrme, Nucl. Phys. **9** (1959) 615,

[14] D. Vautherin, D.M. Brink, Phys. Rev. **C5** (1972) 626,

[15] J. Dechargé, D. Gogny, Phys. Rev. **C21** (1980) 1568,

[16] J.W. Negele, Rev. Mod. Phys. **54** (1982) 913,

[17] P. Quentin, H. Flocard, Ann. Rev. Nucl. Part. Sci. **28** (1978) 523,

[18] M. Brack, C. Guet, H.-B. Håkansson, Phys. Rep. **123** (1985) 275,

[19] Y.M. Engel, D.M. Brink, K. Goeke. S.J. Krieger and D. Vautherin,
Nucl. Phys. **A249** (1975) 215,

[20] K. Bencheikh, P. Quentin, J. Bartel, Nucl. Phys. **A571** (1994) 518,

[21] P. Hohenberg, W. Kohn, Phys. Rev. **136** (1964) 864,

[22] J. Bartel, M. Brack and M. Durand, Nucl. Phys. **A445** (1985) 263,

[23] M. Centelles, M. Pi, X. Vinas, F. Garcia, M. Barranco, Nucl. Phys. **A510** (1990) 397,

[24] J. Bartel, P. Quentin, M. Brack, C. Guet and H.-B. Håkansson, Nucl. Phys. **A386** (1982) 79,

[25] M. Beiner, H. Flocard, Nguyen van Giai and P. Quentin, Nucl. Phys. **A283** (1975) 29,

[26] E. Chabanat, P. Bonche, P. Haensel, J. Meyer, R. Schaeffer, Nucl. Phys. **A627** (1997) 710,

[27] M.J. Giannoni, P. Quentin, Phys. Rev. **21** (1980) 2076,

[28] P. Bonche, H. Flocard and P.-H. Heenen, Nucl. Phys. **A467** (1987) 115,

[29] J.C. Slater, Phys. Rev. **81** (1951) 85,

[30] E.P. Wigner, Phys. Rev. **40** (1932) 749,

[31] J.G. Kirkwood, Phys. Rev. **44** (1933) 31,

[32] G. Baraff and S. Borowitz, Phys. Rev. **121** (1961) 1704,

[33] B. Grammaticos and A. Voros, Ann. Phys. **129** (1980) 153,

[34] K. Pomorski, P. Ring, G. A. Lalazissis, A. Baran, Z. Łojewski, B. Nerlo–Pomorska, and M. Warda, Nucl. Phys. **A624** (1997) 349,

[35] J.F. Berger and K. Pomorski, Phys. Rev. Lett. **85** (2000) 30,

[36] A. Dobrowolski, K. Pomorski, J. Bartel, Phys. Rev. **C65**, 041306R (2002),

[37] W.D. Myers, W.J. Świątecki, Nucl. Phys. **81** (1966) 1,

[38] M. Warda, B. Nerlo–Pomorska, and K. Pomorski, Nucl. Phys. **A635** (1998) 484,

[39] W. Hasse, W. D. Myers, *Geometricl Relationships of Macroscopic Nuclear Physics*, Springer–Verlag, Heidelberg, 1988,

[40] R. Bass, Nucl. Phys. **A231** (1974) 45,

[41] R. Bass, in.: Proc. Conf. on *Deep Inelastic and Fusion Reactions with Heavy Ions*, Berlin, Springer, Berlin 1979,

[42] H.J. Krappe, J.R. Nix, A. J. Sierk, Phys. Rev. **C20** (1979) 992,

[43] H. Feshbach, Ann. Phys. (N.Y.) **19** (1962) 287,

[44] J. Błocki, J. Randrup, W. J. Świątecki, and C.F. Tsang, Ann. Phys. (N.Y.) **105** (1977) 427,

[45] P. Fröbrich and I.I. Gontchar, Phys. Rep. **292** (1998) 131,

[46] I.I. Gonchar, M. Dasgupta, D.J. Hinde, R.D. Butt, and A. Mukherjee, Phys. Rev. **C65** 034610 (2002),

[47] K. Pomorski and K. Dietrich, Z. Physik **A295** (1980) 335,

[48] V.Y. Denisov and W. Nörenberg, Eur. Phys. Journ. **A15** (2002) 375,

[49] E. Chabanat, P. Bonche, P. Haensel, J. Mayer, and R. Schaefer, Nucl. Phys. **A635** (1998) 231, Nucl. Phys. **A635** (1998) 231,

[50] G.F. Bertsch, Z. Phys. **A289** (1978) 103,

[51] A. Lukasiak, W. Cassing, W. Nörenberg, Nucl. Phys. **A426** (1984) 181,

[52] D. Berdichevsky, A. Łukasiak, W. Nörenberg, and P. Rozmej, Nucl. Phys. **A502** (1989) 395,

[53] W.D. Myers and W.J. Świątecki, Phys. Rev. **C62**, 044610 (2000),

[54] W.D. Myers and W.J. Świątecki, Ann. Phys. (N.Y. 55) (1969) 395,

[55] W.D. Myers and W.J. Świątecki, Nucl. Phys. **A336** (1980) 267,

[56] R. Moustabchir and G. Royer, Nucl. Phys. **A683** (2001) 266,

[57] A. Dobrowolski, K. Pomorski, J. Bartel, Nucl. Phys. **A729** (2003) 713,

[58] K. Pomorski, W. Przystupa, J. Richert Acta Phys. Pol. **B25** (1994) 751,

[59] C.J. Batty, E. Friedman, H.J. Gils, and H. Rebel, Adv. Nucl. Phys. **19** (1989) 1,

[60] A. Baran, J.L. Egido, B. Nerlo–Pomorska, K. Pomorski, P. Ring, and L.M. Robledo, J. Phys. **G21** (1995) 657,

[61] A. Dobrowolski, K. Pomorski, J. Bartel, Acta Phys. Pol. **B36** (2005) 1373,

[62] K. Siwek–Wilczyńska, J. Wilczyński, Phys. Rev. **C69** 024611 (2004),

[63] Ch. Leclercq–Willain, Nucl. Phys. **A459** (1986) 227,

[64] F.L.H. Wolfs, Phys. Rev. **C36** (1987) 1359,

[65] J. Marten, P. Fröbrich, Nucl. Phys. **A545** (1992) 854,

[66] P. Fröbrich, B. Strack, M. Durand, Nucl. Phys. **A406** (1983) 557,

[67] A. Dobrowolski, K. Pomorski, J. Bartel, Int. Jour. Mod. Phys. **E13** (2004) 309,

[68] D.H.E. Gross and H. Kalinowski, Phys. Rep. **45C** (1978) 175,

[69] W.Q. Shen *at al.*, Phys. Rev. **C36** (1987) 115,

[70] Electronic database: http://nrv.jinr.ru/nrv/webnrv/fusion/reactions.php,

[71] M. Brack, J. Damgaard, A.S. Jensen, H.C. Pauli, V.M. Strutinsky, C.Y. Wong, Rev. Mod. Phys. **44** (1972) 320,

[72] K. Pomorski, J. Bartel Int. Jour. Mod. Phys. **E15** (2006) 417,

[73] S. Trentalange, S.E. Koonin, A.J. Sierk, Phys. Rev. **C22** (1980) 1159,

[74] A. Dobrowolski, J. Bartel, K. Pomorski, Int. Jour. Mod. Phys. **E14** (2005) 457,

[75] A. Sobiczewski, I. Muntian, Z. Patyk, Phys. Rev. **C63** 034306 (2001),

[76] K.T.R. Davies, J.R. Nix, Phys. Rev. **C14** (1976) 1977,

[77] W.J. Świątecki, *Proceedings of the Second International Conference on Nuclidic Masses*, Vienna, 1963 (Springer, Vienna),

[78] V.M. Strutinsky, Sov. J. Nucl. Phys. **3** (1966) 449; Nucl. Phys. **A95** (1967) 420,

[79] K. Pomorski, Phys. Rev. **C70** 044306 (2004),

[80] S.G. Nilsson, *at al.*, Nucl. Phys. **A131** (1969) 1,

[81] R.D. Woods, D.S. Saxon, Phys. Rev. **95** (1954) 557,

[82] P. Möller, J.R. Nix, Atomic Data and Nuclear Data Tables **59** 185-381 (1995),

[83] V.A. Chepurnov, Yad. Fiz. **6** (1968) 955, Nucl. Phys. **A435** (1985) 397,

[84] N. Schunck, Ph.D. Thesis, ULP, Strasbourg, (2001),

[85] U. Götz, H. C. Pauli, K. Alder, Nucl. Phys. **A175** (1971) 481,

[86] M. Bolsterli, *at al.*, Phys. Rev. **C5** (1972) 1050,

[87] J. Bardeen, L.H. Cooper, I.L. Schriffer, Phys. Rev. **108** (1957) 1175,

[88] S.T. Balyaev, Mat. Fys. Medd. Dan. Vid. Selsk. **31** (1959) 11,

[89] A. Staszczak, S. Piłat, K. Pomorski, Nucl. Phys. **504** (1989) 589,

[90] R. Smolańczuk, J. Skalski, and A. Sobiczewski, Phys. Rev. **C52** (1995) 1871,

[91] P. Möller, J.R. Nix, W.D. Myers, and W.J. Świątecki,
Atomic Data Nucl. Data Tables **59** (1995) 185,

[92] Z. Łojewski and A. Staszczak, Nucl. Phys. **A657** (1999) 134,

[93] A. Dobrowolski, K. Pomorski, J. Bartel, *Influence of different proton and neutron deformations on fission barrier heights*, Physica Scripta, in print,

[94] A. Mamdouh, J.M. Pearson, M. Rayet, F. Tondeur, Nucl. Phys. **A664** (1998) 389,

[95] B. Hayes, Am. Sci. **88** (2000) 481,

[96] P. Möller et al., arXiv: nucl-th/0401058 v1 (2004),

[97] K. Mazurek, Ph.D. Thesis, UMCS, Lublin, (2004),

[98] A. Dobrowolski, K. Pomorski, J. Bartel, Int. Jour. Mod. Phys. **E15** (2006) 432,

[99] B.K. Jennings, PhD thesis, McMaster Univ. (1976),

[100] K. Pomorski, arXiv: physics, 0404018 v1, (2004) 5.

Résumé

Dans ce travail de thèse des ingrédients essentiels pour la description théorique de la dynamique des réactions de fusion et fission nucléaires sont étudiés, tel que le potentiel d'interaction entre noyaux cible et projectile pour le processus de fusion et l'énergie de déformation dans un espace multidimensionel pour la fission. Nous avons évalué en particulier l'importance de la différence des distributions de densités protons et neutrons. Pour le processus de fusion, le potentiel d'interaction entre les noyaux peut être déterminé à travers des densités obtenues d'une façon auto-consistante par des calculs variationnels semi-classiques à partir d'une interaction nucléon-nucléon effective de type Skyrme. Les barrières de fusion ainsi obtenues permettent d'évaluer des sections efficaces de fusion dans le cadre du formalisme de Langevin. Pour le processus de fission il est essentiel de tenir compte de la grande richesse de formes nucléaires qui apparaissent tout au long du chemin de fission de l'état fondamental jusqu'au point de scission. Nous montrons qu'une paramétrisation tenant compte de l'élongation, ainsi que de la possible constriction, asymétrie gauche–droite et non-axialité du noyau, est effectivement capable dans le cadre de notre approche macroscopique-microscopique de donner une description précise de ce phénomène. On peut ainsi *enrichir* l'expression de l'énergie de type *goutte liquide* par un terme qui décrit la variation de l'énergie de liaison nucléaire due aux différentes déformations des distributions protons et neutrons. La réduction des hauteurs des barrières de fission qui en résulte est *seulement* de l'ordre du MeV, mais il peut facilement en résulter un changement de la section efficace de fission d'un ordre de grandeur et ainsi jouer une rôle capital pour la stabilité des noyaux super-lourds ou des noyaux exotiques.

Abstract

This thesis work is centred on some essential ingredients of a theoretical description of the reaction dynamics of the nuclear fusion and fission process, such as the interaction potential between projectile and target nuclei for fusion and the deformation energy landscape in a multidimensional space for the fission process. We have in particular evaluated the importance of the difference between the neutron and proton density distributions on these two precesses. The fusion potential between the two interacting nuclei is obtained through the nucleon densities, determined in a self-consistent way through semiclassical density variational calculations for a given effective nucleon-nucleon effective interaction of the Skyrme type. These fusion barriers can then be used in a Langevin formalism to evaluation fusion cross sections. For the fission process it turns out to be essential to allow for the large variety of shapes which appear between the nuclear ground state and the the scission configuration. We show that a shape parametrisation taking into account elongation, as well as possible neck formation, left-right asymmetry and non-axiality allows, indeed, for a precise description of this phenomena in the framework of the macroscopic-microscopic approach. We are thus able to enrich the expression of the liquid-drop type energy through a term which describes the variation of the nuclear energy due to a deformation difference between the proton and neutron distribution. The resulting reduction of the fission barriers is only of the order of an MeV but this can easily cause an change in the fission cross section by an order of magnitude and thus play an capital role for the stability of super-heavy of exotic nuclei.